

The Pennsylvania State University
The Graduate School
College of Engineering

**EXPERIMENTAL INVESTIGATION OF DYNAMIC
STABILIZATION OF THE RAYLEIGH-BÉNARD INSTABILITY
BY ACCELERATION MODULATION**

A Dissertation in
Acoustics
by
Anand Swaminathan

© 2017 Anand Swaminathan

Submitted in Partial Fulfillment
of the Requirements
for the Degree of

Doctor of Philosophy

December 2017

The dissertation of Anand Swaminathan was reviewed and approved* by the following:

Steven L. Garrett
Professor of Acoustics, Retired
Dissertation Advisor, Chair of Committee

Robert M. Keolian
Associate Professor Emeritus of Acoustics

Diane M. Henderson
Professor of Mathematics

Robert W. M. Smith
Research Associate, Applied Research Laboratory
Special Member

Victor W. Sparrow
Professor of Acoustics
Director of the Graduate Program in Acoustics

*Signatures are on file in the Graduate School.

Abstract

This dissertation presents the results of an experimental investigation of the parametric stabilization of Rayleigh-Bénard convection through the imposition of vibration. It has been theorized for many years that vibration could be employed to suppress natural convection, in an analogous manner to the Kapitza pendulum. The ability to dynamically stabilize Rayleigh-Bénard convection using acceleration modulation is of interest to groups who design and study thermoacoustic machines, as the introduction of parasitic convection can have deleterious effects on the desired operation and efficiency of the device. These performance issues caused by suspected convective instability have been seen both in traveling wave thermoacoustic refrigerators and in cryogenic pulse tube chillers. This dissertation reports the results of an experiment intended to determine the vibratory, fluidic, and geometric conditions under which a small, rectangular container of statically unstable fluid may be stabilized by vertical vibration, incorporating the computational methods of R. M. Carbo [J. Acoust. Soc. Am. **135**(2), 654–668 (2014)]. Measurements are obtained using a large-displacement kinematic shaker of an original design with the convecting gas characterized using both thermal transport measurements and flow visualization employing tracer particles illuminated by a diode laser light sheet phase-locked to the shaker. These experiments are believed to be the first demonstrating the suppression of convection through vibration in rectangular containers of macroscopic scale.

Table of Contents

List of Figures	vii
List of Tables	xiv
List of Symbols	xvi
Acknowledgments	xix
Chapter 1	
Introduction	1
1.1 Modulated Rayleigh-Bénard Convection	3
1.2 Motivation	5
1.3 Parametric Modulation	8
1.4 Rayleigh-Bénard Convection	11
1.5 Parametrically Modulated Rayleigh-Bénard Convection	17
1.6 Prior Numerical Results	21
1.7 Previous Experiments	27
1.8 Choice of Experimental Medium and Geometric Design of the Ex- periment	33
1.9 The Boussinesq Approximation and Linearity	37
1.10 Outline	42
Chapter 2	
Experimental Design	45
2.1 Parameter Evaluation	46
2.1.1 Experimental Fluid Selection	46
2.1.2 Further Evaluation	51
2.2 Shaker Systems	53
2.2.1 Rhombic Shaker	55
2.3 Imaging Techniques Surveyed	63

2.3.1	Shadowgraphy	63
2.3.2	Particle Seeding Techniques	69
2.4	Visualization Techniques Employed	74
2.4.1	Diode Laser System	74
2.4.2	Camera Phase Synchronization	79
2.5	Thermal Measurement Techniques	83
2.5.1	Heater Power Differential	84
2.5.2	Heat Flux Meters	86
2.5.3	In-Flow Temperature Measurement	87
2.6	Experimental Cell Design	88
2.6.1	The $\Gamma = 5$ Cell	89
2.6.2	The $\Gamma = 3$ Cell	97
2.7	Apparatus Fabrication	102

Chapter 3

	Procedures and Techniques	104
3.1	Thermal Measurement Scheme and Data Acquisition	105
3.2	Shaker Control and Measurements	108
3.3	Optical Measurements	109
3.3.1	Impacts of Optical Measurement on Flow Conditions	112
3.4	Static Measurements	117
3.4.1	Instability Determination	119
3.4.2	Goodness of Fit Metrics	122
3.4.3	Static Measurement Refinements	122
3.4.4	Static Measurements with Visualization	124
3.4.5	Static Measurement Interpretation	125
3.5	Shaking Measurements	127
3.5.1	Fixed ΔT , Varying $ \mathbf{v} $	128
3.5.2	Varying ΔT , Fixed $ \mathbf{v} $	131
3.5.3	Shaking Flow Visualization Measurements	133
3.6	Other Experimental Challenges	134

Chapter 4

	Experimental Results	137
4.1	Static Thermal Results	137
4.1.1	Static Results: $\Gamma = 5$ Experiment	137
4.1.2	Static Results: $\Gamma = 3$ Experiment	139
4.1.3	Discussion of Static Thermal Measurements	140
4.1.4	Static Flow Visualization Measurements	141
4.2	Shaking Dynamic Stabilization Results	146

4.2.1	$\Gamma = 5$ Shaking Thermal Measurements	147
4.2.2	$\Gamma = 5$ Shaking Flow Visualization Measurements	150
4.2.3	$\Gamma = 3$ Shaking Thermal Measurements	158
4.2.4	$\Gamma = 3$ Shaking Flow Visualization Measurements	161
4.3	Conclusions	164
Chapter 5		
	Conclusions and Future Work	166
5.1	Conclusions	167
5.2	Potential Experimental Improvements	171
5.3	Future Work and Extensions	173
5.4	Closing Words	175
Appendix A		
	Derivations	177
A.1	Derivation of the Peak Shaker Velocity from Dimensionless Groups	177
Appendix B		
	Nondimensional Results	180
B.1	$\Gamma = 5$ Pre-Disassembly Results	181
B.2	$\Gamma = 5$ Post-Reassembly Results	183
B.3	$\Gamma = 3$ Results	184
Appendix C		
	Laser Diode Array Documentation	186
Appendix D		
	Reprint of Carbo Theory Paper	198
	Bibliography	214

List of Figures

1.1	Image of convection cells as viewed from above (through the free surface in contact with room air) published in Bénard’s original 1900 paper [2]. (Paper obtained from the <i>Bibliothèque nationale de France</i>).	2
1.2	Statically unstable systems of advancing complexity that can be stabilized by vibration parallel to gravity. [Image courtesy of Dr. Robert W. M. Smith]	11
1.3	Geometry of the experimental container with dimensions.	12
1.4	Example of a sample stability map as computed by Carbo [16] for an infinite layer, rigid horizontal boundary, shaken Rayleigh-Bénard convection system with $Ra = 10^4$, $Pr = 7$, and $a = 3.117$. Nondimensional frequency ω^* is plotted on the y-axis and nondimensional acceleration ϵ on the x-axis. Carbo notes that the blotches at the bottom of the plot are associated with poor numerical accuracy in that region.	23
1.5	Critical vibrational Rayleigh number for the upper stability boundary shown as a function of aspect ratio for a square cross-section ($\Gamma_x = \Gamma_y$) container with a rectangular drive and insulating side-walls [16].	26
2.1	Excerpt from the gas experimental parameters spreadsheet for a 2 cm cube. The spreadsheet also includes the parameters required to assess the operating state for adherence to the Boussinesq approximation (seen in Figure 2.2).	48
2.2	A sample of the spreadsheet columns of the parameter evaluation for adherence to the Boussinesq approximation.	48
2.3	Excerpt from the liquid experimental parameters spreadsheet for a 2 cm cube. The spreadsheet also includes the parameters required to assess the operating state for adherence to the Boussinesq approximation (seen in Figure 2.2).	49

2.4	Excerpt from the air experimental parameters spreadsheet for a 2.121 cm cube.	51
2.5	Plot of the upper boundary for a cubical container ($\Gamma_x = \Gamma_y$) with two mechanical boundary conditions. The boxed region corresponds to the accessible region in space determined for a 2 cm cubical container of air under the experimental limits. Note that the region enclosed by the box varies based on the choice of aspect ratio, container size, and experimental fluid.	52
2.6	Performance curves for a sample medium-size electromagnetic shaker produced by Data Physics corporation [57]. The plot on the left shows peak acceleration as a function of frequency and the plot on the right shows peak velocity as a function of frequency (note that the y -axis label is incorrect in the original publication). Specifications for this shaker are: peak sine force: $F = 650$ N, maximum table load: $M_{max} = 25$ kg, frequency range: $f = 2-7,000$ Hz, maximum peak-to-peak stroke: $S_{max} = 2.54$ cm, and maximum bare-table velocity: $v_{max} = 1.5$ m/s. This shaker is equipped with an automatic pneumatic load compensation system.	55
2.7	Detail view of the experimental carriage. Lengths a and l are denoted for reference.	58
2.8	Detail view of the gearing arrangement.	60
2.9	An example image from the shadowgraph testing that was performed. Thermal plumes can barely be seen in the frame convecting away from the heated plate at the bottom of the frame. This image was background subtracted and brightened in post processing. The temperature is displayed at the lower right of the frame.	68
2.10	An example of the computed scattering field of an incense particle.	71
2.11	A diagram of the imaging system used for testing the seeded imaging. Note that the light sheet optic is depicted vertically to clearly show that it is a cylindrical lens. In reality, the length of the lens extends into the plane of the page.	73
2.12	An example image from the smoke flow visualization testing. The red arrows were added to indicate the direction of motion that was noted from the analysis of multiple video images. This image had a $7\times$ intensification applied to the captured values to make the fluid motion plainly visible. Note the striations in the light sheet.	74

2.13	An example image from the smoke flow visualization testing. The Rayleigh number in this image is $Ra = 5.9 \times 10^4$ ($Ra/Ra_c = 18.0$). The red arrows were added to indicate the direction of motion of the large-scale circulation that was noted from the analysis of multiple video images and the green oval highlights a thermal plume emission that was noted. This image had a $7\times$ intensification applied to the captured values to make the fluid motion plainly visible.	75
2.14	Photograph of the 20 W optical output, 675 nm wavelength, diode laser array light sheet source. This laser is mounted on a water-cooled heat exchanger. At the bottom right of the cooling plate one of the two (black rubber) chilled water supply hoses can be seen. The heavy gauge cables attached to the laser emitter are the electrical connections to the anode and cathode of the laser diode array.	77
2.15	Photograph of the laser safety enclosure. The front service access panel has been opened to show the shaker flywheels inside the enclosure; this would normally be closed for operation. The CCD camera is mounted on a tripod, accessing the experiment through a round viewport, and the laser-rated window (green tinted) can also be seen.	79
2.16	Sample triggering signal produced using a Kikusui COS6100A oscilloscope. The input signal was a simulated shaker motion input produced by a function generator. The square wave triggering signal seen superimposed on the trace is manually adjustable through the normal means used for oscilloscope triggering.	81
2.17	A schematic view of the components of the camera triggering circuit employed to produce a camera image phase-locked to a time-harmonic signal.	82
2.18	An example of an early differential heater measurement from a 1935 paper by R. J. Schmidt and S. W. Milverton. This plot is Figure 2 in the paper [98]. Note that this plot arranges the x and y -axes in the opposite orientation from those shown in this work. The horizontal axis here is the square of the electrical current (proportional to power) supplied to the lower plate heater and the vertical axis is the temperature difference between the plates, ΔT . While not denoted here, the current is measured in units of amperes.	85
2.19	CAD rendering of the $\Gamma = 5.0$ cell, as built. In experimental usage, the cell is enclosed in layers of thermal insulation.	90

2.20	Sample of the thermal images obtained while testing the heated plate for the liquid apparatus. The black mark in the center of the image and the line leading away from it are the thermocouple and wire that was attached to the surface of the plate for this testing.	93
2.21	Construction drawing for the cooling plate that was designed for the convection experiment. The entire chamber is topped with a lid that is sealed to this lower portion with an O-ring seal.	94
2.22	Sample of the thermal images obtained while testing the cooled plate for the liquid apparatus. The cooling water through this plate entered at 14.8°C from the temperature controlled circulator. The aberrant small hot spots in the center of the plate are the result of near-room-temperature water droplets pooling on the face of the plate during testing.	95
2.23	A photograph of the fully insulated $\Gamma = 5$ experimental cell. Note that the front face must be left optically transparent as is a rectangular opening (a “slit”) at the side to admit the laser light sheet for illumination.	97
2.24	CAD rendering of the $\Gamma = 3.0$ cell, as built. In experimental usage, the cell is enclosed in layers of thermal insulation.	99
2.25	CAD rendering of the $\Gamma = 3.0$ cell, shown in cross section. Note the double wall experimental enclosure.	100
3.1	A block diagram representing the components of the heater power differential control loop and their interconnections.	106
3.2	Illustration of the light sheet positioning relative to the experimental cell walls.	110
3.3	(a) Plot of the computed results for the depression of the static critical temperature difference ΔT_c as a function of additional carbon dioxide fraction (ranging from 0.0 to 1.0), with 0.0 being normal dry air. These computations are for the $\Gamma = 5$ cell. Crosses denote computed values and the line is a quadratic fit to those points. (b) Equivalent computations for change in Prandtl number Pr	114
3.4	Image from the initial investigation of static convection onset. The anomalous rotational flow near the illuminated side of the container can be seen to the right of the image. In this image $\Delta T = 2.0$ K.	116
3.5	Image from static testing with the pulsed laser (rate = 8 Hz). The dark region at the top of the cell is a consequence of sedimentation of the smoke particulates due to the lack of convective flow. The temperature difference here is the same as in Figure 3.4, $\Delta T = 2.0$ K.	117

3.6	Results from an example static experiment. The experimental data is fit using the two lines SSR approach described. The vertical dotted line shows the theoretical instability prediction of Carbo for this cell.	120
3.7	Results from the 445 point static measurement data set from the $\Gamma = 5$ cell, showing the optimized stable and unstable fit lines. Note that there is one individual run that displays some downward deflecting outlier points in the region $\Delta T \gtrsim 6.0$ K. The cause of this marked deviation is unknown.	124
3.8	Example of a shaking experimental result obtained by varying the shaker velocity with a fixed temperature difference. This shows data from the $\Gamma = 5$ cell at a fixed temperature difference of $\Delta T = 4.32$ K ($Ra = 2062$). X's denote the experimental data and lines fits to the suspected stable and unstable regions. The dotted vertical line shows the theoretical prediction of Carbo for these conditions. . . .	129
3.9	Example of a shaking experimental result obtained by varying the shaker velocity with a fixed temperature difference. This shows data from the $\Gamma = 5$ cell at a fixed temperature difference of $\Delta T = 4.50$ K ($Ra = 2148$). X's denote the experimental data.	130
3.10	Example of a shaking experimental result obtained by varying the temperature difference ΔT while holding the shaker peak velocity $ \mathbf{v} $ fixed. This shows data from the $\Gamma = 5$ cell at a fixed shaker peak velocity of $ \mathbf{v} = 2.49$ m/s. X's denote the experimental data and lines fits to the suspected stable and unstable regions.	133
4.1	Time evolution of the static $\Gamma = 5$ cell with the temperature difference beginning at $\Delta T = 0$ and rapidly increasing to $\Delta T = 6.0$ K. The images progress in time left-to-right and top-to-bottom. All images have been brightened by 25 % in post processing for better reproduction on the page. These images do not show the full width of the experimental enclosure due to the focal length of camera lens employed; this was improved in later measurements.	142

4.2	Time evolution of the static convection flow pattern of the $\Gamma = 3$ cell. The images progress left-to-right and top-to-bottom, and were captured, in order, at temperature differences of $\Delta T = 4.0, 5.0, 6.0, 6.5, 7.0, 8.0, 9.0,$ and 10.0 K. The thermally-determined static transition was found to be $\Delta T_c = 6.264$ K. All images have been brightened by 25 % in post processing for better reproduction on the page. The images have been cropped to the outer edge of the inner enclosure, simplifying the images by neglecting the quiescent insulation gap between the inner and outer enclosures of the $\Gamma = 3$ experiment.	143
4.3	Plot of the shaking dynamic stabilization results obtained on the pre-disassembly $\Gamma = 5$ experimental cell. This data was acquired using the fixed ΔT , variable $ \mathbf{v} $ method and presents graphically the same data as Table 4.4.	148
4.4	Plot of the shaking dynamic stabilization results obtained on the reassembled $\Gamma = 5$ experimental cell. This data was acquired using the variable ΔT , fixed $ \mathbf{v} $ method and presents graphically the same data as Table 4.5.	149
4.5	Flow visualization image from the $\Gamma = 5$ cell exhibiting the anomalous and asymmetrical plume behavior observed in an otherwise stable and quiescent shaken fluid. The red arrows were added to illustrate the direction of plume flow.	151
4.6	Flow visualization images from the reassembled $\Gamma = 5$ cell showing the flow evolution from below to above transition. These images represent (top-to-bottom) $\Delta T = 2.75$ and 5.5 K. These images were taken at $ \mathbf{v} = 2.587$ m/s. The theoretical transition is $\Delta T = 3.675$ K and the thermally measured transition is found to be $\Delta T = 5.006$ K. Images have been brightened in post processing for better reproduction on the page.	154
4.7	Flow visualization images from the reassembled $\Gamma = 5$ cell showing the flow evolution from below to above transition. These images represent (top-to-bottom) $\Delta T = 2.75, 3.25, 4.0, 6.0,$ and 7.5 K. These images were taken at $ \mathbf{v} = 2.300$ m/s. The theoretical transition is $\Delta T = 3.586$ K and the thermally measured transition is found to be $\Delta T = 3.750$ K. Images have been brightened in post processing for better reproduction on the page.	155

4.8	Flow visualization images from the reassembled $\Gamma = 5$ cell showing the flow evolution from below to above transition. These images represent (top-to-bottom) $\Delta T = 2.75, 3.25, 3.5, 3.75, 4.0,$ and 6.0 K. These images were taken at $ \mathbf{v} = 2.347$ m/s. The theoretical transition is $\Delta T = 3.598$ K and the thermally measured transition is found to be $\Delta T = 3.747$ K. Images have been brightened in post processing for better reproduction on the page.	157
4.9	Flow visualization images from the reassembled $\Gamma = 5$ cell showing examples of vibration-induced perturbations on convective motion. These images were obtained over the course of about 2.5 minutes at $\Delta T = 6.0$ K and $ \mathbf{v} = 1.77$ m/s. Images have been brightened in post processing for better reproduction on the page.	158
4.10	Plot of the shaking dynamic stabilization results obtained on the $\Gamma = 3$ experimental cell. This data was acquired using the variable ΔT , fixed $ \mathbf{v} $ method and presents graphically the same data as Table 4.6.	159
4.11	Flow visualization images from the $\Gamma = 3$ cell showing the flow evolution from below to above transition. These images represent (top-to-bottom) $\Delta T = 4.0, 6.0, 7.0, 8.0,$ and 14.0 K. These images were taken at $ \mathbf{v} = 2.444$ m/s. The theoretical transition is $\Delta T = 8.200$ K and the thermally measured transition is found to be $\Delta T = 7.892$ K. Images have been brightened in post processing for better reproduction on the page.	163
B.1	Critical vibrational Rayleigh number for the upper stability boundary shown as a function of aspect ratio for a square cross-section ($\Gamma_x = \Gamma_y$) container with a rectangular drive and insulating side-walls [16].	181
B.2	Plot of the shaking dynamic stabilization results obtained on the pre-disassembly $\Gamma = 5$ experimental cell presented in dimensionless variables. This data was acquired using the fixed ΔT , variable $ \mathbf{v} $ method and presents graphically the same data as Table B.1.	182
B.3	Plot of the shaking dynamic stabilization results obtained on the reassembled $\Gamma = 5$ experimental cell presented in dimensionless variables. This data was acquired using the variable ΔT , fixed $ \mathbf{v} $ method and presents graphically the same data as Table B.2.	184
B.4	Plot of the shaking dynamic stabilization results obtained on the $\Gamma = 3$ experimental cell presented in dimensionless variables. This data was acquired using the variable ΔT , fixed $ \mathbf{v} $ method and presents graphically the same data as Table B.3.	185

List of Tables

1.1	Table denoting the static critical Rayleigh number for a range of square cross section aspect ratios with insulating container side walls and no-slip boundary conditions. Note that the aspect ratio Γ_i is defined as $\Gamma_i = l_i/l_z$	14
1.2	Table denoting the upper stability boundary for a cubical container with rigid boundaries and insulating sidewalls, as predicted by Carbo [16].	25
2.1	Quantification of the non-sinusoidal effects of the shaker system. f_n denotes the relative harmonic.	60
2.2	Demonstrated performance of the shaker system to date.	62
4.1	Static onset testing results from the initial assembly of the $\Gamma = 5$ experimental cell.	138
4.2	Static onset testing results from the second assembly of the $\Gamma = 5$ experimental cell.	139
4.3	Static onset testing results from the $\Gamma = 3$ experimental cell.	139
4.4	Shaking onset testing results from the pre-disassembly $\Gamma = 5$ experimental cell. These results were acquired by fixing ΔT and varying $ \mathbf{v} $. Note that the “deviation from theory” presented here is computed as $(\mathbf{v}_{\text{theory}} - \mathbf{v}_{\text{experiment}}) / \mathbf{v}_{\text{theory}} $	148
4.5	Shaking onset testing results from the reassembled $\Gamma = 5$ experimental cell. These results were acquired by varying ΔT and fixing $ \mathbf{v} $. Note that the “deviation from theory” presented here is computed as $(\Delta T_{\text{theory}} - \Delta T_{\text{experiment}}) / \Delta T_{\text{theory}}$. The average standard deviation in temperature in these measurements is $\sigma_{\Delta T} = 18.3$ mK and in velocity is $\sigma_{ \mathbf{v} } = 6.19 \times 10^{-3}$ m/s.	149

4.6	Shaking onset testing results from the $\Gamma = 3$ experimental cell. These results were acquired by varying ΔT and fixing $ \mathbf{v} $. Note that the “deviation from theory” presented here is computed as $(\Delta T_{\text{theory}} - \Delta T_{\text{experiment}}) / \Delta T_{\text{theory}}$. The average standard deviation in temperature in these measurements is $\sigma_{\Delta T} = 22.7$ mK and in velocity is $\sigma_{ \mathbf{v} } = 4.42 \times 10^{-3}$ m/s.	159
B.1	Shaking onset testing results from the pre-disassembly $\Gamma = 5$ experimental cell presented in dimensionless variables. These results were acquired by fixing ΔT and varying $ \mathbf{v} $	182
B.2	Shaking onset testing results from the reassembled $\Gamma = 5$ experimental cell presented in dimensionless variables. These results were acquired by varying ΔT and fixing $ \mathbf{v} $	183
B.3	Shaking onset testing results from the $\Gamma = 3$ experimental cell presented in dimensionless variables. These results were acquired by varying ΔT and fixing $ \mathbf{v} $	185

List of Symbols

Note: All quantities are dimensioned unless explicitly noted as a nondimensional group.

- a Dimensionless wavenumber. Normalized by l_z .
- \mathbf{a} Acceleration. Units: m/s^2 .
- A Shaking amplitude. Units: m .
- β Isobaric thermal expansion coefficient. $\beta = 1/T$ for an ideal gas. Units: K^{-1} .
- β_T Isothermal compressibility. Units: Pa^{-1} .
- c Speed of sound. Units: m/s .
- c_p Specific heat capacity. Units: $\text{J}/(\text{kg} \cdot \text{K})$.
- χ Thermal diffusivity. $\chi = k/(\rho c_p)$. Units: m^2/s .
- δ Non-dimensional vibration amplitude. $\delta = A/l_z$.
- δ_ν Thermoacoustic viscous penetration depth. Units: m .
- ϵ Non-dimensional acceleration. $\epsilon = A\omega^2/g_o$.
- f Temporal frequency. Units: Hz .
- g Gravitational acceleration. Units: m/s^2 .
- g_o Static, terrestrial gravitational acceleration, $\approx 9.81 \text{ m/s}^2$.
- Γ_i Aspect ratio for a given container direction i . $\Gamma_i = l_i/l_z$. Dimensionless.

- I Rotational moment of inertia. Units: $\text{kg} \cdot \text{m}^2$.
- I_{el} Electrical current. Units: A (amperes).
- k Thermal conductivity. Units: $\text{W}/(\text{m K})$.
- k_{\circ} Hooke's Law spring constant for a simple harmonic oscillator. Units: N/m .
- l Length dimension. Subscripts denote length along a particular axis. Units: m.
- m Mass. Units: kg.
- μ Dynamic viscosity. Units: $\text{Pa} \cdot \text{s}$. Floquet (linear stability growth rate) exponent, where denoted. Dimensionless.
- ν Kinematic viscosity. $\nu = \mu/\rho$. Units: m^2/s .
- p Pressure. Units: Pa.
- $\langle p_{\circ} \rangle$ Mean of the absolute pressure. Units: Pa.
- Pr Prandtl number. Dimensionless.
- Π_{el} Electrical power. Units: W.
- ρ Density. Units: kg/m^3 .
- Ra Rayleigh number. Subscript c denotes the critical value. Dimensionless.
- Ra_{vib} Vibrational Rayleigh number (sometimes referred to as the ‘‘Gershuni number (G_s)’’). Dimensionless.
- Re Reynolds number. Dimensionless.
- S Slope of the upper stability boundary when plotted on an Ra_{vib} vs. Ra plot. Subscript c denotes the critical value. Dimensionless.
- t Time. Units: s.
- T Absolute (Kelvin) temperature. Subscript c denotes the critical value. Units: K.
- $\langle T_{\circ} \rangle$ Mean of the absolute (Kelvin) temperature. Units: K.
- ΔT Temperature difference across the vertical dimension of the experimental cell, i.e. in the \hat{z} direction. Units: K (relative).

- T_λ The helium superfluid transition temperature, ≈ 2.17 K.
- τ Period of vibration. Units: s^{-1} .
- ω Angular frequency = $2\pi f$. Units: rad/s.
- ω^* Non-dimensional frequency. $\omega^* = \omega l_z^2 / \chi$.
- \mathbf{v} Vector velocity. Units: m/s.
- V Volume. Units: m^3 .
- V_{el} Electrical voltage. Units: V (volts).
- x Linear displacement, as for a simple harmonic oscillator. Units: m.
- $\Re(n)$ Real part of a complex quantity n .
- $\Im(n)$ Imaginary part of a complex quantity n .

Acknowledgments

Portions of this work have been supported by the Office of Naval Research, The Pennsylvania State University Applied Research Laboratory Walker Graduate Assistantship Program, the U. S. Department of Energy ARPA-E, the Julian Schwinger Foundation for Physics Research, the Paul S. Veneklasen Research Foundation, and the Pennsylvania Space Grant Consortium Graduate Research Fellowship. The author would like to sincerely thank all of these organizations for their generous support enabling these efforts.

Dedication

I would like to thank my wife, Lisa Mangini, for her endless kindness, caring, and patience, my parents, M. and Helen Swaminathan, for their support and offering me every possible opportunity as a child (and as an adult), and all those faculty members who have advised this research over my years at Penn State, namely Dr. Steven Garrett, Dr. Matthew Poesse, and Dr. Robert Smith. Without you, this work could not exist.

Chapter 1

Introduction

As is well-known, when a container of fluid¹ is cooled from below and heated from above (relative to gravity), this thermal gradient condition does not lead to any buoyancy-induced flows in a stationary container. When the imposed condition is inverted, that is, heated from below and cooled from above with a sufficiently large temperature difference, the result is quite a bit different, resulting in the motion of fluid due to buoyancy forces spurred-on by the inverse dependence of fluid density on temperature.

This instability has been studied in the literature for well over a century. In 1901, Henri Bénard, a French physicist, defended his doctoral dissertation on experiments he designed to investigate convective phenomena. While several types of natural convection now bear his name, there were recorded observations of convective motion in the formal literature dating back at least to the 1830's. In Bénard's layer of spermaceti, heated from below by steam and seeded with particulate matter, he observed and reported the now classical, steady-state patterns of convection cells and noted that the fluid was flowing upwards in the centers of the cells and flowing downwards along the boundaries [1]. An image from Bénard's experiments published

¹with a positive value of its coefficient of thermal expansion

in 1900 may be seen in Figure 1.1. In this arrangement the effects of surface tension, with the upper boundary formed by air, are very significant and were recognized by Bénard himself. This form of convection with surface tension as well as buoyancy effects involved is often referred to as Bénard-Marangoni convection to recognize the influence of thermally induced surface tension inhomogeneities (the Marangoni effect).

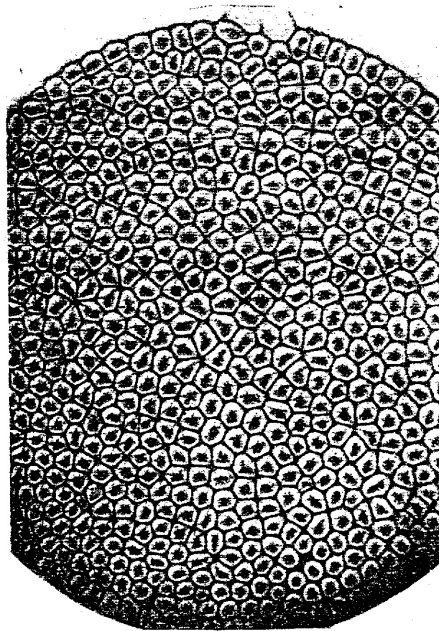


Figure 1.1: Image of convection cells as viewed from above (through the free surface in contact with room air) published in Bénard's original 1900 paper [2]. (Paper obtained from the *Bibliothèque nationale de France*).

Lord Rayleigh [3], in 1916, attempted to investigate the mechanism behind the neatly-ordered convection cells that Bénard observed, however, he solved the problem of a layer of fluid constrained between two plates, one heated and one cooled. For free-slip boundaries of infinite lateral extent, he solved for the critical temperature difference and spatial cell wavenumber at onset. It was noticed that his predictions did not match the experimental results of Bénard, which was due to the lack of the inclusion of surface tension non-uniformities in the model. While Bénard

acknowledged the influence of surface tension effects in his own work, Rayleigh does not appear to have publicly acknowledged this discrepancy before his death three years later in 1919. In 1925 A.R. Low [4] noted that the onset of convection predicted by Rayleigh occurred at approximately 10 times the temperature difference of that experimentally found by Bénard, however, it was not until much later that the importance of surface tension effects was shown. The problem of Rayleigh, that of fluid constrained in the vertical dimension by two horizontal differentially-heated plates is now referred to as Rayleigh-Bénard convection.

1.1 Modulated Rayleigh-Bénard Convection

The focus of this work is an extension of the long line of Rayleigh-Bénard convection experiments to investigate natural convection with the added condition of forced harmonic oscillation (shaking) along the axis of the thermal gradient. This is parametric excitation in the physical and mathematical sense that the gravity vector, essential in the formation of the buoyancy force, is being modulated in time. Parametrically excited Rayleigh-Bénard convection has been studied in two forms in the literature: thermal modulation and acceleration modulation. Time-harmonic thermal modulation was first studied theoretically in 1969 in a paper by Venezian [5] and early experimental investigations were undertaken by Finucane and Kelly [6] in 1976. This work imposed a sinusoidal modulation of the temperature of the heated boundary at a range of frequencies and amplitudes. These early experiments were severely hampered by the restriction to relatively low modulation frequencies imposed by the slow thermal diffusion times of room-temperature experiments. Despite these restrictions, there was limited evidence that high-frequency and large-amplitude parametric modulations of the boundary temperatures did permit

some delayed onset to be observed, with Rayleigh numbers up to 10% above the unmodulated critical Rayleigh number seen to be stable. Niemela and Donnelly [7] (1987) were able to conclusively demonstrate delayed onset of convection with thermal modulation, by reaching higher modulation frequencies using liquid helium at 2.63 K (above the superfluid transition temperature T_λ) and exploiting those faster thermal response times.

Acceleration modulation, the other means of parametrically modulating Rayleigh-Bénard convection, is the focus of this work. In this formulation the standard gravitational acceleration g_o is replaced by a sinusoidally modulated acceleration caused by the shaking of the container $g \rightarrow g(t) = g_o + A\omega^2 \cos(\omega t)$, where A and ω are the dimensioned shaking amplitude and angular frequency, respectively. This problem was first investigated theoretically in the Western literature by Philip Gresho and Robert Sani [8,9] from the University of Illinois, who published their work in 1970. They computed an overall stability map for a laterally unbounded (infinite), thin fluid layer both heated from below and cooled from above and the inverted thermal configuration. The conclusions that resulted from this study, despite being somewhat coarse due to the computational limitations of the period, still provide physical intuition and guidance for current experiments and have been experimentally verified using an experimental configuration that approximated the infinite layer. They determined that for any given thermal configuration and horizontal boundary spacing in the limit of an infinite layer, there is mathematically (although not necessarily experimentally accessible) some point in the plotted plane of vibration amplitude and frequency that will allow the convective motions of the fluid to be suppressed.

1.2 Motivation

This ability to stabilize convection using vibration is of interest to groups which design and study thermoacoustic devices. Many thermoacoustic devices exhibit a thermal gradient of the unstable type described above (i.e. cold over hot) in the presence of high-amplitude acoustic waves. The introduction of convection in this inherently unstable case can have deleterious effects on the desired operation and efficiency of the device, greatly increasing thermal transfer between gas parcels that, by design, should not be in thermal contact.

The investigations into convection suppression by the Penn State Thermoacoustics group were motivated by this fact that performance in a promising number of these new energy conversion and cooling technologies (thermoacoustic and Stirling engines and refrigerators, and pulse tube cryocoolers) can be degraded by these convective flows in the working medium. As engines, these devices are attractive because they are closed cycle, have, in principle, high thermodynamic efficiency, and are agile with respect to heat source, making them interesting for a range of uses, from cookstoves, where they can simultaneously generate both modest amounts of electricity and drive fans to reduce indoor pollutants [10], to engines operating from lower-quality heat sources, such as engine exhaust [11]. Heat-driven heat pumps are also possible, and have been built to create no-moving-parts thermoacoustic natural gas liquefiers. It is noteworthy that these acoustic devices often use helium, which is environmentally benign (unlike, say, modern vapor compression refrigerants, which are powerful greenhouse gases). Pulse tube cryocoolers are the modern workhorses for maintaining cooling fluid temperatures to sustain superconducting magnets and for sensor cooling. There is an expectation that Stirling cycle, thermoacoustic and pulse tube refrigerators will continue to expand beyond their niche applications to

become tools in the portfolio for energy conversion for enhanced sustainability.

Regardless of design, these devices contain hot and cold heat exchangers, as well as surfaces at ambient temperature, all of which are in contact with helium gas that ideally does not have secondary flows—that is, flows which are not simply harmonic in motion. In general, it is impossible to arrange the system in such a way that the cold heat exchanger is not above some warmer surface as acoustic power must flow through the regenerator and heat exchanger. Additionally, in all of these devices, large amplitude oscillatory flows (which are required for operation) are already present—accelerations on the order of 150 g’s are fairly typical, and frequencies tend to be in the audible band.

In thermoacoustic refrigerators, as a specific example, the introduction of convective motion could transport warm gas from the exhaust heat exchanger to the load heat exchanger, contrary to the design goals of the machine to remove heat from the load heat exchanger. These performance issues caused by suspected convective instability have been seen both in traveling wave thermoacoustic refrigerators and in cryogenic pulse tube chillers. The interest in the added dynamics of vibrated convection is introduced since in all of these devices there is an acoustic field superimposed upon the existing thermal gradient. As the acoustic wave within the fluid is isomorphic to the effects of vibration on a container holding the fluid, the effect can either suppress or intensify the buoyancy driven flows, depending on the combination of parameters present.

The Thermoacoustics Group at Penn State has significant experience building thermoacoustic devices over the past 15 years [12–14] and it was noted that some machines, paradoxically, have significantly underperformed relative to well-vetted models. This has led to topological transformations directed toward avoiding secondary flows, however, convective instabilities have remained a potential source

of loss. A further aspect of thermoacoustic cooling systems is that their capacity is easily controlled by amplitude, rather than frequency, and it is a well-known, but underutilized effect that proportional control of cooling systems leads to thermodynamic efficiency improvements [15]. In contrast with the more common “binary control” wherein the variable capacity requirements are met via a variable “duty cycle,” proportional control offers a large benefit that is to some extent technology agnostic, i.e. the benefits derive from the reduced temperature deficits associated with lower heat flows at the load and exhaust sides, regardless of the exact approach used to achieve them; proportional control just happens to be quite easily implemented in thermoacoustic machines. The model, constructed at Penn State, of an ice cream freezer cabinet over a reasonable operating cycle showed an efficiency improvement of about 50%. One must remain cognizant, however, that any system which depends on oscillatory flows to “stabilize away” convective instabilities may have regimes wherein the amplitude is insufficient to suppress this effect, and this may be a limiting factor for proportional control, which this work may help to determine.

These concerns led Randy Carbo, then of the thermoacoustics group at Penn State, to write his doctoral dissertation (2012) [16] developing a computational methodology to determine what areas of parameter space (geometric, thermal, fluidic, and dynamic) are stable and therefore suppress convective flows. His work extended previous efforts in that it was able to determine stability for three-dimensionally bounded, rectangular, vibrated containers of any aspect ratio and for a full range of mechanical and thermal boundary conditions, allowing the modeling of relatively realistic experimental conditions.

The purpose of this work is to experimentally investigate the stability predictions made in Carbo’s work. This is a type of experiment that has not been undertaken

previously and the prior art is rather thin. While experiments on Rayleigh-Bénard convection have a long history, beginning with the formative efforts of Bénard himself, experiments on convective flows in the presence of vibration are very rare and will be discussed further.

1.3 Parametric Modulation

Parametric excitation pertains to a system which has one or more parameters that are not kept fixed, but modulated with respect to their static values in time or space. For example, a parametric oscillator could have the governing equation,

$$\frac{\partial^2 x}{\partial t^2} + \omega(t)^2 x = 0. \quad (1.1)$$

Note that, unlike the canonical harmonic oscillator equation, here we have angular frequency that is permitted to vary with time, instead of being fixed for all time t . If this was a spring-mass oscillator system and we did fix the ω to be a constant ($\omega \neq f(t)$), then, if we give the system an initial “kick,” it will respond in a well-known manner at a fixed frequency $\omega_o = \sqrt{k_o/m}$. If we drive this system directly with a sinusoidal forcing function delivering a constant force at a frequency ω_o , say by attaching a shaker to the mass, it will respond at the frequency of the drive with a linearly growing amplitude in the absence of damping.

We can picture a simple harmonic oscillator with a varying spring constant, for example, as a means to achieve the time-varying natural frequency above. Let the variation of that spring constant be sinusoidal with an undefined frequency ω_p and an amplitude A_p (such that $k = k_o [1 + A_p \sin(\omega_p t)]$), giving us $\omega = \sqrt{(k_o + A_p k_o \sin(\omega_p t)) / m}$. Let us posit, now, that we fix this ω_p to be close to

$2\omega_o$ and then give the system a kick. Here, after a transient period, the system will not respond at the natural frequency ω_o , but at a frequency that is half that of the parametric modulation frequency, $\omega_p/2$. More startlingly, the amplitude of the resulting motion will grow exponentially, not linearly as in the directly-forced case. It can be shown that the larger the amplitude of the perturbation A_p , the wider the range of modulation frequencies around $2\omega_o$ that can excite a response [17].

If Floquet's theorem is applied to this problem, then the response of the system can be described by a set of solutions, each of the form $e^{\mu t}P(t)$. The characteristic exponent μ is a complex-valued constant and the function $P(t)$ has the same periodicity as ω_p . As we can see, the imaginary part of the exponent μ describes an oscillatory motion $\exp(i\Im(\mu)t)$ and the real part describes an exponential growth or decay $\exp(\Re(\mu)t)$. Therefore, simply by knowing the value of the real part of this characteristic exponent μ , the overall stability of the system can be found: $\Re(\mu) < 0$ indicates stability and $\Re(\mu) > 0$ indicates instability, while $\Re(\mu) = 0$ denotes marginal stability. This linear stability analysis methodology permits determination of the stability of the state, although the exact dynamics of the system may not be fully known due to the lack of a defined $P(t)$ function. For the modulated harmonic oscillator, this corresponds to system energy either being added or removed by the parametric drive.

Another common parametrically driven system is the inverted pendulum restricted to one plane of rotation with a sinusoidally oscillated pivot point, sometimes referred to as Kapitza's pendulum, after the Nobel laureate physicist who contributed to its theory. Absent any parametric modulation, a pendulum has two equilibrium angles, the hanging one, which is stable for small displacements, and the inverted one, which is unstable. When a periodic oscillation, in the vertical direction, of the pivot point of the pendulum is added, new dynamics are introduced

and this parametric drive, modulating the effective gravitational acceleration of the system, may make the hanging position unstable for a range of pivot point amplitudes and frequencies. In the same vein, the inverted position may become stable over a range of sufficiently large oscillation frequencies and amplitudes; this is referred to as dynamic stabilization. These regions can be again found by solving for the real parts of the characteristic exponents as described above. A purely phenomenological model for the inverted pendulum absent damping can be constructed, although it clearly does not include all of the relevant dynamics [18]. Without modulation, the pendulum attempts to fall with the exponential growth rate $\omega_o = \sqrt{mgl/I}$. Since the pivot point is oscillating at roughly $2\omega_o$, we can picture this modulation of gravity very much like the modulation of the spring constant above, in that here, the effects of gravity will be at some points in the cycle enhanced and at others diminished. This results in a torque that when averaged may overcome the torque due to gravity. However, if the amplitude of the drive becomes very large for a given frequency, the system may actually become destabilized again, and pass into a region with exponential growth as the solution.

For our shaken Rayleigh-Bénard convection system, the nature of the problem is again one of dynamic stabilization with the system modulated by a vertical vibration, a periodic perturbation on the gravitational acceleration. Here, however, understanding of the mechanisms are more complex. This convection system may also be parametrically stabilized, as with the pendulum, by shaking it at a range of appropriate combinations of frequency and amplitude. The difference, however, is that the convection is no longer a single degree-of-freedom system with one normal mode, but an infinite degree of freedom system, with an infinite number of possible normal modes. This necessitates a rigorous mathematical treatment of the problem, as was undertaken first by Gresho [8] for the infinite layer problem. Regardless,

the stability analysis methods discussed previously still apply.

A final example of an unstable system that may be stabilized by parametric excitation is that of the vibrated Rayleigh-Taylor instability, in which a denser fluid is superimposed over a less dense fluid (with both fluids being immiscible and discrete). Experimentally, Wolf [19, 20] was among the first to investigate stabilization of this instability through acceleration modulation in 1969; it was further investigated by Troyon and Gruber [21]. Illustration of these progressively more complex instabilities may be seen in Figure 1.2.

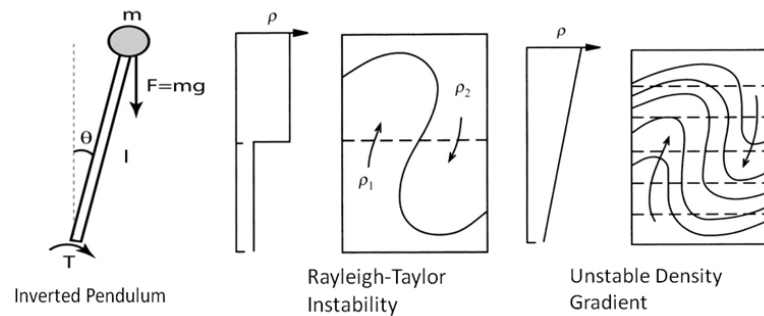


Figure 1.2: Statically unstable systems of advancing complexity that can be stabilized by vibration parallel to gravity. [Image courtesy of Dr. Robert W. M. Smith]

1.4 Rayleigh-Bénard Convection

A phenomenological explanation of Rayleigh-Bénard convection can be rather simple. One may picture a container of fluid with the lower boundary of the container heated above the ambient temperature (the prevailing average bulk fluid temperature) by some very small difference $\Delta T/2$ and the top boundary cooled from the ambient temperature by the same amount. Fluid parcels near the lower heated boundary absorb heat from the plate through thermal diffusion and therefore become less dense than the surrounding fluid. This density gradient leads to an upward-acting

buoyancy force which is balanced by viscous forces and thermal diffusion within the fluid. When the temperature difference between the top and bottom plates is increased sufficiently, the buoyancy force overcomes the counteracting viscous force and thermal diffusion and a net upward acceleration is experienced. As the fluid parcel rises it encounters the now cold upper surface and cools, giving its heat to the fluid near the cold upper boundary. The fluid parcel is now more dense than the fluid below it, so it experiences a net downward force, however, there is already a column of fluid rising beneath it, therefore producing a downward column of adjacent fluid and the cycle is repeated, producing a convection “cell.”

We begin with a rectangular container of fluid, with dimensions as depicted in Figure 1.3.

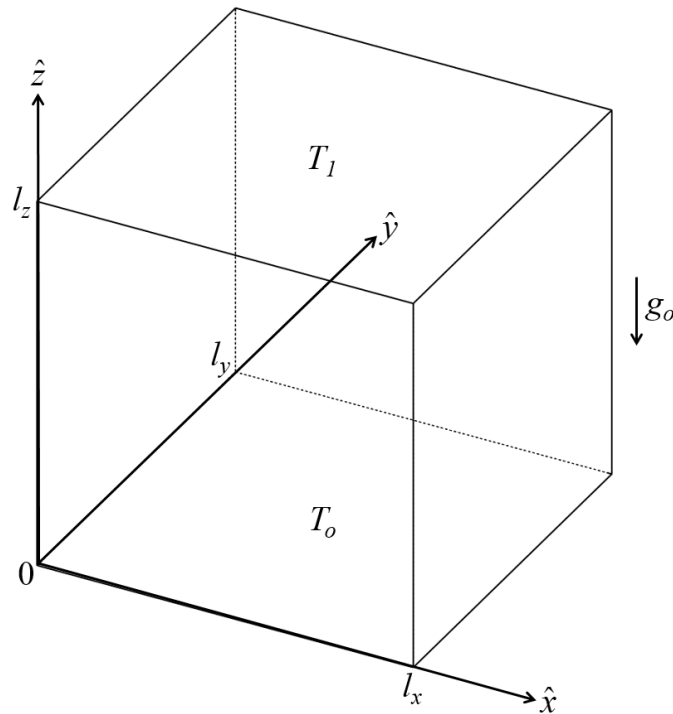


Figure 1.3: Geometry of the experimental container with dimensions.

As was mentioned earlier, the fluid with an imposed cold-over-hot temperature gradient will be stable until the energy imparted by buoyancy is large enough to

outpace the energy dissipated by viscous drag and thermal conduction. This is reflected in the construction of the Rayleigh number, a dimensionless group that describes where a differentially heated fluid transitions from pure conduction to fully-developed convection. It is defined as:

$$Ra = \frac{g_0 \beta \Delta T l_z^3}{\nu \chi} \quad (1.2)$$

where here l_z is the separation between the heated and cooled surfaces of the enclosure, β is the volumetric isobaric expansion coefficient of the fluid, ν is the kinematic viscosity, χ is the thermal diffusivity, and ΔT is the difference in temperature between the top and bottom surfaces of the fluid container (those walls perpendicular to the gravitational force). The term *Rayleigh number* was coined in a 1950 paper by Sutton [22] and has been used to the present day in recognition of his contributions.

As the Rayleigh number is dependent only on the temperature gradient and fluid and geometric parameters of the system, the critical Rayleigh number Ra_c , defines at what critical temperature difference ΔT_c the whole system will theoretically grow exponentially (based on linear theory) from a quiescent, thermally conductive state to a moving, convective state. For an infinite, horizontally unbounded fluid layer, the critical Rayleigh number can be found analytically, the derivation of which can be found in multiple textbooks. The critical Rayleigh number for a bounded container with “free” boundary conditions (i.e. fluid slip is allowed) can be approximated from mathematical computations [23]. For more realistic no-slip boundary conditions, the critical Rayleigh number must be computed numerically [16, 24–27]. A reference table of critical Rayleigh numbers for a range of aspect ratios of square cross section containers with no-slip boundary conditions and thermally insulating sidewalls may

be seen in Table 1.1. One may note that as the aspect ratio increases (denoting wider and shorter, i.e. “squat,” containers), the static critical Rayleigh number asymptotically approaches the classical infinite layer result of 1708, indicating the decreasing importance of the side walls on the convection onset.

Table 1.1: Table denoting the static critical Rayleigh number for a range of square cross section aspect ratios with insulating container side walls and no-slip boundary conditions. Note that the aspect ratio Γ_i is defined as $\Gamma_i = l_i/l_z$.

$\Gamma_x = \Gamma_y =$	0.125	0.25	0.5	1.0	2.0	3.0	4.0	5.0
Ra_c	3011718	203163	17085	3388.5	2084.9	2004	1894	1777
Source	[24]	[24]	[16]	[16]	[16]	[24]	[24]	[16]

The Rayleigh number also makes it clear, through the presence of the thermal diffusivity in the denominator, that there must be both thermal and viscous effects opposing the onset of instability. Without motion, there cannot be a viscous force in the fluid, however, for small, non-zero temperature differences below the critical temperature difference ΔT_c , the fluid is still motionless. We may show this through a consideration of the characteristic natural frequencies of internal waves, the buoyancy frequency, called the Brunt-Väisälä frequency in the Earth sciences such as oceanography and meteorology. This is the angular frequency at which a column of inviscid fluid would oscillate if it was displaced a small amount from its static equilibrium position in a stable system. This is given generally by: [28]

$$N^2 = -\frac{g}{\rho} \left[\frac{\partial \rho}{\partial z} - \left(\frac{\partial \rho}{\partial z} \right)_s \right] \quad (1.3)$$

where N is the angular frequency. If we neglect thermal diffusion in the above expression and assume density changes only depend linearly upon changes in temperature (as they would for an ideal gas under Boussinesq conditions) we may

find that the buoyancy frequency reduces to:

$$N^2 = -g\beta\frac{\partial T}{\partial z} \quad (1.4)$$

where here, β corresponds to the isobaric thermal expansion coefficient of the fluid, which for ideal gases at constant pressure is simply $1/T$.

The conditions for convective stability can be shown using this buoyancy frequency, as absent viscosity, the buoyancy frequency can be used as a stability criterion, in the same vein as the characteristic exponents in the stability analysis discussed prior. Here we assume an expression of the form e^{-iNt} . If $N^2 > 0$, the frequency would be purely real. The system would display an oscillation about its initial position and be stable. This would correspond to a thermal gradient that is less than the adiabatic lapse rate (the rate of change of temperature of a parcel of fluid when it is moved vertically into a region of lower pressure in a stably stratified pressure gradient without exchanging heat with its surroundings) in the fluid and displays the thermal restoring forces that must be overcome. If $N^2 < 0$, the resulting frequency would be pure imaginary and the result would be instability and convection of the fluid.

To close the loop, however, we need to consider both viscous and thermal resistance effects to the convective motion of the fluid. We can see this by considering that using Eq. 1.4 allows us to relate the Rayleigh number and the buoyancy frequency, $N^2 = -Ra \chi\nu/l_z^4$. If the nondimensionalization scheme of Gershuni is used (as Carbo did), the non-dimensional buoyancy frequency reduces to $N^{*2} = PrRa$, where the Prandtl number $Pr = \nu/\chi$ is defined as the ratio between the viscous and thermal diffusivities.

Once the critical Rayleigh number is surpassed, the upward and downward

moving fluid organizes into cells. The size, spatial characteristics, and number of these cells are determined by the geometry and boundary conditions of the container and the imposed temperature gradient. If one were to solve for the overall stability of the system, this would require the assessment of the system reaction to all possible forms of perturbation from the stable condition, which is an intractable problem. If we can instead separate the possible forms of instability into a basis set of possible “modes” that satisfy the boundary conditions imposed by the box, this problem becomes much simpler. We then only need to use the linear stability analysis discussed above to solve for stability or instability, with the understanding that instability of one mode is indicative of instability of the entire system.

Bénard himself laid the groundwork for this analysis by defining a characteristic wavelength, which he measured from the center of one cell to the center of an adjacent cell. Rayleigh then employed this methodology for his infinite layer by using a normal mode solution, decomposing the vertical velocity (and temperature) fields into a series of expressions (one for each mode) of the form $w = W_o W(z^*) e^{i(a_x x^* + a_y y^*)} e^{\mu t^*}$ [1]². From this solution the definition of the non-dimensional wavenumber is familiar to an acoustics student $a^2 = a_x^2 + a_y^2$. Once this has been determined, the boundary between stability and instability of the convection system for each of those normal modes falls on the line of marginal stability, where $\mu = 0$, with the minimum of the resulting values being the critical Rayleigh number and corresponding critical wavenumber. If sidewalls are added to the problem, instead of a continuous spectrum of possible nondimensional wavenumbers, the wavenumbers are now quantized.

We also note that these modes can be organized into classes based on the even or odd nature of the roll cells in each of the physical directions. In this

²Note that this is a nondimensionalized expression following the velocity, length, and time scaling schemes of Koschmieder [1, pg. 15] and Carbo [16, pg. 49] [29].

scheme, there are eight symmetry classes for a three-dimensional container, and the solution process may be broken up accordingly into the various classes in order to simplify the forms of the equations by limiting the symmetry of the solutions. We also note that if the temperature gradient is increased even further, then the distinct circulation patterns caused by the convection are no longer steady, but instead become time-dependent (periodic or chaotic), although still laminar. As the temperature is increased even further, some second critical Rayleigh number Ra_t is reached and the system now becomes dominated not only by the “large-scale circulation,” but also by accompanying small-scale fluctuations. The flow is then turbulent [30,31].

1.5 Parametrically Modulated Rayleigh-Bénard Convection

In the same manner as the other parametric systems that were discussed before, for shaken convection, we introduce a time-dependent parameter into the problem. For a harmonically vibrated convection problem, with the axis of vibration directed along the static gravity vector, the gravitational acceleration can be recast as the conventional static gravitational acceleration summed with a first-order, time-harmonic perturbation, as below:

$$\mathbf{g} \rightarrow \mathbf{g}_o + [A\omega^2 \cos(\omega t)] \hat{\mathbf{n}}. \quad (1.5)$$

In almost all computational solutions of convection problems a standard set of approximations is applied since it greatly improves the computational tractability of the problem. This Boussinesq approximation, named after the French mathe-

matician and physicist Joseph Valentin Boussinesq, implies that density changes observed in the fluid are only the result of changes in temperature and that those thermally induced density changes are themselves small. In other words, all other terms in the Navier-Stokes equations that have density gradient driven effects on the flow which are not temperature-dependent are ignored. The consequences of this approximation will be discussed in detail later.

Applying both the above substitution for the gravitational acceleration and the Boussinesq approximation to the Navier-Stokes equations, the equations simplify, as seen in eq. 1.6. The subsequent constitutional equations in this section follow the derivation of Gershuni and Lyubimov [32].

$$\frac{\partial \mathbf{v}}{\partial t} + (\mathbf{v} \cdot \vec{\nabla}) \mathbf{v} = -\frac{1}{\rho} \vec{\nabla} p + \nu \nabla^2 \mathbf{v} + g_0 \beta T \hat{\mathbf{n}} + \beta T A \omega^2 \cos(\omega t) \hat{\mathbf{n}} \quad (1.6)$$

Considering each individual term in the above equation, the added term at work in the dynamic stabilization becomes clear. Beginning from the left-hand-side, we have the conventional, time-dependent acceleration term $\partial \mathbf{v} / \partial t$ and the time-independent (and spatially dependent) convective acceleration term $(\mathbf{v} \cdot \vec{\nabla}) \mathbf{v}$. Continuing on the right-hand-side of the equation we see the term that permits acceleration due to pressure gradients $-\rho^{-1} \vec{\nabla} p$, the negative sign incorporating the behavior that conventionally, fluid will tend to flow from high to low pressure (opposite the gradient) to reach equilibrium. The next term $\nu \nabla^2 \mathbf{v}$ applies the effects of viscosity, expressed in terms of the kinematic viscosity ν . The next term $g \beta T \hat{\mathbf{n}}$ brings in the effects of thermally driven buoyancy forces. The isobaric thermal expansion coefficient $\beta = \left(\frac{1}{V}\right) \left(\frac{\partial V}{\partial T}\right)_p$ describes the fractional volume change due to a given change in temperature T . Without sinusoidal oscillation, here we see the classical competition between buoyancy forces and viscosity, the buoyancy force providing

an upwards acceleration to a fluid parcel and the viscous forces opposing that acceleration. The final term $\beta T A \omega^2 \cos(\omega t) \hat{\mathbf{n}}$ describes the effects of the sinusoidal oscillation, providing another force that can either oppose or enhance the effects of the convection.

We also have an equation that describes the conservation of thermal energy:

$$\frac{\partial T}{\partial t} = \chi \nabla^2 T - \mathbf{v} \vec{\nabla} T. \quad (1.7)$$

The meaning of this equation is rather straightforward. The first term on the right-hand-side describes thermal transport through thermal diffusion (as denoted by the thermal diffusivity χ) and the second term denotes thermal transport through advection (as denoted by the fluid velocity v). The negative sign in the second term describes the fact that thermal energy flows counter to the thermal gradient, that is from hot to cold.

Finally, we close the system of equations with the continuity equation. This imposes the condition of incompressible flow, denoted here by the divergence of the velocity field being forced to be zero. This is a direct result of the Boussinesq approximation: prohibiting density differences that are not temperature-dependent has the incidental consequence of losing the ability to fully describe compressible fluid flow.

$$\vec{\nabla} \cdot \mathbf{v} = 0 \quad (1.8)$$

As a result, computations that employ the Boussinesq approximation are unable to describe acoustic waves in the fluid, except under conditions where the density differences are a small fraction of the mean static density. From the above condition, we note that the vector field will always be solenoidal, although it is not necessarily

(or in general) Laplacian (irrotational) as the curl is left undefined.

Solving these equations is very difficult. However, applying linear stability analysis to the problem allows the determination of stability without necessarily knowing the exact dynamics of the system. Carbo’s work determined where the transition from convection (instability) to quiescent fluid (stability) would occur without determining the exact form of the fluid flow for rectangular boxes. He determined the stability of the system for a range of physical, geometric, thermal, and vibrational parameters. These parameters dictate the design of an experiment to verify his results as they denote the inputs and outputs of his model.

To fully define the state of a shaken Rayleigh-Bénard convection system, we require four non-dimensional variables: two describing the thermal conditions and material properties of the fluid and two describing the properties of the parametric excitation (shaking). Respectively, they are the Rayleigh number (Ra), the Prandtl number (Pr), the non-dimensional frequency ($\omega^* = \omega l_z^2 / \chi$), and either the non-dimensional acceleration ($\epsilon = A\omega^2 / g_o$, the peak acceleration normalized by gravity) or the non-dimensional shaker drive amplitude ($\delta = A / l_z$). To simplify our view of the vibration parameters, we may fold them into a single dimensionless group that describes both the acceleration and frequency together. This is the so-called *vibrational* Rayleigh number: [32]

$$Ra_{vib} = Pr \frac{Ra^2 \epsilon^2}{2\omega^{*2}}. \quad (1.9)$$

Note that in some papers, the vibrational Rayleigh number is also referred to as the “Gershuni number (Gs)” in recognition of the contributions of G. Z. Gershuni to the theoretical solution to the problem.

With this framework, the physical state of the system may be described through

these two nondimensional groups, the Rayleigh number Ra and the vibrational Rayleigh number Ra_{vib} . The only pieces of information still required are the geometrical constraints of the container and the boundary conditions. The spatial constraints can be described using the aspect ratios of the three-dimensional, rectangular container:

$$\Gamma_x = \frac{l_x}{l_z} \qquad \Gamma_y = \frac{l_y}{l_z} \qquad (1.10)$$

with the dimensions of the container shown in Figure 1.3. There are also the choices of boundary conditions on the top and bottom surfaces and the sidewalls, which include both mechanical conditions (free or rigid) and thermal conditions (conducting or insulating), which determine the form of the solutions.

1.6 Prior Numerical Results

To assess the numerous results of Carbo, we must begin, as he did, with a choice of aspect ratios and boundary conditions for the container of interest. We begin with thermally conducting top and bottom rigid boundaries. These well-approximate the conditions of a realistic experimental system, as the horizontal boundaries are generally formed of metals that have thermal conductivities many orders of magnitude higher than the fluids they are in contact with. For example, for air at a pressure of 1 atm and temperature of 300 K, the thermal conductivity is $k_{\text{air}} = 2.62 \times 10^{-2}$ W/(m-K), whereas for aluminum alloy (6061-T6), it is $k_{\text{AL}} = 167$ W/(m-K). Rigid boundaries (those that correspond to a non-slip boundary condition) are also the most physical choice among the two. For the sidewalls, we again have the same choices. We choose rigid sidewalls since they are

more physical for most experiments. The choice of sidewalls could be approximated as either conducting or insulating, dependent upon the materials selected. Metal sidewalls would present a conducting surface, however, they have the distinct disadvantage of generally being optically opaque. To permit visualization of the fluid, a primarily insulating sidewall of a transparent material (glass, acrylic, or polycarbonate) is chosen.

The aspect ratio of the (rectangular) container must also be determined. As the largest number of numerical results are available for containers of a square cross-section, we limit ourselves to cases where $\Gamma_x = \Gamma_y$, although this restriction can be relaxed in the future with further computational efforts. This still permits containers of varying aspect ratios by altering the height of the container relative to the widths.

With these system parameters determined, Carbo’s methodology determines the stability of the system under a range of Rayleigh numbers and shaking conditions. One slice of these results are shown for an infinite layer (no sidewalls) in Figure 1.4. This condition is for a single Rayleigh and Prandtl number and, since this is an unbounded system, a choice of nondimensional wavenumber a corresponding to that at static convection onset. This stability map is just one of an infinite number of such possible plots, one for each combination of Ra , Pr , and a .

We see here that we actually have two stability boundaries, an “upper” and a “lower,” as seen bounding the stable region on the chart. This terminology is a consequence of the necessity to produce a stability map on a two-dimensional plane, two variables must be left fixed and two allowed to range on the x and y -axes. In this case, the Rayleigh and Prandtl numbers are left fixed and the dimensionless frequency ω^* and dimensionless acceleration ϵ are allowed to vary. This is a departure from the work of Gresho and Sani who kept the Prandtl

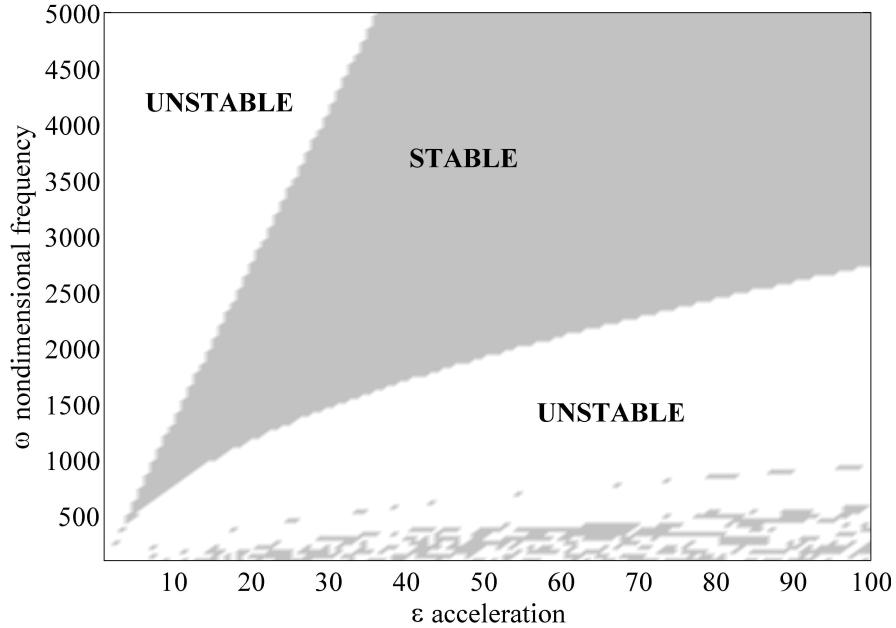


Figure 1.4: Example of a sample stability map as computed by Carbo [16] for an infinite layer, rigid horizontal boundary, shaken Rayleigh-Bénard convection system with $Ra = 10^4$, $Pr = 7$, and $a = 3.117$. Nondimensional frequency ω^* is plotted on the y-axis and nondimensional acceleration ϵ on the x-axis. Carbo notes that the blotches at the bottom of the plot are associated with poor numerical accuracy in that region.

number and shaker amplitude constant and instead ranged in Rayleigh number and frequency. Each of these choices is a natural outgrowth of the type of computational procedure chosen, and each engendered different insights.

The meaning of these boundaries can be seen if we begin on the plot in Figure 1.4, choose a fixed drive frequency ($\omega^* = \text{const.}$), and slowly increase the nondimensional acceleration ϵ from zero (we can imagine setting a shaker at a fixed frequency and slowly increasing the drive amplitude to accomplish this). The system will initially be unstable (assuming the static critical Rayleigh number has been exceeded). This harmonic instability should be perturbed by the parametric modulation with a time dependence that is synchronous with the drive frequency. Once the upper stability boundary has been crossed, in between the two boundaries, the system is

dynamically stabilized by the parametric modulation and the natural convective motion of the fluid is inhibited. As the acceleration is further increased, the lower stability boundary is eventually crossed and the system is again unstable. This destabilization that occurs beyond the lower stability boundary is due to the destabilization of the system by parametric resonances and therefore exhibits the $\omega/2$ dependence that was first noted by Faraday in the 19th century. Additionally, as Carbo demonstrated numerically, the lower boundary still exists for statically subcritical Rayleigh numbers and for negative Rayleigh numbers as well (enclosure heated from above), as would be expected for an instability driven by parametric internal waves. This lower or “parametric” boundary is experimentally unreachable for a reasonably-sized cube-shaped experiment due to the limits of shaking a system so strongly and is therefore not a focus of this investigation.

While the stability diagram shown in Figure 1.4 displays the results for a single choice of Rayleigh and Prandtl number, it is far from a global stability diagram. The global stability diagram for a system would be the overlap of the stable regions for diagrams of all wavenumbers. Gresho and Sani [9], in fact, did just this and computed a large number of diagrams for a full range of wavenumbers. Biringen and Peltier [33] qualitatively confirmed the results of Gresho and Sani employing three-dimensional and nonlinear equations, however, they did not construct their own global stability map, but sampled points inside each region.

What we may notice is that, as a direct consequence of choosing the $\epsilon\text{-}\omega^*$ plane for the stability map, the upper boundary creates a straight line with approximately zero-intercept for all except the very low frequency region. Therefore, the upper boundary is able to be fully described only by its slope S and that by knowing one point, all points on the boundary above a small nonzero frequency are known. Considering all the possible modes, the critical slope S_c will be that for the mode

that stabilizes last when increasing drive parameters, that is the mode with the minimum slope. Another aspect that we note is that this critical slope has a dependence on Prandtl number of $S_c \propto \sqrt{Pr}$ for all $Pr \lesssim 10$. This was shown numerically by Carbo [16]. Therefore, for Prandtl numbers in this range, knowing the critical slope of the upper boundary is sufficient to solve for the points along that boundary for a given Rayleigh number and boundary conditions. Knowing the critical slope, we may write the vibrational Rayleigh number in terms of this slope:

$$Ra_{vib} = Pr \frac{Ra^2}{2S_c^2}. \quad (1.11)$$

Therefore, instead of creating a stability boundary of the type shown in Figure 1.4 for every possible combination of Rayleigh number, Prandtl number, and mode and correlating them all to determine global stability, we may express the global upper stability boundary for a range of Rayleigh numbers simply in terms of ordered pairs of the form (Ra_{vib}, Ra) . An example of this data is given in Table 1.2 for a cubical container ($\Gamma_x = \Gamma_y = 1$) and thermally insulating, rigid sidewalls.

Table 1.2: Table denoting the upper stability boundary for a cubical container with rigid boundaries and insulating sidewalls, as predicted by Carbo [16].

Ra	10^4	10^5	10^6	10^7
Ra_{vib}	1.25×10^4	3.08×10^5	7.74×10^6	1.89×10^8

The upper stability boundary can also be displayed in a graphical form (reproduced from the Carbo dissertation), as seen in Figure 1.5. This plot covers the critical vibrational Rayleigh number for the upper stability boundary for a range of aspect ratios with a square cross-section ($\Gamma_x = \Gamma_y$) ranging to $\Gamma = \infty$, representing the infinite layer. Note that this plot is for a rectangular, square-wave drive instead of a sinusoidal one. There is a simple mapping between the results for a sinusoidal

drive and a rectangular drive: $Ra_{vib\text{-sinusoidal}} \approx 1.67Ra_{vib\text{-rectangular}}$, which was also shown numerically by Carbo [16]. Additionally, we see that the form of the stability boundaries are not perfectly straight lines, but display cusps in their progression. These represent transitions between the mode that is governing the overall stability (the mode that stabilizes last with increasing vibration parameters, i.e. the most unstable mode).

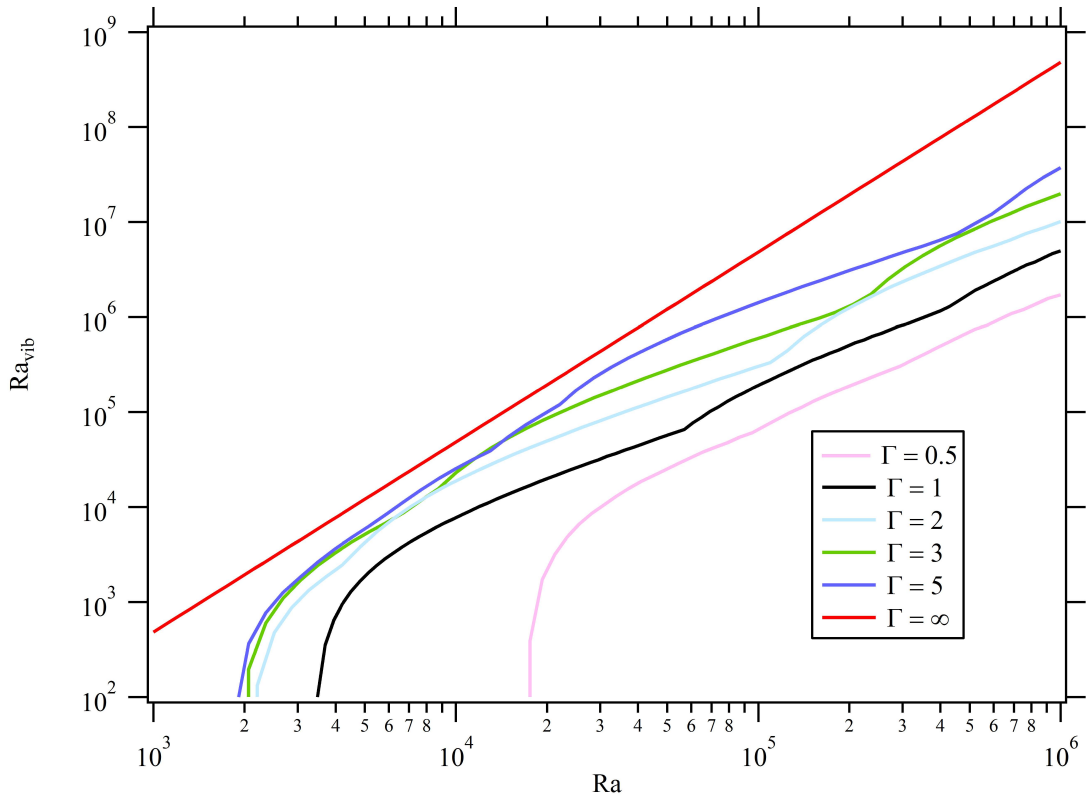


Figure 1.5: Critical vibrational Rayleigh number for the upper stability boundary shown as a function of aspect ratio for a square cross-section ($\Gamma_x = \Gamma_y$) container with a rectangular drive and insulating sidewalls [16].

In a similar manner to the upper boundary being described by a line on the stability diagram, the lower boundary can be approximated by a square root function of the form $\omega^* = P\sqrt{\epsilon}$, where here P is defined as the parametric number [16]. In much the same way as for the upper boundary, the lower boundary may be described

as an ordered pair of (Ra, P_{vib}) , with this new dimensionless group, referred to as the vibrational parametric number, defined as:

$$P_{vib} = Pr \frac{Ra^2 \epsilon}{2\omega^*2}. \quad (1.12)$$

1.7 Previous Experiments

The challenge faced is to apply the above numerical results to an achievable, realistic experimental test. Prior experiments are few in number and for various reasons, which will be discussed, provide a poor basis for comparison of the above theory to known data sets. While theoretical work on shaken Rayleigh-Bénard convection has a history of over forty years, beginning in the English language literature with the publications of Gresho and Sani, the literature on experimental work is severely limited. In addition to the work reviewed in this section, there are several experiments found in the literature which made use of a vibrated, heated object in free space, however, this discussion will limit itself to more applicable experiments performed on a vibrated container enclosing a differentially heated fluid.

In 1968, two graduate students from Mississippi State University, Gary Smith and Richard Forbes both published their theses (a master’s and doctoral, respectively) [34–36], which involved an experiment that investigated a cavity heated and cooled from the sides (that is, perpendicular to the direction of both vibration and gravity). They were motivated by the need to better understand how thermal heat transfer is affected by vibration, particularly in the design of space launch vehicles, and their literature review found no prior published work that had analyzed the effects of vibration on enclosures filled with convecting fluid. The design and construction of their experimental apparatus were the master’s thesis

of E. W. Wellborn, however, this work was not found to be available in print. They constructed water-filled enclosures with spacings between the side-heated walls ranging from 0.375 to 1.7 inches (0.953 to 4.32 cm) and applied temperature differences between 10 and 34 K. Their experiments were designed such that after a steady-state, static thermal condition had been reached, they tuned their shaker to produce either a peak velocity of 0.043 m/s or a peak acceleration of $25g_0$. This parameter (either velocity or acceleration) was kept constant across all the various thermal conditions employed and were chosen to remain within the performance envelope of their electrodynamic shaker. By using a guarded hot plate and a low-conductivity spacer, they were able to compute the heat flux and therefore the Nusselt number during their tests. They demonstrated enhancement of heat transfer when the cavity was driven at frequencies near those of the acoustic resonance of the fluid column, however, the side-heated arrangement of the experiment and the relatively low velocity and amplitude vibration employed make this experiment of limited relevance to the current problem.

Another series of experiments were undertaken by a joint group from Georgia Institute of Technology and *Physikalisches Institut der Universität Bayreuth* (Bayreuth, Germany) [37–41]. This experiment formed the doctoral dissertation of Jeffrey Rogers and was focused primarily on the effects of vibration on the planform of the convection cells. Their goal was to employ vibration to perturb the static convection patterns (such as straight rolls) into complex patterns, both spatially and temporally, such as periodic square lattices, bullseye targets, and harmonic stripes. While their focus was on pattern formation, they were able to confirm the predictions of Gresho and Sani to determine both the upper (harmonic) and lower (subharmonic) stability boundaries. They also developed a theoretical treatment to computationally determine the stability boundaries for their infinite

layer, using a two-dimensional (spatial) scheme and the Boussinesq approximation and linear stability analysis. They chose a single drive frequency on the order of 7-10 Hz (dependent on their static pressure and mean temperature) and were able to make small adjustments to their drive amplitude in order to step across the stability boundaries. These experiments were performed in very thin layers (650 and 672 μm) of compressed CO_2 gas at static pressures around 475 psi (3.28 MPa). Additionally, they were able to make comparisons to the infinite layer theory of Gresho and Sani since their experimental aspect ratio was large: $\Gamma = \frac{\text{diameter}}{\text{height}} = \frac{3.80\text{cm}}{6.50 \times 10^{-2}\text{cm}} = 58.5$. By working in such thin layers of fluid, and by employing a hydraulic shaker intended for long-stroke, low frequency operation, the level of vibration required to reach both stability boundaries was accessible to their experiment. This investigation opened significant new ground, however, the infinite layer problem is not a good approximation for acoustic machines and, as was shown by Carbo, there is significant added complexity to the structure of the stability boundaries when sidewalls are added.

A further experimental study of note to those in the thermoacoustics community is that of Gregory Swift and Scott Backhaus [42] at Los Alamos National Laboratory. They undertook a series of experiments to determine the effects of convection on pulse tube-type cryocoolers rotated to various orientations relative to gravity to observe when that convection might be inhibited due to the acoustic conditions inside the device. They built a simplified pulse tube apparatus that consisted of a stainless steel tube with two heat exchangers placed inside them. The heat exchangers consisted of blocks of copper with parallel passages drilled through them and were placed at an adjustable spacing within the tube. One heat exchanger was electrically heated and the other was maintained at room temperature using a circulated water bath. An acoustic standing wave was driven from the cold

heat exchanger end and an acoustic bounce space was placed at the hot heat exchanger end. The whole device was filled with helium gas at a mean pressure of approximately 450 psi (3.10 MPa) and the hot heat exchanger was heated to 523 K while the cold exchanger was held at 293 K. The heat transport of the device was measured as a function of angle relative to gravity by determining the discontinuity in thermal transport with the onset of convection. Their experiment, while designed to address a problem of commercial concern, deviated from the idealized case that is generally modeled in numerical studies. The heat exchangers, being porous, present a penetrable boundary condition, a case which is not accounted for in the theory. The container itself is placed in an acoustic standing wave, which leads to an acceleration gradient across the tube, again not accounted for in the models. Additionally, the large temperature difference between the heat exchangers, up to approximately 230 K, render its adherence to the Boussinesq approximation questionable. Carbo [29] made rough comparisons between results for his rectangular cross section geometry and their circular cross section tubes and found that his solutions bounded, but did not match, all of their observed results.

Two other efforts investigating the effects of orientation of pulse tube refrigerators were found in the literature [43, 44]. These experiments, unlike that of Swift and Backhaus, which employed an experimental apparatus specially designed to be an analogue of the pulse tube for the determination of the onset of convection, used commercially produced pulse tube coolers and rotated them, recording their cooling performance as a function of the rotation angle. Both found significant performance losses associated with rotating these commercial cryocooler designs from their preferred orientation. Unsurprisingly, if natural convection is suspected as the mechanism behind the loss of efficiency at tipped angles, the preferred orientation with the hot side above the cold side (a statically convectively stable

situation) lead to the highest performance.

A less often-cited investigation was undertaken by Ishikawa and Kamei [45] from the Mitsubishi Research Institute in Tokyo. Their experiment appears to be the first involving a rectangular shaken Rayleigh-Bénard experimental cell (of dimensions $5.45 \text{ cm} \times 1.2 \text{ cm} \times 1.0 \text{ cm}$, corresponding to $\Gamma_x = 5.45$ and $\Gamma_y = 1.2$). They filled this glass cell with distilled water and placed it on an electrodynamic shaker. As their interest was spacecraft vibrations (so-called g-jitter) influencing materials processing in reduced gravity environments, they focused on the vibratory regime of $f = 0\text{--}10 \text{ Hz}$ and $g = 0\text{--}1.5g_0$ with a displacement of 3.7 mm . They imaged their cell by injecting methylene blue dye into the water in the enclosure and tracking its motion using a CCD camera that was placed on the shaker (possible due to their mild shaking parameters). They also seeded the fluid with polystyrene latex particles ($d_p = 3 \mu\text{m}$) and used laser Doppler velocimetry to measure the flow velocity at 30 locations inside the cell, however, they only appear to use this technique in the unmodulated (static) investigations due to the difficulties of making these measurements in the shaking system. They also placed a thermistor inside the cell and analyzed linear spectra of the resulting temperature data. Statically, they found their cell to show stable roll cell behavior up to $30Ra_c$, which consisted of five roll cells in the horizontal direction and a single roll cell in the vertical. They then saw periodic flow patterns (with varying numbers of constituent frequencies) at higher Rayleigh numbers (up to $70Ra_c$). Since their shaking parameters were relatively modest, they were not able to demonstrate inhibition of convective motion, however, they were able to find signs that they attributed as steps toward dynamic stabilization. With vibration in the non-time-dependent convection regime, they saw a perturbation of their roll cells into an oval shape and also observed a horizontal propagation of the dye along the roll cell, leading their streaklines

to form a toroid. They attributed this as indicative of dynamic stabilization. In the periodic Rayleigh number regime, they saw that the fundamental frequencies (measured by the linear spectrum of their in-flow thermistor) did not change with vibration, however, they saw that the relative weights of the frequency components in the spectrum changed, including a transition from three frequencies to two, which they also interpreted as an indication of dynamic stabilization.

Another experiment of note is that of a group from the Microgravity Research Center at the *Université Libre de Bruxelles* [46–49]. These experiments were performed in a small (5 mm cube) container of isopropyl alcohol, which was subjected to translational vibrations perpendicular to the applied temperature gradient under microgravity conditions (research aircraft flying parabolic loops and later on the International Space Station). They used both interferometry and particle seeding to visualize the flow conditions. With this experimental setup, they were able to demonstrate that convective flows could be induced by vibration in microgravity that were consistent with convective flows that occur naturally in terrestrial gravity. While the mechanisms here are somewhat different, as they are attempting to dynamically *destabilize* a naturally stable system, the experimental techniques and challenges that they faced are still highly pertinent, particularly as their experiment needed to be spaceflight certified. Additionally, the theorists associated with their group developed a paper on the specific criteria required for the Boussinesq approximation to be used in shaken convection experiments, a set of requirements that previously had not been so explicitly codified for this problem.

Finally, Ivanova and Kozlov [50] undertook a study of convection modulated by non-translational oscillations. Their experiment placed an experimental convection cell on a track that followed an oscillating-pendulum-like path. The effect was of replacing the mass bob on the end of an inverted pendulum (of variable length)

with the experimental apparatus. They worked in a rectangular glass enclosure (of dimensions $8.0 \times 5.6 \text{ cm}^2$ and 0.83 cm deep) filled with a water-glycerin mixture. They made thermal measurements using a heat flux sensor embedded in one of the heat exchangers and visualized the flow by seeding the liquid with aluminum powder visualized by a strobed light sheet. Unfortunately, their papers detailing their experimental setup do not appear to have been translated from the original Russian. They did demonstrate that pendulum oscillations could both destabilize stable convective systems (heating from above) and perturb naturally unstable systems.

1.8 Choice of Experimental Medium and Geometric Design of the Experiment

The most fundamental choice in the experiment is that of the experimental medium: gas or liquid (at room temperature and atmospheric pressure). Initially, it appears desirable that a liquid be used in the experiment. Liquids offer several advantages. First and foremost, visualization is greatly simplified in a liquid experiment. If refractive index-based techniques are to be employed (direct shadowgraphy, schlieren, interferometry, etc.), the dependence of refractive index on changes in density, described by the Gladstone-Dale relation, is several orders of magnitude larger in liquids than in gases [51, 52], requiring much lower optical sensitivity to detect the small changes caused by thermal gradients.

If the goal is alternately to employ conventional particle seeding techniques, liquids again offer a much simpler route, as the goal in particle seeding is to introduce foreign matter that is both small enough in particle diameter d_{particle} and close

enough in density to the fluid $\rho_{\text{particle}}/\rho_{\text{fluid}} \approx 1$ to faithfully follow the streamlines. Finding a particle that is close to neutrally buoyant in a gas is nearly impossible, therefore some error must be assumed due to settling effects. In contrast, the history of using techniques to seed liquids, particularly water, is lengthy and density matching the experimental particles to the fluid is relatively straightforward.

There are, of course, disadvantages to employing a liquid experiment. The density of most liquids at atmospheric pressure being several orders of magnitude larger than those of most gases leads to an increased load that must be shaken. In addition, it is desired that the liquid chosen be relatively safe for the experimenters and the environment, however, many chemicals with useful physical properties pose potential hazards due to toxic and/or carcinogenic effects.

Most notably, however, the majority of gases have much lower required velocities (and therefore accelerations) for the the same point on the stability boundary (as described by the ordered pair (Ra, Ra_{vib}) for a given aspect ratio. This effect is easy to see if one manipulates the form of both the Rayleigh and vibrational Rayleigh numbers, substitutes one into the other, and returns to dimensional variables.

$$\omega^2 A^2 = \frac{2Ra_{\text{vib}}g_o^2 l_z^4}{\chi^2 Ra^2 Pr} \quad (1.13)$$

Recalling that for sinusoidally oscillating systems the maximum velocity can be expressed in terms of the displacement as $\mathbf{v} = j\omega\mathbf{x}$ [53], quickly reveals that the preceding equation is an expression for the magnitude of the maximum shaker velocity. Further substitution results in the velocity as a function of vibrational Rayleigh number and fluid parameters:

$$|\mathbf{v}| = g_o \frac{\sqrt{2Ra_{\text{vib}}}}{Ra} \left(l_z^2 \rho \sqrt{\frac{c_p}{k\mu}} \right). \quad (1.14)$$

Here the thermal diffusivity has been expressed as $\chi = k/\rho c_p$, where k is the thermal conductivity, ρ is the density, and c_p is the specific heat capacity at constant pressure. The kinematic viscosity, $\nu = \mu/\rho$, is expressed in terms of the dynamic viscosity μ and the density ρ . The full algebraic derivation of this result is shown in an appendix. Analyzing this result, we see that the required velocity for a given combination of Rayleigh number Ra and vibrational Rayleigh number Ra_{vib} depends upon the square of the plate separation l_z^2 and a host of fluid parameters. The velocity was chosen here since it both allows for an easy comparison factor (encompassing the two shaking variables: the angular frequency ω and the amplitude A and being dependent, in Carbo's construction of his results, only on the Rayleigh and vibrational Rayleigh numbers) and is generally the performance limit of most shakers. Equivalently, if we wish to consider the problem in terms of acceleration, we may cast Eq. 1.14 in that form:

$$|\mathbf{a}| = 2g_o^2 \frac{Ra_{vib}}{Ra^2} \left(\frac{l_z^4}{A} \right) \left(\frac{\rho^2 c_p}{k\mu} \right). \quad (1.15)$$

Note that despite the difference in form, the acceleration and velocity expressions carry the same information. For any given input of Rayleigh number Ra and vibrational Rayleigh number Ra_{vib} , a choice of dimensioned amplitude A is required. Once this choice has been made, a required acceleration is found in standard SI units ([m/s²]). However, since the physical displacement amplitude has already been fixed, assuming a sinusoidal displacement profile, the drive frequency has been fixed, since for a sinusoidal process $\mathbf{a} = -\omega^2 \mathbf{x}$. Thus, knowing a required dimensioned acceleration $|\mathbf{a}|$ for a given dimensioned displacement A , the linear drive frequency required for that peak acceleration is given simply by $\omega = 2\pi f = \sqrt{|\mathbf{a}|/A}$.

Another way to look at this is the methodology through which Carbo solved

for the vibrational Rayleigh number [16]. His code chose a given non-dimensional frequency and increased the acceleration in constant steps until a stable solution was found. We may think of this in an experiment as setting a frequency on a shaker and increasing the vibration amplitude until the system stabilizes; this is the same conceptual framing used in describing Figure 1.4. This was repeated for all symmetry classes until the lowest (in acceleration) stable solution was found and then the highest acceleration among the totality of the symmetry classes was chosen to be the marginal acceleration (as this acceleration represents the shaking point at which the last of the unstable modes will be stabilized). For sufficiently high velocities, the upper stability boundary appears as a straight line with very nearly zero intercept on the ω^* - ϵ plane, it is only this slope, $S = \omega^*/\epsilon = 1/|\mathbf{v}^*|$, that is needed to characterize the upper stability boundary. Thus, for a given vibrational Rayleigh number, the invariant quantity is the velocity, as long as the frequency is sufficiently high enough to ensure the linearity of the upper stability boundary.

In Carbo's results, the Rayleigh number Ra and the vibrational Rayleigh number Ra_{vib} for the upper boundary of a cubic container with insulating side-walls follow the approximate asymptotic scaling as Ra becomes large of $Ra_{\text{vib}} = (3.32 \times 10^{-2}) Ra^{1.3939}$ (corresponding to the black curve of Figure 1.5). The required acceleration goes down with increasing Rayleigh number due to the presence of the Ra_{vib}/Ra^2 term, resulting in $|\mathbf{a}| \propto Ra^{-0.6061}$ [16]. This can be illustrated by the fact that the Brunt-Väisälä frequency (when utilizing the nondimensionalization scheme of Carbo/Gershuni) for the Rayleigh-Bénard system is equivalent to \sqrt{PrRa} . Comparing to the undamped inverted pendulum, we see that for that system, the synchronous (upper) boundary is characterized by a pivot point acceleration of $\omega \propto \epsilon\omega_o$. Therefore, comparing to this analogous, simple system, with increas-

ing natural frequency, and therefore increasing Rayleigh number, the acceleration required to stabilize the system decreases.

Parameters that make gases advantageous now become clear. Since the velocity is given in terms of the density ρ , the three orders of magnitude reduction in the density between most liquids and gases (at atmospheric pressure and room temperature) reduces the required velocity tremendously. In addition, keeping the vertical dimension of the container l_z small also results in a significantly reduced velocity (and acceleration) due to the l_z^2 (and l_z^4) dependence. The result is that small containers, while still within a reasonable size for an experiment, are advantageous. These small containers are not uncommon in the literature, although they are generally used in order to approximate an infinite layer by means of a shallow depth (of several cm or less) and a significantly larger horizontal dimension.

1.9 The Boussinesq Approximation and Linearity

As was discussed earlier, in most convection computations, the Boussinesq approximation is applied to the governing equations of fluid mechanics before any other manipulations are performed as it greatly simplifies the form of the equations. If the comparison of an experiment to numerical results derived using the Boussinesq approximation is desired, the experiment must observe the physical restrictions of the approximation.

Generally, the consequence of this approximation is stated as limiting the system to operation at small pressure and temperature deviations from the mean and driving at “high” frequency and “small” amplitude, although those terms are left unquantified and generally undefined. Ilya Ryzhkov and Yuri Gaponenko [54] have published a paper deriving specific numeric criteria to determine the applicability

of the Boussinesq approximation for vibrated convection problems. They give the following conditions:

1. The deviations of temperature and pressure from the mean values are small, resulting in:

$$\left| \frac{\Delta T}{\langle T_o \rangle} \right| \ll 1, \quad \left| \frac{\Delta p}{\langle p_o \rangle} \right| \ll 1. \quad (1.16)$$

where $\langle T_o \rangle$ and $\langle p_o \rangle$ indicate the mean values of the absolute temperature and pressure, respectively. In the case of the shaken cavity, the pressure produced may be approximated by the known frequency and shaking amplitude of the container, $\Delta p \approx \rho_o A \omega^2 l_z$. This allows the above conditions to be rewritten as:

$$\left| \frac{\Delta T}{\langle T_o \rangle} \right| \ll 1, \quad \frac{\rho_o A \omega^2 l_z}{\langle p_o \rangle} \ll 1. \quad (1.17)$$

If we limit ourselves to relatively small thermal gradients, even a large maximum of $\Delta T = 50$ K at a mean temperature of 300 K results in $|\Delta T / \langle T_o \rangle| = 0.167$, which is still significantly less than 1. In addition, for the example of Nitrogen gas (N_2) at a pressure of one atmosphere ($\langle p_o \rangle = 101.325$ kPa) at a drive amplitude $A = 3.00$ in = 7.62 cm, frequency $f = 8.00$ Hz $\rightarrow \omega = 50.3$ rad/s, and mean temperature $T = 300$ K, the condition for pressure is given by $\Delta p / \langle p_o \rangle = 2.17 \times 10^{-5}$ which is most certainly much less than 1.

2. The density variation with pressure is much smaller than that with temperature and they are both small:

$$|\beta_T \Delta p| \ll |\beta \Delta T| \ll 1 \quad (1.18)$$

where here, the β_T is the isothermal compressibility and is equal to the reciprocal of the isothermal bulk modulus $B_T = 1/\beta_T$. Recall that for a gas, the speed of sound may be defined as the square root of the ratio of the adiabatic bulk modulus to the mean density $c^2 = B_s/\rho_o$. Also, for an ideal gas, we know that the adiabatic bulk modulus and the isothermal bulk modulus may be related by the polytropic coefficient $B_s = \gamma B_T$. Thus, the result of substitution, $c^2 = \gamma B_T/\rho_o$, allows us to solve for the isothermal bulk modulus $B_T = \rho_o c^2/\gamma$ and therefore the isothermal compressibility $\beta_T = \gamma/\rho_o c^2$ [53].

3. For externally forced systems, the period of the imposed vibration must be much smaller than those associated with the viscous and thermal diffusion and larger than that associated with the acoustic propagation over the length of the cavity:

$$\frac{l_z}{c} \ll \tau \ll \min\left(\frac{l_z^2}{\nu}, \frac{l_z^2}{\chi}\right). \quad (1.19)$$

One additional condition is imposed by linear stability analysis, since it is convenient to linearize the equations. To assure that linearization is acceptable, the displacement of oscillating fluid parcels must be significantly smaller than the characteristic length scale (in this case the separation between the heated and cooled boundaries l_z). This consequence of linear equations can be expressed in the form of the following condition that must also be fulfilled: [32]

$$\frac{A}{l_z} \ll \frac{1}{\beta \Delta T}. \quad (1.20)$$

Or, if cast in terms of a restriction on amplitude:

$$A \ll \frac{l_z}{\beta \Delta T}. \quad (1.21)$$

While the linearity condition is required for the analysis performed by Carbo [16] to be valid, several papers have employed full nonlinear stability analysis in their computational solutions with no notable effects on the stability boundaries that were produced with linear stability analysis. In particular, the 1990 paper by S. Biringen and L. J. Peltier [33] came to the conclusion that for the parameter regimes that they considered, full nonlinearity was not an “important factor” for the problem. The most extreme set of parameters that they used had the non-dimensional set of variables of Rayleigh number $Ra = 10,000$, non-dimensional angular frequency $\omega^* = \omega l_z^2 / \chi = 1,332$, and non-dimensional vibration amplitude $\beta_{\text{Biringen}} = A/l_z = 21.2$.³ For the nitrogen gas at 1 atm used above, a 1 cm cube corresponds to a very large $\Delta T = 104.94$ K, $f = 46.25$ Hz, and amplitude of $A = 21.2$ cm. Interestingly, this corresponds to a non-linearity parameter of $l_z/\beta\Delta T = 2.9$ cm which our A is not even less than, let alone much less than. For a 3 cm cube, these parameters correspond to $\Delta T = 3.886$ K, $f = 5.139$ Hz, and an amplitude of $A = 0.636$ m. Here the non-linearity parameter is $l_z/\beta\Delta T = 2.316$ m which is 3.64 times larger than our A . While for these parameters, Biringen computationally found that non-linearity was unimportant, it does beg the question of what exactly is meant by “much less than.”

Ryzhkov and Gaponenko developed their paper describing the applicability of the Boussinesq approximation in support of a shaken convection experiment in microgravity that was flown on parabolic flights and later on the International Space Station. They derived the limits on frequency and amplitude for this problem (a 0.5cm) cube of isopropyl alcohol. They found their vibration limits to be $0.011 \ll f \ll 787$ Hz, $A \ll 0.228$ m, and $A(2\pi f)^2 \ll 26,352$ m/s². In their

³Note that Biringen and Peltier use this β to denote a vibration amplitude and not a thermal coefficient.

experiment, they drove their cell up to 140 mm, which is 0.61 of the amplitude limit [46,47]. Here “much less than” appears to be considered met at less than a factor of two of the amplitude limit on linearity.

Gershuni and Lyubimov cite in their book *Thermal Vibrational Convection* [32] an experimental study performed by Zavarykin, Zorin, and Putin, the results of which were published in 1988 in the Russian-language journal “Proceedings of the USSR Academy of Sciences” and do not appear to be available in English. The shaker they employed had a fixed amplitude of vibration $A = 4$ cm and the thinnest layer that they used was 0.8 mm. Assuming a temperature difference of 20K and water as the experimental liquid, the non-linearity parameter is $A \ll l_z/\beta\Delta T = 5 \text{ mm}/((2.7569 \times 10^{-4} \text{ K}^{-1})(20 \text{ K})) = 14.5 \text{ cm}$. Therefore, here, the worst case scenario has an amplitude that is 0.28 of the non-linearity limit.

Ishikawa and Kamei undertook their experiment in a container with a depth of 1.0 cm and a fixed displacement amplitude of 0.37 cm. They used distilled water and investigated the region up to $70Ra_c$. Since their container had an aspect ratio of 5.45, their container should have had a critical Rayleigh number in the range of a container with aspect ratio 5.0, which was found by Carbo [16] and Mizushima *et al.* [27] to have a critical Rayleigh number $Ra_c = 1,777$. Assuming a mean temperature of 300 K, this leads to an approximate critical temperature gradient of $\Delta T_c = 0.11$ K. Therefore, a Rayleigh number of $70Ra_c$ corresponds to $\Delta T = 7.69$ K. This leads to a non-linearity parameter of $A \ll l_z/\beta\Delta T = 0.37 \text{ cm}/((2.7569 \times 10^{-4} \text{ K}^{-1})(7.69 \text{ K})) = 1.867 \text{ m}$. Therefore, here, the bounds of linear stability analysis are well-satisfied.

Finally, the work of Rogers *et al.* [37–41] does not appear to make mention of the non-linearity parameter, perhaps because a goal of their work was to investigate non-linear and non-Boussinesq effects on the pattern formation in their systems.

Their experiment used a thinnest layer depth of $650 \mu\text{m}$ and a temperature difference of 15-30 K. Solving for the linearity factor for even the $\Delta T = 15 \text{ K}$ condition, we find that $A \ll l_z/\beta\Delta T = 1.3 \text{ cm}$. Their experiment was reported to have been driven much further than that amplitude, violating the linearity criterion by a wide margin, however, they were able to confirm the predictions of Gresho and Sani regardless.

A further point of consideration is that the experiments of Zavarykin and Rogers were intended to approximate the conditions of infinite layer theory, therefore they use very large aspect ratios ($\Gamma \rightarrow \infty$). The microgravity experiments of Shevtsova *et al.* were performed in a cubical cavity, albeit of small physical size ($5 \text{ mm} = 0.197 \text{ in}$).

The general answer to the question of how close to this dividing line ($A \ll l_z/\beta\Delta T$) between linearity and requiring the inclusion of nonlinear effects one can drive the system and still be confident of the relative validity of the linear stability predictions remains unclear. Of course, the further below the limit of this inequality the amplitude falls, the higher the confidence that can be placed in the linear stability analysis. However, both theoretical and experimental treatments of the stability boundary appear to find that nonlinearity is not a significant influence upon the stability boundary for problems that are less than, but not necessarily much less than the nonlinearity factor. It is still desirable to follow this criterion as closely as possible to assure agreement with the numerical work, however, the literature shows that this is a difficult boundary to reach in practice.

1.10 Outline

With the theoretical and numerical underpinnings of these experiments now established in this first chapter, the remainder of this description will be structured as

follows:

- The second chapter will outline the design choices made to make this experiment possible, including the exhaustive evaluation of the reams of numerical data from Carbo to determine the conditions and parameters under which convective stabilization through acceleration modulation might be possible, the devising of a novel shaker design to permit achieving sufficiently high peak shaking velocities to cross stability boundaries, and the designs for apparatus (experimental cells) to contain the fluid and establish and control the thermal conditions required for convection to be studied. This chapter also describes the measurement techniques employed, including thermal and optical flow visualization measurements.
- The third chapter will describe the experimental techniques developed and employed for these experiments and their incremental modification and improvement.
- The fourth chapter will present the results of these experiments, including the experimental determinations of the transition to stability under shaking modulation for containers of two separate physical dimensions and associated aspect ratios and their comparison to the theoretical numerical predictions of Carbo.
- The fifth chapter will present the conclusions of this work and posit avenues for both further investigation and future application of these results.

Due to the very nature of the development of this experiment, much of the following description will take more of a narrative form than some doctoral dissertations, detailing the incremental steps in its development and its modifications

and successive improvements. The author hopes that the reader will find this approach equal parts informative and interesting, and bear with the necessary digressions and important side paths that this work has, at times, occasioned and demanded. Where these digressions showed themselves to be fruitless, they are generally omitted herein for brevity and clarity, although they have at times been significant in the time and effort devoted to them and the broader understanding they have engendered.

Chapter 2

Experimental Design

A successful experiment to test the stabilization of Rayleigh-Bénard convection needs to account for numerous choices of parameters. The working experimental fluid must be chosen to allow the stability boundaries to be successfully reached, be experimentally practical, relatively safe and nontoxic, and ideally inexpensive and not particularly exotic. The dimensions of the experimental chamber must be chosen such as to bring the predicted stability boundaries into reach, obey the linearity and Boussinesq requirements of the computational method as closely as possible, and not be so small as to be impracticable to build or manipulate. The temperatures of the horizontal boundaries of the experimental cell must be controlled as precisely as possible. The entire experiment must be shaken as sinusoidally as possible, rather forcefully, however in a controlled manner with the parameters of frequency and amplitude modified as needed. And, ideally, the fluid flow within that experimental container should be visualized using intrusive or non-intrusive techniques. These elements of experimental design will be discussed in this chapter and the solutions developed will be presented.

2.1 Parameter Evaluation

2.1.1 Experimental Fluid Selection

To determine the feasibility of an experiment capable of reaching the upper stability boundary at any physical scale or in any medium, a series of spreadsheets were constructed to probe the possibilities in parameter space. The three-dimensional data for the upper stability boundary for the variety of aspect ratios and boundary conditions that Carbo computed for his dissertation were recovered from his plot files and imported into a PTC Mathcad¹ worksheet, in which all computations were performed. When possible, the data directly from Carbo's computations were employed; to allow the extension to higher Rayleigh numbers than Carbo computed, the data for the asymptotic segment of the stability boundary was fit to a power law function via a least-squares algorithm.

Whenever possible, thermophysical properties for the experimental fluids in question were taken directly from the online version of the NIST Standard Reference Data [55]. When the fluid of interest was not found in that database a variety of computerized and print sources were employed. The gases considered included: nitrogen, carbon dioxide, helium, sulfur hexafluoride, hydrogen, oxygen, argon, propane, methane, butane, neon, xenon, krypton, and air. Liquids considered included: distilled water, methanol, toluene, ethanol, isopropyl alcohol, acetone, gasoline, kerosene, turpentine, mercury, tetrahydrofuran, and carbon tetrachloride.

The computed experimental parameters were cataloged for a range of Rayleigh number and vibrational Rayleigh number pairs. Representative excerpts from these spreadsheets can be seen in Figures 2.1 and 2.3. Recorded were the required

¹PTC, Inc.: <<http://www.ptc.com/product/mathcad/>>.

vertical temperature difference ΔT for each target Rayleigh number, the required dimensioned velocity amplitude $|\mathbf{v}| = \omega A = 2\pi f A$ for the given vibrational Rayleigh number, the corresponding dimensioned drive frequency f , the non-dimensional frequency, acceleration (in units of g_o), and the critical temperature difference ΔT_c for static instability. In addition, the parameters required to determine adherence to the Boussinesq approximation were recorded: the product of the isothermal compressibility and the maximum time-periodic pressure $\beta_T p$, the product of the volumetric expansion coefficient and the vertical temperature difference $\beta \Delta T$, the ratio of the vertical temperature difference to the mean absolute temperature $|\Delta T / \langle T_o \rangle|$, the ratio of the maximum time-periodic pressure to the mean pressure $|\Delta p / \langle p_o \rangle|$, the ratio of the vertical dimension of the container to the sound speed in the medium l_z / c , the period of oscillation $\tau = f^{-1}$, and the characteristic viscous and thermal diffusion times over the length of the cavity l_z^2 / ν and l_z^2 / χ , respectively.

The gases were assessed based on a simple criterion: those operating points that had a temperature difference of $\Delta T \lesssim 50$ K and also were accessible through the demonstrated performance of the rhombic shaker system ($|\mathbf{v}| < 3.7$ m/s), which will be discussed later. A temperature difference of 50 K was chosen as a reasonable upper limit for an experiment based both on the practical concerns of reaching that gradient and maintaining adherence to the thermal elements of the Boussinesq approximation and the non-linearity parameter. The gases were also evaluated at static pressures of 1.0, 1.5, and 2.0 atmospheres. The majority of work was focused on the 1.0 atm pressure due to the ease of operating an experiment at atmospheric pressure. No significant advantage was seen in the accessible region of experimental points by raising the static pressure to 1.5 and 2.0 atm. While operation at significantly higher static pressures might be advantageous, the necessity to now construct an oscillating pressure vessel complicates those possible gains.

Gas:	Pressure (atm)	Rayleigh Number (dimensionless)	Vibrational Rayleigh Number (dimensionless)	ΔT (deg K)	Velocity $\omega A = 2\pi f A$, (m/s)	Frequency (Hz at 3 in. disp.)	Non-Dim. Freq.	Non-Dim. Accel.	Critical ΔT (deg K)
2 cm cubical container (0.787" cubical container)	Aspect Ratio: Critical Rayleigh Number:		$\Gamma_x = \Gamma_y = 1$ 3388.5	T_c (K) =	300				
Nitrogen	1	1.00E+04	1.25E+04	13.117	3.349	6.995	805.685	15.004	4.445
N ₂	1	2.00E+04	4.03E+04	26.234	3.005	6.276	722.928	12.080	4.445
	1	3.00E+04	5.98E+04	39.351	2.441	5.098	587.243	7.971	4.445
	1	4.00E+04	8.29E+04	52.468	2.156	4.503	518.679	6.218	4.445
Carbon Dioxide	1	6.00E+04	1.38E+05	21.028	3.593	7.505	1720.884	17.270	1.188
CO ₂	1	7.00E+04	1.70E+05	24.533	3.415	7.133	1635.630	15.601	1.188
	1	8.00E+04	2.04E+05	28.038	3.274	6.838	1568.098	14.339	1.188
	1	9.00E+04	2.41E+05	31.542	3.159	6.598	1513.018	13.350	1.188
	1	1.00E+05	3.08E+05	35.047	3.216	6.717	1540.318	13.836	1.188
	1	1.10E+05	3.20E+05	38.552	2.979	6.222	1426.806	11.872	1.188
	1	1.20E+05	3.62E+05	42.057	2.907	6.072	1392.321	11.305	1.188
	1	1.30E+05	4.07E+05	45.561	2.843	5.938	1361.668	10.813	1.188
	1	1.40E+05	4.53E+05	49.066	2.785	5.817	1333.889	10.376	1.188
	1	1.50E+05	5.01E+05	52.571	2.733	5.708	1308.983	9.992	1.188
Sulfur Hexafluoride	1	7.00E+04	1.70E+05	20.411	3.668	7.661	646.344	17.998	0.988
SF ₆	1	8.00E+04	2.04E+05	23.327	3.517	7.346	619.736	16.547	0.988
	1	9.00E+04	2.41E+05	26.243	3.394	7.089	598.062	15.410	0.988
	1	1.00E+05	3.08E+05	29.159	3.454	7.214	608.635	15.960	0.988
	1	1.10E+05	3.20E+05	32.075	3.2	6.684	563.877	13.699	0.988
	1	1.20E+05	3.62E+05	34.991	3.122	6.521	550.133	13.039	0.988
	1	1.30E+05	4.07E+05	37.907	3.053	6.377	537.974	12.469	0.988
	1	1.40E+05	4.53E+05	40.823	2.992	6.249	527.225	11.976	0.988
	1	1.50E+05	5.01E+05	43.739	2.936	6.132	517.357	11.532	0.988
	1	1.60E+05	5.50E+05	46.654	2.885	6.026	508.370	11.134	0.988
	1	1.70E+05	6.01E+05	49.57	2.839	5.930	500.265	10.782	0.988
	1	1.80E+05	6.54E+05	52.486	2.796	5.840	492.688	10.458	0.988
Oxygen	1	1.00E+04	1.25E+04	13.467	3.305	6.903	778.684	14.612	4.563
O ₂	1	2.00E+04	4.03E+04	26.934	2.966	6.195	698.813	11.768	4.563
	1	3.00E+04	5.98E+04	40.401	2.409	5.032	567.579	7.763	4.563
	1	4.00E+04	8.29E+04	53.869	2.128	4.445	501.374	6.058	4.563
Argon	1	1.00E+04	1.25E+04	11.17	3.629	7.580	910.606	17.618	3.785
Ar	1	2.00E+04	4.03E+04	22.339	3.256	6.801	817.011	14.182	3.785
	1	3.00E+04	5.98E+04	33.509	2.645	5.524	663.696	9.359	3.785
	1	4.00E+04	8.29E+04	44.679	2.337	4.881	586.411	7.306	3.785
Methane	1	1.00E+04	1.25E+04	15.593	3.071	6.414	681.062	12.616	5.284
CH ₄	1	2.00E+04	4.03E+04	31.186	2.756	5.756	611.204	10.161	5.284
	1	3.00E+04	5.98E+04	46.779	2.238	4.674	496.326	6.700	5.284
Xenon (Xe)	1	4.60E+05	2.64E+06	49.204	3.706	7.741	2998.469	18.373	5.284
Krypton	1	7.00E+04	1.70E+05	21.947	3.611	7.542	1712.320	17.443	1.062
Kr	1	8.00E+04	2.04E+05	25.082	3.461	7.229	1641.191	16.024	1.062

Figure 2.1: Excerpt from the gas experimental parameters spreadsheet for a 2 cm cube. The spreadsheet also includes the parameters required to assess the operating state for adherence to the Boussinesq approximation (seen in Figure 2.2).

$\beta_p p$?	$\beta \Delta T$?	$\Delta T/T_0$?	p'/p_0	?	h/c	?	τ	?	l_z^2/ν	l_z^2/χ	A/l_z	?	Linearity Factor:	Lin. Factor/ A/l_z
3.31E-05	<<	0.044	<< 1	0.0437	<< 1	3.31E-05	<< 1	5.66E-05	<<	0.14296	<<	25.439	18.336	3.81	<<	22.871	6.0029
2.67E-05	<<	0.087	<< 1	0.0874	<< 1	2.67E-05	<< 1	5.66E-05	<<	0.15933	<<	25.439	18.336	3.81	<<	11.436	3.0016

Figure 2.2: A sample of the spreadsheet columns of the parameter evaluation for adherence to the Boussinesq approximation.

Liquids were evaluated at a range of Rayleigh number from 10^4 to 10^9 , regardless of the resulting outputs. Due to the strong dependence of the shaking velocity and acceleration on the height of the cavity l_z (to the second power in velocity and

Gas:	Pressure (atm)	Rayleigh Number (dimensionless)	Vibrational Rayleigh Number (dimensionless)	ΔT (deg K)	Velocity $\omega A = 2\pi f A$, (m/s)	Frequency (Hz at 3 in. disp.)	Non-Dim. Freq.	Non-Dim. Accel.	Critical ΔT (deg K)
2 cm cubical container (0.787" cubical container)	Aspect Ratio:		$\Gamma_x = \Gamma_y = 1$	$T_s(K) =$	300				
	Critical Rayleigh Number:		3388.5						
Water	1	1.00E+04	1.25E+04	0.072	175.069	365.657	6.27E+06	4.10E+04	0.026
H ₂ O	1	1.00E+05	3.08E+05	0.773	86.902	181.508	3.11E+06	1.01E+04	0.026
	1	1.00E+06	7.74E+06	7.729	43.564	90.990	1.56E+06	2.54E+03	0.026
	1	1.00E+07	1.89E+08	77.286	21.527	44.962	7.71E+05	6.20E+02	0.026
	1	1.00E+08	9.14E+09	772.863	14.966	31.259	536257.200	299.632	0.026
Methanol	1	1.00E+04	1.25E+04	7.80E-03	229.728	479.821	11474036.725	70599.867	2.64E-03
CH ₃ OH	1	1.00E+05	3.08E+05	0.078	114.034	238.177	5695563.031	17395.813	2.64E-03
	1	1.00E+06	7.74E+06	0.78	57.165	119.398	2855173.550	4371.560	2.64E-03
	1	1.00E+07	1.89E+08	7.801	28.248	59.000	1410879.777	1067.460	2.64E-03
	1	1.00E+08	9.14E+09	78.01	19.644	41.029	981142.819	516.221	2.64E-03
	1	1.00E+09	3.00E+11	780.103	11.254	23.506	562094.343	169.430	2.64E-03
Toluene	1	1.00E+04	1.25E+04	7.68E-03	243.209	507.978	13300215.273	79128.932	2.60E-03
C ₇ H ₈	1	1.00E+05	3.08E+05	0.077	120.726	252.154	6602065.668	19497.442	2.60E-03
	1	1.00E+06	7.74E+06	0.768	60.519	126.403	3309563.906	4899.587	2.60E-03
	1	1.00E+07	1.89E+08	7.676	29.906	62.463	1635450.324	1196.445	2.60E-03
	1	1.00E+08	9.14E+09	76.755	20.797	43.438	1137312.258	578.599	2.60E-03
	1	1.00E+09	3.00E+11	767.552	11.915	24.886	651587.996	189.917	2.60E-03
Ethanol	1	1.00E+04	1.25E+04	1.60E-02	165.994	346.703	9346343.238	36860.464	5.53E-03
C ₂ H ₅ OH	1	1.00E+05	3.08E+05	0.163	82.397	172.098	4639388.434	9082.362	5.53E-03
	1	1.00E+06	7.74E+06	1.633	41.305	86.272	2325690.732	2282.345	5.53E-03
	1	1.00E+07	1.89E+08	16.326	20.411	42.631	1149247.634	557.320	5.53E-03
	1	1.00E+08	9.14E+09	163.261	14.194	29.646	799197.537	269.517	5.53E-03
	1	1.00E+09	3.00E+11	1.63E+03	8.132	16.985	457874.762	88.465	5.53E-03
Isopropyl Alcohol	1	1.00E+04	1.25E+04	1.30E-02	188.922	394.591	15918403.458	47746.450	4.25E-03
C ₃ H ₈ O	1	1.00E+05	3.08E+05	0.125	93.779	195.871	7901737.002	11764.872	4.25E-03
	1	1.00E+06	7.74E+06	1.255	47.011	98.189	3961105.985	2956.480	4.25E-03
	1	1.00E+07	1.89E+08	12.546	23.231	48.521	1957423.861	721.958	4.25E-03
	1	1.00E+08	9.14E+09	125.461	16.155	33.742	1361206.254	349.132	4.25E-03
	1	1.00E+09	3.00E+11	1.26E+03	9.255	19.330	779818.253	114.585	4.25E-03
Acetone	1	1.00E+04	1.25E+04	3.87E-03	297.827	622.056	14735120.881	118659.948	1.31E-03
C ₃ H ₆ O	1	1.00E+05	3.08E+05	0.039	147.837	308.779	7314300.133	29237.639	1.31E-03
	1	1.00E+06	7.74E+06	0.387	74.11	154.790	3666624.613	7347.332	1.31E-03

Figure 2.3: Excerpt from the liquid experimental parameters spreadsheet for a 2 cm cube. The spreadsheet also includes the parameters required to assess the operating state for adherence to the Boussinesq approximation (seen in Figure 2.2).

fourth power in acceleration), both liquids and gases were tested for several sizes of container, ranging from 1 - 4 cm cubical containers. Unfortunately, even at the 1 cm scale, liquids, posed far too high required velocities (and accelerations) for stabilization. For example, for a 1 cm cubical container of water, to stabilize the system at a Rayleigh number of $Ra = 1 \times 10^6$, $|\mathbf{a}| = 159g$. ($|\mathbf{v}| = 10.9$ m/s) would be required at a temperature difference of 61.8 K. In order to bring this container to a stability boundary accessible to the velocity limit of the current shaker system, an unrealistic ΔT of 6.18×10^3 K is required.

Assessing the gas charts overall, the stability boundaries calculated for plain dry air follow those for Nitrogen, Oxygen, and Argon relatively closely. Considering the chemical composition of the atmosphere, this is unsurprising, but does lend a simplification to the design of an experiment, as it obviates the necessity to supply a controlled gas from a pressurized supply, as would be required from a commercial cylinder. Additionally, air is intrinsically safe, avoiding gases that are toxic or are asphyxiants.

The other advantage of air is that if a smoke seeding technique is employed, the use of plain air allows combustion to take place in the experimental medium. This allows many common (and relatively simple) seeding techniques to be employed, generally involving the combustion of materials (tobacco smoke, incense, cotton fibers, etc.). In a gas other than air, non-combustion methods of seeding must be employed. These include smoke wires (heater wire dipped in a mineral oil or other smoke fluid), oil droplet seeding (with the atomizing gas being the experimental medium), or various chemical reaction techniques (many of which use or result in toxic substances). These techniques will be discussed further in the imaging section.

The selection of air does bring about some significant disadvantages. The properties of air are relatively constant, however, they do vary, particularly with the daily changes in water vapor content due to meteorological conditions. Additionally, with only one choice of experimental gas, the range of Rayleigh numbers accessible becomes somewhat limited as can be seen in Figure 2.4.

Thus, using a near 2 cm cube filled with air and with the performance of the current shaker system, the range of $Ra = 1.1\text{--}4.7 \times 10^4$ ($(3.25\text{--}13.9) R_c$) is accessible, which corresponds to a temperature difference ranging from 12–52 K and a drive velocity of 3.7–2.1 m/s. This region corresponds to the boxed segment on Figure

Gas:	Pressure (atm)	Rayleigh Number (dimensionless)	Vibrational Rayleigh Number (dimensionless)	ΔT (deg K)	Velocity $\omega A = 2\pi f A$, (m/s)	Frequency (Hz at 3 in. disp.)	Non-Dim. Freq.	Non-Dim. Accel.	Critical ΔT (deg K)
2.121 cm cubical container (0.787" cubical container)	Aspect Ratio:		$\Gamma_x = \Gamma_y = 1$	T_0 (K) =	300				
	Critical Rayleigh Number:		3388.5						
Air	1	1.12E+04	1.53E+04	12.484	3.697	7.722	1553.323	18.284	3.783
	1	1.36E+04	2.02E+04	15.178	3.498	7.306	1469.712	16.369	3.783
	1	1.65E+04	2.61E+04	18.453	3.269	6.828	1373.496	14.296	3.783
	1	1.88E+04	3.08E+04	21.02	3.116	6.508	1309.211	12.989	3.783
	1	2.14E+04	3.61E+04	23.944	2.963	6.189	1244.927	11.745	3.783
	1	2.44E+04	4.22E+04	27.275	2.811	5.871	1181.063	10.571	3.783
	1	2.78E+04	4.89E+04	31.069	2.658	5.552	1116.779	9.451	3.783
	1	3.17E+04	5.71E+04	35.391	2.52	5.263	1058.797	8.495	3.783
	1	3.61E+04	6.62E+04	40.314	2.383	4.977	1001.236	7.597	3.783
	1	3.85E+04	7.07E+04	43.027	2.307	4.819	969.304	7.120	3.783
	1	4.39E+04	8.23E+04	49.012	2.184	4.562	917.624	6.381	3.783
	1	4.69E+04	8.85E+04	52.31	2.123	4.434	891.995	6.029	3.783
2.121 cm square cs x 4.242 cm high	Aspect Ratio:		$\Gamma_x = \Gamma_y = 0.5$						
	Critical Rayleigh Number:		17085						
Air	1	2.22E+05	3.59E+05	31.026	3.605	7.530	1514.669	17.385	2.385
	1	2.44E+05	4.05E+05	34.084	3.483	7.275	1463.409	16.229	2.385
	1	2.68E+05	4.55E+05	37.442	3.36	7.018	1411.730	15.103	2.385
	1	2.95E+05	5.09E+05	41.132	3.238	6.763	1360.471	14.026	2.385
	1	3.24E+05	5.92E+05	45.185	3.177	6.636	1334.841	13.502	2.385
	1	3.56E+05	6.87E+05	49.638	3.116	6.508	1309.211	12.989	2.385
	1	3.91E+05	7.97E+05	54.529	3.055	6.381	1283.582	12.485	2.385
2.121 cm square cs x 2.828 cm high	Aspect Ratio:		$\Gamma_x = \Gamma_y = 0.75$						
	Critical Rayleigh Number:		?						
Air	1	4.00E+04	5.65E+04	18.842	3.532	7.377	1483.997	16.689	
	1	4.50E+04	6.70E+04	21.197	3.419	7.141	1436.519	15.638	
	1	5.00E+04	8.27E+04	23.552	3.418	7.139	1436.099	15.629	
	1	6.00E+04	1.15E+05	28.263	3.359	7.016	1411.310	15.094	
	1	8.00E+04	1.80E+05	37.648	3.152	6.583	1324.337	13.291	
	1	1.00E+05	2.46E+05	47.105	2.946	6.153	1237.785	11.610	

Figure 2.4: Excerpt from the air experimental parameters spreadsheet for a 2.121 cm cube.

2.5. We note that while this region is limited in scope, it falls well above the non-linear regime near the critical Rayleigh number and provides the ability to probe the linearity of the asymptotic range of the vibrational Rayleigh number.

As a result of these evaluations, air was selected as the experimental medium for all further experimental efforts.

2.1.2 Further Evaluation

While the procedure outlined in the previous section was an effective means to investigate the broad range of materials and container dimensions, it is analogous to pointing a flashlight into a pitch-dark night. It provides only a point-by-point

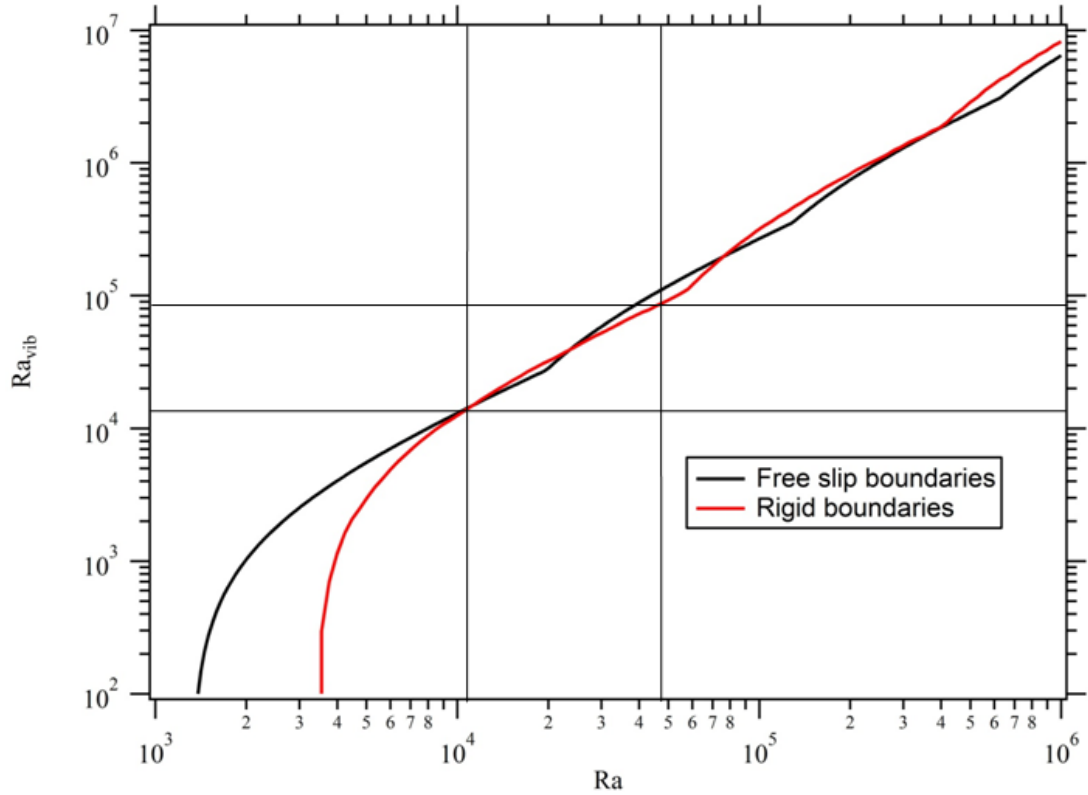


Figure 2.5: Plot of the upper boundary for a cubical container ($\Gamma_x = \Gamma_y$) with two mechanical boundary conditions. The boxed region corresponds to the accessible region in space determined for a 2 cm cubical container of air under the experimental limits. Note that the region enclosed by the box varies based on the choice of aspect ratio, container size, and experimental fluid.

interrogation of the parameter space instead of an overall synoptic view of the stability boundaries for individual choices of materials and containers. As a result, a further Mathcad worksheet was developed to probe the parameters for these individual configurations.

These worksheets again began with the raw data from Carbo's efforts for a wide range of square cross-section containers. Many of these data sets require some pre-processing from their raw forms. Carbo discovered computationally that the parametric stabilization effect was relatively insensitive to higher order harmonics and that the computational efficiency of his method could be improved by

implementing a square-wave shaking excitation (he refers to this as a “rectangular drive”) and that the results using this method could be converted to those obtained with a sinusoidal excitation by simply employing a multiplicative constant between the two results for vibrational Rayleigh number. The full details of this scheme can be found in Chapter Five of his dissertation [16].

The raw data must also be aligned such that the Rayleigh numbers are correlated between data sets and extraneous zero-value results are removed. At this point, the fluid properties must also be input, again using the highest quality sources available, such as the NIST reference employed earlier. There were also computations that took account of the effect of water vapor content on the thermophysical properties of the ambient air [56], however, the differences in the final computed stability boundaries when these empirical correlations were used were not significant.

2.2 Shaker Systems

Unfortunately, referring to the computations discussed earlier, we quickly realize that the velocities listed there are unrealistically high for most shakers, even in the low velocity limits. Thus, we are immediately limited in the number of experimental points that can be realistically accessed in an experiment. Even the lowest velocity fluid, plate separation, thermal configurations require rather large velocities and accelerations. Typical electrodynamic shakers are rated in terms of a handful of properties, generally, the force rating (measured in newtons), the stroke rating (in $\text{mm}_{\text{peak-peak}}$), the maximum bare-table (no load) acceleration (in g_{pk}), the maximum bare-table velocity (in m/s), and the bandwidth accessible (in Hz). Generally, for large electrodynamic shakers, these values are in the range of strokes (peak-to-peak displacement) of 12–75 mm, maximum accelerations of 75–150 g_{\circ} , and

maximum velocities of 1–3 m/s. Referring back to our spreadsheets, we see that the velocities that are required are significantly higher than those of a standard electrodynamic shaker. It also bears notice that the shaker ratings are provided as bare-table values, which are then derated by loading. In addition, a standard electrodynamic shaker’s bare-table velocity limit v_{rate} is often an electrical limit, not a mechanical one, resulting from the difference between the available amplifier power and the back-emf generated by the motion of the shaker’s coil within the magnetic field of the gap [57]. The result of this restriction is that the shaker reaches its peak velocity at only a single frequency, which drops off approximately in a power law relation to the frequency. This restricts high velocity performance to a small region around this peak. If the shaker is equipped with an automatic load-leveling system, the maximum acceleration is actually met across a broad range of frequencies, although the stroke is limited at higher frequencies. In addition, the attachment of a significant test load often results in maximum accelerations of less than ten percent of the bare-table rating. A typical electrodynamic shaker performance curve may be seen in Figure 2.6.

The only currently commercially available electrodynamic shaker that is capable of achieving a velocity as high as 3.0m/s is the Brüel & Kjær/Ling Dynamic V9 Shaker. Unfortunately, shakers of this capability are not only costly, but also size, weight (5,700 kg), and infrastructure (water cooling, 208 V/500 A supply) prohibitive. The Rogers experiment [37] used a mechanical shaker that employed a servo-actuated hydraulic ram to oscillate the test cell. The attendant support infrastructure (hydraulic pump, ram, etc.) and the cost (these shakers are purpose-built for the needs of the automotive, aerospace, and defense industries) make this an impractical option for this experiment. With this apparatus, their group was able to attain a displacement amplitude of 7.625 cm at a frequency of up to 20 Hz.

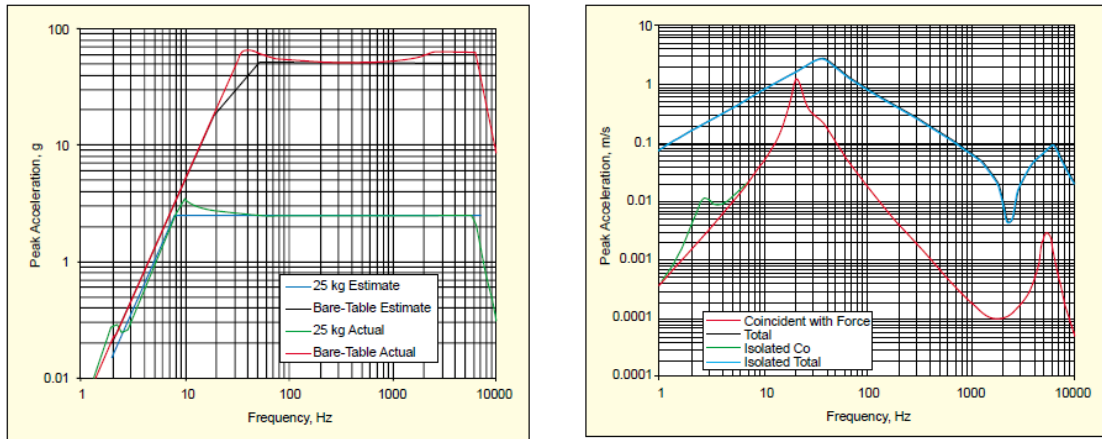


Figure 2.6: Performance curves for a sample medium-size electromagnetic shaker produced by Data Physics corporation [57]. The plot on the left shows peak acceleration as a function of frequency and the plot on the right shows peak velocity as a function of frequency (note that the y -axis label is incorrect in the original publication). Specifications for this shaker are: peak sine force: $F = 650$ N, maximum table load: $M_{max} = 25$ kg, frequency range: $f = 2-7,000$ Hz, maximum peak-to-peak stroke: $S_{max} = 2.54$ cm, and maximum bare-table velocity: $v_{max} = 1.5$ m/s. This shaker is equipped with an automatic pneumatic load compensation system.

Assuming that they ran their shaker up to the full displacement and frequency limits, the maximum attainable velocity of this system was 9.6 m/s.

What is needed here is a shaker system of similar capabilities, but that is less costly to produce and operate. A new shaker design will be discussed in the next section.

2.2.1 Rhombic Shaker

Note: This section is adapted from A. Swaminathan, M. E. Poese, R. W. M. Smith, and S. L. Garret, “Note: A kinematic shaker system for high amplitude, low frequency vibration testing,” Rev. Sci. Inst. **86**(11), 116102 (2015).

In addition to the specific experimental problem addressed here, many other research applications can be noted that require a shaker system that produces high

peak vibration velocities: excitation of parametric resonance in dynamic systems [58], shaken granular materials experiments [59], Faraday waves, and package, vehicle, and aerospace component testing [60], among others. As was discussed in the previous section, peak shaking velocities at and beyond 3.0 m/s are difficult to achieve through most conventional means, including standard mechanical and electrodynamic shakers. Presented in this section is a design for and demonstration of a simple shaker system that is able to produce high peak velocities at low frequencies and high displacements.

A shaker system of such capabilities is required for experiments on parametric stabilization of statically unstable systems, namely those here of Rayleigh-Bénard convection under the influence of high-amplitude vibration. As was discussed, theoretical predictions of the peak shaker velocities required to stabilize such systems imply that even for optimal fluid and geometric conditions, velocities approaching and exceeding 3.0 m/s are needed for demonstrations of full stabilization [29]. This problem is not unlike those of other parametric resonances, such as the inverted (Kapitza) pendulum, and predictions of such high shaking velocities are consistent with prior theoretical work [9].

Commercially-available electrodynamic shakers are unable to reach such high peak velocities, as the most capable electrodynamic shakers on the market today are able to reach peak speeds of 3.0 m/s. Additionally, very large electrodynamic shakers are prohibitive in resources for fundamental research projects in terms of size, device weight, infrastructure and significant power requirements, cooling systems, and cost.

Hydraulic shaker systems, utilizing a hydraulic ram controlled by servovalves, are widely used in vehicle and component packaging, electronics, and seismic testing and are capable of high velocity output and long displacement amplitudes. They

are, however, prohibitive in cost and infrastructure requirements for a basic research investigation. Mechanical shakers are widely employed in applications as diverse as product and packaging vibration qualification testing and shaking fruit off of trees for harvest, however, they are generally limited to low velocities due to the shaker motor being placed in the moving frame.

The solution that was developed for this experiment was to create a mechanical shaker that employs two counter-rotating flywheels driven by a rotary electric motor, producing near-sinusoidal oscillation of a platform riding on linear guidance bearings. Single-flywheel shakers of this type have been used with success in the shaken granular materials community at relatively lower velocities [61]. The advantages observed in this system are a high degree of simplicity and very low amounts of transverse acceleration, to which granular material experiments, and the Rayleigh-Bénard instability, are highly sensitive.

The implementation of two flywheels allows the canceling of forces on the carriage in the direction transverse to the desired oscillation, reducing both potential binding of the guidance bearings and the transmission of undesirable off-axis accelerations to the experimental fluid. This design was inspired by the construction of rhombic drive β -Stirling engines [62]. This type of Stirling engine also employs two counter-rotating flywheels, each connected by linkages to driving pistons at two points on the wheel, to ensure appropriate phasing for the Stirling cycle, however, here the flywheels are only connected at one position.

As this shaker is driven by a rotary, electric induction motor, it is not limited by the restrictions on velocity of a typical electrodynamic (moving coil or moving magnet) shaker. The shaker operates at a single vertical displacement controlled by the radius of the pivot bearing within the flywheels. The peak velocity of the shaker is linearly proportional to the rotation rate of the motor, described by $|\mathbf{v}| = a\omega$,

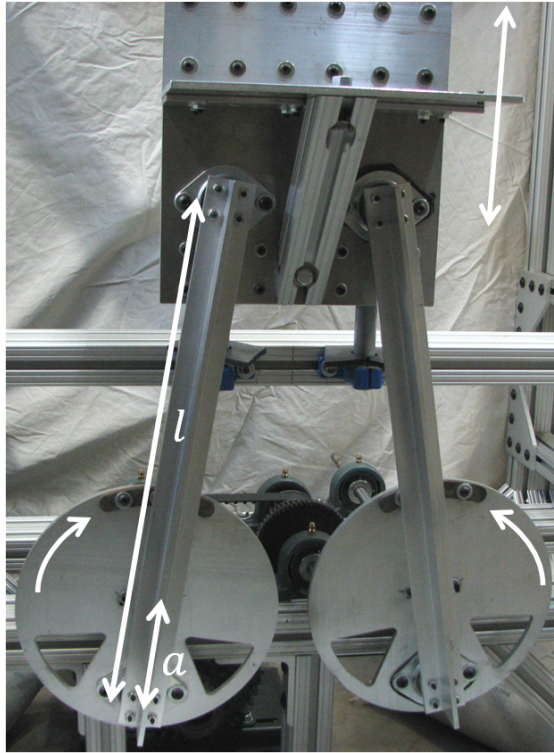


Figure 2.7: Detail view of the experimental carriage. Lengths a and l are denoted for reference.

where a is the (zero-to-peak) displacement amplitude of the vibration and ω is the angular frequency of the shaker. In this way, the peak velocity of the shaker may be controlled using a standard variable frequency inverter drive.

The flywheels are the primary rotational component of this shaker system, which, as constructed, operates with a 7.62 cm displacement (15.2 cm peak-to-peak stroke). This was chosen to enable high velocities to be reached at relatively low rotational speeds, although the system may be constructed to deliver comparable velocities through lower amplitudes coupled with higher rotational speeds. As noted previously, the amplitude is controlled only by the placement of the pivot point for the pushrods within the flywheel itself, therefore, the amplitude may be adjusted within a broad range by varying the attachment point. The flywheels

are constructed of 0.635 cm thick aluminum (6061 alloy) with inset rotary ball bearings and a steel counterweight to rotationally balance the bearing and associated hardware. The wedge-shaped cut-away sections were also added to reduce the required mass of the steel counterweight and further rotationally balance the system. These balance computations were performed using the center of mass computation functions of a CAD program, in which the component was designed and from which CNC machine tool instructions were derived.

These flywheels are mounted on a 1.27 cm diameter steel shaft by means of a flanged shaft collar. This connection is designed to permit adjustment of the rotational alignment of the flywheel using screws fitted into the arced slots. This shaft is supported by a pair of ABEC-1 tolerance ball bearings supported by cast iron pillow blocks.

The degree of non-sinusoidal motion of the shaker carriage is determined by the ratio in length between the shaker amplitude a (determined by the radius of the bearing from the center of the flywheel) and the length of the pushrod l . The equation of motion of the carriage (from the center of its travel) is given by $x_{\text{shaker}} = \sqrt{a^2 + l^2 + 2al \cos [\omega t + \arcsin \{(a/l) \sin (\omega t)\}]} - l$. The relative harmonics produced by this system as a function of the ratio of l/a are given in Table 2.1. Note that there are no odd-numbered higher harmonics produced.

Between the two bearings lies the gearing system (shown in detail in Figure 2.8). Both flywheels are driven by the electric motor through a heavy-duty toothed timing belt. This belt directly drives one flywheel by passing over a timing belt pulley and then over an idler shaft with a second timing belt pulley. This idler shaft is also fitted with a 9.53 cm pitch diameter spur gear. This gear is meshed with an identical gear on the shaft driving the second flywheel, ensuring a one-to-one counter-rotation of the two flywheels. All the rotational shaft connections are made

Table 2.1: Quantification of the non-sinusoidal effects of the shaker system. f_n denotes the relative harmonic.

l/a	$f_2/f_1 (\times 10^{-2})$	$f_4/f_1 (\times 10^{-4})$	THD (%)
1.1	25.40	316.1	25.60
1.5	15.41	69.28	15.43
2.0	10.83	24.01	10.84
3.0	6.940	6.309	6.940
4.0	5.138	2.558	5.138
5.0	4.087	1.285	4.087

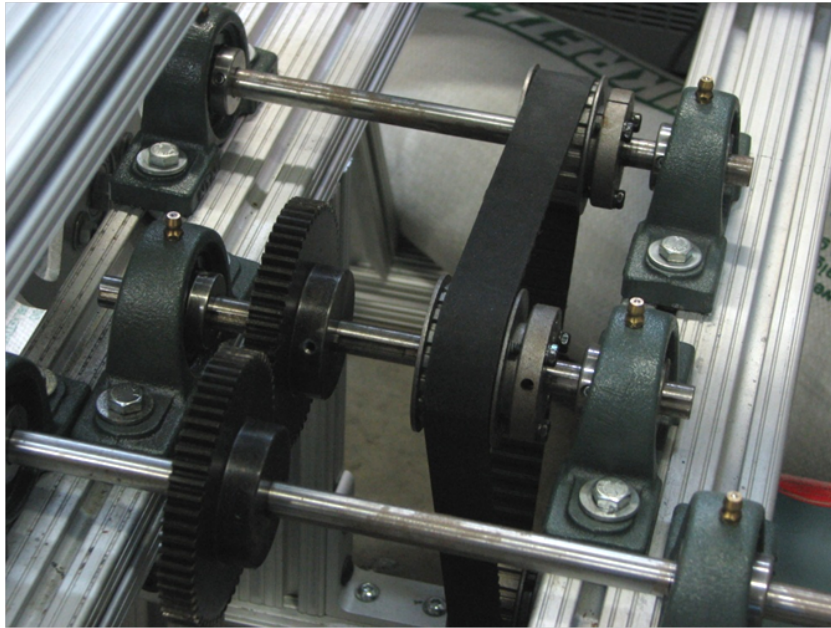


Figure 2.8: Detail view of the gearing arrangement.

using parallel keyed joints.

The linkages between the flywheels and the carriage, which carries the experimental payload, are made by means of aluminum T-bar extrusions with flanged idler shafts fixed to their ends. These shafts engage the rotating bearings set in the flywheel and also the bearings fixed in the carriage upon which the experiment rides to translate the rotational torque from the flywheels to a linear force applied to oscillate the carriage. A T-extrusion was chosen to provide sufficient structural

rigidity, which was confirmed using finite element modeling.

The carriage (shown in Figure 2.7) is guided by four bushing-type bearings. These bearings have a ceramic coated contact surface that permits high velocities, accelerations, and rapid oscillatory loading without the skidding that can result from linear rolling-element bearings.² These bearings, mounted in aluminum pillow blocks, run on a pair of parallel hardened precision ground 440C stainless steel shafts with a chromium coating applied and lubricated by application of non-detergent motor oil applied during stoppages in experimental runs. This requirement for open lubrication of the bearings has not proven to be overly taxing in practice as several hours of operation may take place between the application of lubricant and the oil adheres well to the shafting, without significant drips or runs. Due to the cantilevered load presented by the experimental payload, care was taken to ensure that the bearings were sufficiently spaced along the direction of travel to control the edge loading of the bearings.

The shaker is driven by a 3-HP (2.2 kW), inverter-rated induction motor housed in a NEMA-standard 145T frame. The rotational speed of this motor is controlled by a 3-phase variable frequency drive, operating at a supply voltage of 208 V_{ac} with a peak current draw of 11 A. Speed feedback for the motor is obtained through an optical shaft encoder affixed to one of the system's drive shafts. This encoder provides rotational speed accuracy of 1,000 counts/revolution and is read by a frequency counter. Additionally, the encoder signal may be employed as a feedback signal for speed control. A speed reference of this type is required due to the usage of an induction motor with its inherent slip. This requirement for a reference may be avoided by using a synchronous-type permanent magnet motor.

²Black Racer™ ceramic coated linear bearings, P/N: LPB 1220-13; LM-Tarbell, Inc.: <<http://www.lm76.com/>>.

Table 2.2: Demonstrated performance of the shaker system to date.

Performance Parameter	Demonstrated Value
Bandwidth	3.5–7.75 Hz
Displacement (peak-peak)	152 mm
Acceleration (sine peak)	18.4 g
Velocity (sine peak)	3.7 m/s

The shaker is supported by a frame constructed from an extruded aluminum track system, employing fasteners that slide in a t-slot on the extrusion, permitting ease of construction and adjustment. The frame rests on a reinforced concrete slab floor and is kept in contact with the floor by means of either a load of sandbags (totaling 136 kg) or a series of steel hold-downs bolted to the support. This requirement is due to the large reaction forces generated by the system in the vertical direction during operation.

This shaker system has been demonstrated in the laboratory to be capable of operating to a peak velocity in excess of 3.7 m/s with an experimental payload of approximately 2 kg in the course of experiments on the stabilization of thermal convection, permitting initial observations of stabilization to be taken. This system has now been operated in excess of 250 hours with no failures and has enabled the exploration of regimes of peak velocity that would be otherwise inaccessible. Demonstrated performance figures are given in Table 2.2.

In summary, a mechanical shaker system of high peak velocity capacity has been designed, constructed, tested, and employed in these experiments on the dynamic stabilization of Rayleigh-Bénard convection. This ability to reach peak velocities in excess of 3.7 m/s has enabled this research to move forward in a cost-effective manner and reach performance outside the capabilities of commercially available electrodynamic vibration exciters. The design and capabilities of the

system described in this section have raised interest from researchers in the fields of parametric resonance, shaken granular materials, turbulence, aerospace, and sonoluminescence and this system may be appropriate for any application requiring high peak velocity, low frequency, long excursion vibration testing or excitation.

2.3 Imaging Techniques Surveyed

Nearly every fluid mechanics experiment involves some method of determining the flow field throughout the fluid. Hot-wire anemometers and laser Doppler anemometry provide a quantitative measurement of local, pointwise velocities in the flow field. Particle image velocimetry provides a global map of the streamlines and velocity gradients in the fluid. Bénard himself utilized a seeding method to visualize his roll cells. In this section, several global, qualitative means of flow visualization for this experiment will be assessed.

2.3.1 Shadowgraphy

One common methodology for visualizing convective flows is the family of techniques that rely on the change in refractive index of the fluid with changes in density. The simplest to implement of these refractive index-based techniques is the direct shadowgraphy method. This is a time-tested methodology, dating to the work of Robert Hooke, who used it in 1672 to observe the plume of heated air generated by a candle flame [63]. Direct shadowgraphy requires only a bright, ideally collimated, light source and a method to capture the resulting shadowgraph: a projection screen or some form of photodetector (CCD/CMOS camera, photodiode, film, etc.). While the shadowgraph method does not have the highest sensitivity of the refractive imaging methods, it is by far the most robust. While schlieren

and interferometry methods offer much higher sensitivity and the ability to make quantifiable temperature measurements, they are also much more sensitive to alignment and positioning of their optical components. As Settles noted in his monograph *Schlieren and Shadowgraph Techniques* [52], quoting Reichenbach, who was cursed with a laboratory that had wooden floors that transmitted vibration, “Once the schlieren knife had been adjusted with great difficulty, nobody was allowed to move until the picture was taken.” In addition, interferometry relies upon phase shifts between light beams and therefore is sensitive to sub-optical-wavelength misalignment. It quickly becomes apparent that both these techniques, due to their highly alignment dependent optical trains are incompatible with an experiment that is fundamentally dependent on vibration for its functioning.

In many convection apparatuses, particularly those focusing on the roll cell planform in experiments that are approximating infinite layers, the shadowgraphs are taken *through* the heated and cooled boundaries. The difficulty with that setup is that now transparent surfaces must be heated and cooled. This is generally accomplished through the use of a beam splitter and a mirrored heated plate with a transparent cooled plate. The image taken of the planform is generally relatively easy to interpret [64, 65], with bright lines indicating regions of relatively cold fluid moving downwards and dark lines indicate hot fluid moving upwards.

Another vein of shadowgraphy, the side-viewed cavity, has been employed [66–75]. The advantage here is its simplicity, in that there is no requirement to have a transparent upper or lower boundary, and to cool or heat them, allowing a much less complicated experimental design. The downside is that the image is now integrated over the width of the cell, seen from the side and interpretation of the resultant data is not as clear-cut.

Unfortunately, in a gas at atmospheric pressure, it is difficult to produce sufficient

optical sensitivity with a direct shadowgraph to detect the small deviations in density that result from a convection experiment that relies upon small thermal gradients. For illustration, the Gladstone-Dale constant K , describing the linear dependence of the refractivity ($n - 1$) on the density of the fluid, is on the order of $2.3 \times 10^{-4} \text{ m}^3/\text{kg}$ for air at room temperature depending on the wavelength of the incident light [51]. There are several methodologies to improve the sensitivity of a shadowgraph in gas. One may increase the mean pressure, which increases the refractivity of the gas, although this requires the use of a pressure vessel to contain the experiment, which leads to a significant increase in the size and mass of the experiment, in addition to the added hazards of oscillating a high-pressure system. The intensity of the light source may also be increased, although there are limits to that as well, since the filament footprint of high-output lamps have a lower limit on size. An ideal solution would be an arc lamp with the attendant collimating optical train (either a spherical mirror or a converging lens), however, this requires an increased degree of complexity, space, and power supply requirements. Additionally, as there is no such thing as a point source, if using a converging lens (the less expensive of the two options for collimation), there will always be a small divergence of the beam.

The other means of increasing the sensitivity of a shadowgraph is to increase the overall throw of the optical system as the sensitivity of the system in divergent light is dependent on the distance between source, object of interest, and the screen (while keeping the distance between the object and the screen half of the total throw). This has led to some very large experiments, such as that of Schmidt and Saunders [76], who used a side-viewing shadowgraphy system that was 30 meters in length to capture clear images at a $\Delta T = 34 \text{ K}$ over an optical path through the convection experiment that was 22.9 cm deep x 1 cm tall. This is obviously not a

practical physical setup for most laboratory environments due to the great length and also introduces a long air path which may contribute to optical deflections unrelated to the experiment of interest. Fifteen years later, J. G. A. de Graaf and E. F. M. van der Held [77] used a modified version of the Schmidt and Saunders system with a collimated incident light beam, instead of diverging, and were able to cut the distance between their experimental cell and their projection screen to 7 m, however, they still cited difficulties in gaining much insight from the resultant images and therefore turned to a smoke seeding technique.

An attempt was made to capture shadowgraphs of the simplest of systems in the laboratory. The schliere object was the region above a 4.5 inch (11.4 cm) square \times 3/8 inch (0.953 cm) thick plate of aluminum which had a silicone resistance heater affixed to its underside. This component had been constructed for an early version of the experimental cell, although as was demonstrated above, it is far too large for the current experimental parameters. Illumination was provided by a Kodak Ektagraphic III AMT slide projector rated to produce a 1300 lumen output and fitted with a Buhl Optical 2.25" F:2.8 lens (corresponding to roughly a 57 mm lens). The spacing was set up for maximum sensitivity as described by Settles, with the objective lens of the source 15 inches (38.1 cm) from the test object and the screen another 15 inches (38.1 cm) from the object (these spacings dictated by the size of the laboratory bench), which was made up of white contact paper laid onto a segment of 3/4 inch (1.91 cm) thick plywood for good stability. The screen was imaged by an AVT ProSilica GX 1050 CCD camera recording monochrome images at 1024 x 1024 pixels at a resolution of 14 bits fitted with a Fuji 25 mm lens. The camera communicated via Gigabit Ethernet with a PC operating National Instruments LabView, which captured the image and recorded it into a .AVI file (which necessitates downsampling to 8 bit pixel depth, which was acceptable for the

proof-of-concept nature of this test, but can be remedied with additional coding). Within LabView a tare (or background) image was acquired at the beginning of each run, which was subtracted from the subsequent images to highlight only those changes that had time evolution characteristics as the plate was heated. In addition, subsequently, the image had a “linear contrast stretch” applied by multiplying all pixels by a constant factor. Temperature data from the thermocouple affixed to the plate was least squares fit to a power law, which allowed the absolute and relative temperatures to be printed on the frame to allow easy correlation. An example image can be seen in Figure 2.9.

It was found by reviewing the video recording by eye that the first clearly detectable convective motions were observed at approximately 311 K. This is 14.5 K above the ambient temperature in the room and corresponds to a 4.65 % deviation in density from the measured atmospheric pressure that day, which implies that the sensitivity of this shadowgraph measurement was to a 1.20×10^{-3} % change in refractive index. This is an excellent result, and is consistent with the sensitivity that Merzkirch [51] gave for a full schlieren system in 1987. While this is certainly an encouraging result, enabled by powerful image processing technology, it unfortunately has some challenges. The sensitivity of a shadowgraph measurement unfortunately scales with the size of the schliere object, therefore, going from a 4.5 inch (11.4 cm) plate to a 2 cm cube imposes some challenges. In addition, the presence of sidewalls in the convection cell results in optical losses that are not present in the current test configuration. Generally, there have been significant difficulties in the literature generating clear and useful shadowgraphs in ambient pressure gases, therefore shadowgraphy becomes a difficult methodology for imaging flows under those conditions. While there is not significant space in the lab for increasing the length of the optical train, a more intense light source might be able

to better detect changes in the refractive index. This, however, would require the acquisition of specialized optical components. Additionally, the usefulness of the background subtraction technique in a moving system is unknown, as it is sensitive to even single pixel shifts, which could very well be induced by small instabilities in the motion of the shaker as much as they might be due to deviations induced by convective motion.

While shadowgraphy may not be practical under the current geometric constraints, the associated techniques (illumination, image capture coding, etc.) are still useful for other visualization techniques.

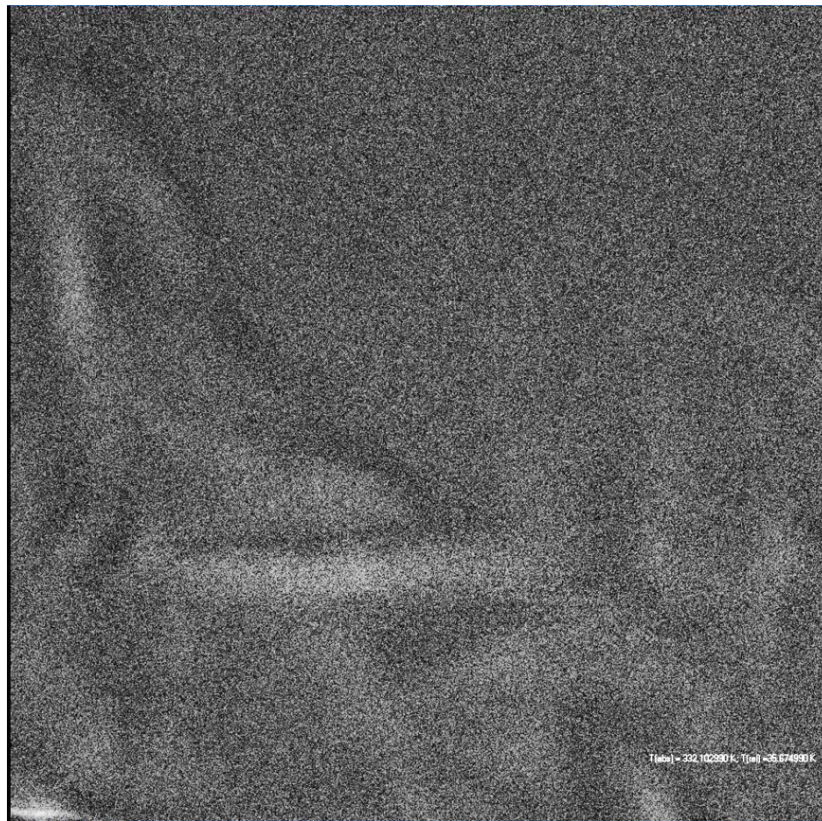


Figure 2.9: An example image from the shadowgraph testing that was performed. Thermal plumes can barely be seen in the frame convecting away from the heated plate at the bottom of the frame. This image was background subtracted and brightened in post processing. The temperature is displayed at the lower right of the frame.

2.3.2 Particle Seeding Techniques

If shadowgraphy likely possesses insufficient sensitivity to capture the dynamics of a convective flow in an atmospheric pressure gas, then perhaps seeding the gas with some appropriate particulate matter would allow the visualization of the flow field. Ideally, the size of a seeding particle for a gas is as small as possible, however, to have a large enough optical return from light scattering the particles should be roughly larger than about $0.15 \mu\text{m}$ [51]. While tobacco smoke has a mean particle diameter in the range of 0.2 to $0.4 \mu\text{m}$, it poses too many hazards to health and indoor air quality to be used widely for extended periods. Graham [78], Chandra [79], De Graaf and van der Held [77], Ruth *et al.* [80], and Inaba [81] successfully made use of tobacco smoke to image their convection roll cells and produced clear and insightful experimental visualizations.

Many other smokes are described in the literature, with varying degrees of success. Here in the Graduate Program in Acoustics at Penn State, M. W. Thompson [82] had success in determining acoustic streaming velocities using laser Doppler anemometry and seeding with the smoke produced by burning cotton rope, which was measured by a scanning electron microscope to have a particle diameter on the order of $1 \mu\text{m}$. A. Graham [78] employed ammonium chloride smoke in his experiment. Unfortunately, this technique required the mixing of ammonia and hydrochloric acid vapors, both of which pose some hazards, particularly in an experiment in which the entire apparatus is oscillating. Torrance *et al.* [83] used the spores of the puffball mushroom, which when they proved to be difficult to work with, were replaced with metaldehyde, which is a toxic solid that is commonly used as a pesticide. Tobacco smoke was common in early experiments, and various schemes for mechanically smoking cigars and cigarettes were devised and described in the literature [84, 85].

Many experiments use aerosolized oil droplets as their seeding material [86–88]. This is a popular choice, particularly for particle image velocimetry, and there are many commercially available oil droplet seeders on the market to produce micron-scale particles. The disadvantage is that many groups appear to find issues with the rapid agglomeration of oil droplets on the walls of the experiment, making the accessible experimental run times relatively brief before cleaning is required.

Several groups have found success with incense smoke [89, 90], which they reported required re-seeding for their LDA measurements relatively infrequently compared to other smoke sources and also was plainly visible with the naked eye. Incense smoke is also a well-characterized material as it is seen as an indoor air contaminant in areas where its use is widespread, particularly in religious ceremonies, and has been reported to produce significantly more particulate matter than cigarette smoke, which may explain its long-lasting qualities in experiments. In addition, it has been reported that there is significant variability in individual types of incense, however, 95% of the particles are said to fall in the sub-1.0 μm size and, if the appropriate incense is chosen, almost all of the particles can be made to fall above the target 0.15 μm range [91]. One study [92] found that a range of incense sticks produced spherical particles displaying a median diameter range by count from 0.19 to 0.20 μm , a median diameter range by mass of 0.25 to 0.30 μm , and a particle density ranging from 0.90 to 1.14 gm/cm^3 .

Using the mean of the above values, we find that this gives an undriven sedimentation velocity for the incense smoke particles on the order of 10^{-6} m/s, a particle response time on the order of 0.1 μs and a Stokes number on the order of 10^{-7} , all of which imply that the smoke should have an excellent ability to follow fluid streamlines closely [93].

In order to better determine the suitability of the incense smoke as a flow

visualization medium, the relevant parameters were fed into a freely-available computer program package³ that implements a Mie scattering solution in order to determine the optical scattering pattern of a representative incense particle. As this is a Mie solution, the incense particles are approximated as perfect spheres and the spheres are on the order of the incident optical wavelength and a constant optical refractivity are assumed. These results show the relative suitability of the incense particles as a flow visualization medium. A sample plot may be seen in Figure 2.10.

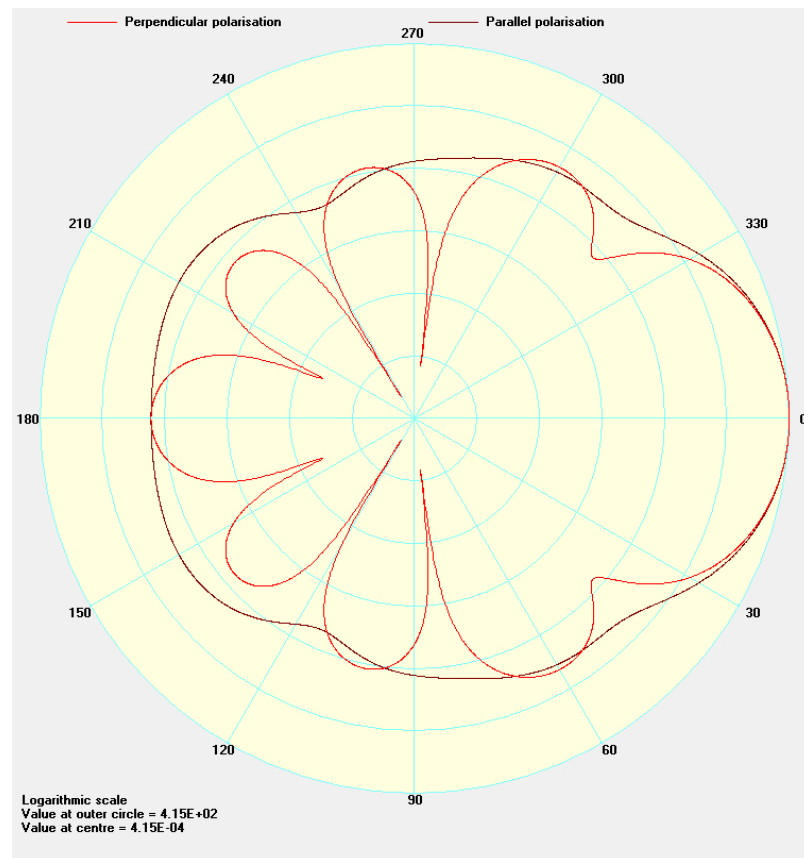


Figure 2.10: An example of the computed scattering field of an incense particle.

With seeded flows, volume illumination across the entirety of a cavity quickly

³MiePlot v.4.3.05; Philip Laven: <<http://www.philiplaven.com/mieplot.htm>>.

becomes difficult as the sealed enclosure fills with smoke and discerning specific flow structures becomes nearly impossible. The use of a light sheet can remedy this issue by restricting the illumination to a thin, planar sheet through the enclosure. While this limits the flow visualization to effectively two dimensions, very clear images of the flow field streamlines on that plane can be made. While many experiments have used white light sheets by shining a light source through a narrow slit, most of the illumination is wasted by falling outside the slit. Additionally, light sheets formed in this way will always have a significant amount of horizontal dispersion, forming a wedge-like shape. With the advent of particle image velocimetry (PIV) as a standard technique of experimental fluid mechanics and the availability of inexpensive, powerful lasers, laser light sheets have become easily accessible. The formation of a laser light sheet is as simple as placing a cylindrical lens in the laser beam path, spreading the beam into a sheet that is restrained to approximately the width of the incident beam. Satisfactory results can be made using non-optical components, such as an acrylic or glass rod for the lens. Additionally, with a reasonably fast electronic shutter on the camera, there is no need for pulsed lasers, a major contributor to the cost of PIV systems.

Testing was performed using a laser light sheet and incense seeding in the 3.5 inch (8.9 cm) test cell that had already been constructed. A laser light sheet was formed by spreading the beam from a 5 mW He-Ne laser (wavelength = 632.8 nm) using a cylindrical lens (a 0.318 cm diameter acrylic rod). The seeding material was the smoke from “Sandal Incense Sticks” (Brand: Hari Darshan Sevashram Pvt. Ltd.), which were chosen for their ubiquity, low cost, and relatively inoffensive scent. This incense produces a copious amount of white-colored smoke when burned. In addition, the incense smoke appears to stay in suspension for well over 20 minutes, a time that could likely be improved if the container was better sealed from the

atmosphere. A diagram of the experimental imaging setup is shown in Figure 2.11.

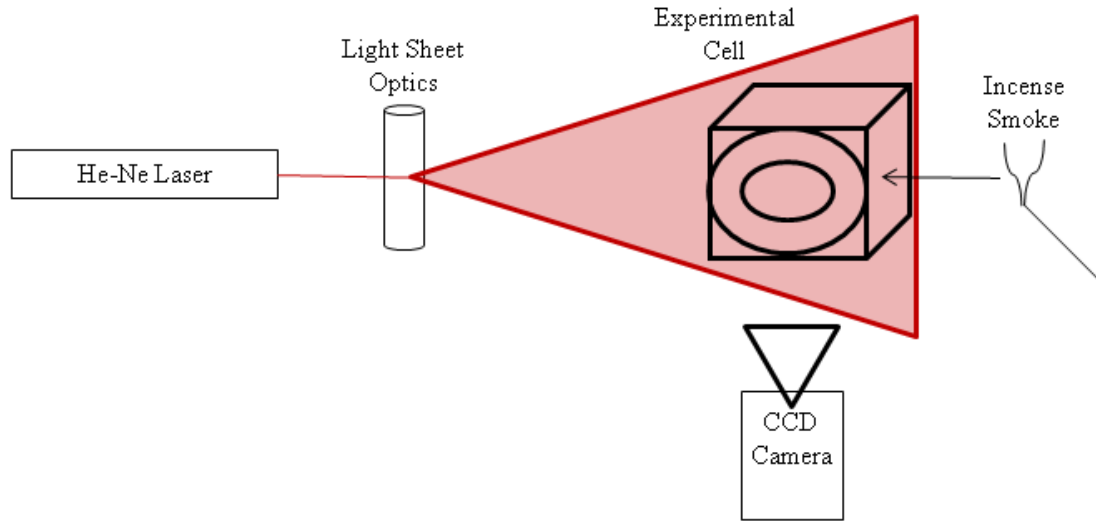


Figure 2.11: A diagram of the imaging system used for testing the seeded imaging. Note that the light sheet optic is depicted vertically to clearly show that it is a cylindrical lens. In reality, the length of the lens extends into the plane of the page.

While the light sheet was not of the best quality (it showed multiple striations and other defects within the sheet), usable images that revealed the flow structure were produced. The quality of the light sheet could be improved with better optics, perhaps a glass rod or a purpose-built cylindrical lens as opposed to the relatively scratched piece of scrap acrylic that was used in the test. To make the images clearly visible, a 7-times multiplication was performed on the image in order to intensify the outline of the structure in the frame. Histogram equalization was suggested as a more effective, albeit complex, method for improving the contrast of the image, in particular due to the fact that the initial images are taken in 14-bit pixel depth, however, no significant qualitative improvement was noted during tests of a histogram equalization algorithm. An image from the steady state of this testing can be seen in Figure 2.12. A plume emission can be seen in Figure 2.13.

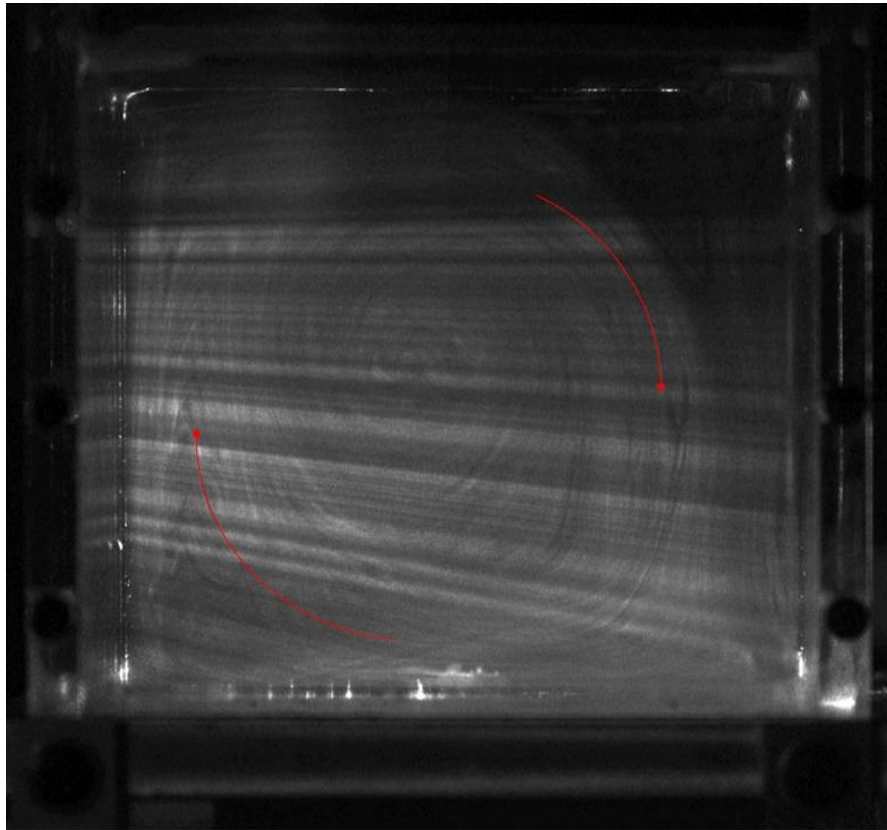


Figure 2.12: An example image from the smoke flow visualization testing. The red arrows were added to indicate the direction of motion that was noted from the analysis of multiple video images. This image had a $7\times$ intensification applied to the captured values to make the fluid motion plainly visible. Note the striations in the light sheet.

2.4 Visualization Techniques Employed

2.4.1 Diode Laser System

As was shown in the initial tests, an image (of low quality and intensity) may be formed with even a relatively low output illumination source. In order to develop a higher quality image, a more intense laser light sheet source would be required. Ideally this source would produce a uniform, intense, and relatively thin and non-dispersive sheet of light in a controllable manner at a reasonable cost. For

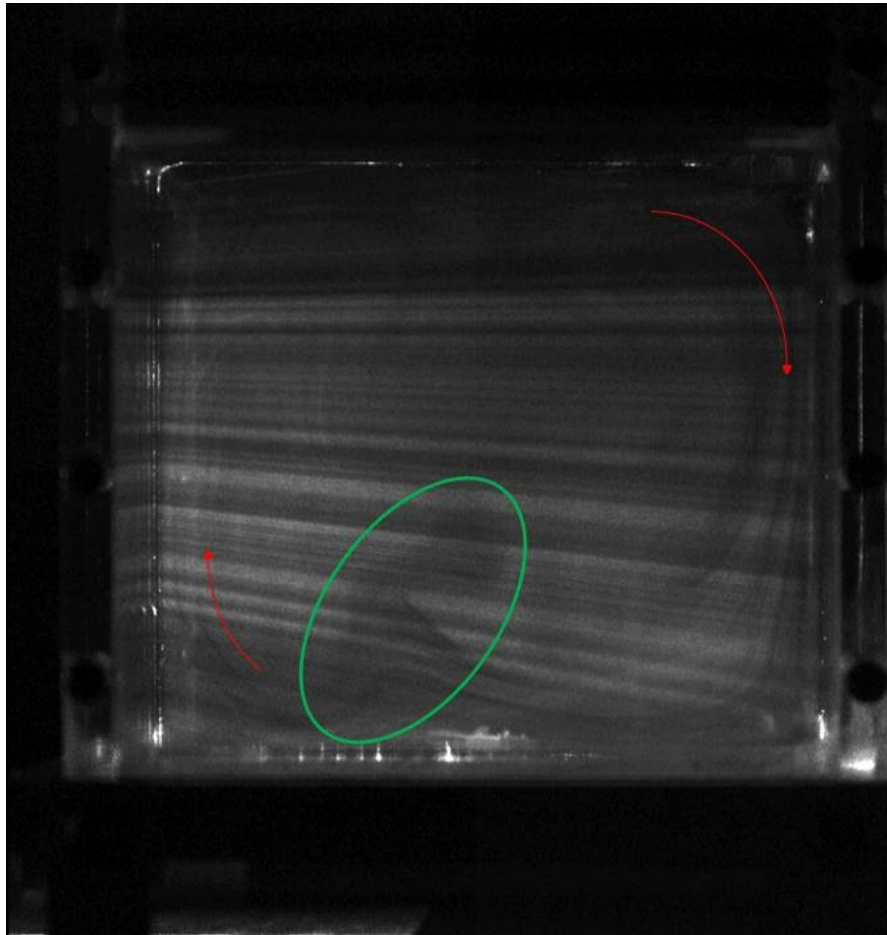


Figure 2.13: An example image from the smoke flow visualization testing. The Rayleigh number in this image is $Ra = 5.9 \times 10^4$ ($Ra/Ra_c = 18.0$). The red arrows were added to indicate the direction of motion of the large-scale circulation that was noted from the analysis of multiple video images and the green oval highlights a thermal plume emission that was noted. This image had a $7\times$ intensification applied to the captured values to make the fluid motion plainly visible.

safety reasons, it is ideal that the laser be in the visible spectrum as opposed to the infrared, so that the hazardous path of the beam may be seen. The solution for this illumination was achieved through the usage of a high intensity laser diode array.

The diode array used is manufactured by DILAS Diode Laser, Inc.⁴ It is

⁴<http://www.dilas.com/>

the model M1Y-675.5-20C-T25, which emits a maximum of 20 W optical at a wavelength of 675 nm. This array consists of 19 laser emitters, each 100 μm in dimension, and wired in parallel. Without further optics, the array has a divergence of less than 10 degrees along the linear array direction and 65 degrees perpendicular to the linear array. For the purposes of this type of experiment, however, the array is supplied with a factory-mounted permanent cylindrical (600 μm diameter) collimating lens to reduce the 65 degree divergence to less than 8 mrad.

The laser is driven by a purpose-built laser diode driver/controlled (Amtron GmbH⁵ model CS412 4L80). This power supply is capable of supplying up to 4 V and 80 A of direct current, conditioned to a high stability in order to avoid laser diode failure. It also allows control of the laser to produce CW or pulsed illumination with up to 5 kHz modulation, controlled through either the face panel or a remote analog or digital control signal.

As the most common failure mode for laser diodes is insufficient cooling, the entire array package is conduction cooled through the baseplate of the array package, which functions as a heat sink. The array is mounted to a liquid-cooled cold plate, produced by Elite Thermal Engineering, LLC⁶ (model WP-03). This plate is drilled with a closed circuit of channels through which distilled water is circulated from a controlled temperature chilled water source. Care must be taken to avoid water which is too cold, as condensation of moisture from the ambient air on the laser diode array would likely lead to array failure. To avoid this, the dew point is calculated each experimental day using temperature and relative humidity measurements from an OMEGA Engineering⁷ PTH-1XA handheld tester. These raw measurements are then converted into an approximate dew point using the

⁵<http://www.amtron.net/>

⁶<http://www.elitethermalengineering.com/>

⁷<http://www.omega.com/>

Magnus formula, and the temperature of the chilled water is set at least two degrees Fahrenheit warmer than that value. An image of this laser diode mounted on the cooling plate may be seen in Figure 2.14.

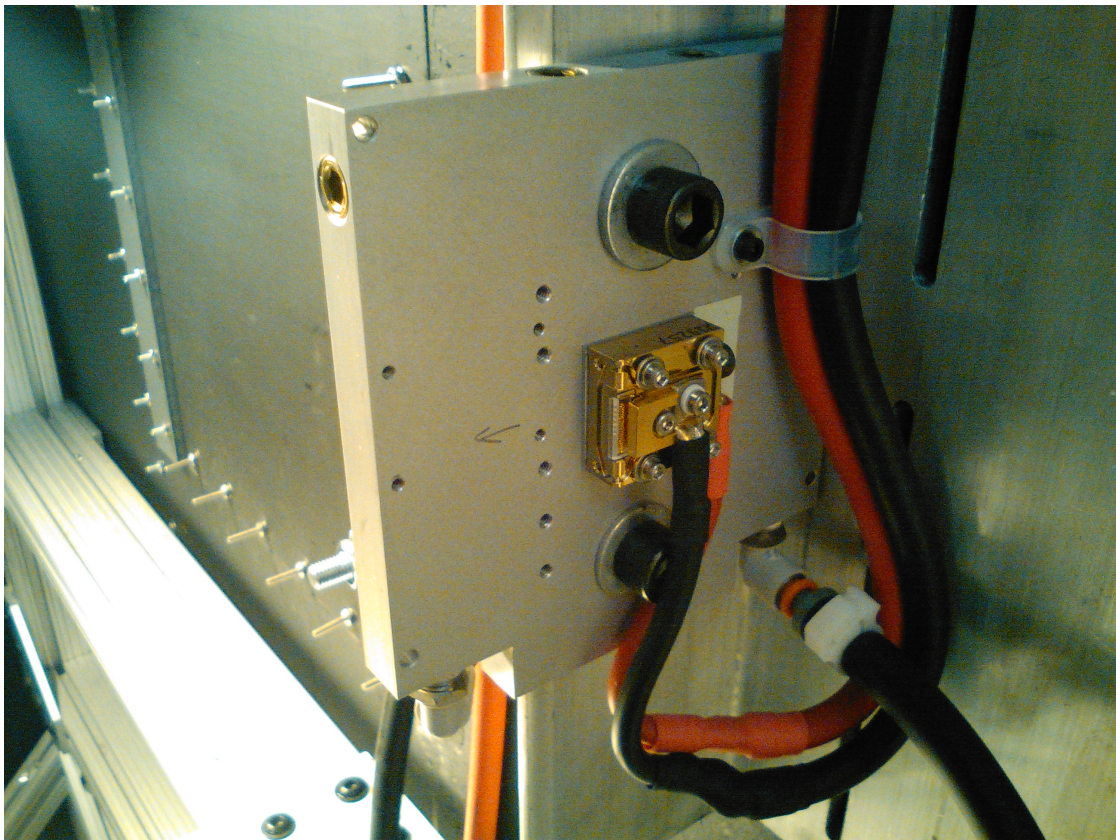


Figure 2.14: Photograph of the 20 W optical output, 675 nm wavelength, diode laser array light sheet source. This laser is mounted on a water-cooled heat exchanger. At the bottom right of the cooling plate one of the two (black rubber) chilled water supply hoses can be seen. The heavy gauge cables attached to the laser emitter are the electrical connections to the anode and cathode of the laser diode array.

To ensure sufficient thermal contact between the laser diode array heatsink and the cold plate, while also ensuring electrical isolation from the plate, a mica wafer is sandwiched between the two components. This mica is coated with a foil of Indium to improve the thermal conductivity and fill any surface imperfections on both parts. The assembly is bolted together using stainless steel screws, electrically

isolated from the laser by way of nylon shoulder washers, and allowance is made for thermal expansion by using stacked Belleville washers.

Finally, there is a need for laser safety precautions due to the high potential output of this laser diode array. The entire experiment and the shaker itself is enclosed in a custom built enclosure constructed of birch plywood. This enclosure has two doors for access to the experiment when it is not operating, with the gaps around each door blocked by baffles. The doors are secured to be light-tight by means of compression latches. The front panel also features an access port for the remotely operated video camera for the flow visualization and an acrylic observation window that is certified to be rated to optical density (OD) 5+ at the wavelength of the laser. The entire interior of the enclosure is painted in flat black latex paint with a mineral-salt based flame inhibitor additive mixed in. The exterior of the laser safety enclosure is shown in Figure 2.15.

For further safety, a laser-controlled area was established outside this inner enclosure. This is protected and denoted by flame resistant canvas welding curtains, hung from a schedule 40 black steel pipe frame to a height of eight feet. This controlled area is accessed through overlapping flaps and is marked with the appropriate danger signs, as required by regulation. There is a manually-activated amber strobe light that is activated when there is a laser-safety hazard present inside the curtains.

For alignment procedures pairs of appropriate laser safety goggles are provided, rated at OD 4+. All procedures are governed by a written laser safety plan. All laser safety precautions and training are reviewed and inspected annually by the Penn State Environmental Health and Safety office's Laser Safety Officer.

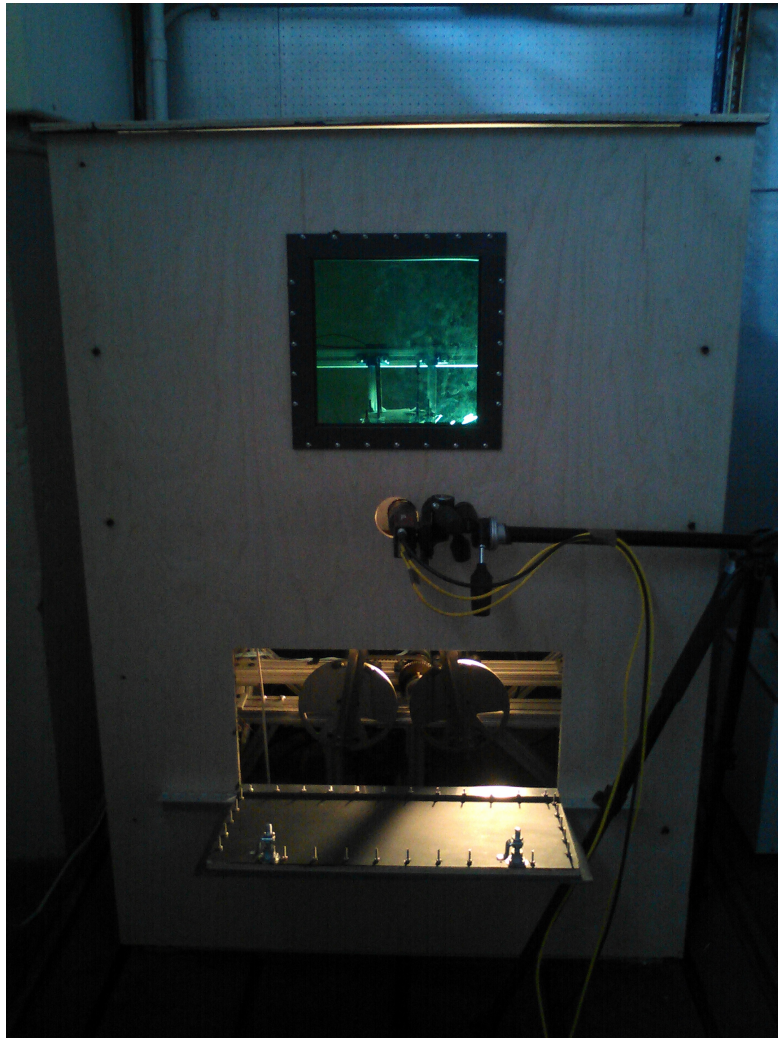


Figure 2.15: Photograph of the laser safety enclosure. The front service access panel has been opened to show the shaker flywheels inside the enclosure; this would normally be closed for operation. The CCD camera is mounted on a tripod, accessing the experiment through a round viewport, and the laser-rated window (green tinted) can also be seen.

2.4.2 Camera Phase Synchronization

In any imaging scheme, where to place the camera in reference to the moving experiment presents a design challenge. In experiments with lower acceleration systems, it is feasible to place the camera in the same frame as the moving

experiment, capturing the experiment at every point in the oscillation cycle at the maximum frame rate of the camera. This is a strategy that had been employed in some shaken granular materials experiments [61, 94], which made use of small, lightweight, solid state cameras and low shaking parameters. For stronger shaking, this tactic becomes impractical for several reasons. While cameras rated to survive high accelerations (up to $100g_o$) are available on the market, these cameras, directed primarily at the vehicle crash test market, range from \$30,000 and up, putting them outside the range of reasonable cost. Additionally, these cameras need to be stable enough to avoid vibration corrupting the image, which would be nearly impossible at the accelerations required.

The other option available is to leave the camera in the stationary frame and phase lock the camera to the moving object. In this way, the shaken experiments may be imaged once per shaker cycle at the same point in space. This is a technique also represented in the shaken granular media literature [95, 96] and the pattern formation experiments of Rogers [37]. In these experiments, synchronization is rather straightforward, as the drive waveform supplied to the amplifier/servo valve for the electrodynamic or hydraulic shakers used is a known quantity from the function generator or computer program used to generate the waveform, and a synchronization signal is an intrinsic part of that stage. Here, as the shaker is driven by a rotary motor, some other means of triggering the system must be found as there is no natural synchronization signal resulting from the drive electronics. Options for capturing the motion of the shaker include optical photogate sensors, magnetic tachometers, gear tooth sensors, accelerometers, and LVDT's. In this experiment, we use a piezoresistive accelerometer⁸ mounted on the carriage of the shaker as the triggering source sensor.

⁸Endevco Corp./Meggitt Sensing Systems, Model 2262A-1000: <<https://www.endevco.com/>>.

With this acceleration signal in place, there is still the need, however, to generate a synchronization signal from the (nominally) sinusoidal output of the accelerometer. While a simple circuit involving Schmitt triggers and flip-flops can be developed to generate a TTL-type output signal from a sinusoidal input, optimized and highly adjustable versions of these circuits are integrated into every analog oscilloscope. Certain oscilloscopes, including the Kikusui COS6100 series, used here, permit direct access to the gate signal generated by the triggering circuitry through a direct BNC output. By using the oscilloscope, the complex analog signal processing circuitry upstream of the trigger can be exploited, including adjustable gain preamps and noise discrimination circuitry, that would be complex to build into a from-scratch circuit. By manipulating the triggering controls of the oscilloscope judiciously (and without regard for producing a suitable visual trace), a stable triggering signal can be produced. A sample signal produced from the output of a signal generator is shown in Figure 2.16.

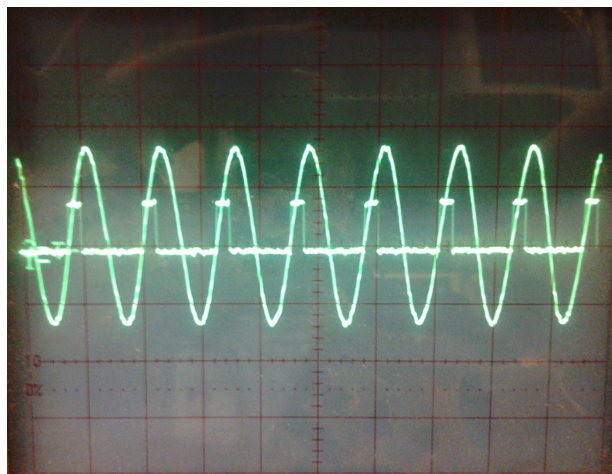


Figure 2.16: Sample triggering signal produced using a Kikusui COS6100A oscilloscope. The input signal was a simulated shaker motion input produced by a function generator. The square wave triggering signal seen superimposed on the trace is manually adjustable through the normal means used for oscilloscope triggering.

The output of the trigger gate circuit is less than 1 V, thus to produce a roughly 0-5 V TTL signal, an amplifier is employed. This signal is then sent to the synchronization input of the CCD camera employed. A representative schematic of the control circuit can be seen in Figure 2.17.

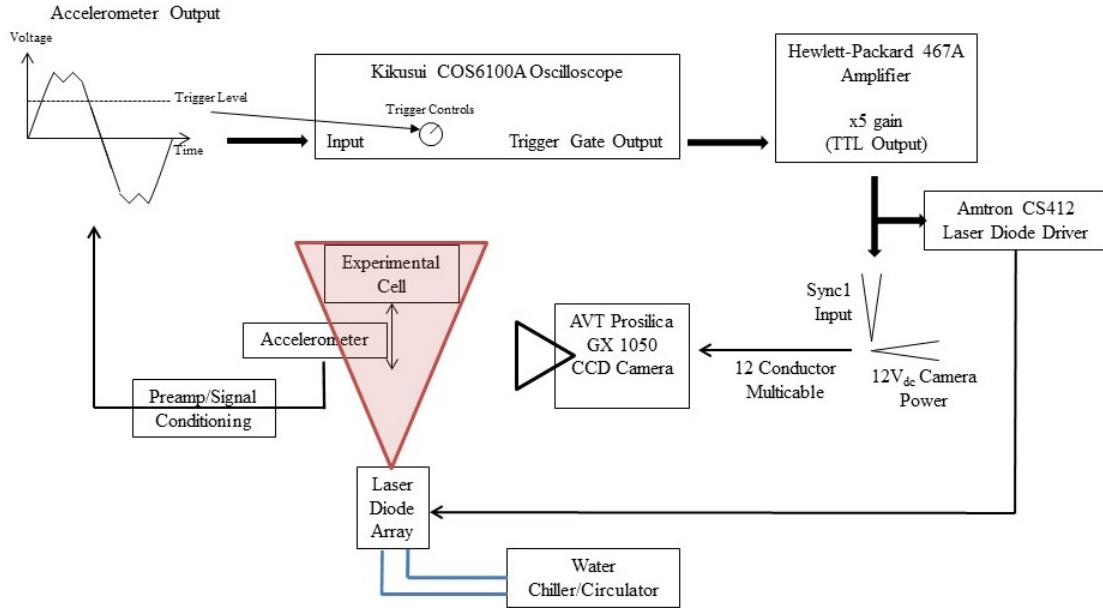


Figure 2.17: A schematic view of the components of the camera triggering circuit employed to produce a camera image phase-locked to a time-harmonic signal.

The camera used (an Allied Vision Technologies⁹ Prosilica GX 1050) has the ability to be triggered on the rising or falling edge or the high or low static conditions of the trigger TTL signal. By triggering on the rising edge of the TTL signal, precise triggering may be achieved, with a trigger latency of less than $2 \mu\text{s}$ (corresponding to $6 \mu\text{m}$ at a peak velocity of 3 m/s). Additionally, the exposure time can be independently adjusted from the triggering, thus once the camera is triggered, it will expose a single frame for a duration that is independent of the triggering signal length.

The camera also has the ability to output another square wave signal that

⁹<https://www.alliedvision.com/>

corresponds to the open time of the camera’s electronic shutter. Thus, this output is high only in the period that the camera is actively exposing the CCD chip and not while the camera is reading out, processing, and transmitting the exposed frame or otherwise in an idle state. By using this exposure follower signal, we may trigger the exposure of the laser to match only the exposing period of the camera. This permits the experimental cell to be illuminated only when an image is being taken, reducing the opportunity for secondary thermal flows to be produced due to the laser heating the smoke particles when compared to a continuous CW illumination scheme. The laser power supply is configured to accept these TTL-type trigger signals and will also trigger the laser, and therefore illumination, either for the high period of the trigger signal (i.e. “gated CW”) or for a pre-defined time period in μs (“pulsed”).

In testing of the circuit described here, the stability of the triggering mechanism was determined (for the noiseless signal from a signal generator) to be 0.01 s or better. This was determined by filming the display of a digital stopwatch with an input signal of 1 Hz and noting that with the resulting triggering signal fed to the camera, the recording of the watch showed motion only in the seconds column while the fractions of seconds remained unchanged frame to frame.

2.5 Thermal Measurement Techniques

Thermal transport measurements have been an intrinsic part of convection experiments since the work of Nusselt in 1907 (cited in [97]). Several methodologies for thermal measurements are discussed in this section.

2.5.1 Heater Power Differential

A traditional means to determine the stability/instability of the fluid is to analyze the current (and therefore power) required to be delivered to a resistance (Joule) heater to maintain a constant temperature measured at the bottom plate. This provides a differential measurement: prior to the onset of convection (or if convective motion is suppressed), the fluid has heat transfer by diffusion alone, while after convective motion begins, heat transfer by advection is added as well. Recalling that the square of the current delivered is proportional to the power dissipated as heat in our heater, $\Pi_{\text{el}} = I^2 R = IV$, by tracking the current, after the critical Rayleigh number has been reached, the current required will rise significantly due to the higher heat transfer of convective motion. This technique has been employed since at least the 1930's. An example of a seminal use of this technique from the 1935 paper of R. J. Schmidt and S. W. Milverton [98] is shown in Figure 2.18.

While this transition in the thermal transport is a sufficient indicator of the onset of convection and has been used since the 1930's to determine when criticality has been reached, it is unsatisfying by itself as there will always be some ambiguity to that transition. This is one of the challenges in analyzing the Swift and Backhaus data, as the exact point of transition is difficult to find precisely in the sloped transition of their plots [29], which are given in the form of power supplied \dot{Q} [W] vs. the particle velocity ωa [m/s]. Additionally, since the thermal conductivity of air is relatively low, the change in thermal transport, from conduction to convection, is small (less than one watt for a 2 cm cubical container across an entire run), this can be a difficult measurement to make, even with great care applied to tracking the current through the transition. A much more satisfying means of confirming stability/instability of the fluid is when a thermal measurement is coupled to a

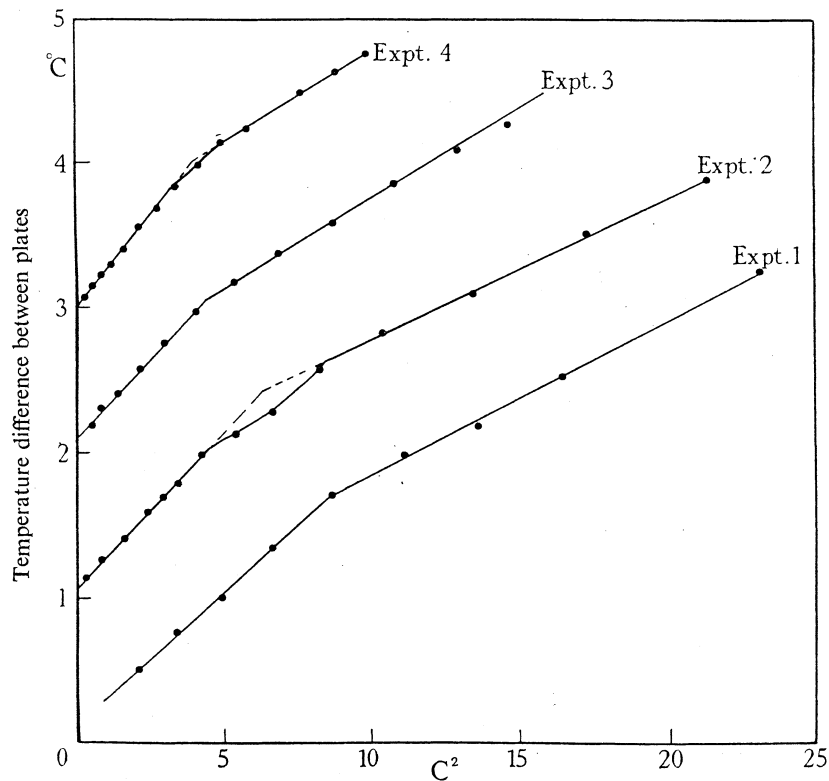


Figure 2.18: An example of an early differential heater measurement from a 1935 paper by R. J. Schmidt and S. W. Milverton. This plot is Figure 2 in the paper [98]. Note that this plot arranges the x and y -axes in the opposite orientation from those shown in this work. The horizontal axis here is the square of the electrical current (proportional to power) supplied to the lower plate heater and the vertical axis is the temperature difference between the plates, ΔT . While not denoted here, the current is measured in units of amperes.

visualization, as discussed in the previous section.

Despite these challenges, in this way, by tracking the power across the cell, a precise transition point may be determined in this experiment while also maintaining the temperature difference across the cell to within several hundredths of a degree kelvin. The details of the implementation of this measurement will be discussed in the following chapter.

2.5.2 Heat Flux Meters

Since the change in thermal transport with the onset of convection in gases is so small, determining the point of onset has been an ongoing issue in the literature. One attempt to overcome this challenge was an experiment by Thompson and Sogin [99] that used a package of heat flux meters bonded inside the heated and cooled boundaries of the experimental cell to make a direct measurement of the heat flux through those boundaries. The heat flux sensors of this experiment consisted of a strip of mica (with a well known thermal conductivity), upon which 600 turns of constantan wire had been installed to form a series of differential thermocouples (a thermopile). Using the well-known properties of the spacer material, along with the carefully measured thermal gradient across it, the heat flux can be accurately ascertained. Using this methodology and exceedingly careful experimental techniques, Thompson and Sogin were able to plot sharp and clear transitions in the heat flux and determine the critical Rayleigh number to within 5% of the theoretical value. A similar strategy was used in the side-heated experiments of ElSherbiny *et al.* [100] and Mamun *et al* [101]. Ivanova and Kozlov [50] also employed an embedded heat flux meter in their studies of convection modulated by pendulum oscillations.

Commercially, modern heat flux meters are available in small packages from several manufacturers, although constructed of more advanced materials than the earlier lab-produced devices [102]. As an example, the Omega Engineering HFS-4 Heat Flux Sensor provides an output of $2.06 \mu\text{V}_{\text{dc}}/(\text{W}/\text{m}^2)$. Constructed of layers of laminated Kapton[®] film, this sensor has a thickness of only 0.007 inches (0.018 cm) and dimensions of 35.1 mm \times 28.5 mm, which would allow it to be easily placed within the heated boundary in order to measure the differential heat

flux through that boundary. The voltage generated by the sensor would still be small, based on a CFD model of the cavity, which determined the average heat flux to be approximately 300 W/m^2 , this would result in an output of 0.62 mV , which is well within the measurement capabilities of current voltmeter systems. Unfortunately, the cost of these sensors is relatively high per unit and would require another set of electrical leads between the moving experiment and the fixed frame. A heat flux sensor was considered but not employed in these experiments. However, if an extension of this work was undertaken, it may provide a useful redundant measurement method.

2.5.3 In-Flow Temperature Measurement

Another option, which has been used throughout the literature on convection, is to place a thermocouple or thermistor probe inside the flow to measure temperature changes inside the experimental cell, particularly those temperature changes that are time-dependent. These temperature measurement approaches are necessarily intrusive to the flow. However, very small probe sizes are available commercially (as small as approximately $80 \mu\text{m}$ in diameter). Unfortunately, the resultant probe is not particularly rigid, a concern when the probe will be cantilevered into the fluid and the entire system will be subjected to vibration. While no papers assessing the resonant mode structure of thermocouple wire were found in the literature, there is a paper that computed the resonant modes of hot-wire anemometers [103]. This was of concern as velocity measurement errors can be induced in turbulence experiments if the modal resonance of the probe is sufficiently close to the range of frequencies associated with the turbulence cascade. Their model is sufficiently different from that of a cantilevered thermal probe that similarities cannot be

drawn.

Since no literature assessing the resonant modal structure of a thermocouple wire were found, a simple model was analyzed to determine the resonant frequencies of a small probe (approximating the probe as a cylindrical beam of suitable dimensions with the material properties of Chromel and mechanically fixed at one end). This model finds a lowest resonant frequency of approximately 540 Hz for a wire of diameter 0.003 inches (0.0076 cm) and 0.375 inches (0.953 cm) long. This relatively high resonant frequency lends credence to the possibility of employing a temperature measurement inside the flow cavity, however, without further testing, there will always be doubt as to whether the flexing of the probe is corrupting the accuracy of the measurement.

Additionally, in stationary experiments [72, 88, 104–106], these thermal sensors are often mounted on a complex system of positioning stages, permitting the precise (tens of micron accuracy) positioning of the sensor. Such a system would be difficult to implement in this experiment due to the physical demands imposed by the vibration. Such in-situ temperature measurements are not employed in this experiment, however, they were considered.

2.6 Experimental Cell Design

In well over one-hundred years of experimental investigation of Rayleigh-Bénard convection, the variation in apparatus designs is relatively small. All provide some method for the heating of one boundary and the cooling of the other. In this description of the current design of the experimental cell, the focus will be on the literature of experiments in gases, which is significantly smaller than that for condensed liquids.

The experiments described in the remainder of this work were conducted on two separate experimental cells. One is configured with a square cross-section of $l_x = l_y = 3.50$ inches (8.89 cm) (which will be referred to as the “ $\Gamma = 5$ ” cell) and tested at a height of $l_z = 0.7$ inches (1.8 cm). The other has a square cross-section of $l_x = l_y = 1.75$ inches (4.45 cm) (referred to as the “ $\Gamma = 3$ ” cell). The height of this second cell was $l_z = 0.583$ inches (1.481 cm). The construction of both experimental cells will be discussed in this section.

2.6.1 The $\Gamma = 5$ Cell

The first experimental cell designed for this work implemented an experimental chamber with a fixed square cross-section of $l_x = l_y = 3.50$ inches (8.89 cm). The cell was designed with the intention that the height of the enclosure would be able to be adjusted within a broad range to produce a number of aspect ratios. As this cell was designed early in the project, it was designed to be able to operate with both liquids and gases. A rendering of the cell is shown in Figure 2.19.

As has been discussed, the largest challenge in the design of a convection experiment is the need to tightly control the temperature difference across the experimental fluid enclosure. Many conventional convection experiments are not concerned with weight, and thus employ large pieces of metal as the heated surface. Koschmieder and Biggerstaff [107] used a copper plate, 2 inches (5.1 cm) thick, as their heated surface, for example. This is not a possible solution for this experiment due to the tremendous mass added by this metal, all of which would need to be shaken. In addition, many experiments [108, 109] use an adiabatic barrier of poorly conducting material, such as acrylic or another plastic, sandwiched in-between thermally conducting plates in order to better maintain a uniform temperature.

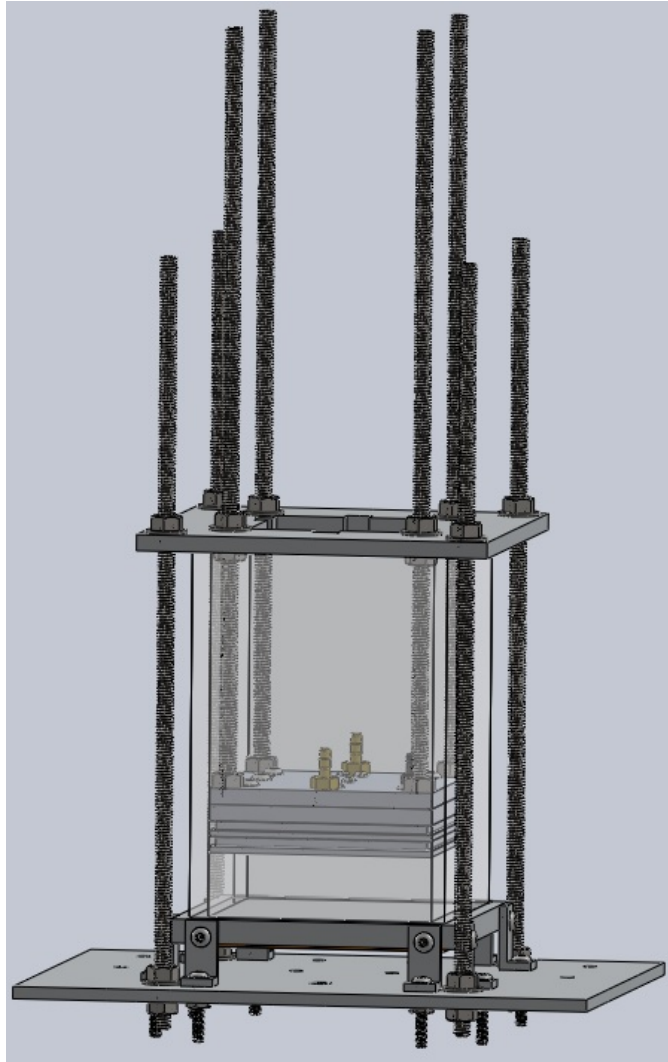


Figure 2.19: CAD rendering of the $\Gamma = 5.0$ cell, as built. In experimental usage, the cell is enclosed in layers of thermal insulation.

These efforts may have been required due to the spatial distribution of their individual heating elements (electrical resistance wires or heat exchanger fluid passages) being relatively coarse compared to the present experiment, requiring more complex horizontal boundary designs to ensure thermal uniformity.

These strategies are not particularly practicable for shaken convection experiments. The Forbes experiment [34, 35] of the 1960's actually employed a guard heater to limit heat loss into the environment for better absolute heat transfer

measurements, but did not strive for thermal uniformity of better than 1 °F (0.56 K), thus there were fewer concerns with thermal uniformity. The Rogers experiment [37] used a 0.25 inch (0.64 cm) thick, gold-plated aluminum plate to which a “resistive heating pad” was attached. This is very similar to the solution used in this experimental cell. The microgravity experiments of the Université Libre de Bruxelles [46] used thermoelectric (Peltier) modules to control the temperatures of both their heated and cooled surfaces, which does not appear to be seen elsewhere in the literature, but was likely advantageous for their space-certified and flown experiment.

The final design consisted of a 0.375 inch (0.953 cm) thick, 4.5 inch (11.4 cm) square, aluminum plate (6061-T6) with a flexible silicone heater adhered to it employing a high temperature rated RTV silicone adhesive. Aluminum was chosen to minimize the mass that would need to be moved by the shaker system. This heater is an an Omega Engineering¹⁰ model SRFG-404/10, which is a 4.0 inch (10.2 cm) square etched foil, silicone encased heater and delivers 160 W when supplied with 120 V current (although the maximum used in the experiment is 50 V, leading to a maximum power of 67 W available). The plate is machined top and bottom to ensure a smooth surface is presented to the fluid and to eliminate any voids in the junction between the plate and heater, which could lead to the heater failing. The plate also has a square groove cut into it to accept the enclosure with an O-ring sealing the joint. The bottom plate is also tapped to accept eight aluminum support brackets that support the entire apparatus.

Attempts were made to optimize the thickness of the plate, balancing thermal uniformity across the surface in contact with the experimental fluid with the excessive moving mass required by employing an overly thick plate. This was

¹⁰Omega Engineering, Inc.: <<http://www.omega.com>>.

accomplished using a finite element model of the hot plate with models for a variety of attached, commercially available heaters. The model was constrained by imposing reasonable choices for a range of convective surface heat transfer coefficients upon the surface inside the experimental container, approximations for the convective losses to the ambient air on other surfaces, and an approximation for the thermal contact resistance between the heater and the plate. This model was implemented in the finite element package integrated into the SolidWorks¹¹ CAD software, which was employed for all 3-D modeling, drafting, and construction drawings for this project.

This design resulted in relatively good thermal uniformity (variation less than approximately ± 0.3 K over the temperature range of interest) when the plate was tested in air. The heater was operated with a thermocouple attached to both the top (fluid-side) of the plate and on the bottom of the heater while applied current and voltage were measured. The plate was also imaged from above with a thermographic camera to obtain a full-plate thermal measurement. An example of these images can be seen in Figure 2.20. For all thermal camera measurements, the surfaces were temporarily painted with matte black spray paint, in order to both control unwanted optical reflections from the shiny aluminum and to present a constant emissivity. This paint is easily removed employing acetone as a solvent after the images are taken.

The other element that must be dealt with is the necessity to have a uniformly cooled upper boundary as well. This was accomplished by circulating cooled water through an aluminum plate on the upper side of the experimental chamber. This is a common solution found in many convection experiments, almost all of which use forced water cooling supplied by a laboratory circulating chiller, excepting

¹¹Dassault Systèmes: <<http://www.solidworks.com>>.

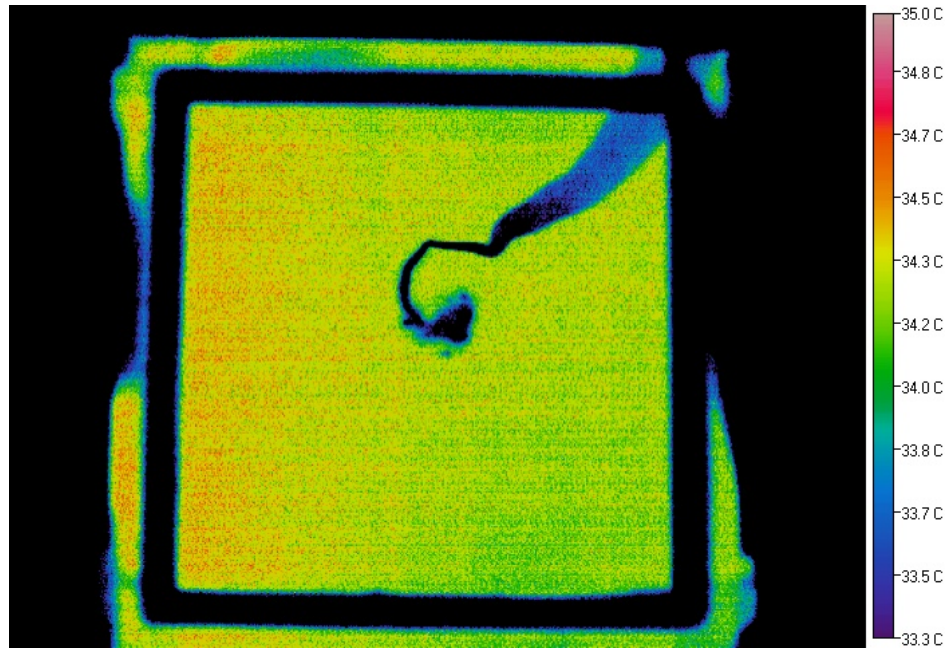


Figure 2.20: Sample of the thermal images obtained while testing the heated plate for the liquid apparatus. The black mark in the center of the image and the line leading away from it are the thermocouple and wire that was attached to the surface of the plate for this testing.

some early experiments which used an ice water bath. The advantage to using a circulating chiller is that the temperature control of these devices is rather precise (generally within ± 0.1 °C) and are limited primarily by their ability to accommodate and compensate for large swings in temperature in the system.

While water cooling is the most common solution to cooling the upper boundary, the means through which the water is introduced to the plate varies. Many experiments form a simple cavity with a single inlet and outlet for the circulating of water. Others [97] construct complicated systems of multiple jets that introduce water from all sides at the edge of the cooling cavity and lead to a single outlet at the center of the chamber. The solution used here involves a series of channels of varying widths in an attempt to maintain an even temperature across the entirety of the cooling plate. The optimization of the widths of these channels was accomplished

using a simple CFD program (the Flow Simulation package, also implemented in SolidWorks) to attempt to equalize flow across the width of the plate. This also provided a solution for the pressure drop in the static cooler plate, which gave an estimate of the pump requirements that might be required when the system was not shaken. The design of the plate can be seen in Figure 2.21. The challenge that this design poses is the necessity to deliver chilled water to a moving device, which may be difficult to achieve without interruption or breakage in the tubing.

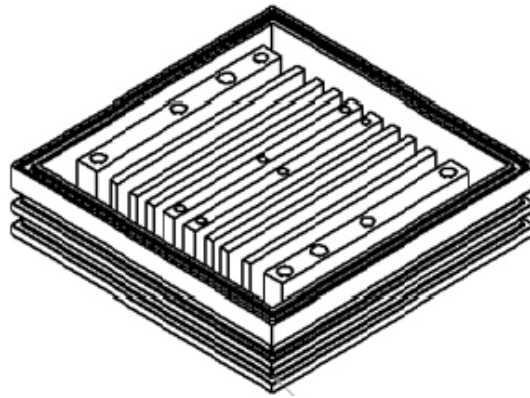


Figure 2.21: Construction drawing for the cooling plate that was designed for the convection experiment. The entire chamber is topped with a lid that is sealed to this lower portion with an O-ring seal.

This plate was tested in much the same way as the heater plate. Once the plate had reached a stable thermal condition, thermographic images were again taken. An example of the resultant thermal images can be seen in Figure 2.22.

The cooling plate was designed to permit adjustment of aspect ratio by sliding along the height of the enclosure, like a piston, with a double O-ring seal (small amounts of silicone RTV sealant were used to ensure the corners were also adequately sealed). In this way l_z could be changed and the entire cooling plate was secured by means of four 1/4-20 threaded rods that suspend the plate from above. Access for visualization was provided by two threaded holes, which either accept an O-ring

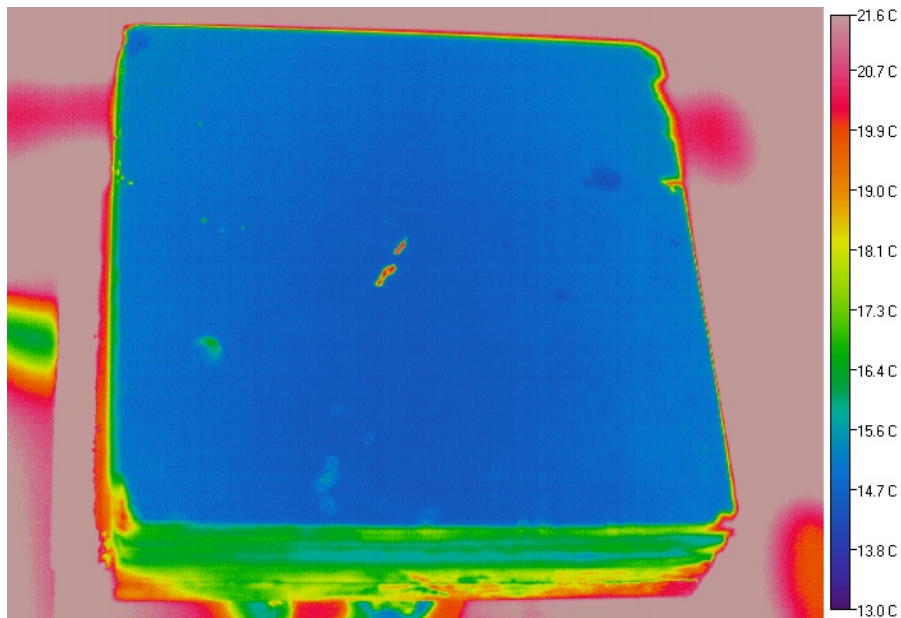


Figure 2.22: Sample of the thermal images obtained while testing the cooled plate for the liquid apparatus. The cooling water through this plate entered at 14.8°C from the temperature controlled circulator. The aberrant small hot spots in the center of the plate are the result of near-room-temperature water droplets pooling on the face of the plate during testing.

sealing screw head or an O-ring sealed hose barb, which allows the seeding particles to be introduced from the stationary frame into the chamber through an attached length of flexible tubing.

While the experiment was designed to tightly control the temperature of the upper boundary of the experiment using water cooling, this was not employed in the experiments presented here. As was noted above, it is difficult to introduce flowing water into the moving frame of the experiment. Additionally, there were concerns about excessive pump pressures being required due to the large displacement motion of the shaker. In early shaking experiments with the cell, it was found that the insulated top plate maintained a relatively constant temperature without active cooling being required. Also, as the temperatures of both surfaces are being tracked, any temperature changes are accounted for.

Convection experiments are often designed such that the mean temperature in the enclosure is that of the ambient temperature, therefore, the temperatures of the plates are $T_{\text{cold}} = T_{\text{ambient}} - \Delta T/2$ and $T_{\text{hot}} = T_{\text{ambient}} + \Delta T/2$. This measure is intended to minimize heat leaks to the exterior. However, by choosing simplicity in this shaking experiment, the temperature span now ranges from $T_{\text{cold}} = T_{\text{ambient}}$ to $T_{\text{hot}} = T_{\text{ambient}} + \Delta T$. Since the Rayleigh numbers used here (and therefore temperature differences ΔT) are relatively small in order to maintain linearity and the validity of the Boussinesq approximation, these heat leaks were of lesser concern. Many experiments also make extensive efforts to maximize thermal insulation, including placing the entire experiment within an evacuated vacuum chamber, however, techniques such as these would unacceptably increase the moving mass of the experiment. The apparatus for this experiment is therefore insulated only with lightweight materials, including spun polyester fibers and a variety of foams and foamed rubbers. There are also further restrictions on the insulation possible in this experiment, as the front face of the experiment must be left clear for visualization and the illuminated side must have at least a narrow slot in the insulation to admit the laser light sheet. The fully-insulated experiment is shown in Figure 2.23.

The lateral walls of the experimental enclosure were constructed from 0.25 inch (0.64 cm) thick cast acrylic material. Each of the four sides of the rectangular enclosure were cut from larger sheet stock and machined to dimension. Attempts were made to solvent weld the joints. However, there was difficulty in avoiding crazing of the face of the material due to the solvent extruding from the joint, making segments of the enclosure optically opaque. Attempts to flame polish these marks with propane, MAPP gas, and oxyacetylene torches were unsuccessful. As a result, the final enclosure was mechanically joined using 2-56 machine screws mated

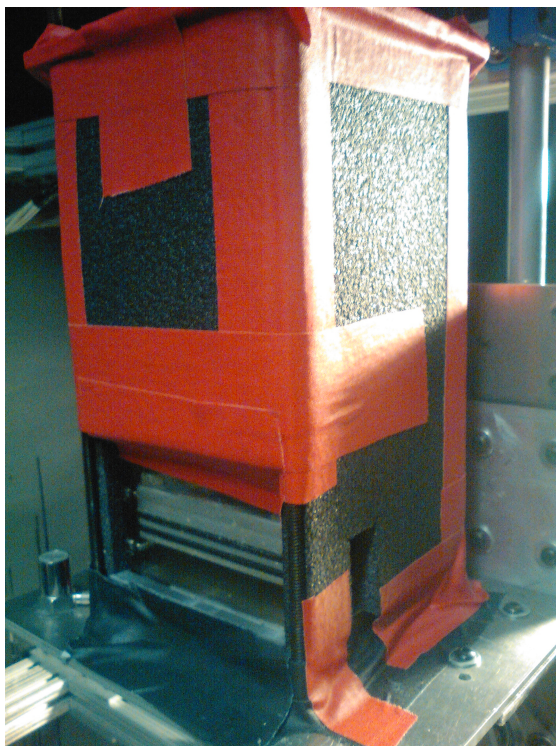


Figure 2.23: A photograph of the fully insulated $\Gamma = 5$ experimental cell. Note that the front face must be left optically transparent as is a rectangular opening (a “slit”) at the side to admit the laser light sheet for illumination.

to helical coil thread inserts. The joint was sealed with a thin, sandwiched layer of RTV silicone adhesive, as is common practice for many acrylic aquarium tanks.

2.6.2 The $\Gamma = 3$ Cell

As the $\Gamma = 5$ cell was designed relatively early in the project, it was intended to be as flexible as possible, accommodating a wide range of aspect ratios and experimental media. What could not be adjusted in the $\Gamma = 5$ cell were the lateral $l_x = l_y$ dimensions, which were fixed by the machined outer acrylic enclosure. The choice of $l_x = l_y = 3.50$ inches (8.89 cm), was a best guess, based on the reality that the theoretical predictions had not yet been fully completed. The conclusion that was reached after the work of Carbo was completed and the

extensive parameter investigation described earlier in this chapter was undertaken, was that the experiment would be most successful in a much smaller container, on the order of one to two centimeters in lateral and vertical extent. Therefore, to range beyond the $\Gamma = 5$ dimensions described above, a new cell would need to be constructed.

Additionally, there were further shortcomings, beyond the size of the container, inherent in the original experimental design that were noted. These included the general complexity of the support structure of the apparatus, which consisted of twelve mechanical connections, the unnecessary complexity of the cooling plate, and the larger than optimal heat leaks from the hot plate, through the contacts of the supporting structure of the cell, to the shaker carriage itself. The second cell, designed for an aspect ratio of $\Gamma = 3$, and described in this section, was intended to obviate the majority of these drawbacks.

In order to achieve experimentally accessible stability boundaries, obey linearity and the Boussinesq approximation, and not have too small of an experimental cell, the $\Gamma = 3.0$ cell was designed around an enclosure size of $l_x = l_y = 1.75$ inches (4.45 cm) and $l_z = 0.583$ inches (1.48 cm). Therefore, $\Gamma_x = \Gamma_y = l_{(x,y)}/l_z = 3.0017$. A rendering of the cell is shown in Figure 2.24.

As was practice in the $\Gamma = 5$ cell, the cold plate was allowed to be maintained at the ambient temperature, $T_{\text{cold}} = T_{\text{ambient}}$ and no provision will be made for active control of the cold plate temperature. While a design was drafted using a thermoelectric module to actively cool the upper boundary, this was not used due to its complexity and requirement for a heavy finned heat exchanger to couple the hot side of the Peltier module to the ambient air. The hot plate is again maintained at a controlled higher temperature by a flexible heating pad. In this cell, however, the heater is an etched foil resistance element type with the outer

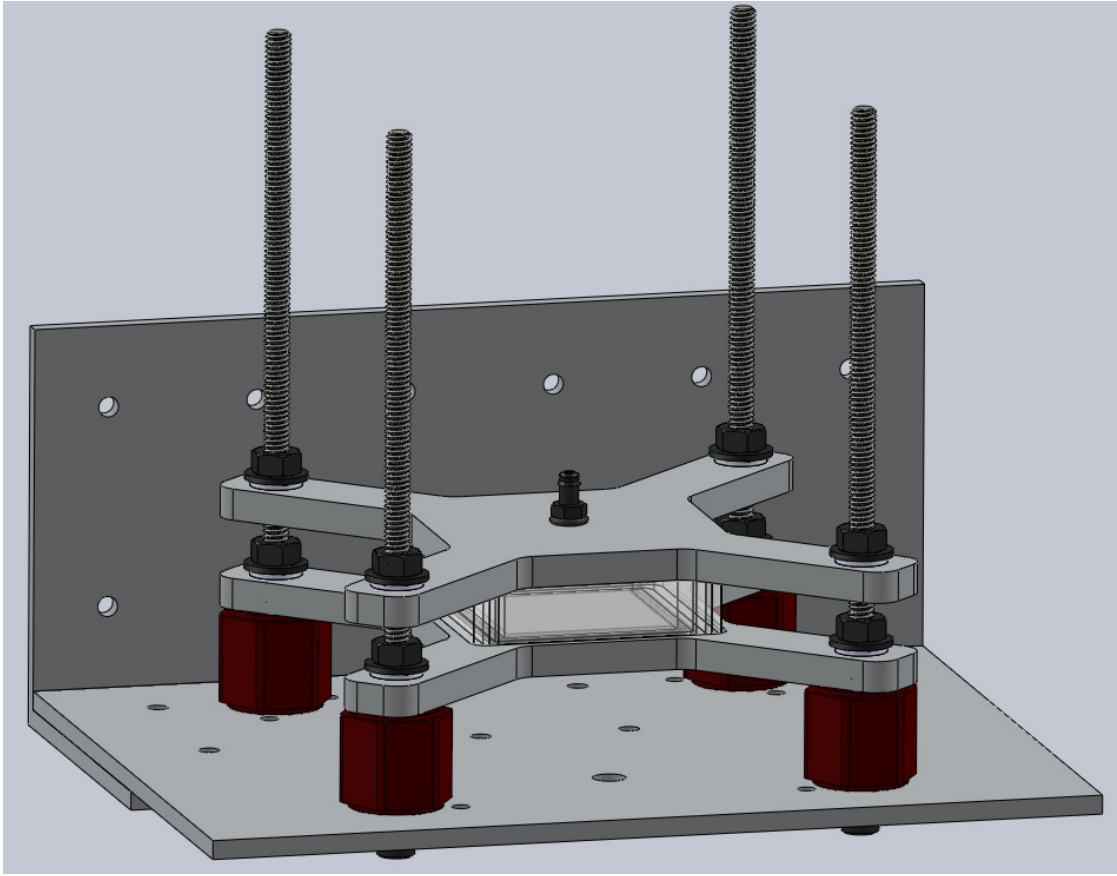


Figure 2.24: CAD rendering of the $\Gamma = 3.0$ cell, as built. In experimental usage, the cell is enclosed in layers of thermal insulation.

envelope comprised of polyimide plastic (often referred to by its DuPont trade name Kapton[®]) sheet. The entire heater assembly is 2.0 inches (5.1 cm) square and 0.007 inches (178 μm) thick. To better match the computer-controlled power supply used in the experiment, a maximum 28 V unit was specified. This heater can deliver 40 W and draws a current of 1.43 A at that voltage.

A further goal of this cell was to improve the thermal isolation of the cell from its underpinnings and the surrounding air. The most radical of these changes was the incorporation of a double side wall to further insulate the lateral boundaries of the experimental fluid from the surrounding air. This permits both enhanced

insulation while maintaining optical transparency. The gap between the inner and outer walls is 0.318 cm. While the relatively close spacing of the walls in this gap relative to the height of the cavity ($\Gamma_{\text{gap lateral}} = 0.21$) leads to requiring a numerical solution for the critical Rayleigh number within it, these solutions for a variety of rectangular geometries have been tabulated [24]. Following these results, we may approximate the critical Rayleigh number to be $Ra_{c,\text{gap}} = 10,757$, which corresponds to a critical temperature difference of $\Delta T_{c,\text{gap}} = 35.3$ K. Therefore, as long as we restrict ourselves to experimental temperatures less than that result $\Delta T < \Delta T_{c,\text{gap}}$, the insulation space should not exhibit convective instability of its own that would complicated the results. To illustrate this double wall design, a cross section view of the cell is shown in Figure 2.25.

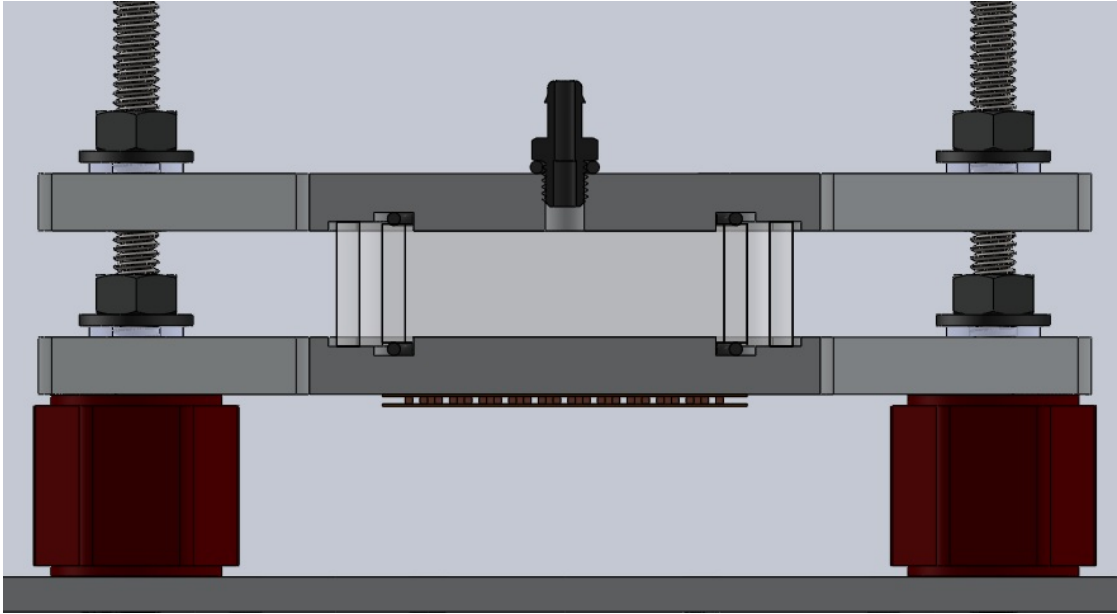


Figure 2.25: CAD rendering of the $\Gamma = 3.0$ cell, shown in cross section. Note the double wall experimental enclosure.

A further advantage of this design is how it lends itself to an intrinsic precision alignment of the top and bottom boundaries. In the $\Gamma = 5$ cell, there was always a significant amount of adjustment required to ensure that the hot and cold plates

were both parallel to each other and aligned at the correct separation. This was due both to the adjustable cold plate design and the necessary compression of the sealing O-rings, reducing the gap by some small amount. In this design, the outer enclosure forms a gauge block to impose the correct spacing and parallelism of the plates. With a minimal amount of silicone sealant in the outer enclosure joint, the top and bottom plates are therefore fixed to the precision of the machined length of those outer walls. As long as the inner enclosure is long enough to sufficiently compress the O-ring to seal the inner (experimental) chamber, and excessive force is not used clamping the enclosures, leading the outer walls to bow or deform, the height should be exact to within the thickness of the sealant layer. While there was generally a preference for cast acrylic material as opposed to extruded for these experiments, due to its superior optical qualities, commercially available stock tubes of the type used here are only manufactured through an extrusion process. While there was some small amount of extrusion marks noted on the tubing, these did not significantly effect the optical clarity of the wall.

To reduce the number of parasitic heat leaks through the cell into the structure, the number of supports for the cell itself was reduced to only four 1/4-20 threaded rods. These rods are arranged using the same spacing as the earlier cell, permitting this apparatus to be mounted without modification to the shaker itself. To reduce the amount of temperature controlled surface area exposed to the ambient air, the hot and cold plates were fabricated in an “x” pattern, extending as cantilevers from the center experimental container to their points of support at the outer corners. At any point where these rods pass through a heated or cooled plate, they are thermally insulated by being surrounded by a nylon shoulder washer insert, reducing the flow of heat through any mechanical fasteners from the hot to cold plates. Additionally, to reduce thermal contact with the shaker carriage,

the entire cell is supported on plastic composite spacers, without a direct metal through-fastener. These commercially available standoffs are constructed of a fiberglass reinforced plastic which has metal thread inserts at opposing ends which do not connect to each other, allowing a 1/4-20 fastener to be threaded at both ends without making direct metallic contact.

As before, the inner enclosure may be accessed through a threaded hose barb. The hot and cold plates of the cell are insulated in a similar manner to the $\Gamma = 5$ cell, using a variety of thermally insulating materials.

2.7 Apparatus Fabrication

All apparatus components for both cells were fabricated in-house at Penn State, with most parts being fabricated on conventional manual milling and turning machines by the author. A few complex parts, such as the $\Gamma = 5$ cell cooling plate, were milled using CNC machining techniques by professional machinists. Additionally, many components with complex outer dimensions were cut to rough form using an abrasive waterjet cutter for both the significant time savings and precision and finished on a manual mill. Using this range of techniques, attention was paid to the maintenance of tolerances of ± 0.005 inch ($\pm 127 \mu\text{m}$) when possible in general, and in all measurement sensitive dimensions.

Material selection was also considered: non-fastener metal components (such as hot and cold plates) were generally constructed from 6061 aluminum alloy to reduce moving mass. Designs were constructed to avoid the mechanical resonances of structural components coinciding with the desired shaking frequencies. Stainless steel was used for fasteners where thermal conductivity was of high concern. Due to the significant forces on some moving components, grade 8 rated fasteners were

employed at critical junctures.

All experimental apparatuses were designed with insight from the prior art for convection experiments, although the relative paucity of prior shaking convection experiments required some new and unproven designs to be employed. Over the course of this experimental investigation, there was continual modification, improvement, and simplification of the experimental design and techniques. With each improvement, the quality of the data has improved, at times in large steps. The description of the experimental cells that proceeded generally described the final, most successful, incarnations of these experiments, from which most of the data presented in the following chapters was obtained.

Chapter 3

Procedures and Techniques

This chapter will discuss the experimental procedures and techniques that have been employed in these experiments, their development, and illustrate the means through which the experimental results presented in the following chapter were acquired and interpreted. These include thermal transport and optical flow visualization measurements as applied to, first, as a preliminary validation, stationary, and then the desired shaking experimental configurations.

All data acquisition functions for these experiments are implemented in a custom-written National Instruments LabVIEW 2012¹ program, controlling and interfacing with a variety of external instrumentation. The separate measurement elements presented are all individual components of this overarching acquisition program, running simultaneously during experimental measurements. The sources of these measurements, their processing in near-real-time during the experiments themselves, the control functions that are implemented, the storage of the resulting data, and the interpretation procedures used to determine the stability of the fluid are all addressed.

¹National Instruments Corp.: <<http://www.ni.com/labview/>>.

3.1 Thermal Measurement Scheme and Data Acquisition

As was presented in the previous chapter, a common methodology to determine the transition from stability to instability in convection experiments is to track the change in thermal transport occasioned by the onset of advection. The details of this thermal measurement scheme, as implemented, are discussed here.

The source sensors for these thermal measurements in this experiment are thermocouples affixed to the heated and cooled boundaries of the experimental cell to measure the temperatures of both horizontal enclosure surfaces. These thermocouples are wired to a Keithley² Model 740 System Scanning Thermometer. As this is a purely differential measurement, no cold junction compensation error is introduced as both thermocouples are wired to the same thermal junction block, placing both cold junctions at the same reference temperature. Significant effort was also taken to ensure that the thermocouple cable runs were kept to the same length and were made with the same manufacturing lots of thermocouple wire in order to avoid unnecessary errors. The thermocouple cables were kept away from electrical noise sources, the most significant of which is the motor control cabling. The thermocouples were initially checked for accuracy (in end-to-end calibration) by using a water and ice bath (which equilibrates at approximately 0 °C) and an acetone and ice bath (which equilibrates at approximately −10 °C), ensuring that the difference measured was close to that temperature span.

After being read by the Keithley thermocouple reader and transmitted to the computer via a GPIB (IEEE 488) interface bus, these two temperatures are

²Keithley Instruments, Inc.: <<http://www.tek.com/keithley>>.

subtracted in software to find the temperature difference between the two plates. This temperature difference ΔT is the “process variable” of the control system. The PI (proportional-integral) control loop algorithm compares this to the “setpoint” (the desired ΔT) and then computes the “control variable” to the system, which in this case is the commanded voltage to be delivered to the resistive hot plate heater. That voltage is sent, again via GPIB, to an Agilent³ E3634A digital power supply, which sets its output voltage to the commanded value. A full PID (proportional-integral-derivative) algorithm was also tried. However, at times with the derivative term implemented, the loop would show signs of instability [110]. A block diagram of this control loop is shown in Figure 3.1.

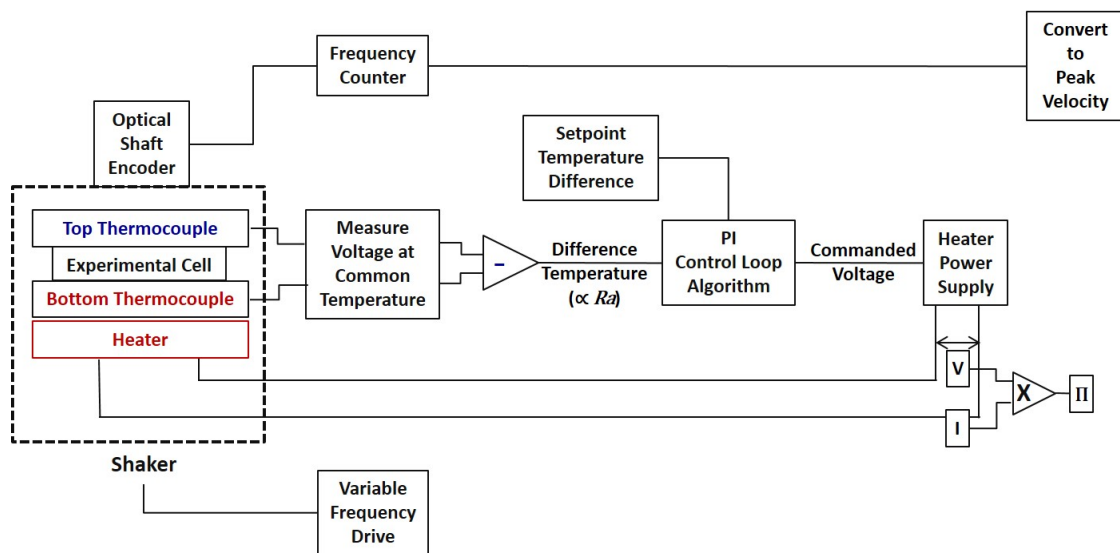


Figure 3.1: A block diagram representing the components of the heater power differential control loop and their interconnections.

After remotely setting the voltage of the DC power supply, the power supply then returns the actual, measured electrical voltage and current. The electrical power is computed in the software by multiplying those measurements, $\Pi_{el} = V_{el}I_{el}$. It is changes in these electrical power measurements with respect to the measured

³Keysight Technologies: <<http://www.keysight.com/>>.

ΔT that allow the convective stability or instability of the fluid to be inferred. The ambient temperature inside the laser safety enclosure is also measured by means of a separate thermocouple, that is fed to a Stanford Research Systems⁴ SR630 Thermocouple Monitor, which provides that measurement to the computer, as well. The ambient temperature is tracked to indicate any large swings in temperature outside the experimental cell and also permits the recognition of the development of thermal conditions conducive to the shaker motor or laser overheating.

These thermal measurements are written to a TDMS (Technical Data Management Streaming) file, which records, for each measurement, the following data: a time stamp (referenced to the computer system clock, written in a 24-hour clock format to an accuracy of a hundredth of a second), the desired setpoint ΔT in degrees kelvin, the measured ΔT , the temperature deviation from that setpoint, the ambient temperature, and the electrical voltage, current, and power delivered to the heater. The loop is run as quickly as the computer and the instruments will allow, normally about once per second. The data file is buffered to memory and written to the hard drive every sixty measurements, to limit any loss of data by computer failure or power outage to less than approximately one minute. This file format was used as it is well-integrated with LabVIEW (having been espoused by National Instruments), allows the storing of measurement metadata to the file itself, and is easily opened in other software programs.

Tuning the PI loop was primarily a matter of trial and error. While the Ziegler-Nichols method [110] was used to find initial approximate gain settings, those results were found to be too aggressive for this application. Tuning the gains was found to be primarily a tradeoff between too much “hunting” in the power input (resulting in heater powers that would swing wildly between loop iterations) and

⁴Stanford Research Systems, Inc.: <<http://www.thinksrs.com/>>.

too little disturbance rejection (allowing the controlled temperature to wander too far from the desired setpoint). The best compromise was found to be when the PI loop was tuned to permit the heater power to vary less than $\pm 5\text{-}7\%$, which resulted in the temperature varying less than $\pm 1\%$ of ΔT .

3.2 Shaker Control and Measurements

As was described in the previous chapter, the shaker motor is controlled by a variable frequency drive (VFD) motor controller. In this case, that unit is an Eaton⁵ M-Max Series drive appropriately sized for the motor used. While this VFD can be remotely controlled through both digital signals and analog inputs, in practice in this experiment, the front panel controls are used, with the VFD operating in a Volts/Hz configuration.

Because the front panel controls are used, shaker speed control is accomplished through a human-in-the-loop scheme. The shaker speed is directly read through a Hewlett Packard optical rotary encoder, which outputs a TTL-type signal at a resolution of 1000 counts/revolution. This signal is read by a Hewlett Packard⁶ 53131A counter, which reads the signal for five seconds and then outputs the frequency of the TTL counter signal. This frequency is displayed on the face panel and read into the computer through GPIB, where it may be converted to shaker frequency, shaker peak velocity, or revolutions per minute. As the experiments are generally designed around a target shaker frequency, deviations from that target are noted by eye and the variable frequency drive is adjusted. As changes in shaker speed are generally gradual and over long time spans, this manual control methodology has been sufficient.

⁵Eaton Corporation Plc: <<http://www.eaton.com>>.

⁶Keysight Technologies: <<http://www.keysight.com/>>.

The shaker frequency is also recorded in the TDMS file, however, those measurements are unsynchronized with the thermal measurements as they are registered approximately every seven seconds, due to the relatively long averaging period of the counter. Those measurements are written into a separate measurement group in the same file, however, they are given their own set of time stamps.

The variable frequency drive is also configured to implement a variety of helpful features, including soft starter-like startup behavior and overheating and overcurrent monitoring and protection.

3.3 Optical Measurements

As was described in the previous chapter, the cell is illuminated by a laser light sheet. The light sheet illuminates incense smoke that is injected into the cell and captures the flow patterns inside the experiment. The implementation of this is relatively simple. The end of the stick incense is lit in the customary manner, allowed to burn for a few seconds until the smoke from the direct flame changes color from gray to near black and the stick is then shaken until the direct flame is extinguished and it exudes copious amounts of white-gray smoke. This smoke is captured in an overturned 100 cc syringe with care being made to maintain the burning end of the incense stick outside the syringe, so that the oxygen supply to the flame is not restricted. The smoke is sealed in the syringe by inserting the plunger, after which the smoldering end of the incense stick is quenched in a container of water for safety. A brief pause is taken for the smoke to remain in the syringe so that it may cool somewhat and distribute evenly within the volume of the syringe. The plunger of the syringe is then slowly depressed, feeding the smoke through a length of flexible laboratory tubing, which enters the laser safety

enclosure, follows the electrical connections from the stationary frame to the moving shaker carriage, and enters the cell through a hose barb inserted through the cold plate. This long distance of tubing also allows the smoke to further cool before it enters the cell.

The smoke is illuminated by the light sheet in its plane and the side scatter of the particles is captured and imaged by the monochrome CCD sensor inside the camera. As the mount of the laser diode array was designed to allow positioning of the plane of the light sheet within the volume of the experimental cell, a choice of light sheet alignment relative to the apparatus side walls was required. The choice was made to position the light sheet approximately one-third of the cell horizontal dimension from the front wall, that is $l_{y, \text{light sheet}} \approx l_y/3$. The orientation of the light sheet is depicted in Figure 3.2.

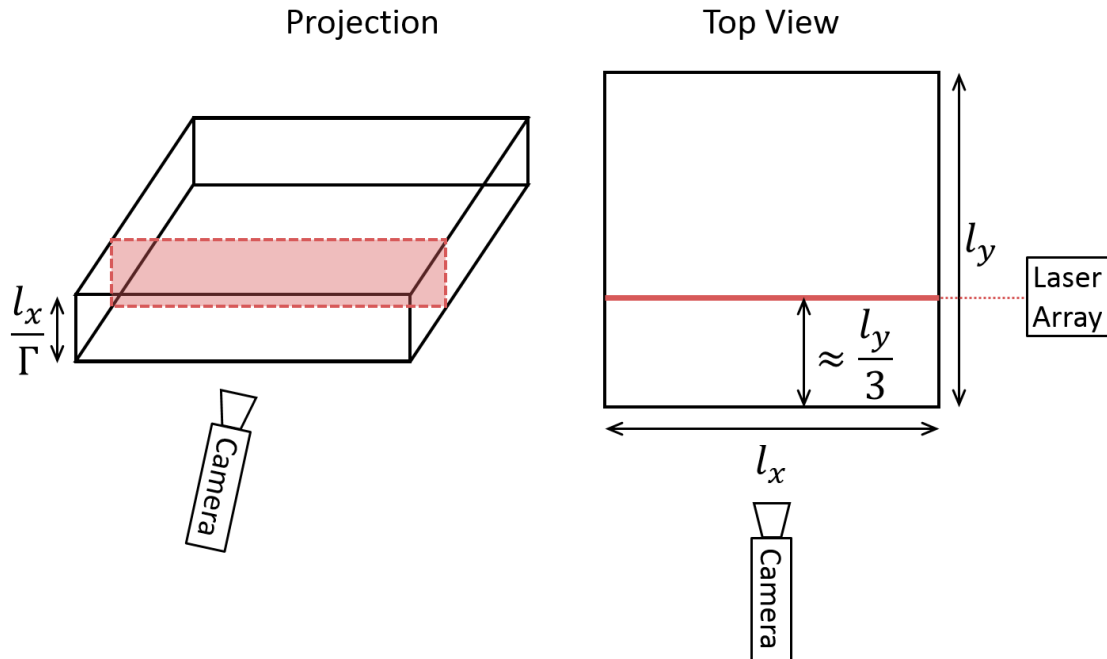


Figure 3.2: Illustration of the light sheet positioning relative to the experimental cell walls.

As was previously described, this camera is synchronized to the moving shaker

carriage so that the experiment is repeatedly imaged at the same point in space and the same time in the shaking cycle. These images are read into the computer via a pair of linked Gigabit ethernet cables run to a dedicated dual network interface card, that then reassembles the data packets from both cables into an image stream. The connection follows the GigE Vision standard for high-performance ethernet-based cameras. Within the data acquisition LabVIEW program, each frame of the video is superimposed in the lower right corner with a printed time stamp generated by the computer system clock, again in a 24-hour format, allowing the video to be correlated to the thermal data. Those frames are placed in sequence and then saved to a standard AVI video file format. The raw size of the images is large, as the image is 1024 pixels \times 1024 pixels at 14 bit depth, resulting in a size of over 1.8 MB per frame. At a shaker frequency of 6 Hz, that corresponds to about 650 MB per minute, a very large amount of data. The use of the AVI file format, while convenient due to its ubiquity, limits the images to 8 bit depth, which reduces the file size and in most of the experiments, a lossless compression method is used to further reduce the size of the data files. This results in video files for most experimental runs that are between 20 and 40 GB in size.

As the only linkage between the videos and their corresponding thermal data is through that superimposed time stamp on the video frame itself, a further software routine was written that uses a character recognition algorithm to read that portion of each video frame, extract the time stamp into an array of numeric times, and further correlate each frame with an element of the thermal data. As the time stamps take the same form in every frame, the character recognition algorithm has very high reliability in deciphering the text and where there are multiple video frames for each entry in the thermal data set, the code interpolates those thermal results.

The camera may be remotely controlled in many aspects from the LabVIEW code. This includes switching the camera exposure arming mode from free-running to triggered, changing the exposure duration, amplifying the images post exposure, and reading out camera frame rate and other statistics. Lens functions must be adjusted manually, including focus and iris, requiring laser safety precautions to be taken.

3.3.1 Impacts of Optical Measurement on Flow Conditions

Unlike the the thermal measurements, the optical flow visualization method fundamentally requires the perturbation of the convective flow in some way, as the gas inside the cell itself must be mixed with the injected smoke. This section will describe those checks and measures that were undertaken to ensure that the implementation of optical measurements changed the flow conditions within the experiment as little as possible.

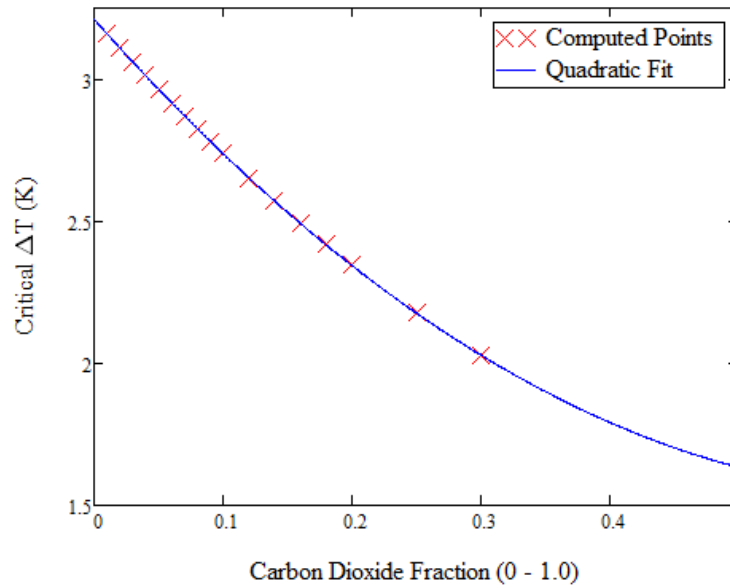
As was described prior, there is the possibility that the smoke may be entering the chamber at a temperature higher than the prevailing fluid. A series of computations were made to estimate the entry temperature in the cavity of the smoke after traveling through the over eight feet of tubing it traverses and it was found that the smoke should have cooled to the ambient temperature, even in the worst case scenario that the smoke plume had not been permitted to expand from the combustion source into the large syringe, which it does before it is injected.

There may also be other perturbations resulting from the introduction of the smoke, namely the introduction of combustion products, primarily CO_2 and CO . As CO_2 is significantly heavier in terms of its molecular mass than the other combustion components, an analysis was undertaken to determine the theoretical effect of an

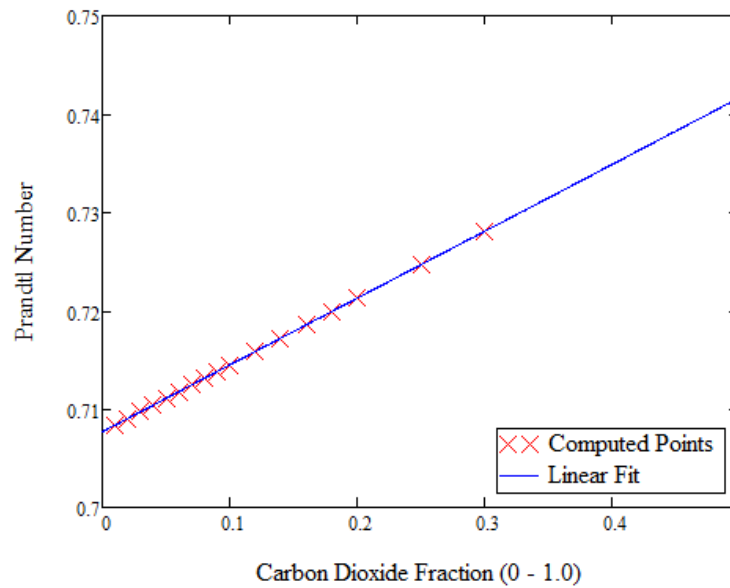
increased fraction of carbon dioxide on the critical Rayleigh number. Using the empirical correlations of C. R. Wilke, *et al.* (now referred to as Wilke’s Mixture Rule) [111, 112], the relevant fluid properties of the mixture (density, thermal conductivity, viscosity, specific heat capacity, and the derived diffusivities) were computed for varying concentrations of carbon dioxide and the critical temperature difference was computed. The effect of increasing carbon dioxide fraction was to depress the critical temperature difference quadratically with respect to carbon dioxide fraction, however, the concentrations would need to be unrealistically high to significantly change the critical Rayleigh number Ra_c of the system. For reference, a 2004 study [113], which burned one to three sticks of incense inside an environmental chamber, found the highest CO₂ concentration to be 938 ppm. The results of these computations are shown in Figure 3.3.

There has been past concern raised in the literature that the very presence of particulate matter in the experimental fluid itself might lead to changes in the critical nature of the instability. Wollkind and Zhang [114, 115] made a theoretical treatment of the Rayleigh-Bénard system in the presence of tobacco smoke, using a multi-phase computational approach, showing a lowering of the critical temperature due to a smoke-associated secondary instability, however, this effect is notable only for thin layers (which they define as those less than 10 mm in depth) and strongly significant only for those even shallower. The experimental containers of interest in these experiments are much deeper than this limit, so this “columnar instability” should not be of concern.

There was also concern that the laser itself may cause localized heating of the fluid in the presence of the smoke. This may not be particularly surprising, as incense smoke exhibits a high amount of particulate matter, making it attractive for flow visualization applications, in much the same way as tobacco smoke was



(a) critical temperature difference ΔT_c



(b) Prandtl number Pr

Figure 3.3: (a) Plot of the computed results for the depression of the static critical temperature difference ΔT_c as a function of additional carbon dioxide fraction (ranging from 0.0 to 1.0), with 0.0 being normal dry air. These computations are for the $\Gamma = 5$ cell. Crosses denote computed values and the line is a quadratic fit to those points. (b) Equivalent computations for change in Prandtl number Pr .

popular for earlier experiments. This large amount of particulate matter may also lead to localized heating when illuminated with the laser. This may be particularly true in the convectively stable regime during static measurements (those that are stationary without shaking imposed), where the overall heat flux due to thermal conduction is very small and the predominant fluid flow visually observable is the slow sedimentation velocity (computed to be on the order of $2 \mu\text{m/s}$) due to the settling of the particles out of suspension.

In initial investigations, there was in fact some indication of localized heating of this type. These initial tests, run to establish the static flow patterns and their transitions, allowed the system to stabilize at a specified ΔT over a period of time and then smoke was injected into the cavity and the flow pattern was observed at each stable temperature difference. This allowed a systematic and cautious mapping of the flow across the range of temperature differences of concern. What was noted was that the fluid would appear to be quiescent across the majority of the cavity, as would be expected at temperature differences ΔT below the critical difference ΔT_c . However, the region closest to the illumination source (along the cavity wall where the light sheet entered the cavity) would begin to display a slow rotational flow. This flow would generally take several minutes to develop and was distinctly localized. An image showing this phenomenon can be seen in Figure 3.4. Each point required one to two hours to capture due to the desire to ensure a steady thermal state.

To test whether this behavior could be avoided, a means to reduce this localized heating is to reduce the duty cycle of the laser, by decreasing the fraction of time the laser is emitting into the fluid. As illumination is only required while the camera is exposing the CCD and not during the interline readout and data transmission phases, the laser may be synchronized to the camera, in much the same way as a

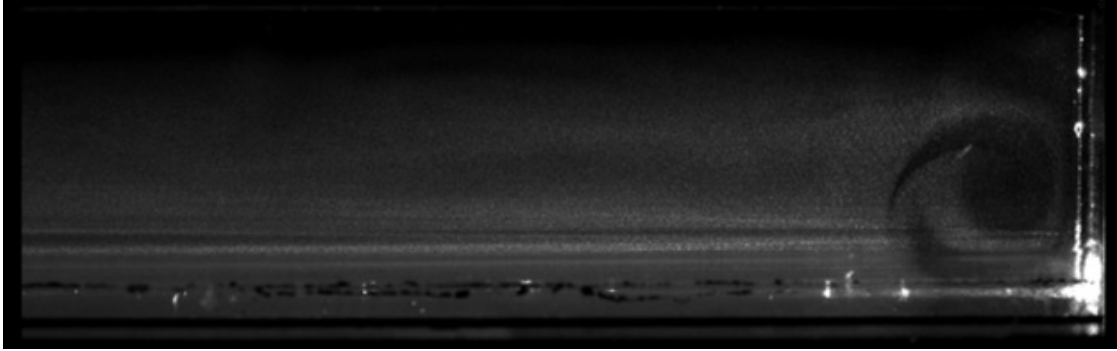


Figure 3.4: Image from the initial investigation of static convection onset. The anomalous rotational flow near the illuminated side of the container can be seen to the right of the image. In this image $\Delta T = 2.0$ K.

conventional camera strobe is.

To implement this, the operating mode of the laser was changed from continuous wave (CW) to a pulsed mode to gate the laser in response to the digital logic (TTL-type) trigger signal. As was described earlier, this signal is generated as an output of the camera and is synchronized to the electronic shutter signal internal to the camera circuitry. The laser is then triggered to emit along with this signal. As the total time latency of the entire circuit from camera external trigger rise to laser emission is less than $40 \mu\text{s}$, the switching of the laser is indiscernible to the eye on the video taken at 55 frames/second.

Extensive testing was performed with a variety of exposure/illumination times from $50 - 1000 \mu\text{s}$, varying laser intensities, and illumination rates ranging from 0.1 to 50 Hz. After this extensive testing, the ideal condition was found to be the lowest practicable peak laser illuminations (corresponding to currents of approximately $I_{\text{el}} = 7.0$ A) and illumination times of approximately $200 \mu\text{s}$ at repetition rates consistent with those in the shaken experiment ($4-10$ Hz). With the duty cycle of the laser so reduced, a notable change was seen in this sub-critical onset of convection. The spurious rotations were either eliminated or took

significantly longer to develop and an observable change in the fluid flow took place just below the theoretically predicted convection onset temperature. Therefore, it would appear that localized heating of the fluid due to the presence of the laser impinging upon the smoke particulates would be the most logical explanation for the depressed onset that was observed. For comparison to Figure 3.4, another image at the same temperature difference $\Delta T = 2.0$ K is shown in Figure 3.5.

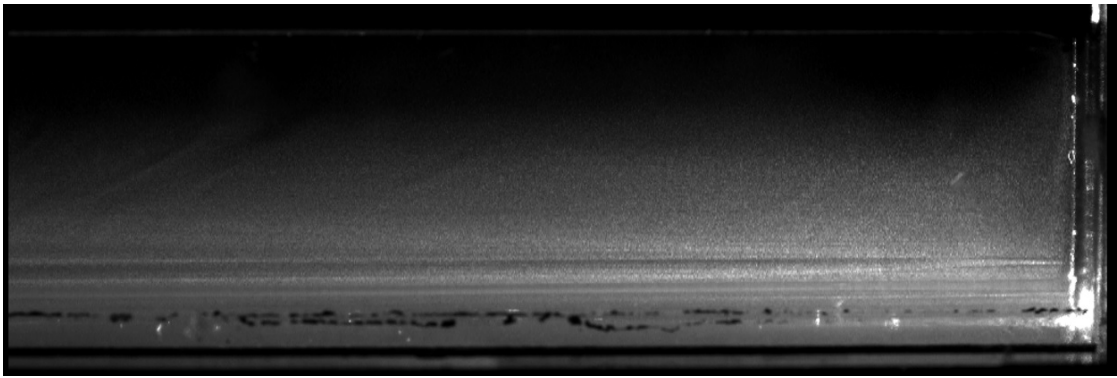


Figure 3.5: Image from static testing with the pulsed laser (rate = 8 Hz). The dark region at the top of the cell is a consequence of sedimentation of the smoke particulates due to the lack of convective flow. The temperature difference here is the same as in Figure 3.4, $\Delta T = 2.0$ K.

3.4 Static Measurements

In this section, the procedures employed for static measurements (those without any imposed vibration) are discussed. These measurements were a necessary preliminary to build confidence before the added complexity of vibration was introduced. Static measurements reach back to the tradition of the earliest convection experiments.

The methodology used for these static measurements follows the path started in 1935 by Schmidt and Milverton [98], as discussed earlier. The process is relatively straightforward: the system is initially allowed to equilibrate at a specified temper-

ature for some period of time, generally several hours. The setpoint temperature is then increased (or decreased) by some defined temperature step, ranging from a few degrees kelvin to 0.1 K. After each change in temperature, the system is permitted to equilibrate to the new temperature and the temperature and power input are tracked for a period.

After the system has been allowed to sweep through the entire range of temperatures of interest, the data is then processed. At each setpoint, the data points prior to the achievement of equilibrium are discarded. Once stability has been reached (as determined by the temperature fluctuations being less than some defined range, generally ± 0.03 K), all data points until the next temperature change are averaged. This is convenient since the control algorithm (when properly tuned) will oscillate more or less symmetrically about the mean power input, as it responds to small deviations in the measured temperature difference ΔT away from the desired setpoint. In a similar fashion, while the temperature deviates very little from the setpoint ΔT , the mean of that measurement is also taken, instead of using the setpoint itself, in case there is any offset in the oscillation. In practice, though, that mean ΔT was found to deviate from the setpoint value by less than ± 0.001 K. The further analysis concerns itself with those means alone.

The determination of a stable controlled temperature state for each setpoint value is determined by eye. As in many PI algorithm-based controllers, the amplitude of the control variable (the heater electrical input power) will oscillate around the new setpoint with rapidly diminishing amplitude after responding to a drastic change in setpoint value. As a result, in response to that control variable oscillation, the temperature will also briefly oscillate in turn. As the PI algorithm is tuned to have stable control behavior, these oscillations quickly diminish (damp away) over time until the temperature reaches an approximately stable value about the setpoint

with the small amplitude deviations discussed above. Once that time has been determined, a Microsoft Excel Visual Basic macro script determines the range of data of interest, collects it in an array and determines both of the mean values. Those values, along with other computations of interest, are recorded on a separate worksheet.

Those values may then be plotted with average power input (in watts) on the y -axis and the temperature for each point (in degrees kelvin) on the x -axis. This is equivalent to the plots of Schmidt and Milverton [98], as shown in Figure 2.18, however, with the axes exchanged. From this plot, the transition from stability to instability must be determined, which will be discussed at length in the following section.

3.4.1 Instability Determination

The expected plot of heater power input vs. ΔT should transition from one shallow slope, due to conduction alone, in the region that is suspected to be stable, to a steeper slope, due to convection-associated advection being added to the baseline conduction, in the region suspected to be unstable. To determine this, we begin, as is canonical in these experiments, by attempting to fit one line to the stable region and another to the unstable region and then determining their intersection in order to ascertain the temperature of suspected transition.

Initially, this was accomplished crudely by selecting a point of transition n , where n denotes an index in the array of data points, one for each setpoint temperature ΔT (arranged in ascending order), such that the first line fits the data from the initial point until the point n , and the second line fits the data from the point $(n + 1)$ until the last data point. The wrinkle here, of course, is the determination

of n . In the very early measurements, this was accomplished solely by eye, however, that leaves the result somewhat open to the confirmation bias of the experimenter.

A next step was to compute the sum of the square of the residuals, the SSR, for each line, rendering one for the stable fit and one for the unstable fit. Additionally, a third SSR was computed for a straight line that was fit to the entirety of the data, with no distinction between regions. These were compared to determine how much better the two line fit reduced the residuals when compared to the straight fit, and by maximizing that difference, the transition point could be found in a more quantitative manner. Therefore, a variety of values for n were tested while that difference $SSR_{\text{straight line}} - (SSR_{\text{stable}} + SSR_{\text{unstable}})$ was compared to determine which value of n resulted in the maximum difference. A set of static experimental data, fit using the technique described here, is shown in Figure 3.6.

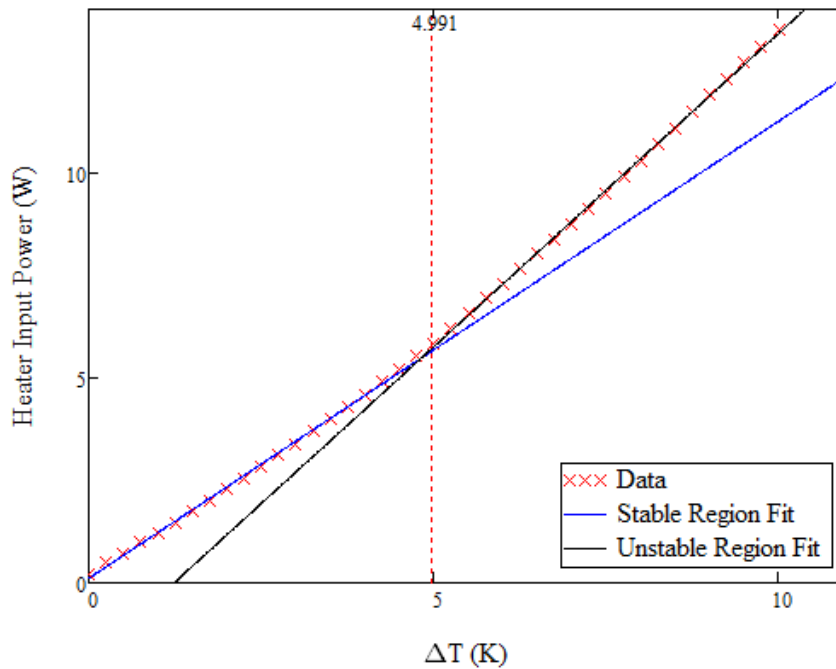


Figure 3.6: Results from an example static experiment. The experimental data is fit using the two lines SSR approach described. The vertical dotted line shows the theoretical instability prediction of Carbo for this cell.

A further step was taken to fit a “bent line” that had a second slope that “turned on” at some given value of temperature. This fitting function takes the form of:

$$\Pi(\Delta T) = \Pi_o + S_{\text{stable}}\Delta T + S_{\text{secondary}}(\Delta T - \Delta T_c)H(\Delta T - \Delta T_c) \quad (3.1)$$

where here, $H(x)$ is the unit step (Heaviside) step function and the intercept Π_o , the slopes S_{stable} and $S_{\text{secondary}}$, and the transition temperature ΔT_c are all parameters that are allowed to be fit. To maintain correct dimensionality, the function gives a result in watts. By using this fitting function, the entire process of determining the transition point may be automated. However, there is some sensitivity to the initial guesses provided to the fitting algorithm. In practice, it was found that as long as the step size in ΔT between experimental points was not overly coarse, both the SSR minimization approach and the automated “bent line” approach gave nearly the same result.

In a few runs, it was noted that the data displayed the expected two-straight-line behavior indicative of a transition from stability to instability, however, the few points in the immediate region of the suspected transition deviated from either line. This is not necessarily uncommon in convection onset experiments (refer to the traces corresponding to “Expt. 2” and “Expt. 4” in Figure 2.18 [98]). In these few cases, the two lines were fit to all points below and above the transition while excepting the few points near the transition point. In this way, the stability transition was determined from the extrapolated intersection of those lines.

3.4.2 Goodness of Fit Metrics

As was described in the previous section, the sum of the square of the residuals for the individual fits was computed and compared to that for a single straight-line fit to the entirety of the data. In addition to that measure, the square of the correlation coefficient R^2 is computed for each fit. Additionally, a t-test, comparing the data fit to the null hypothesis, and the resultant p-value are computed, however, with the small sample sizes being used in these experiments, these metrics are of dubious value and not relied upon.

In consultation with the Statistical Consulting Center, a unit of the Department of Statistics at Penn State, computation of the Akaike information criterion (AIC) was also added to the panel of metrics already being computed. While the AIC will not show whether the model is a good one for the data, it allows the comparison of multiple models to each other for the given data set, meriting the model for goodness of fit and penalizing it for model complexity [116–119]. In this case, the models being compared are the single, straight line and the “bent” line fits. By looking for that model with the smaller AIC, some confidence may be gained that the particular model is preferable to the other. It does not, however, indicate that either is a good model in and of itself. Regardless, it indicates that for the given experimental run, a model with two slopes, representative of a transition from stability to instability is preferable to a single straight line model that does not indicate a transition.

3.4.3 Static Measurement Refinements

Initially, the static measurements were performed, as was described earlier, as single, individual sweeps either up or down in temperature ΔT . Each of these setpoints

stepped up or down by a constant step size and held the ΔT at each individual setpoint for the same prescribed time period. To both ease the acquisition of large amounts of data and afford added flexibility to the design of these static measurements, the code was rewritten to permit arbitrary ΔT step profiles with arbitrary step times. After this modification, the static measurements could be configured to run consecutive sweeps, both ascending and descending in ΔT , over a period of multiple days and with changes in dwell time at each step and granularity of step size in regions of interest. Due to this enhancement, these runs would often take place over the course of two or three days, generating data at over one hundred equilibrium points for some runs.

This large number of points, with the concomitant variation in run steps and design and ambient conditions, allows the stability transition to be determined in aggregate. For the $\Gamma = 5$ cell, 445 points were acquired over the course of several long runs. These points represented both ascending and descending sweeps and varying step sizes (in ΔT), with particular focus on maintaining a high density of data near the anticipated transition point and below $\Delta T = 1.0$ K, as there were some initial concerns about early onset in that low range.

These points, from across all the runs, were collected into a single array of correlated ΔT values and corresponding average input powers. Each point was then disassociated from its individual run by sorting the meta-array into ascending order by ΔT . This collection of stable points was then fit to two lines to precisely determine the average transition point for this cell. This data set, along with its fitted lines, are shown in Figure 3.7.

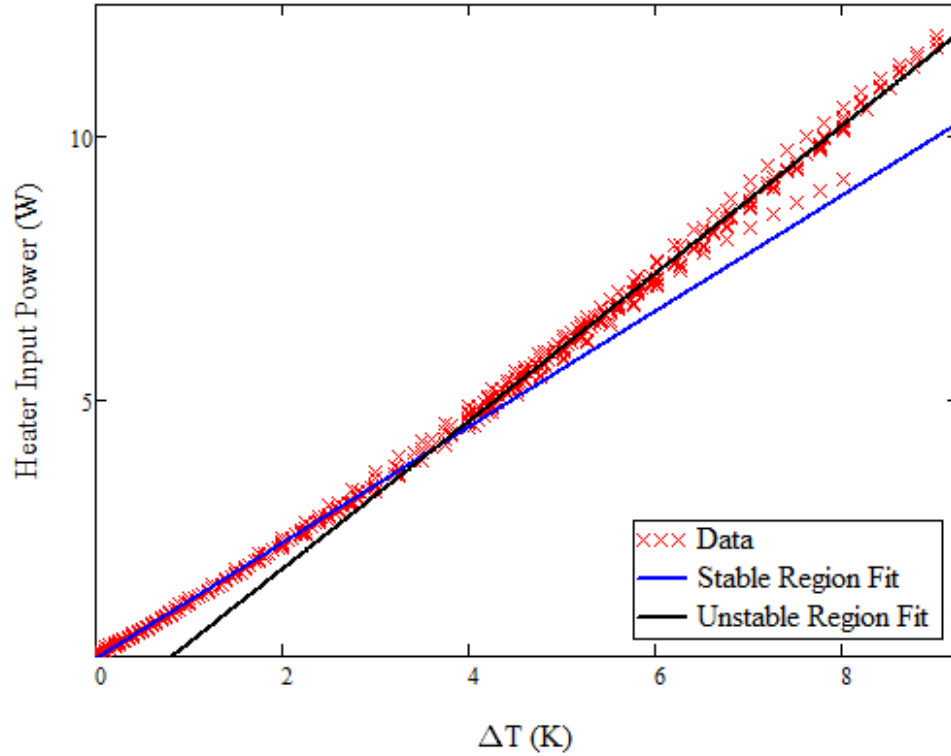


Figure 3.7: Results from the 445 point static measurement data set from the $\Gamma = 5$ cell, showing the optimized stable and unstable fit lines. Note that there is one individual run that displays some downward deflecting outlier points in the region $\Delta T \gtrsim 6.0$ K. The cause of this marked deviation is unknown.

3.4.4 Static Measurements with Visualization

The static measurement techniques described here allow the fine determination of the transition to instability absent vibration, giving a precise result for the critical temperature difference ΔT_c and therefore the critical Rayleigh number Ra_c . Flow visualization techniques may then be added to these static experiments to gain some understanding of the overall flow in the cell at any given temperature difference. This has been attempted in two ways in this work.

One option is to permit the cell to equilibrate at some small ΔT , well below the critical value ΔT_c , and then rapidly increase the temperature to a value above

the critical. This “ramp up” shows a notable transition from stability to instability, however, these rapid changes open the measurement to the introduction of potential errors, not the least of which that the thermal conditions within the cell may be changing more rapidly than the thermal measurements are able to capture. The thermal measurement control feedback loop and temperature data acquisition has a maximum sample rate of about 1 Hz as programmed with the hardware employed. While this is more than sufficient for the generally slowly changing conditions inside the cell, in a rapid heating condition like that described here, this may be insufficient to capture the relevant behavior with accuracy. Optically, however, this shows the transition to instability in a visually arresting manner.

A more quantitatively substantial technique (and a better analogue to the shaking measurements) is to allow the cell to equilibrate to a given ΔT , dwell there for some defined time period, and then inject the smoke and illuminate the cell to interrogate the flow condition at that equilibrium point. This is repeated for a range of ΔT values of interest, permitting correlated thermal and optical measurements and allowing the convective flow patterns, as indicated by the flow visualization, to be compared to thermal determinations of stability. This technique, while more time consuming, appears to be significantly more accurate.

By employing the coupled measurement techniques, thermal and flow visualization, simultaneously, both may be refined in the static experiments before the added confounding factor of vibration is introduced.

3.4.5 Static Measurement Interpretation

The static measurements described here are an important bridge to the full shaking measurements that are the goal of these experiments. Additionally, they are

required for the full characterization of the cell and the gaining of confidence in the measurement techniques to be employed while vibration is imposed.

That characterization is crucial as the range of literature on the determination of critical Rayleigh numbers is both rather large and lengthy and the precision of theoretical predictions of the critical values have been shown to be rather accurate in well-controlled experiments. Therefore, if the static results in these cells were found to be inaccurate, no confidence could be carried forward into the shaking experiments. These static measurements lead to improvements and refinement in the overall experimental techniques. In particular, the importance of knowing the height of the cell with precision was underlined, as the Rayleigh number is proportional to the height of the cell l_z (the distance between the heated floor and the cooler ceiling) to the third power, making small imprecision in the height patently obvious in the static results. Additionally, inaccuracy in the temperature measurements and suboptimal choices for the PI gains in the ΔT thermal control loop were highlighted by these static measurements and remedied before the transition to experiments with imposed vibration. Finally, the importance of the role of sufficient thermal insulation of the cell in improving the distinctness of the “bend” in the transition (and easily identifying the anticipated “two slope” behavior) was driven home. That thermal leakage adds to the baseline increase of each individual line, reducing the apparent change in slopes that is being sought in these thermal measurements. It was only after these issues had been identified and addressed and static thermal measurements that were in sufficient agreement with the theoretical predictions of Carbo and others were obtained that the next step was taken to impose vibration upon the cell.

3.5 Shaking Measurements

The goal of this work is, in fact, to determine the conditions under which Rayleigh-Bénard convection may be suppressed under the influence of vibration, therefore, the next logical step in the investigations is to mount the experimental cell on the shaker and impose controlled vibrations on it. As many of the static experimental techniques described prior in this chapter may be extended to the shaking case, there was great effort expended in perfecting those as much as possible before moving to the vibrated problem.

There are, fundamentally, only a relatively small number of parameters that may be varied to change the experimental conditions in this system. The Rayleigh number $Ra = g\beta\Delta T l_z^3 / (\nu\chi)$ may be changed, although, by choosing the experimental fluid to be ambient air, β , ν , and χ are material properties that are fixed and, by setting the geometry of the container, l_z is now fixed. Therefore, the only thermal variable remaining to be manipulated is the temperature difference ΔT . Similarly, we may adjust the vibrational Rayleigh (Gershuni) number. However, the only adjustable parameter remaining there is, when all other factors are disentangled, the peak shaker velocity $|\mathbf{v}|$. Since the design of the mechanical shaker fixes the displacement amplitude, the physically adjustable control is the frequency of the vibration $|\mathbf{v}| \propto f_{\text{shaker}}$.

Thus, for each shaking experiment, one or the other (ΔT or f_{shaker}) may be fixed and the other ranged as the experimental parameter. Both have been performed, each with varying results.

3.5.1 Fixed ΔT , Varying $|\mathbf{v}|$

The first option would be to fix the temperature difference ΔT for the entirety of the run and adjust the frequency of the shaker f_{shaker} (and therefore the peak shaking velocity $|\mathbf{v}|$) through a range in an ascending sweep from low to high. This is perhaps the most mentally tractable option, as the system is beginning, statically and in the low shaking velocity range, in a convectively unstable condition and being brought through the increasing of shaking parameters to a stable state. This fits with the notion of inhibition in the literal sense of “turning off” the convection through increasing vibration.

This was, in fact, the first technique employed, before any flow visualization techniques were used in the shaking experiment. The temperature difference was established with the shaker stationary at some chosen point above the static critical $\Delta T > \Delta T_c$. The shaker was then started and the shaker frequency was increased in fixed increments, pausing for a period of minutes at each step to allow the system to equilibrate, after which the shaker dwelled at that frequency for a further defined period to acquire the desired thermal data. The shaker frequency was then increased and the process was repeated until the highest desired peak shaking velocity, an amount above the predicted stability boundary, was reached, upon which point the experiment was terminated.

As was done in the static measurements, the heater input power was averaged for each frequency point, as was the shaker frequency feedback measurement (taken from the optical shaft encoder on the idler shaft of the shaker). Instead of plotting, as in the static measurements, heater input power vs. ΔT , the plot now shows heater input power as a function of peak shaker velocity, as velocity is now the independent variable in the shaking experiment. These plots may now again be

fit to two straight lines, although the slope arrangement would be negative and the region of suspected stability would be preceded by the region of suspected instability. An example of one of the experiments of this type is shown in Figure 3.8.

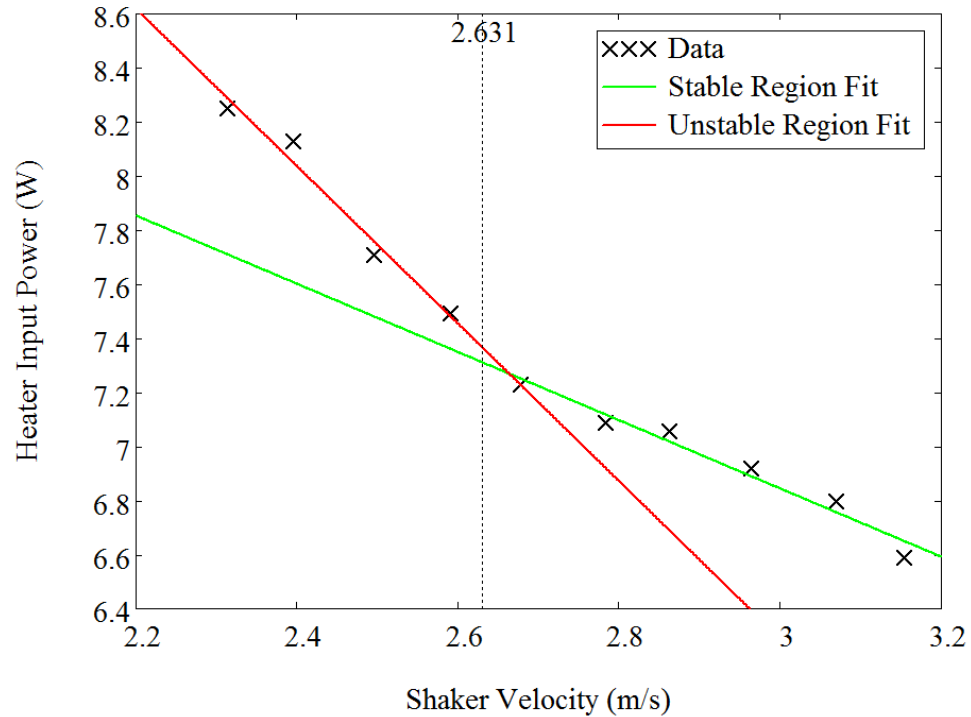


Figure 3.8: Example of a shaking experimental result obtained by varying the shaker velocity with a fixed temperature difference. This shows data from the $\Gamma = 5$ cell at a fixed temperature difference of $\Delta T = 4.32$ K ($Ra = 2062$). X's denote the experimental data and lines fits to the suspected stable and unstable regions. The dotted vertical line shows the theoretical prediction of Carbo for these conditions.

While this technique is intuitively tractable and rather conceptually elegant, it has shown some significant drawbacks. The experimental run shown in Figure 3.8 is relatively tidy, however, many experiments performed using this procedure did not resolve quite so nicely. One immediately notable concern is that the suspected stable region, despite being held at a fixed ΔT does not reach a horizontal line, indicating a constant thermal input, despite being believed to be stable. Other runs using this technique, for example that shown in Figure 3.9, despite appearing to

reach that constant thermal input in the stable region, do so far above (in $|\mathbf{v}|$) the prediction of Carbo, perhaps indicative of a partial stabilization or an experimental problem.

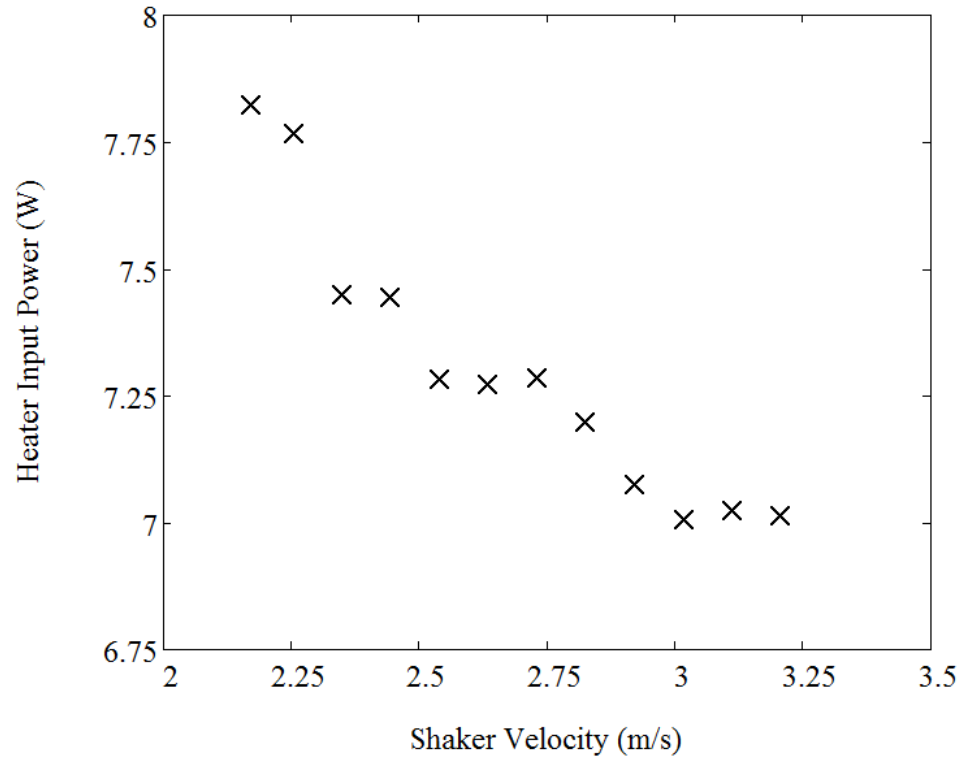


Figure 3.9: Example of a shaking experimental result obtained by varying the shaker velocity with a fixed temperature difference. This shows data from the $\Gamma = 5$ cell at a fixed temperature difference of $\Delta T = 4.50$ K ($Ra = 2148$). X's denote the experimental data.

One potential issue with this procedure is that the shaker tends to perform best when it is operated at a single shaker frequency. Each time the motor speed is changed, there is some settling period where the shaker frequency often overshoots the desired value, requiring the VFD drive to be reduced to precisely tune the shaker to that desired peak velocity. As is common with control loops, even those, like this one, that have a human-in-the-loop element, the process variable oscillates around the desired setpoint. Therefore, the changes between frequencies are not

instantaneous and can be rather imprecise in practice. This may lead to unwanted noise in the data due to the variability in the shaker peak velocity.

Another issue that may occur with this procedure involves parasitic thermal losses in the experiment. As the shaker peak velocity is increased, the forced convective losses on the exterior of the experimental apparatus are likewise increased. Therefore, as the velocity rises, the thermal input to the lower boundary is altered not only by changes in the internal, Rayleigh-Bénard convective state, but also by losses to this secondary, and unwanted, thermal path. Therefore, by increasing the shaker velocity, there may also be this second factor in play that confounds the measurements in some way. For these reasons, among others, another measurement procedure was pursued.

3.5.2 Varying ΔT , Fixed $|\mathbf{v}|$

To alleviate some of the issues raised by changing the shaker peak velocity and maintaining a fixed temperature difference, another alternative for the varying of parameters to determine the stability boundary is to maintain a fixed shaker velocity $|\mathbf{v}|$ and vary the temperature difference ΔT . This avoids the velocity wandering that is associated with each change in the shaker frequency. Additionally, the velocity of the air external to the apparatus relative to the shaking experimental cell is now fixed. While the thermal loss from the hot plate will still change with increases in ΔT , the velocity of that external air is fixed.

The procedure begins with the cell stationary. A ΔT well below the anticipated stability transition is established over the course of several hours until the temperature is well controlled and the power input to the lower boundary heater is as near constant as possible. The shaker is then started and the VFD drive frequency is

adjusted to maintain the shaker at the desired shaker frequency for the particular experiment. The entire system is permitted to equilibrate to a constant thermal input and the cell is then held at that ΔT for a further defined period to acquire the desired thermal data. After that period has passed, the ΔT is then increased by some given amount, the temperature and heater power input are again allowed to stabilize and the data acquisition period is allowed to pass. Each measurement point may require up to one hour, depending on the time to equilibrate for the given experimental configuration. The ΔT is then increased again and the process is repeated until the temperature difference has reached a value well above the anticipated transition to instability. At this point the experiment is ended: the shaker frequency is ramped down to a slow value and the shaker is stopped.

The resulting correlated pairs of average heater input powers (in watts) and the temperature differences (in degrees kelvin) are plotted and fit to two straight lines. The fitting procedure is identical to that for the static experiments and the same codes and techniques are employed.

This procedure may be a bit more difficult to readily grasp, however, in essence, the experiment is seeking to precisely determine the increase (in ΔT) of the transition to instability due to the introduction of the shaking. Therefore, while the static experiment may transition to instability at some value ΔT_c , there will be a separate, higher transition for each shaking velocity $\Delta T_{\text{shaking}, i}$. The data acquired then takes the form of a set of shaking critical transition temperatures $\{\Delta T_{\text{shaking}}\} > \Delta T_c$.

The change to this technique was accompanied by a corresponding qualitative improvement in the clarity and stability of the resulting data. An example of the results obtained using this technique may be seen in Figure 3.10.

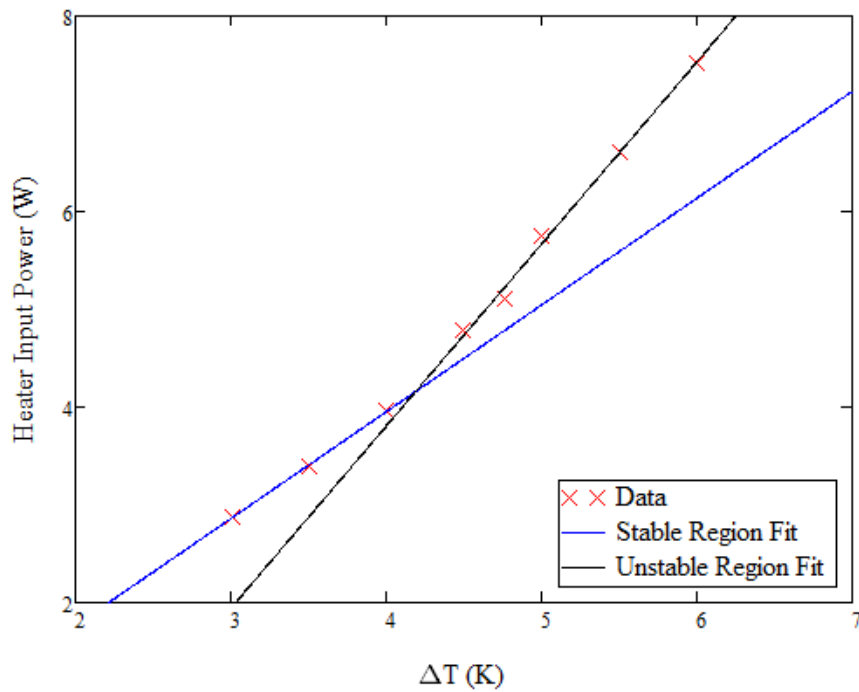


Figure 3.10: Example of a shaking experimental result obtained by varying the temperature difference ΔT while holding the shaker peak velocity $|\mathbf{v}|$ fixed. This shows data from the $\Gamma = 5$ cell at a fixed shaker peak velocity of $|\mathbf{v}| = 2.49$ m/s. X's denote the experimental data and lines fits to the suspected stable and unstable regions.

3.5.3 Shaking Flow Visualization Measurements

In very much the same way as flow visualization was leveraged to determine the convection flow pattern in the static case, flow visualization was employed to determine flow patterns in the shaking experiments. The procedure was comparable to those static measurements, in that the system was allowed to equilibrate at the desired ΔT and then the smoke was injected and the flow visualization within the cell was recorded to a video. The temperature difference ΔT was then increased, allowed to settle, and further visualization video was recorded. This continues in lock step with the thermal measurements already described until the final temperature

difference is reached. The result is, therefore, a video with several minutes of flow visualization for each ΔT point, again correlated through the imprinted time stamp on each frame.

3.6 Other Experimental Challenges

As with any experiment, there were unforeseen challenges encountered in this experiment. A few of the most common are discussed here.

The integrity of sensor and control wiring that leads from the shaker platform to the stationary (laboratory) frame was an ongoing concern, understandably, as these cables must undergo tens of thousands of shaking cycles every hour of experimental operation at the amplitude of ± 3 inches (7.62 cm). While those relatively simple electrical voltage connections (heater supply wiring, accelerometer, etc.) were generally problem-free, thermocouple extension cables are significantly more fragile under these oscillating conditions. Over time, the internal insulation between the individual conductors would wear away inside the outer jacket, shorting the two conductors and causing a thermocouple measurement at an undesired point within the extension cable. As these failures were hidden by the external jacket, they were difficult to find and generally required the replacement of the entire moving portion of the extension wire. The primary attempt to increase the mean time between failures consisted of building a cable “bridge” consisting of a length of laboratory tubing that sheathed the two thermocouple extension wires to control the maximum radius of the cable curvature. As this cable page was designed, there was caution taken to attempt to tune the cable length to be near a quarter-wavelength resonance at the shaker frequencies of interest. This would allow minimal displacement at the fixed (stationary end) and an anti-node near the moving shaker platform.

This improved the results, along with a change to stranded (as opposed to solid) thermocouple extension conductors with a PTFE (DuPont Teflon[®]) insulation. There was further improvement with a change to a coiled (telephone handset-type) thermocouple extension cable for the upper boundary extension cable, so long as the cable was maintained in a tensioned state throughout the range of shaker motion.

As the shaker platform guide rails and gearing require open lubrication, some care must be taken to adequately lubricate those moving parts prior to the commencement of experimental runs. Long runs, generally over four hours at high peak velocities, may also lead to the overheating of the shaker drive motor, despite having selected a motor with an open drip proof (ODP) enclosure, as opposed to the often less well ventilated totally enclosed fan cooled (TEFC) motor chassis. The only practicable solution found to this problem is to choose to perform more demanding experiments on days with a cooler ambient temperature. Also related to ambient conditions, days with high relative humidity pose the challenge of avoiding condensation of water vapor on the cooled laser diode array head while still cooling the diode sufficiently. As was described earlier, the dew point temperature inside the laboratory was tracked to avoid this condensation and a few days with exceedingly humid conditions (generally during the summer) were deemed to be inconsistent with laser operation. The prevailing ambient relative humidity was also noted to change the apparent optical qualities of the incense smoke, presumably due to influence on the quality of their combustion.

Despite the challenges enumerated here, among others, employing the techniques and procedures described in this chapter, the experiments have produced results for the transition from instability to stability (and vice versa) in static and shaking experiments through both thermal and flow visualization means. Those results are

presented and discussed in the following chapter.

Chapter 4

Experimental Results

In this chapter, the results of these experiments, both static and shaking, will be presented and discussed.

4.1 Static Thermal Results

The static measurement results, obtained through the procedures that were described in the previous chapter, will be presented here for both the $\Gamma = 5$ and $\Gamma = 3$ cell designs.

4.1.1 Static Results: $\Gamma = 5$ Experiment

The $\Gamma = 5$ experimental cell was disassembled and then reassembled between two periods of experimentation. This was required by the necessity to move the experimental setup to a different laboratory after the initial set of measurements was taken. Due to slight variation in the final heights l_z of the assembled cells, each had slightly different static critical Rayleigh numbers.

The first set of measurements, which were presented at the 169th Meeting of the Acoustical Society of America in May 2015 in Pittsburgh, PA [120], were

made on the pre-disassembly experimental cell, which had an assembled height of $l_z = 0.667$ inches (1.694 cm). These results were obtained by making a series of ten separate measurements and averaging the results of those multiple sweeps. These results for the static stability transition are shown in Table 4.1.

Table 4.1: Static onset testing results from the initial assembly of the $\Gamma = 5$ experimental cell.

Parameter	Rayleigh Number	Temperature
Theoretical Prediction: Thermal Insulating Sidewalls	$Ra_c = 1777$	$\Delta T_c = 3.893$ K
Experimental Result: Mean Critical Onset	$Ra_c = 1776 \pm 14.02$ %	$\Delta T_c = 3.891$ K ± 14.02 %
Deviation of Mean from Theory	-0.06 %	-0.06 %
Theoretical Prediction: Conducting Sidewalls	$Ra_c = 1790$	$\Delta T_c = 3.922$ K

Number of averaged runs = 10.

The reassembled $\Gamma = 5$ cell exhibited a slightly different cell height of $l_z = 0.701$ inches (1.781 cm). This is significantly closer to the desired $l_z = l_{\{x,y\}}/\Gamma = 3.5$ inches/5.0 = 0.7 inches, primarily due to much closer attention to precision when assembling the experiment in this second assembly. The final results for the determination of static onset for this reassembled $\Gamma = 5$ cell were made using the method of multiple sweeps presented in Section 3.4.3. The 445 data points for this static onset determination were shown in Figure 3.7. The results for the static critical Rayleigh number (and critical temperature difference) are shown in Table 4.2.

Table 4.2: Static onset testing results from the second assembly of the $\Gamma = 5$ experimental cell.

Parameter	Rayleigh Number	Temperature
Theoretical Prediction: Thermal Insulating Sidewalls	$Ra_c = 1777$	$\Delta T_c = 3.637$ K
Experimental Result: Critical Onset	$Ra_c = 1781$	$\Delta T_c = 3.645$ K
Deviation from Theory	0.22 %	0.22 %
Theoretical Prediction: Conducting Sidewalls	$Ra_c = 1790$	$\Delta T_c = 3.672$ K

4.1.2 Static Results: $\Gamma = 3$ Experiment

Determination of the static stability boundary for the $\Gamma = 3$ experimental cell was accomplished through the same method as that used for the pre-disassembly $\Gamma = 5$ cell, averaging 14 separate experimental runs, consisting of sweeps both up and down in ΔT . The results for these static stability measurements are shown in Table 4.3.

Table 4.3: Static onset testing results from the $\Gamma = 3$ experimental cell.

Parameter	Rayleigh Number	Temperature
Theoretical Prediction: Thermal Insulating Sidewalls	$Ra_c = 1895$	$\Delta T_c = 6.217$ K
Experimental Result: Mean Critical Onset	$Ra_c = 1909 \pm 12.60$ %	$\Delta T_c = 6.264$ K ± 12.60 %
Deviation from Theory	0.751 %	0.751 %
Theoretical Prediction: Conducting Sidewalls	$Ra_c = 1968$	$\Delta T_c = 6.457$ K

Number of averaged runs = 14.

4.1.3 Discussion of Static Thermal Measurements

As was discussed in the previous chapter, there are two separate methods that were used to determine these points of static onset. It is difficult to quantitatively determine which methodology is more accurate, as the runs in both interpretation methods show some spread in their transition points. To that point, in those two sets where the transition was determined by running a large number of single runs and averaging the transition temperatures for each, the percentage range provided as the uncertainty on the measurements is dominated by a few runs that are relative outliers, transitioning at ΔT values either much higher or much lower than the mean. The majority of runs are within a few percent of the mean transition value. The cause for these few transitions that stray from the mean are unknown, although they may be a consequence of a change in ambient conditions (an overnight storm passage, a large swing in room temperature, etc.) that changes those conditions from their initial values. This may be particularly true for those measurement sweeps that are of long duration, overnight or even multiple days in duration.

Additionally, it is noted that the mean transition points obtained using both methods deviate from the theory by less than 1% and, in two of the three cases, this deviation is noted to be above the predicted value. This may be due to the fact that the theoretical predictions assume a perfectly thermally insulating sidewall, that is one with a thermal conductivity $k = 0$. This, while theoretically tractable, is a physical impossibility, therefore, it is a lower bounding case. Note that in the theory produced by Carbo, these insulating and conducting designations pertain to the transverse direction of the sidewall (through the thickness) and presume a perfectly insulating or perfectly conducting (infinite thermal conductivity) thermal condition. Being a real material, the thermal conductivity of generic acrylic plastic

(from which the cell sidewalls are made) is 0.170–0.200 W/(m K), which, while relatively small, particularly when compared to a metal, is still non-zero. Therefore, this deviation from the ideal case assumed by the theory may be a cause of the small mismatches in the measured values for ΔT_c . For comparison, the theoretical predictions for the other bounding case, that of a perfectly thermally conducting sidewall condition, are also shown in the results tables. As one would expect, the experimental values generally fall between the two bounding cases and the range between the two is small.

4.1.4 Static Flow Visualization Measurements

As was described in the preceding chapter, the static visualization experiments were conducted in two manners. Figure 4.1 shows an example of a series of snapshots that are representative of the convective flow pattern changes that were observed when the temperature difference across the cell was rapidly increased from $\Delta T = 0$ to $\Delta T = 6.0$ K.

The first image (top left) shows the cell at $\Delta T = 0$. The smoke had been injected about three minutes prior, and the visual intensity gradient from top to bottom is due to the settling of particles out of suspension in the quiescent fluid. The second image is after the bottom of the cell has begun to be heated. There is a clear rising of the fluid from bottom to top, however, there is no indication yet of overturning of the flow. In the next image, indications of overturning flow begins and the system appears to show the early signs of Rayleigh-Bénard convection. As time progresses, the flow self-organizes into a row of multiple parallel roll cells. These cells then coalesce with their adjacent cells and expand to form parallel roll cells that are fewer in number, but larger in lateral extent.

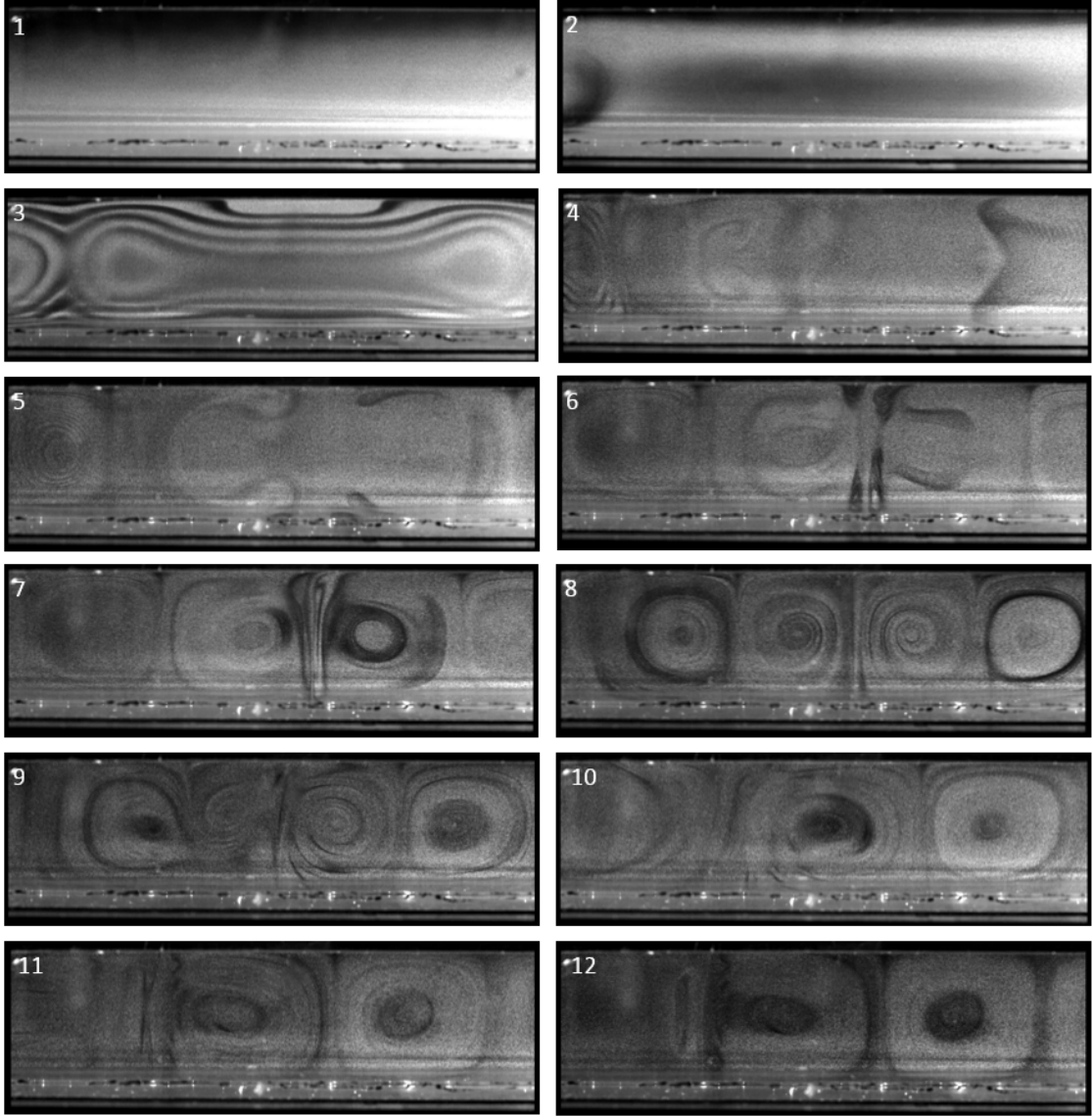


Figure 4.1: Time evolution of the static $\Gamma = 5$ cell with the temperature difference beginning at $\Delta T = 0$ and rapidly increasing to $\Delta T = 6.0$ K. The images progress in time left-to-right and top-to-bottom. All images have been brightened by 25 % in post processing for better reproduction on the page. These images do not show the full width of the experimental enclosure due to the focal length of camera lens employed; this was improved in later measurements.

As was described previously, further experiments were performed employing a procedure stepping through increasing values of ΔT . The system was permitted to equilibrate at a given temperature difference ΔT for some time period, after which

the smoke was inserted and the flow was visualized. The temperature difference ΔT was then raised to some higher value and the process was repeated. The results from one such experiment performed in the $\Gamma = 3$ cell are shown in Figure 4.2.

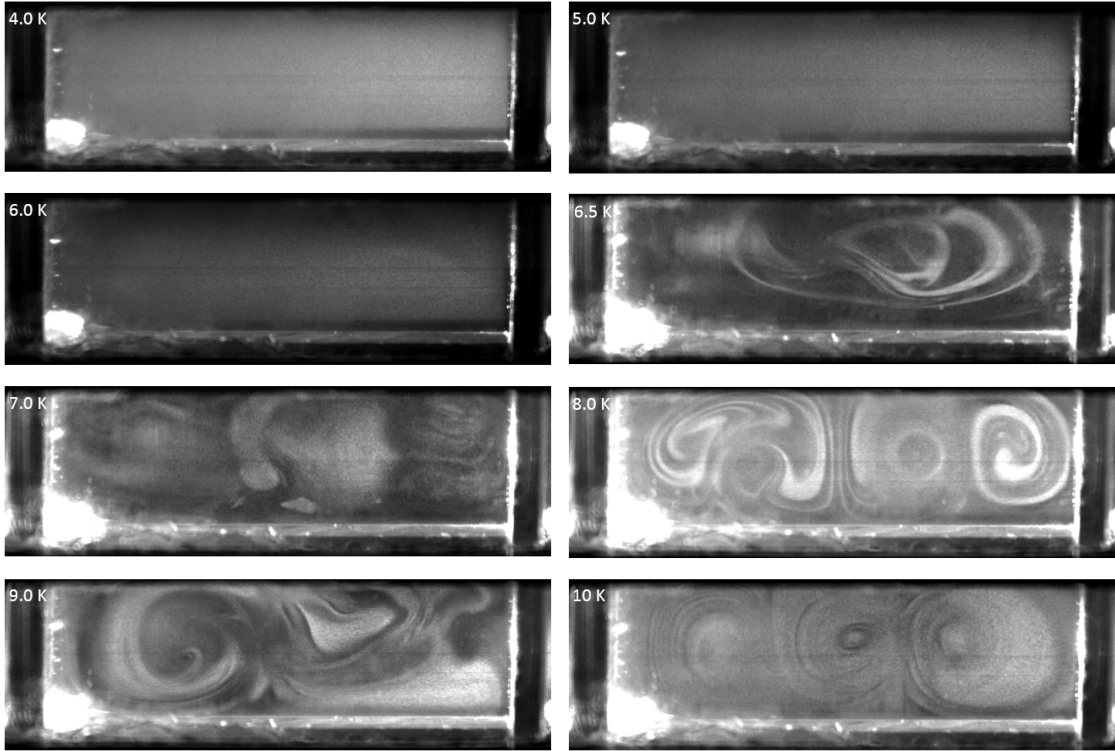


Figure 4.2: Time evolution of the static convection flow pattern of the $\Gamma = 3$ cell. The images progress left-to-right and top-to-bottom, and were captured, in order, at temperature differences of $\Delta T = 4.0, 5.0, 6.0, 6.5, 7.0, 8.0, 9.0,$ and 10.0 K. The thermally-determined static transition was found to be $\Delta T_c = 6.264$ K. All images have been brightened by 25 % in post processing for better reproduction on the page. The images have been cropped to the outer edge of the inner enclosure, simplifying the images by neglecting the quiescent insulation gap between the inner and outer enclosures of the $\Gamma = 3$ experiment.

Referring to the figure, it can be seen that in the first two images, the fluid appears to be quiescent, nicely correlating with their static sub- ΔT_c temperature differences of $\Delta T = 4.0$ and 5.0 K. In the third image, taken at $\Delta T = 6.0$ K, the fluid is mostly quiescent, however, there are the first indications of some fluid rising from the lower boundary, however, there are no indications of overturning flow. In

the fourth image, acquired at $\Delta T = 6.5$ K, just above the thermally-determined static ΔT_c of 6.264 K, there is now some instability noted, although no organized convection pattern. The fifth image indicates the onset of more vigorous convective motion, here at $\Delta T = 7.0$ K, as is indicated by the plume emission that may be seen emanating from the vicinity of the upper boundary near the center of the fluid enclosure. The sixth image, corresponding to a temperature difference of $\Delta T = 8.0$ K, now shows the first hints of self-organization into a multiple parallel roll cell configuration. However, this pattern shows neither clear delineations between the cells, nor is it a particularly long-lasting or stable pattern. The remaining two images, representing temperature differences of $\Delta T = 9.0$ and 10.0 K, indicate further progressions towards a three-across parallel roll cell configuration. However, at $\Delta T = 10.0$ K = $1.6\Delta T_c$, there are still no clearly defined and fully discrete cell boundaries. These may develop at higher ΔT values or even longer observation times.

These static measurements were enabled by the realization that the duty cycle of the laser was initially perturbing the flow conditions. That having been said, while these image series are rather clear, interpretation of the images was consistently difficult with respect to precisely determining the convective stability boundary. This is contributed to by a number of factors, the largest of which is the challenge of divining the onset of overturning fluid flow associated with the stability transition point from an image that shows the large-scale flow patterns with a limited resolution. The task for the investigator here is to perceive a nearly imperceptible change in the flow condition, which at times could be compared in relation to its challenge to “reading the,” proverbial, “tea leaves,” all within the particle settling time. The flow visualization measurements can be coarsely read with general reliability, insofar that, it can be noted that well below (in ΔT or Ra) the transition the fluid is clearly

quiescent, and well above the transition, the fluid shows characteristic hallmarks of convective instability, including overturning fluid flow, clear rotational flows, plume emissions from the boundaries, and the eventual transition to cellular and quasi-cellular patterns. The difficulty here is to ascertain at small ΔT values above and below the transition (say $\Delta T = \Delta T_c \pm 0.1$ K), the onset of that convective motion as a means to determine ΔT_c . The flow visualization does perform very well at ascertaining the convective flow pattern at varying points in the temperature difference continuum.

Additionally, by its very nature, the flow visualization images are imaging a thin plane through the experiment, leaving the rest of the enclosure uninterrogated by the visualization measurement. This stands in contrast to the thermal measurements, which provide little insight into the convective flow patterns, but provide a synoptic view into the global stability of the fluid, with significant sensitivity to determine the exact transition with relatively little uncertainty. While the initial hope for the visualization was that it would serve as the gold standard for the instability determination, showing a big bang-like global critical stability transition, with a clear defined onset of convective motion, that has not been found to be true in reality, with the visualization instead showing a very gradual transition to visibly perceptible convective motion as ΔT (and therefore Ra) is increased. Based on the totality of the static measurement results, there is a clear need in an experiment of this type for both the coupled measurement methodologies, thermal and flow visualization, to be employed in tandem, with the interpretation of the results of one informing that of the other.

Adding to that conclusion is the noted fact that the fluid flow exhibits a series of relatively disorganized (although clearly unstable) states as ΔT is increased above the critical ΔT_c , finally reaching the, classically anticipated, apparently time-

insensitive parallel roll cell behavior only at ΔT (and, by association, Ra) values well above that critical value (seen to be at or around $\Delta T \approx 1.5\Delta T_c$, although there were run-to-run variations observed). This realization, gleaned from the experience of executing these static measurements, that the best path forward into the shaking dynamic stabilization experiments was to leverage both measurement techniques at the ready in a coupled fashion, informed the plan of action for the final acquisition of those results. Additionally, these static measurements enabled the tackling of the shaking problem with some confidence having been gained in the validity of the measurement methodology and post-processing techniques, prior to entering the more demanding environment of fluid being shaken at peak velocities exceeding, at times, 3.0 m/s. Finally, these static measurements have revealed a rich range of static convective behavior, which do eventually resolve to an expected parallel roll cell behavior.

4.2 Shaking Dynamic Stabilization Results

The results for the dynamic stabilization experiments will be presented and discussed in the remainder of this chapter. These will be further separated into the results from the separate experimental cells and the measurement methodology used.

Please note that all results in the remainder of this chapter will be presented as dimensioned values to allow better evaluation of the direct experimental results. The same experimental data are presented in the form of dimensionless groups in Appendix B for direct comparison in the same form as presented in Carbo's dissertation [16].

4.2.1 $\Gamma = 5$ Shaking Thermal Measurements

There were a large number of shaking measurements performed on the $\Gamma = 5$ experimental cell, using a variety of techniques. These will be described in the order they were performed chronologically. Flow visualization results will be presented separately.

The earliest dynamic stabilization experiments performed were conducted on the pre-reconstruction $\Gamma = 5$ experimental cell using the fixed ΔT , varying $|\mathbf{v}|$ methodology. The earliest of these results, as with the static measurements, have been presented at a meeting of the Acoustical Society of America [120].

As was described in the previous chapter, this methodology had some significant shortcomings and was abandoned for an alternate means of acquiring the data. For the $\Gamma = 5$ cell, these measurements were taken at two separate ΔT values: 4.32 and 4.50 K. These were chosen to correspond to points already computed by Carbo [16]. The raw results, along with averages of them, are presented in Table 4.4. These results are also represented graphically in Figure 4.3.

Thus, while the individual runs range up to 7 % from the theoretical stabilization velocity value, the averages of the results of those experiments are within 4 % of the theoretical prediction. The limitations of this measurement technique were described in the preceding chapter.

Further measurements were made on the post-reconstruction $\Gamma = 5$ experimental cell using the fixed $|\mathbf{v}|$, varying ΔT technique. These results are presented in Table 4.5 and graphically in Figure 4.4.

Analyzing these results, it appears that the data varies at points widely from the theoretical predictions. That having been said, however, the theoretical results were not computed by Carbo with great granularity in this region, requiring

Table 4.4: Shaking onset testing results from the pre-disassembly $\Gamma = 5$ experimental cell. These results were acquired by fixing ΔT and varying $|\mathbf{v}|$. Note that the “deviation from theory” presented here is computed as $(|\mathbf{v}_{\text{theory}}| - |\mathbf{v}_{\text{experiment}}|) / |\mathbf{v}_{\text{theory}}|$.

Setpoint ΔT (K)	Transition		Deviation from Theory (%)
	Theory (m/s)	Experiment (m/s)	
4.32	2.631	2.511	-4.54
		2.720	3.40
		2.586	-1.69
		2.562	-2.62
		2.664	1.27
		2.454	-6.71
		Mean: 2.583	-1.82
4.50	2.838	2.876	1.34
		2.982	5.07
		Mean: 2.929	3.21

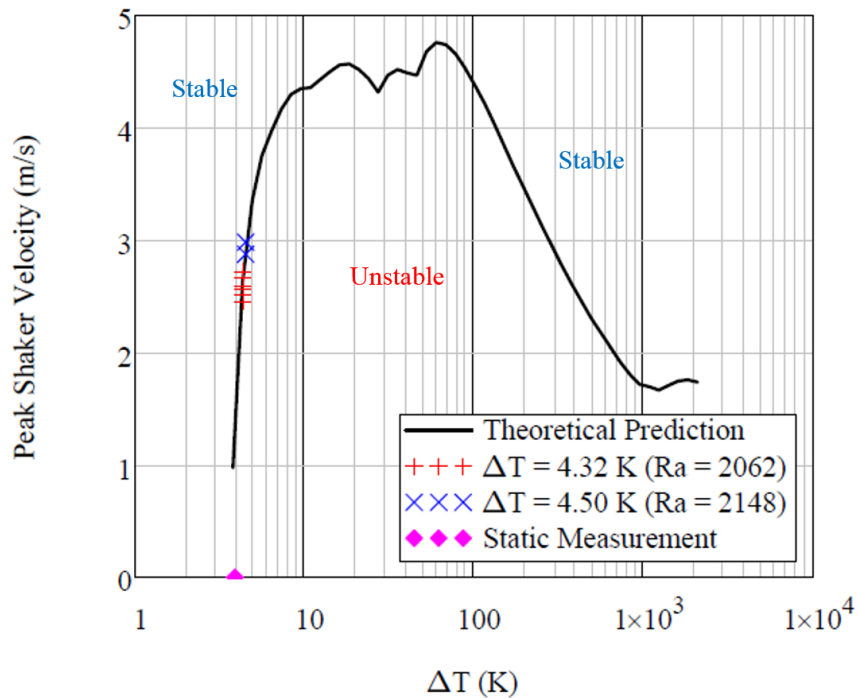


Figure 4.3: Plot of the shaking dynamic stabilization results obtained on the pre-disassembly $\Gamma = 5$ experimental cell. This data was acquired using the fixed ΔT , variable $|\mathbf{v}|$ method and presents graphically the same data as Table 4.4.

Table 4.5: Shaking onset testing results from the reassembled $\Gamma = 5$ experimental cell. These results were acquired by varying ΔT and fixing $|\mathbf{v}|$. Note that the “deviation from theory” presented here is computed as $(\Delta T_{\text{theory}} - \Delta T_{\text{experiment}}) / \Delta T_{\text{theory}}$. The average standard deviation in temperature in these measurements is $\sigma_{\Delta T} = 18.3$ mK and in velocity is $\sigma_{|\mathbf{v}|} = 6.19 \times 10^{-3}$ m/s.

Shaker Velocity (m/s)	Transition		Deviation from Theory (%)
	Theory (K)	Experiment (K)	
2.300	3.586	3.750	4.57
2.347	3.598	3.747	4.14
2.442	3.625	3.988	10.0
2.490	3.641	4.191	15.1
2.533	3.655	3.956	8.24
2.538	3.657	3.999	9.35
2.587	3.675	5.006	36.2
2.628	3.691	4.890	32.5
2.681	3.714	3.708	-0.16
2.724	3.733	5.319	42.5
2.778	3.759	4.998	33.0

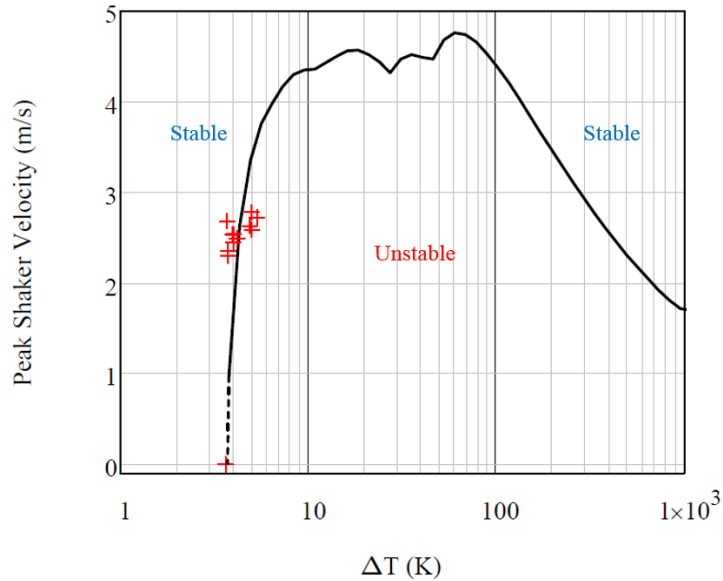


Figure 4.4: Plot of the shaking dynamic stabilization results obtained on the reassembled $\Gamma = 5$ experimental cell. This data was acquired using the variable ΔT , fixed $|\mathbf{v}|$ method and presents graphically the same data as Table 4.5.

the interpolation between points. It is also possible that the deviation from the theoretically predicted results may be due to the necessary deviations from the idealized conditions that were modeled. Additionally, there may also be some change in ambient atmospheric conditions that are not tracked that may be changing the fluid properties day-to-day between experimental runs. There is good confidence in the quality of these measurements, however, as the transitions in the thermal data between flow regimes are seen to be much more distinct in these experiments in relation to those found by fixing the ΔT value and varying the shaker parameters.

4.2.2 $\Gamma = 5$ Shaking Flow Visualization Measurements

Due to the timing of the allocation of funds to purchase the diode laser light sheet system, flow visualization experiments were only carried out on the second assembly of the $\Gamma = 5$ cell. Therefore, all flow visualization examples were taken from that second cell.

As was described in the prior chapter, there were significant efforts made to ascertain what laser illumination conditions might have been associated with the spurious onset of rotational flow along the transparent wall of the experimental enclosure. This was motivated both by noting that these rotations appeared during static measurements and that anomalous behavior also occurred during early shaking measurements. An example image of this anomalous behavior is shown in Figure 4.5.

As may be seen in this image, this unexpected flow takes the form of a “plume” that emanates from the wall along which the laser enters the enclosure, generally seen to nucleate from the lower corner. This plume has a critical phenomenon-like behavior in that it does not appear until some sufficiently large peak shaker velocity

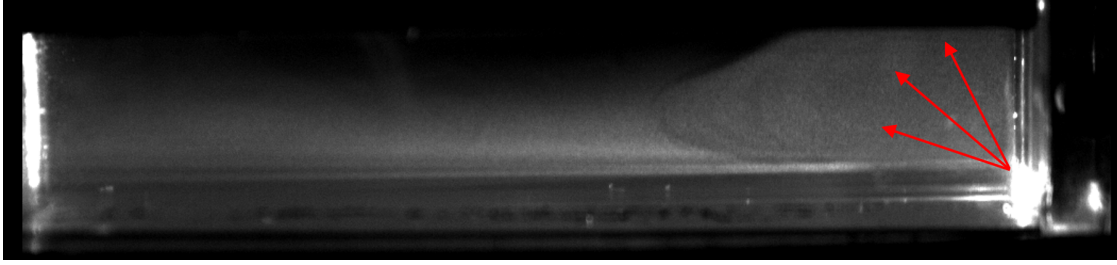


Figure 4.5: Flow visualization image from the $\Gamma = 5$ cell exhibiting the anomalous and asymmetrical plume behavior observed in an otherwise stable and quiescent shaken fluid. The red arrows were added to illustrate the direction of plume flow.

$|\mathbf{v}|$ has been reached. This behavior was observed both in the usual dynamic stabilization experiments (with a temperature gradient imposed) and runs in which there was no heating applied (intended to specifically investigate this problem). This plume appears to depend on this shaker velocity, with a strong, clearly delineated onset as shaker parameters are changed.

The fine structure within this flow from the wall is noted to be temporally varying and characterized as being composed of swirling rotating eddies; that is, to say, it appears to be turbulent in nature. It has been suggested that this behavior looks very much like a classical boundary layer separation, however, it is unexpected that there would be a sufficiently large shear gradient in this flow as the fluid motion should be, in theory, near to an ideal piston motion with the sidewalls moving along with the gas.

Computing the Reynolds number (Re), employing the thermoacoustic viscous penetration depth as the characteristic length scale, we find that $Re_{\delta_v} \approx 167$. This is significantly lower than one would expect to associate with turbulent onset [121]. There was also a suggestion that this behavior might be an acoustic streaming effect, however, this seems unlikely since the peak acoustic Mach number in this case is very small, $M \approx 0.01$. Therefore, it is logical to ask whether the system is

being perturbed by some change in the wall condition.

By necessity, the visualization of the flow requires two perpendicular walls to be optically transparent. This makes the full insulation of the cell significantly more complicated and opens the possibility of some thermal effect coming into play. These may be twofold: the reduced insulation may lead to temperature non-uniformities along the cell wall and/or there may be flows induced by localized heating due to the laser impinging upon the smoke particles or the walls of the cell enclosure itself. These are both coupled (in an indirect manner) to the peak shaker velocity. The higher that velocity, the more forced convective cooling would be anticipated along the outer wall of the experimental container, perhaps leading to convective motion driven by the temperature gradient from the sidewall. There is some precedent for this; in the side-heated experiment of Forbes [36], there were certain vibratory conditions under which he observed the development of turbulent boundary layers along all or some portion of their heated and cooled sidewalls. Additionally, the higher the peak shaker velocity, there may be increased potentiality for the development of a flow velocity mismatch and shearing of the flow.

The second possible cause mentioned was localized heating due to the laser. This may be associated with increased peak shaker velocities, as well, due to the design of the mechanical shaker employed in these experiments. As the increase in peak velocity (and acceleration) is controlled only through the frequency (as the displacement is fixed), an increase in velocity is also accompanied by an increase in shaking frequency. As the cell is illuminated and imaged once per shaking cycle, an increase in shaker frequency also results in an increase in repetition rate. This may increase the localized heating due to the higher number of laser pulses per second.

Experiments were performed with thermoacouples affixed to the sidewalls of the

experiment, however, the data from these was inconclusive and the thermocouple wires quickly failed due to the challenges associated with their mounting. It is likely that the two phenomena (or some other thermally associated cause not postulated) will not be disentangled through experimental means, thus both potential problems were addressed simultaneously.

Investigations of the potential laser heating perturbations were involved and described in detail in the previous chapter. These results from the static experiment led to the minimization of laser power and illumination duration. The enclosure was also better insulated, with the illuminated side insulated with the exception of a “slot” cut out of the foam to admit the laser light sheet. Both of these interventions appeared to reduce the onset of this anomalous flow. However, it was not until the $\Gamma = 3$ cell was introduced, with its superior sidewall insulation, that this behavior was completely eliminated.

That having been said, there was still ambiguity remaining in the interpretation of the flow visualization results that were obtained. As in the static measurements, there was distinctly quiescent fluid noted well below stabilization and organized cellular flow well above. The region about the transition is indistinct, however, as it largely was in the static measurements. As may be seen in Figure 4.6, the fluid is mostly quiescent at a ΔT well below the transition and shows classical, cellular convection patterns at a ΔT well above the transition. The realm between those extremes, however, is indistinct and it is difficult to precisely determine the point of transition from the optical measurements alone without the thermal measurements as a reference.

Another example of this path in a shaking experiment through transition is shown in Figure 4.7. As may be seen in this run, the initial image is seen to be quiescent. The second image, about 0.75 K below the thermally measured transition,

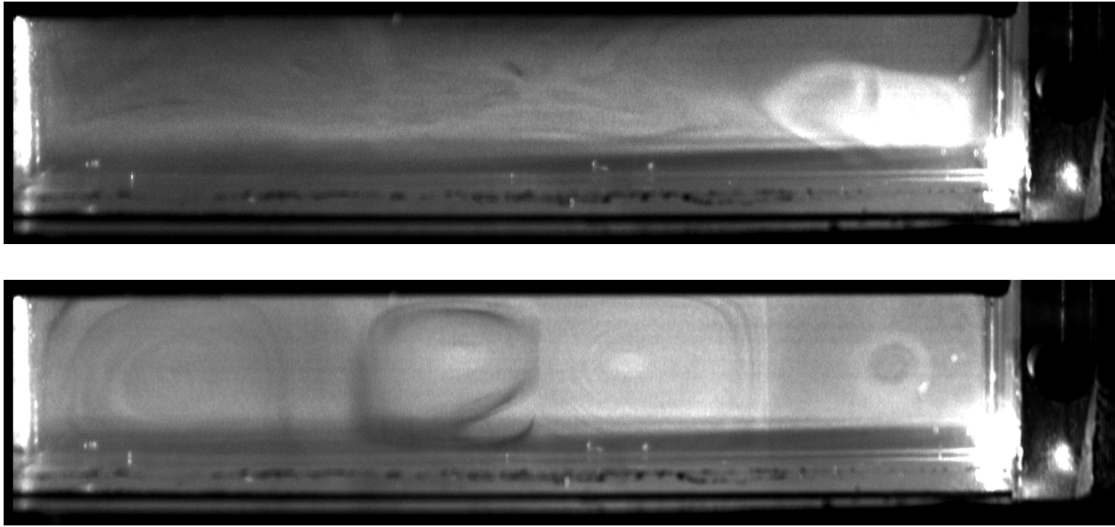


Figure 4.6: Flow visualization images from the reassembled $\Gamma = 5$ cell showing the flow evolution from below to above transition. These images represent (top-to-bottom) $\Delta T = 2.75$ and 5.5 K. These images were taken at $|\mathbf{v}| = 2.587$ m/s. The theoretical transition is $\Delta T = 3.675$ K and the thermally measured transition is found to be $\Delta T = 5.006$ K. Images have been brightened in post processing for better reproduction on the page.

there are the first signs of non-quiescent fluid, however, there is no overturning noted to the eye. The third image, 0.25 K above the measured transition, shows more active motion and the first indications of what appear to be overturning flow, although it is hard to make that determination by eye. The final two images, well above both the measured and anticipated transition, show various configurations of parallel roll-cells, although the cells do not appear to be as distinctly formed across the entire cell. As was seen previously, there is a notable transition from stable fluid to unstable convection, however, the exact point of that transition, based only on the flow visualization, is unclear and, for lack of a better word, “fuzzy.”

A third example of an experimental run is shown in Figure 4.8. This set of images also follows a similar progression to that of the previous experiments already presented. As was noted in all of these experiments, the transition from quiescent to non-quiescent fluid appears to be present, although the exact point is impossible

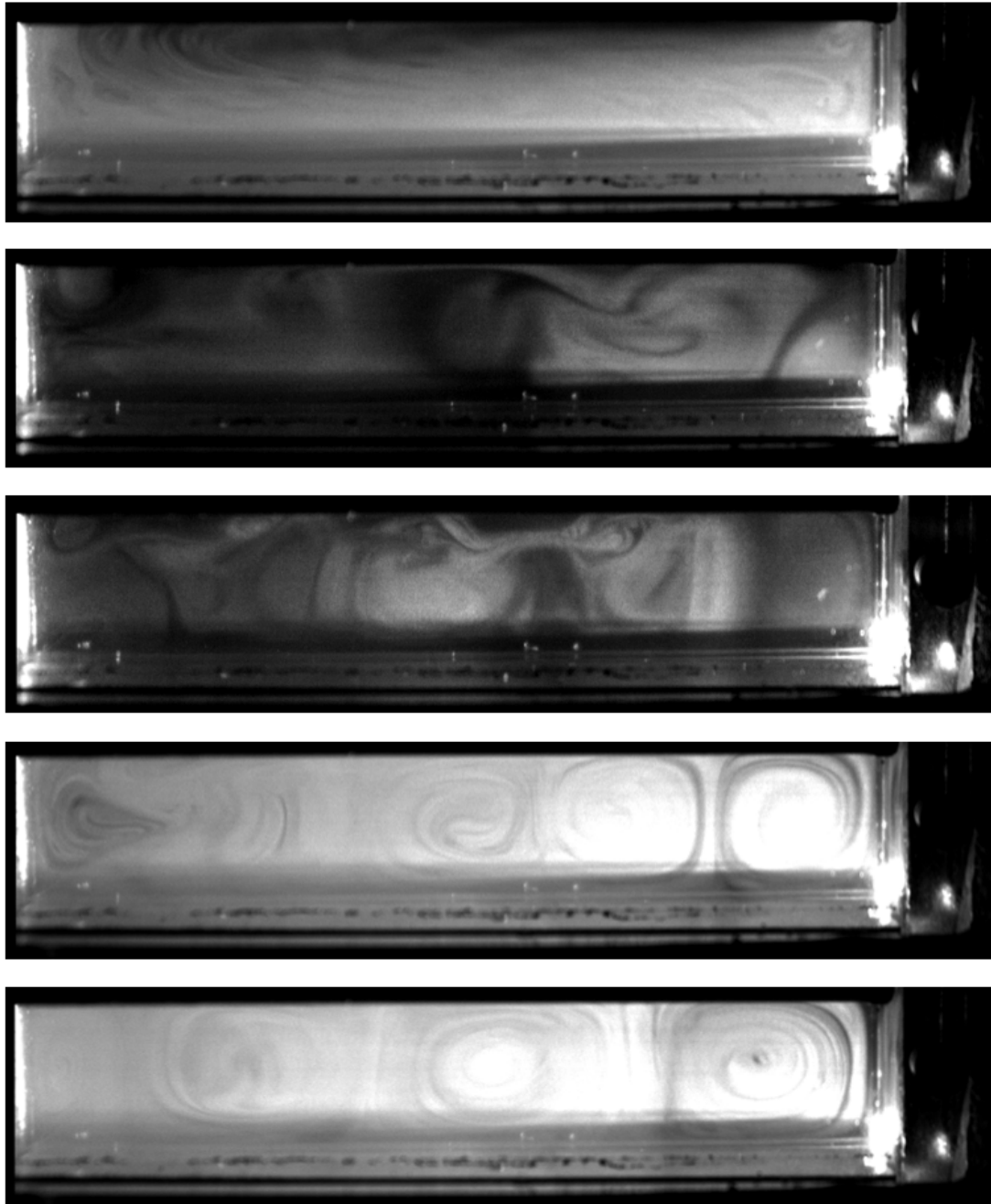


Figure 4.7: Flow visualization images from the reassembled $\Gamma = 5$ cell showing the flow evolution from below to above transition. These images represent (top-to-bottom) $\Delta T = 2.75, 3.25, 4.0, 6.0,$ and 7.5 K. These images were taken at $|\mathbf{v}| = 2.300$ m/s. The theoretical transition is $\Delta T = 3.586$ K and the thermally measured transition is found to be $\Delta T = 3.750$ K. Images have been brightened in post processing for better reproduction on the page.

to divine from the flow visualization measurements alone.

Another characteristic that was also noted is that, in a few instances, there were interesting perturbations produced when the experiment was shaken while the fluid was convectively unstable. An example of these are shown in Figure 4.9. As can be seen, these appear to include horizontally emanating wavefront-like behavior and a jet-like horizontal plume that spins off vortices from its body. These were unexpected, although the theoretical predictions upon which this work is based provides no predictions on the flow behavior in these regimes. It is additionally worth noting that while, in these images, the experiment is being shaken at $|\mathbf{v}| = 1.77$ m/s, which is not a trivial shaking velocity, although significantly below predicted dynamic stabilization boundary for this configuration.

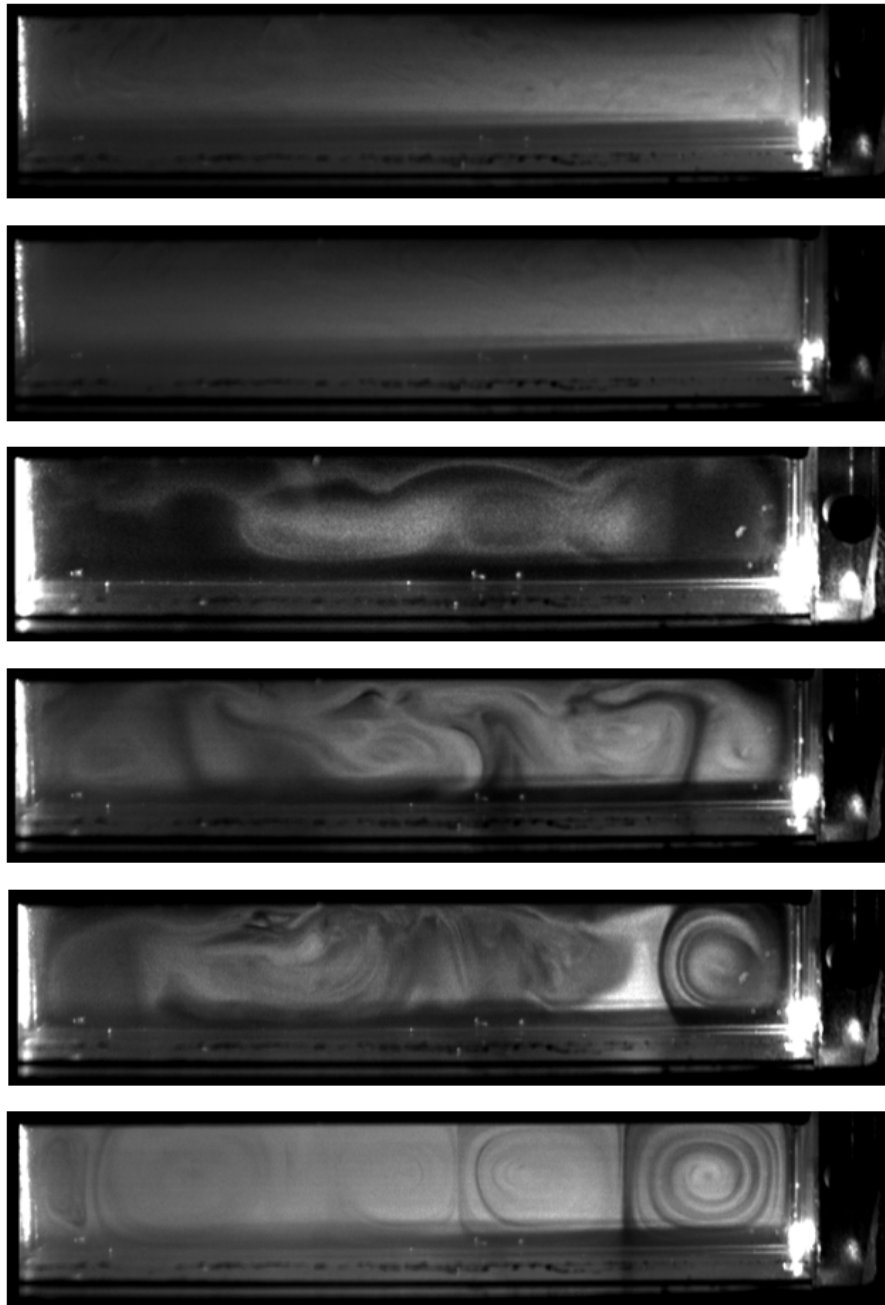


Figure 4.8: Flow visualization images from the reassembled $\Gamma = 5$ cell showing the flow evolution from below to above transition. These images represent (top-to-bottom) $\Delta T = 2.75, 3.25, 3.5, 3.75, 4.0,$ and 6.0 K. These images were taken at $|\mathbf{v}| = 2.347$ m/s. The theoretical transition is $\Delta T = 3.598$ K and the thermally measured transition is found to be $\Delta T = 3.747$ K. Images have been brightened in post processing for better reproduction on the page.

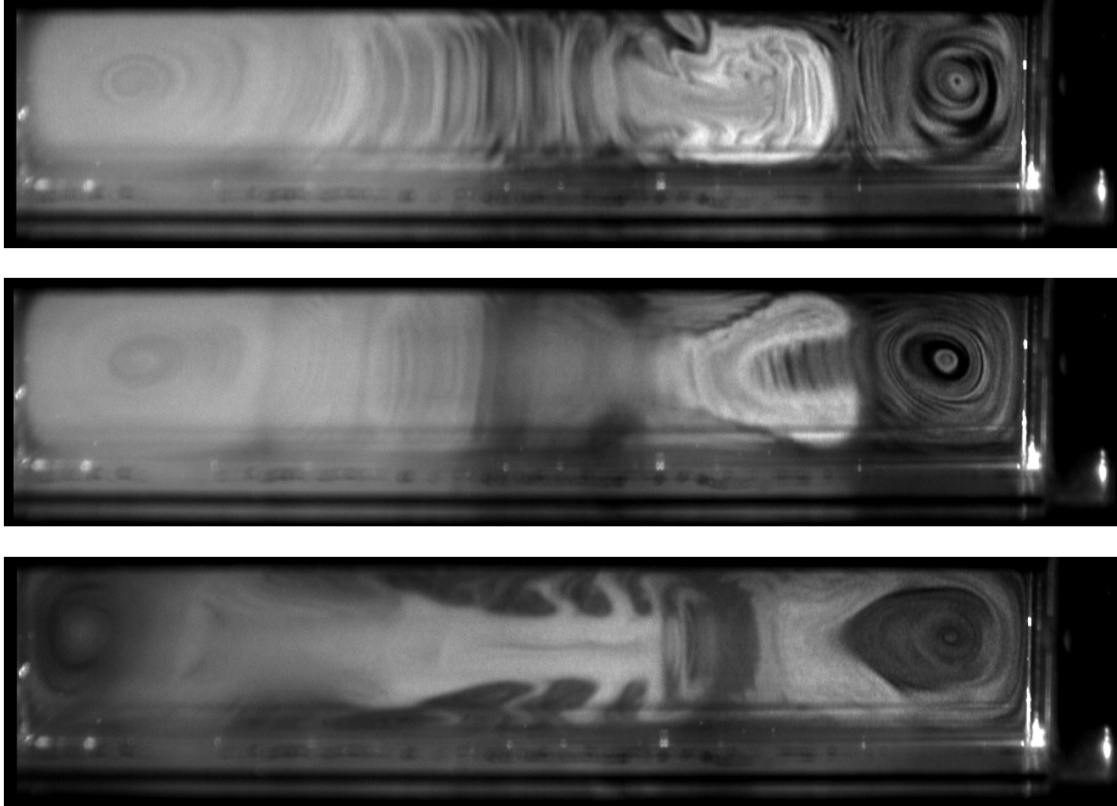


Figure 4.9: Flow visualization images from the reassembled $\Gamma = 5$ cell showing examples of vibration-induced perturbations on convective motion. These images were obtained over the course of about 2.5 minutes at $\Delta T = 6.0$ K and $|\mathbf{v}| = 1.77$ m/s. Images have been brightened in post processing for better reproduction on the page.

4.2.3 $\Gamma = 3$ Shaking Thermal Measurements

As was previously described, the $\Gamma = 3$ experimental apparatus was developed to remedy learned shortcomings associated with the $\Gamma = 5$ cell. To recall, the dimensions of the $\Gamma = 3$ experimental enclosure are $l_x = l_y = 1.75$ inches (4.45 cm) and $l_z = 0.583$ inches (1.481 cm). It would appear that the experimental results obtained from this cell would bear out that the improvements attempted were helpful. The results for this $\Gamma = 3$ cell are presented in tabular form in Table 4.6 and in graphical form in Figure 4.10.

Table 4.6: Shaking onset testing results from the $\Gamma = 3$ experimental cell. These results were acquired by varying ΔT and fixing $|\mathbf{v}|$. Note that the “deviation from theory” presented here is computed as $(\Delta T_{\text{theory}} - \Delta T_{\text{experiment}}) / \Delta T_{\text{theory}}$. The average standard deviation in temperature in these measurements is $\sigma_{\Delta T} = 22.7$ mK and in velocity is $\sigma_{|\mathbf{v}|} = 4.42 \times 10^{-3}$ m/s.

Shaker Velocity (m/s)	Transition		Deviation from Theory (%)
	Theory (K)	Experiment (K)	
2.176	7.497	7.313	-2.52
2.396	8.043	8.313	3.36
2.444	8.200	7.892	-3.76
2.492	8.374	8.025	-4.17
2.586	8.766	8.501	-3.02
2.683	9.253	9.000	-2.73
2.778	9.823	9.589	-2.38

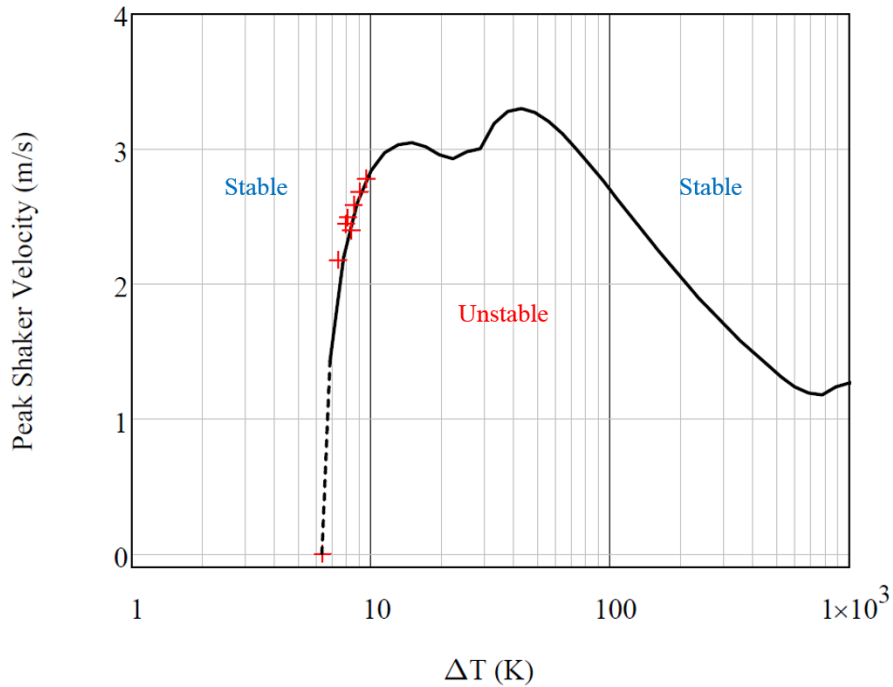


Figure 4.10: Plot of the shaking dynamic stabilization results obtained on the $\Gamma = 3$ experimental cell. This data was acquired using the variable ΔT , fixed $|\mathbf{v}|$ method and presents graphically the same data as Table 4.6.

Analyzing these transition results, it can be seen that the resulting measurements follow the theory much more closely than those obtained from the $\Gamma = 5$ cell. The largest deviation from theory is 4.17 % and the mean deviation across all the runs is -2.17 %. It is also notable that all runs, save one, deviate from the theory in that the experimentally measured transition falls below (in ΔT) the theoretical prediction, although this deviation is small. As in the theoretical predictions for the $\Gamma = 5$ cell, there is not great granularity in the theoretical predictions, with the data at those small ΔT values relatively widely spaced. This may lead to a change in the governing convection mode (that is, since Carbo’s predictions are a global stability prediction, the mode which stabilizes at the highest value of $|\mathbf{v}|$) that is not captured in the existing computations. This single experimental value that falls above the prediction line may, just as easily, be due to random experimental variation, a change in the equilibrium fluid properties during that particular set of measurements, or some small error introduced by the experimentalist.

The fact that these measurements follow the theoretical predictions so closely is likely due to the improved design and thermal insulation of this experimental apparatus. This design improvement, due to the double-wall configuration of the experimental enclosure, isolation of the thermal hot plate from the shaker carriage and from the cold plate, and the further minimization of exposed area, was in addition to the improvements made in experimental technique in these experiments.

Another notable feature of this data, as may be seen in Figure 4.10, is that the measured data appears to follow the “curve” of the theoretical prediction, showing that the gradual flattening of the stability boundary at higher temperatures appears to be a demonstrated feature of the overall stability boundary plot. This is of interest, as there should be a range of ΔT values that should be able to be stabilized with a given peak shaking velocity. This finding, demonstrated at least (in part) in

this one case, may permit the design of thermoacoustic devices that are dynamically stabilized against convection for a range of temperature differences. For the design of real-world devices, this may be advantageous, as it may indicate the bounds of proportional control that dictate the minimum $|\mathbf{v}|$ that must be maintained to suppress convection during warm-up or cool-down cycles (varying the ΔT in the space of convective interest).

4.2.4 $\Gamma = 3$ Shaking Flow Visualization Measurements

As the flow visualization experiments in the $\Gamma = 5$ cell were less than fruitful in their ability to divine the stability transition, fewer of these experiments were performed with a coupled visualization component, as this also permitted the experimental cell to be better insulated and eliminates the possibility for laser-induced heating of the fluid and the associated flow perturbations. It was also noted that the double-wall nature of the $\Gamma = 3$ enclosure led to some deterioration of the quality of the flow visualization. This was likely due to several factors: The double-walled nature of the enclosure tended to diffuse the light sheet, leading the illumination to spread out and become less planar. Additionally, the double walls produced an optical intensity loss that was observable with the naked eye. Finally, the optical quality of the walls themselves was reduced as they used a relatively thin-walled extruded acrylic material, as opposed to the cast material used in the previous experiment. The usage of this square tubing improved the structural integrity, gas-tightness, and ease of fabrication of the enclosure. However, extruded acrylics generally have poorer optical uniformity qualities, as did this tubing, which displayed faint, but noticeable, extrusion die lines.

The flow visualization results were very much in keeping with those found from

the previous cell, with quiescent fluid at ΔT values well below the expected and measured transitions and clearly convectively unstable fluid at values of ΔT well above the transition. The region about the transition were indistinct and it was found to be impossible to determine the exact transition through visualization means alone. An example visualization sequence may be seen in Figure 4.11.

As can be seen in the figure, the first image is mostly quiescent, as would be expected from a ΔT value that is 3.9 K below the measured transition. The second image, at a ΔT two degrees higher, shows the first hints of a swirling-type flow. In the third image, taken at $\Delta T = 7.0$ K, there is now notable time-dependent swirling behavior, although no organized convection cells noted. In the penultimate image, representing $\Delta T = 8.0$ K, lying between the measured and theoretically predicted transition points, the first indications of a cellular convection type rotation is found to be forming along the right-hand-side of the cell. In the final image, well above transition at $\Delta T = 14.0$ K, a partially distinct set of rotating roll cells develop, although this is not shown to be a stable configuration and devolves into perturbed convectively unstable motion after a brief time period.

Again, as was seen in the $\Gamma = 5$ experiments, there is a noted transition between convectively stable and unstable fluid flow between low and high ΔT values, although, the region about transition is indistinct and it was found to be impossible to precisely determine the transition point by optical means.

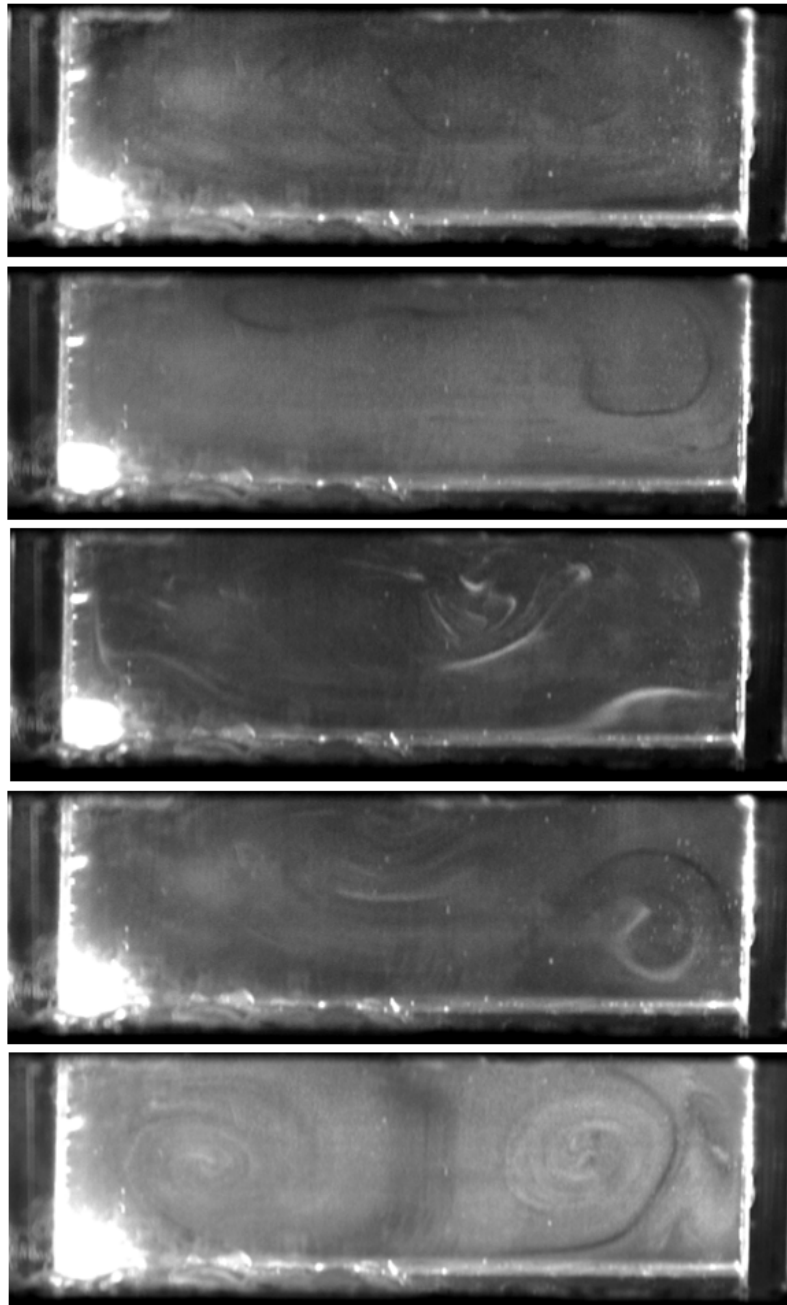


Figure 4.11: Flow visualization images from the $\Gamma = 3$ cell showing the flow evolution from below to above transition. These images represent (top-to-bottom) $\Delta T = 4.0, 6.0, 7.0, 8.0,$ and 14.0 K. These images were taken at $|\mathbf{v}| = 2.444$ m/s. The theoretical transition is $\Delta T = 8.200$ K and the thermally measured transition is found to be $\Delta T = 7.892$ K. Images have been brightened in post processing for better reproduction on the page.

4.3 Conclusions

In this chapter, results for the determination of the transition to convective instability were presented for containers of two aspect ratios $\Gamma = 5$ and $\Gamma = 3$. These were performed, initially, with the convection cell stationary, in concert with established theory, and then followed by the desired experiments in which the cell was vibrated at a range of peak shaking velocities. It was attempted to determine that dynamic stability boundary through both thermal measurements and flow visualization techniques. As the static measurements, a necessary precursor to the experiments performed with vibration, were discussed in detail in the first section of this chapter, they will not be repeated here, beyond to say that they provided many of the necessary checks, preliminary confidence building experiments, and technique validations that were required to make the advance to shaken experiments.

Those shaking thermal results for the first incarnation of the $\Gamma = 5$ cell were found to have a run-to-run spread of less than about 10 % and when the individual experiments were averaged for each value of ΔT , those averages fell less than 4 % from the theoretical prediction. That experimental technique was found to be difficult to implement and left the experiment open to imprecision, though, and was exchanged for a more cautious approach after the experimental cell was disassembled and reassembled. Those results were found to exhibit a clearer thermal transition, which allowed that point of apparent convection onset to be determined with some confidence at higher precision. The actual results for transition differed somewhat from the theoretical predictions, in a few runs by as much as over 40 % in velocity.

The thermal results for the $\Gamma = 3$ experiment deviated from theory much less, conforming to the theoretical predictions within 4.2 %. This was a good validation

of the second iteration of these experimental apparatus, as the cells were designed for improved thermal performance, based on the lessons learned from the first cell. These experimental results also followed the contours of the theoretical predictions, not only matching the steep rise away from the static onset result, but following the curvature as the experiment moved to higher values of ΔT .

The flow visualization results were found to be less transparent to interpretation regarding a specific transition point. While they provided a window into the flow patterns and convective planform of the experiments, they were found to be unable to determine the point of transition with any precision approaching that of the thermal determination. What they did show, however, was that there is a transition from convective stability to instability, as indicated by a change from near-quiescent fluid at low values of ΔT to fully or near-fully developed cellular convection at high ΔT . It is that region of transition that was found to be indistinct, particularly for the shaken experiments.

Chapter 5

Conclusions and Future Work

This work set out to determine the conditions under which a container of convectively unstable fluid could be stabilized by vibration parallel to gravity and to observe that phenomenon through experimental means, by verifying the theoretical predictions of Carbo. This investigation was motivated by accounts of performance losses observed in thermoacoustic Stirling-type refrigeration systems. Additionally, the performance losses associated with suspected convection in pulse tube cryocoolers have been documented relatively widely in studies, both in commercial and operational models [44, 122] and purpose-designed experimental analogs [42, 123, 124].

These pulse tube experiments are difficult to compare to theory; those performed in commercial devices were intended to be primarily empirical, driven by a desire to rotate the cryocooler with respect to gravity in order to improve the flexibility of their implementation. The laboratory analogs, in their efforts to mimic the reality of a pulse tube, were designed with boundary conditions that are difficult to model theoretically. By necessity, there is a standing wave present in the container, bounded by heat exchangers, which present non-ideal vertical boundary conditions in both allowing flow through the boundaries and the possibility of thermal gradients within the exchangers themselves. Additionally, pulse tubes tend

to operate at values of ΔT that are, by design, large. Therefore, their violation of the Boussinesq approximation and their potential lack of suitability for linear stability analysis, make the problem quickly computationally intractable. There have also been experiments performed in systems that approximate the infinite layer problem [37–41], an extrapolation that contains very interesting physics, however, is of lesser utility for the design of functional machines.

This experiment was designed, from the ground up, to mimic idealized experimental conditions for which Carbo had developed a stability theory. There are impenetrable boundaries on all six sides of the container. The top and bottom surfaces of the experimental cell were designed to maintain ideally isothermal conditions, which was verified through both finite element simulations and thermal imaging visualizations. The sidewalls were constructed of acrylic plastic and insulated where possible. The whole experiment was shaken at low frequencies and large displacements in a near-sinusoidal manner. This is believed to be the first experimental demonstration of this type represented in the literature. While the results of these experiments were presented in other fora, a broad overview of the experimental design, development, operation, and accomplishments will be summarized in the following section.

5.1 Conclusions

1. The experimental underpinnings for this experiment began with the work of Carbo [16, 29]. He made a range of theoretical predictions using a linear stability analysis approach to determine the bounding stability conditions for a range of experimental configurations. His work, and these experiments, were intended to investigate problems of interest to developers of thermoacoustic

devices.

2. Comparable experiments were sought in a detailed and, to the best knowledge of the author, as exhaustive a literature review as possible. No comparable experiments were found, further motivating this investigation.
3. Those nondimensionalized theoretical predictions were returned to dimensioned units for experimental design purposes. In that derivation, it was found that the peak shaking velocity $|\mathbf{v}|$ and the temperature difference across the cell ΔT were the relevant controllable parameters for the experiment. These could be computed for a broad range of container sizes and fluid properties, determining the parameters that could be realistically accessible in an experiment.
 - (a) An investigation of a broad range of container sizes and candidate experimental fluids was completed. This led the experiment to containers of heights l_z on the order of a few centimeters with gases (at atmospheric conditions) as the experimental medium. For ease and safety, ambient air was employed.
 - (b) A significant result of this parameter investigation was the realization that higher peak shaking velocities would be required than could be obtained from commercially available electrodynamic shakers. A mechanical shaker of an original type was designed, built, and tested that operated at a 15.2 cm peak-to-peak stroke to enable these experiments.
4. Methodologies to determine the transition from quiescent to thermal-buoyancy driven convecting fluid were investigated and implemented.
 - (a) These included the development of a system to both precisely control

the temperature difference ΔT across the experimental enclosure and to determine the stability transition through change in thermal transport. This is in keeping with a number of experiments in the historical body of literature on static (non-vibratory) Rayleigh-Bénard convection. Other techniques were investigated, including various direct heat-flux sensors.

- (b) There was also an investigation of a range of experimental flow visualization techniques, including refractive index-based methods such as shadowgraphy and schlieren, interferometric techniques, and particle tracking methodologies. The solution finally employed was to use side scattering from aerosols, seeded in the fluid, using a diode laser-based light sheet for illumination. Suitable aerosol sizes and sources were identified to track the flow.
- (c) The necessary measurement automation and data acquisition equipment and coding was developed. This included the implementation, simultaneously, of a temperature control loop, flow visualization acquisition, laser control, and the saving of that data in both numerical and video formats.

5. Experimental cells were designed and tested, representing two discrete aspect ratios Γ , for comparison with the theory of Carbo. These cells were designed with an eye towards minimizing moving mass and maximizing the thermal insulation of the sidewalls.

- (a) The cells were designed using both analytic and finite element computations to verify that they would perform to within the required specifications.
- (b) The $\Gamma = 5$ cell, being the first constructed, was tested using surface

temperature measurements (giving a point-by-point determination of temperature) and infrared thermal imaging tests (giving a synoptic determination of the temperature field).

- (c) The $\Gamma = 3$ apparatus, having been designed second, improved the performance of the previous experiment in terms of thermal insulation and simplicity.
6. Initial experiments were performed to determine the onset of static Rayleigh-Bénard convection in the stationary frame. This is a problem that has been investigated for over 100 years and, therefore, the anticipated results are well-known.
- (a) These experiments determined the onset of convection using thermal methods and compared those to well-vetted theoretical predictions.
 - (b) Flow visualization measurements were made and potential thermal interactions between the illumination source and fluid were investigated and mitigated.
7. Those static measurement approaches were then translated to the sinusoidally accelerating frame.
- (a) The experiments were performed in two ways: one keeping the temperature difference ΔT fixed and varying the peak shaker velocity $|\mathbf{v}|$, the other varying the temperature difference ΔT and fixing the peak shaker velocity $|\mathbf{v}|$.
 - (b) All thermal measurements fell within approximately 40 % of the theoretically predicted value, with the vast majority of results falling much closer

to the theoretical predictions, particularly later experiments, which all clustered within 5 % of the theoretical predictions.

- (c) Flow visualization results were of interest and displayed unexpected phenomena. However, it was found to be very difficult to precisely determine the transition from stability to instability from the images alone without the coupled thermal measurements. Far from the critical ΔT_c the visualization results behaved as expected.

Through this path, the first testing of the theoretical predictions of Carbo was performed and additionally, the first known demonstrations of suppression of Rayleigh-Bénard convection through vibration in rectangular containers were made.

5.2 Potential Experimental Improvements

As the old adage goes, “Hindsight is always 20/20,” and there is a reason the U.S. Army has established a unit called the “Center for Army Lessons Learned.” In this investigation there were a number of challenges encountered, some unforeseen, and some that were anticipated, however underestimated in magnitude of their importance.

The usage of a custom-built shaker, while making possible this experiment, was a large investment of time and effort, both initially and also in ongoing adjustment, repair, and maintenance. An electrohydraulic shaker would likely be an improvement in performance and reliability, however that was not a realistic option based on the financial resources available for this experiment. Additionally, even in the Rogers experiment [37], which used a hydraulic shaker system, there were significant engineering modifications required to adapt the shaker with pneumatic

bearings to reduce excessive lateral motion. A hydraulic shaker system would allow arbitrary shaking profiles (within limits, namely low frequency), which might also be of interest. Related to the problem of shaking, while great strides were made in ensuring the control and sensor cabling remained functional over many hours of testing, a better solution would have improved experimental reliability and productivity. Perhaps this may have taken the form of a linear oscillating slip ring-type device, some better-design for a cable pantograph, or perhaps wireless thermal sensors. Due to the inherent vibration, this is a situation where energy harvesting may be viable to power RF systems.

It was initially not fully appreciated quite how crucial having excellent thermal insulation was to obtaining high-quality experimental results, although, as the experiments progressed, the thermal decoupling to ambient was progressively improved. A modification that was initially considered was to employ a vacuum space as the insulation, although there were concerns about the additional moving mass this would add to the payload, which might need to be substantial to avoid crushing under ambient atmospheric pressure. Therefore, the addition of such a pressure vessel might require a more substantial shaking system. A solution, such as is used in an insulated window, of filling the gap between enclosures with an inert gas, such as xenon, might result in the unwanted onset of convection in the gap, muddying the results, unless great caution is taken, particularly if a wide range of ΔT values are desired.

This experiment could have also been enhanced by the implementation of different sensing techniques, such as a direct heat flux sensor or an in-situ temperature probe or hot wire anemometer, although each has their own drawbacks, which were discussed in greater detail in Chapter 2. An additional extension could also involve quantitative flow visualization measurements, such as laser Doppler anemometry or

particle image velocimetry, although the implementation in a moving frame would be a challenge not presented in other, less violent, applications.

5.3 Future Work and Extensions

There are many avenues through which this work could be continued and expanded; a few will be discussed in this section.

There is certainly value in extending the range of aspect ratios investigated towards more cubical shapes ($\Gamma = 2, 1$, etc.) and perhaps beyond into containers in which $l_z > l_{\{x,y\}}$ ($\Gamma = 0.75, 0.5$, and so forth). These are all computable using the Carbo theory, although as the aspect ratio Γ becomes smaller, the overall container must shrink as well in order to maintain the transition within achievable peak shaking velocities, due to the l_z^2 dependence of $|\mathbf{v}|$ for a given pair of Rayleigh number Ra and vibrational Rayleigh number Ra_{vib} . These further experiments would extend confidence in the computational methods of Carbo to a wider range of enclosure sizes and aspect ratios, testing the theory for use by the designers of a broader range of thermoacoustic devices. These extended aspect ratio tests may not require a trivial investment of time, however, as the best performance has been seen, thus far, in an experimental apparatus that is custom-tailored to each container size. This allows both the optimization of the fluid and container parameters for each aspect ratio and the avoidance of undesirable fluid leaks and thermal losses in the experimental enclosure. Additionally, some aspect ratios may expand beyond those cases investigated by Carbo in his dissertation, which would require returning to his computational routines to recalculate the stability boundaries for those specific Γ 's or a broader range of Ra .

Another extension that may be of interest is a turn to cylindrical geometries,

which is of particular concern to the pulse tube cryocooler community. Such an effort may be significant as a large element of the motivation for this work was interest from those who design and build pulse tubes. That having been said, pulse tubes, being cryocoolers, by their nature involve large temperature swings from ambient to liquid nitrogen temperatures (77 K) or lower. Therefore, their adherence to the Boussinesq approximation and the applicability of the linear stability analysis used by Carbo may be questionable. This type of experimental testing may extend or invalidate his theory.

There are, however, additional challenges introduced when performing flow visualization measurements in a cylindrical container due to that container's curved outer surface and the inherently larger degree of potential convective flow pattern degeneracy in circular geometries. Additionally, Carbo explored square cross-section containers because his theory was extended from two dimensions to three based on Cartesian geometries. Computations for cylindrical geometries do not yet exist.

This vein of experiments may further be extended to employ an acoustic drive as opposed to the current shaker approach. While this would further move the experiment away from the idealized case, it may serve as a useful bridge to application towards more realistic thermoacoustic devices.

Finally, the anomalous flows that were observed while the convectively unstable system was shaken at peak velocities $|\mathbf{v}|$ that were lower than the theoretically anticipated (and experimentally measured) dynamic stabilization would be an interesting area of further study. These flows are of the type shown in Figure 4.9. There are no studies known, to this author, in the literature that have vibrated a container of thermally convectively unstable fluid at peak shaking velocities $|\mathbf{v}|$ nearly this high, and therefore, those flow phenomena have not been reported previously. Additionally, several fluid dynamics researchers who have been shown

the corresponding video from the experiment performed here have been unable to posit a phenomenological explanation. The potential complexity of this problem may mean that it will remain theoretically intractable, however, a fuller experimental investigation may be of great interest. A shift to direct CFD modeling may also shed further light on these observations.

As the investment in experimental techniques, sensors, and infrastructure have been substantial to this point, other related experiments may now be possible without substantial modifications. Some of these may include the inversion of the container (hot over cold or $\Delta T < 0$), a statically stable configuration that may be destabilized by the imposition of vibration. Another may be an extension of the large displacement shaker into other systems of research interest, such as the Rayleigh-Taylor instability or shaken granular materials.

5.4 Closing Words

As the theoretical predictions of Carbo have now demonstrated validity, so far, and promise towards further applicability beyond that which has been tested in this work, his computational procedures are applicable to a circumscribed range of cases. This work, limited in scope as it has been, has borne out, in this author's opinion, that fact.

While this experiment has not been simple or, often, particularly elegant in its nature or execution, it has been as thorough, cautious, and circumspect as has been possible under the circumstances. It is hoped that from these nascent beginnings, further work may be launched and further investigations may be engendered. The author also sincerely hopes that this work may permit some scientist or engineer designing a thermoacoustic device to better consider the potentiality for convective

flows that may be robbing their device of its desired performance and perhaps provide a starting point for further investigations of this phenomenon.

Appendix A

Derivations

A.1 Derivation of the Peak Shaker Velocity from Dimensionless Groups

We begin with the definition of the vibrational Rayleigh Number:

$$Ra_{vib} = Pr \frac{Ra^2}{2 \frac{\omega^{*2}}{\epsilon^2}} \quad (\text{A.1})$$

And, we perform some algebraic manipulations to solve for Ra^2/Ra_{vib} :

$$\frac{Ra_{vib}}{Ra^2} = \frac{Pr}{2} \frac{\epsilon^2}{\omega^{*2}} \quad (\text{A.2})$$

$$\frac{Ra^2}{Ra_{vib}} = \frac{2}{Pr} \frac{\omega^{*2}}{\epsilon^2} \quad (\text{A.3})$$

Substituting dimensioned quantities for the non-dimensionalized frequency $\omega^* = \omega l_z^2 / \chi$ and $\epsilon = a/g$ results in:

$$\frac{Ra^2}{Ra_{vib}} = \frac{2}{Pr} \frac{\left(\frac{\omega l_z^2}{\chi}\right)^2}{\left(\frac{a}{g}\right)^2} \quad (\text{A.4})$$

We now presume sinusoidal motion, allowing the acceleration a to be characterized as $a = \omega^2 A$, where A is the amplitude of vibration:

$$\frac{Ra^2}{Ra_{vib}} = \frac{2}{Pr} \frac{\left(\frac{\omega l_z^2}{\chi}\right)^2}{\left(\frac{\omega^2 A}{g}\right)^2} \quad (\text{A.5})$$

We make some further algebraic manipulations in order to solve for $\omega^2 A^2$:

$$\frac{Ra^2}{Ra_{vib}} = \frac{2}{Pr} \frac{\left(\frac{\omega^2 l_z^4}{\chi^2}\right)}{\left(\frac{\omega^4 A^2}{g^2}\right)} \quad (\text{A.6})$$

$$= \frac{2}{Pr} \frac{g^2 l_z^4}{\chi^2 \omega^2 A^2} \quad (\text{A.7})$$

$$\frac{Ra_{vib}}{Ra^2} = \frac{Pr \chi^2 \omega^2 A^2}{2 g^2 l_z^4} \quad (\text{A.8})$$

$$\frac{2Ra_{vib}g^2l_z^4}{Ra^2Pr\chi^2} = \omega^2 A^2 \quad (\text{A.9})$$

And, we note that for a sinusoidal excitation, we have $v_{\text{peak}} = \omega A$, thus:

$$|\mathbf{v}| = \omega A = \sqrt{\frac{2Ra_{vib}g^2l_z^4}{Ra^2Pr\chi^2}} \quad (\text{A.10})$$

And, simplifying give us:

$$|\mathbf{v}| = \frac{\sqrt{2Ra_{vib}}}{Ra} \frac{gl_z^2}{\chi\sqrt{Pr}} \quad (\text{A.11})$$

$$= \frac{\sqrt{2Ra_{vib}}}{Ra} \frac{gl_z^2}{\chi \sqrt{\frac{\nu}{\chi}}} \quad (\text{A.12})$$

$$= \frac{\sqrt{2Ra_{vib}}}{Ra} \frac{gl_z^2}{\sqrt{\chi\nu}} \quad (\text{A.13})$$

$$= \frac{\sqrt{2Ra_{vib}}}{Ra} \frac{gl_z^2}{\sqrt{\frac{k}{\rho c_p} \nu}} \quad (\text{A.14})$$

$$= \frac{\sqrt{2Ra_{vib}}}{Ra} \frac{gl_z^2 \sqrt{\rho c_p}}{\sqrt{k\nu}} \quad (\text{A.15})$$

$$|\mathbf{v}| = \frac{\sqrt{2Ra_{vib}}}{Ra} \frac{gl_z^2 \sqrt{\rho c_p}}{\sqrt{k \frac{\mu}{\rho}}} \quad (\text{A.16})$$

Here we have used the definition of the kinematic viscosity, $\nu = \mu/\rho$, and the thermal diffusivity, $\chi = k/(\rho c_p)$. We now reach our final result of:

$$|\mathbf{v}| = g \frac{\sqrt{2Ra_{vib}}}{Ra} l_z^2 \left(\rho \sqrt{\frac{c_p}{k\mu}} \right) \quad (\text{A.17})$$

Appendix B

Nondimensional Results

As the shaking experimental results in Chapter 4 were presented in the form of dimensioned variables, enabling a direct evaluation of the experiment developed, a more universal and direct comparison to the theory of Carbo may be made by returning the results to dimensionless variables. This allows a direct comparison to the upper boundary computations first shown in Figure 1.5 and reproduced below for convenience in Figure B.1.

To restate, the dimensionless groups employed by Carbo [16] and used here are:

$$Ra = \frac{g_o \beta \Delta T l_z^3}{\nu \chi} \quad (\text{B.1})$$

$$Ra_{vib} = Pr \frac{Ra^2 \epsilon^2}{2\omega^{*2}}. \quad (\text{B.2})$$

For completeness, we recall that these employ the dimensionless frequency and acceleration:

$$\omega^* = \omega l_z^2 / \chi \quad (\text{B.3})$$

$$\epsilon = A \omega^2 / g_o. \quad (\text{B.4})$$

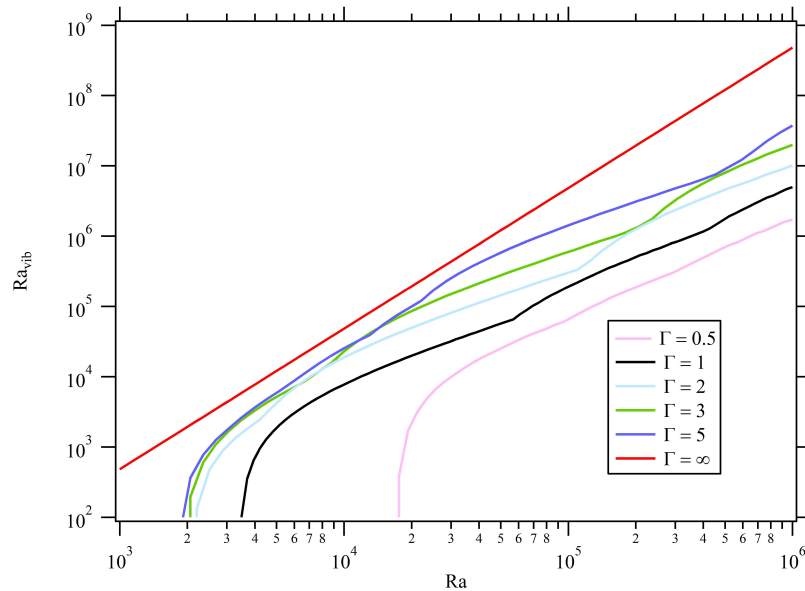


Figure B.1: Critical vibrational Rayleigh number for the upper stability boundary shown as a function of aspect ratio for a square cross-section ($\Gamma_x = \Gamma_y$) container with a rectangular drive and insulating sidewalls [16].

In order to complete the comparison, the nondimensionalized results are presented in this Appendix. Unlike Figures 1.5 and B.1, which show computations for a rectangular modulation, the following predictions are returned to a sinusoidal modulation basis for comparison to the experimental results. The section and figures these results correspond to are denoted here to permit easier comparison. Also, please note that the plots of the upper boundary (in the form of Ra_{vib} vs. Ra) are plotted in a log-log format and over multiple decades to better match the visual form of Carbo's results.

B.1 $\Gamma = 5$ Pre-Disassembly Results

The results presented here were obtained from the pre-reconstruction $\Gamma = 5$ cell. These results were initially presented in dimensioned form in Section 4.2.1. The table of results corresponds to Table 4.4 and the plot corresponds to Figure 4.3.

Table B.1: Shaking onset testing results from the pre-disassembly $\Gamma = 5$ experimental cell presented in dimensionless variables. These results were acquired by fixing ΔT and varying $|\mathbf{v}|$.

Setpoint ΔT (K)	Rayleigh Number Ra	Transition Ra_{vib}	
		Theory	Experiment
4.32	2062	609.5	555.1
			651.3
			588.7
			577.6
			624.8
			530.1
			Mean: 587.9
4.50	2148	769.5	790.1
			849.4
			Mean: 819.7

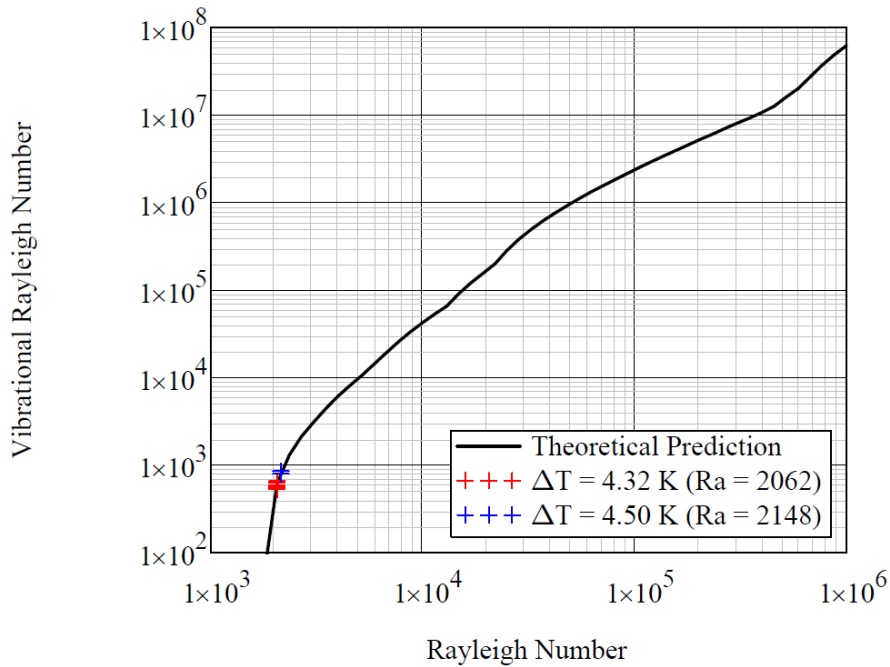


Figure B.2: Plot of the shaking dynamic stabilization results obtained on the pre-disassembly $\Gamma = 5$ experimental cell presented in dimensionless variables. This data was acquired using the fixed ΔT , variable $|\mathbf{v}|$ method and presents graphically the same data as Table B.1.

B.2 $\Gamma = 5$ Post-Reassembly Results

The results presented here were obtained from the post-reconstruction $\Gamma = 5$ cell. These results were initially presented in dimensioned form in Section 4.2.1. The table of results corresponds to Table 4.5 and the plot corresponds to Figure 4.4.

Note that as the vibrational Rayleigh number Ra_{vib} depends upon the Rayleigh number Ra itself, there is a separate theoretical and experimental result for the vibrational Rayleigh number and Rayleigh number for each point on the stability boundary; this is reflected in the table.

Table B.2: Shaking onset testing results from the reassembled $\Gamma = 5$ experimental cell presented in dimensionless variables. These results were acquired by varying ΔT and fixing $|\mathbf{v}|$.

Shaker Velocity (m/s)	Transition Ra_{vib}		Transition Ra	
	Theory	Experiment	Theory	Experiment
2.300	343.9	376.1	1900	1987
2.347	360.6	391.1	1906	1985
2.442	396.2	479.6	1921	2113
2.490	415.6	550.6	1929	2221
2.533	433.4	507.7	1937	2096
2.538	435.5	520.8	1938	2119
2.587	457.1	848.1	1947	2652
2.628	476.0	835.5	1956	2591
2.681	501.5	499.9	1968	1965
2.724	523.0	1062	1978	2818
2.778	551.4	974.9	1992	2648

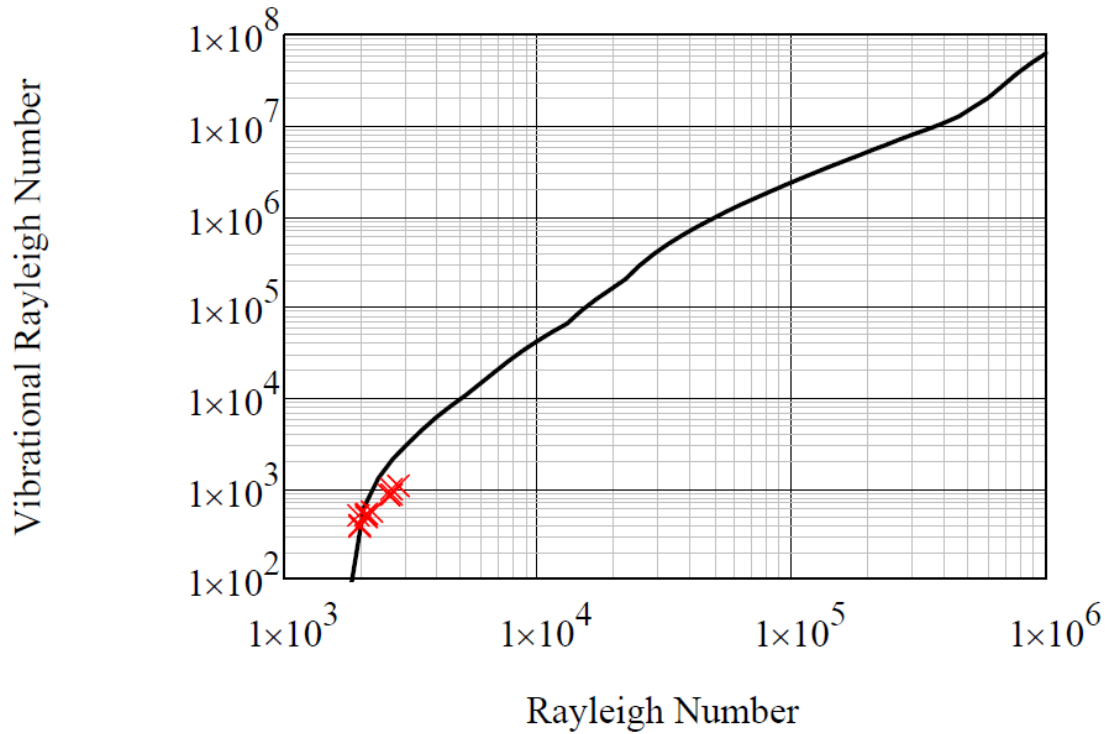


Figure B.3: Plot of the shaking dynamic stabilization results obtained on the reassembled $\Gamma = 5$ experimental cell presented in dimensionless variables. This data was acquired using the variable ΔT , fixed $|\mathbf{v}|$ method and presents graphically the same data as Table B.2.

B.3 $\Gamma = 3$ Results

The results presented here were obtained from the $\Gamma = 3$ cell. These results were initially presented in dimensioned form in Section 4.2.3. The table of results corresponds to Table 4.6 and the plot corresponds to Figure 4.10.

Table B.3: Shaking onset testing results from the $\Gamma = 3$ experimental cell presented in dimensionless variables. These results were acquired by varying ΔT and fixing $|\mathbf{v}|$.

Shaker Velocity (m/s)	Transition Ra_{vib}		Transition Ra	
	Theory	Experiment	Theory	Experiment
2.176	931.3	886.2	2285	2229
2.396	1299	1388	2451	2534
2.444	1405	1301	2499	2405
2.492	1523	1398	2552	2446
2.586	1798	1691	2672	2591
2.683	2155	2039	2820	2743
2.778	2605	2482	2994	2923

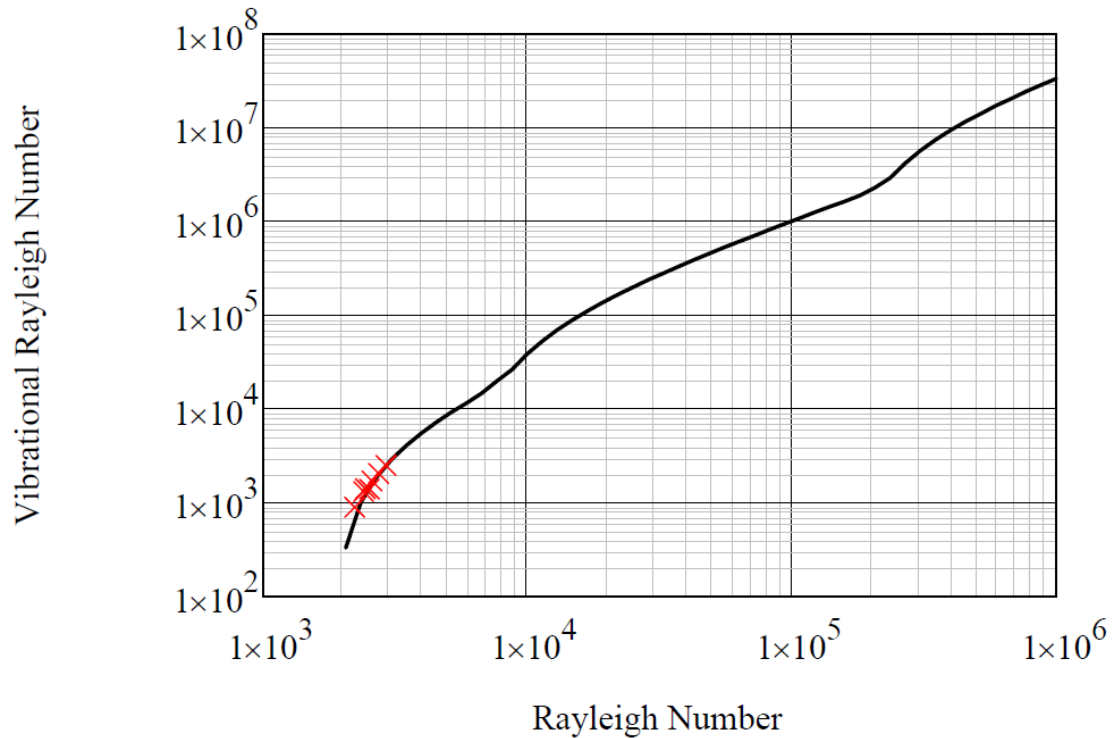


Figure B.4: Plot of the shaking dynamic stabilization results obtained on the $\Gamma = 3$ experimental cell presented in dimensionless variables. This data was acquired using the variable ΔT , fixed $|\mathbf{v}|$ method and presents graphically the same data as Table B.3.

Appendix C

Laser Diode Array Documenta- tion

As the type of visible spectrum diode laser array used in this experiment may not be familiar to many readers, the specific testing data sheet, showing the relationship between optical power output and input current, and the relationship between voltage and current, is reproduced here. There were two laser diode arrays supplied by the manufacturer for this experiment, one lensed and the other with no additional optics. Both display similar output characteristics, therefore only one data sheet is reproduced here.

The approved laser safety Standard Operating Procedure is also reproduced for reference in this appendix.

M1.8-clO-N-670-Z3.2.15

229256

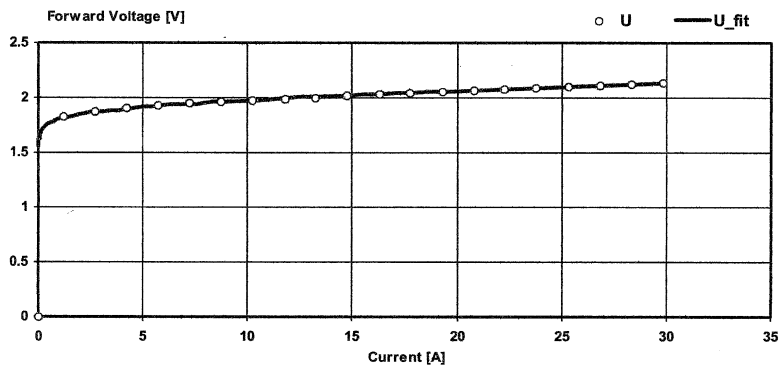
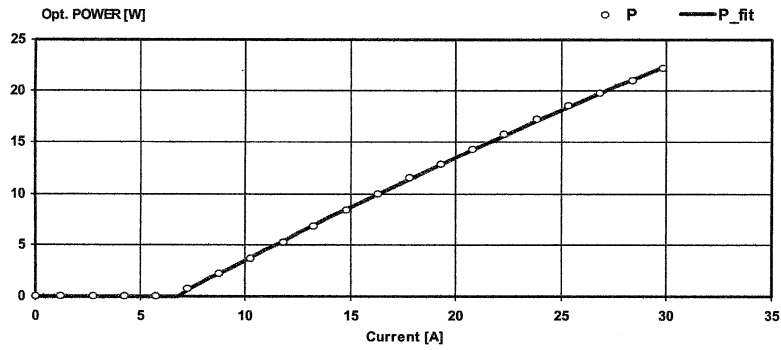
DILAS

The diode laser company.

7/22/2015

PUI measuring data
Continuous Wave-Operation

P (30 A)	22.5 W	Overall efficiency	34.9 %
I (20.0 W)	27.1 A	UF	2.11 V
Threshold	6.7 A	UE	1.93 V
Slope	1.10 W/A	Rs	6.8 mOhm
		Temperature	25.0 °C





PennState
College of Engineering

**GRADUATE PROGRAM
IN ACOUSTICS**

**Thermoacoustics Laboratory
Graduate Program in Acoustics
The Pennsylvania State University**

STANDARD OPERATING PROCEDURE

for Safe Operation of the

DILAS 675 nm Diode Line Source Laser Array

for the purpose of shaken flow visualization experiments
in Hammond Building Room 20/22

Rev. 2, 16 March 2016

This equipment and documentation are to be used only by authorized and trained personnel.

**STANDARD OPERATING PROCEDURE
for the DILAS 675 nm Diode Line Source Laser Array
in Hammond Building Room 20/22**

PURPOSE

This is a Standard Operating Procedure (SOP) for the DILAS 675 nm Diode Laser in Hammond Building Rooms 20 and 22 in the College of Engineering at The Pennsylvania State University. This SOP applies to a specific laser system, and has been written for application of that laser system in a specific work area and application. Other lasers will have their own specific SOP's, and use of this laser in another work area or for another experimental application will also require its own SOP to be developed and approved.

This document outlines the specifications and hazards, and the startup, programming, operation, and safety procedures established for the use of the laser system within the confines of the flow visualization experiment.

This procedure is not intended to be an all-encompassing manual describing every detail needed by a person to operate, program, and maintain the laser system and apply it to this experiment, but rather it is intended to be a supplemental overview describing general function and procedures required to set up and use the laser system safely. It is a minimum expectation that all persons operating, programming, or servicing this laser system have been trained appropriately and adequately for their intended functions and will utilize that knowledge in the safe and effective application of the laser system.

This document will be reviewed annually by the Laser Safety Officer and the Safety Designate of the Thermoacoustics Laboratory/Graduate Program in Acoustics, and, as necessary, to conform to new regulations or changes in the equipment. For training information please refer to the appropriate section in this SOP.

TRAINING

All laser operators are required to take the Environmental Health & Safety General Laser Safety Training and quiz at:

<https://ehs.psu.edu/radiation-protection/laser-safety/laser-safety-training-procedures> and must be trained in the safe operation of the laser and the SOP associated with the laser. All training must be documented and maintained with a copy of this SOP in a binder in the immediate vicinity of the laser.

Operators of this laser must be one of the following: Full-time or part-time PSU employees, paid consultants, or full-time or part-time graduate students. Additionally, operators must be qualified as operators by receiving a) the proper laser safety training, per PSU SY17 Laser Policy, and b) must be approved by the Experiment Supervisor (Robert W. M. Smith). Those currently listed as qualified operators are named later in this document.

MEDICAL

In the event of any accident of medical emergency, the laser system should immediately be shut down and immediate medical attention should be sought. For a severe emergency, 911 should be called for assistance.

After seeking immediate medical attention, any accidental eye exposure due to either the direct or indirect radiation of the laser beam must be reported to the Experiment Supervisor, COE Safety Officer, and the Laser Safety Officer.

RESPONSIBILITIES

Any individuals not approved as operators are to be under direct supervision by an approved operator at all times whenever they are working in Hammond Room 20/22 when the laser is in operation. They must also wear the required personal protection equipment as detailed below. They are not permitted to operate this laser at any time. The laser operator will be responsible for ensuring the safety of individuals who are not qualified as operators (as defined above) and who are under their direct supervision.

When required, approved Personal Protection Equipment (PPE) including laser safety eyewear shall be worn whenever the laser systems are “active” in the work area AND the enclosure is unsecured (during alignment operations). The operator is responsible for wearing the necessary PPE when operating the laser system.

Only Robert W. M. Smith and the Penn State Laser Safety officer shall approve future operators once they have received the proper laser safety training, per PSU SY17 Laser Policy.

The operator shall be required to place the appropriate warning signs and administrative controls for the current laser operating state and enforce the exclusion of non-essential personnel from the controlled area for the particular operation.

At no time will this laser system be operated unattended. An operator must be in attendance at all times during these tests to ensure that the enclosure is not breached.

MAINTENANCE

Only qualified operators or manufacturer's trained technicians shall be allowed to perform maintenance or repairs to the laser system.

VISITORS

All visitors who wish to view or tour the lab space when the experiment is in operation will be pre-approved by the Experiment Supervisor. All visitors shall receive and wear the appropriate Personal Protection Equipment (PPE) for the current operating state prior to entering the controlled area. The responsibility of enforcing this policy shall fall to the Experiment Supervisor. Group size will be limited to the amount of PPE available for the given experimental state.

**SPECIFICATIONS and HAZARDS of the
DILAS 675 nm Diode Line Source Laser Array
in Hammond Building Room 20/22**

LASER HEAD SPECIFICATIONS

Manufacturer:	DILAS Diode Laser Inc./DILAS Diodenlaser GmbH
Model:	M1.8-cJO-N-670.5-Z3.2.15
Mfg. Part Number:	600-02777-M1Y-675.5-20C-T25
Power:	20 W max (CW)
Wavelength:	675 nm
Lasing Medium	Semiconductor Diode Array
Normal Operation:	Pulsed
Rep Rate:	4 – 20 Hz
Alignment Operation:	Continuous (CW) at reduced powers
Delivery Mode:	Permanently manufacturer installed 600 μm FAC cylindrical lens
Focus Range	Linear (light sheet) source diverging in slow axis
Emitter Dimensions:	100 μm x 19 emitters
Beam Divergence:	< 10 mrad fast-axis with lens, < 10 degrees slow-axis
Aperture diameter:	100 μm x 10.6 mm
Optical Stability:	$\sim 0.16 \text{ nm}/^\circ\text{C}$
Spectral Width:	< 2.0 nm (FWHM)
Center Wavelength:	$\pm 5 \text{ nm}$
Input Voltage:	< 2.20 V_{dc}
Input Current:	12 to 30 A_{dc}
Operating Temp.:	+20 to +25 $^\circ\text{C}$
Storage Temp.:	0 to +55 $^\circ\text{C}$

This laser is a Class 4 device.

LASER POWER SUPPLY SPECIFICATIONS

Manufacturer:	Amtron GmbH
Model:	CS412 4L80
Max. Voltage:	4 V_{dc}
Max Current:	80 A_{dc}
Cooling:	Forced air cooled
Manufacture Date:	23 June 2015
Form Factor:	2 rack units
Access Control:	Key switch activation
Safety Control:	Latching face panel emergency stop switch
Modes:	CW, Analog/Digital Trigger

CLASS 4 LASER HAZARDS

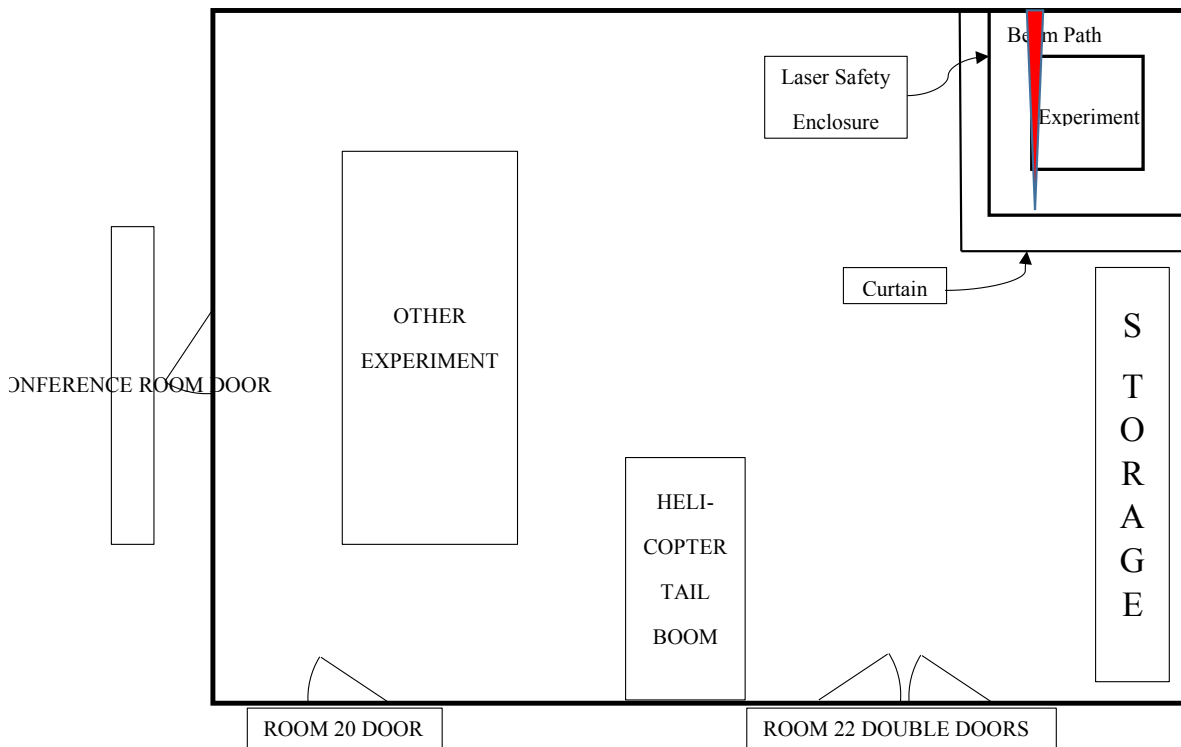
- This laser does not have a mechanical shutter.
- This laser can cause damage if the beam enters the eye. This may include photochemical and thermal retinal injuries and result in permanent blindness.
- Both diffuse and specular reflection of the beam are hazardous.
- This device may also pose electrical shock hazards to the user when energized if terminals are contacted.

PERSONAL PROTECTIVE EQUIPMENT

Laser Safety glasses:
675 nm with minimum OD 4+

LOCATION

This laser is located in the CAV Structural Acoustics Lab, which encompasses the interconnected rooms 20 and 22 in the Hammond Building. A diagram of the exact placement follows:



EXPERIMENT SUPERVISOR

Robert W. M. Smith, 204M Applied Science Building, (814) 865-5883,
rws100@psu.edu.

SAFETY DESIGNEE

Robert W. M. Smith

ACOUSTICS DEPARTMENT SAFETY OFFICER

Stephen C. Thompson, Professor of Acoustics, N-249 Millennium Science Complex,
(814) 865-0190, sct12@psu.edu.

LASER SAFETY OFFICER

Yuanqing Guo, 228 Academic Projects Building, (814) 865-6391, yxg14@psu.edu.

STAFF AUTHORIZED for OPERATION

Robert W. M. Smith

Anand Swaminathan, Hammond Room 20/22, (848) 448-5920, azs5363@psu.edu.

**STANDARD OPERATING PROCEDURE
for the DILAS 675 nm Diode Line Source Laser Array
in Hammond Building Room 20/22**

SAFETY NOTES

- *This document is to be used only by authorized operating personnel.*
- *The authors assume no liability for the misapplication or misinterpretation of information contained in this document.*
- *Before operating this laser, the operator must be trained by lab safety designee Robert W. M. Smith and read and be familiar with the Amtron Instruction Manuals.*
- *The DILAS laser is a Class 4 laser device.*

This laser will be operated in two states for this experiment. One is solely for alignment and testing. The other is for normal experimental operation.

For alignment and testing, the laser safety enclosure will need to be opened during laser operation. An image of the enclosure is shown below.

GENERAL OPERATION PRINCIPLES:

- 1.) The laser power supply operates on a key interlock system, as required by regulations. There are only two copies of this key. One is to be stored in Research Building West room 17-U (the main thermoacoustics laboratory space). The other is to be kept in Hammond with the laser. This key is the primary interlock control. When operations not requiring laser operation are performed, the key should be carried by the person performing the operation, avoiding the possibility of inadvertent turn-on by another person in the lab. When not in use, the key should be stored in a safe location and not left in the power supply to prevent activation by unauthorized personnel.
- 2.) In order to activate the laser, the key may be turned to one of two positions. The first position is manual operation. This position permits the firing of the laser from the front-panel controls, namely the laser on (green) and laser off (red) buttons. The second position is for remote. This permits the laser to be fired by external logic signals or RS-232 bus. This setting should only be used for experimental operation and not for alignment or setup, as the laser may fire without warning based on trigger signals.
- 3.) For the laser to operate, the Emergency stop mushroom button must be rotated to release it from its disabled position. After this is completed, the laser is armed and able to emit light. When shutting down for a period, the emergency stop button should always be latched in the closed position before shutting down the power supply.
- 4.) All setup of the power supply mode and operation can be accomplished through the front-panel display, using the three multi-function soft keys and the rotary encoder.

ALIGNMENT PROCEDURES:

The laser will never be operated with the outer curtains open. For the alignment and testing procedures, only the side door of the enclosure should be opened at any time. Opening the front door may expose personnel to the beam path if they are in a kneeling or crouching position.

While the laser is being operated in the alignment mode, laser output should be limited to approximately 50 mW optical. The lowest practical power less than this limit should be used.

- 1.) The laser safety flashing light beacon will be placed outside the curtain along with appropriate class IV laser warning signage. Signs will also be placed outside the curtain and on the hallway door to the room. The light will remain lit and signage in place until the laser has been returned to normal experimental operations.
- 2.) All work will still take place behind the opaque curtains due to the presence of uncovered windows above the experiment. All alignment procedures will be carried out with an awareness of the potential beam path. By working with only the side access door open, as discussed above, the potential for a stray beam outside the enclosure will be avoided.
- 3.) As both direct beam exposure and specular reflections from this laser may be hazardous while the enclosure is open, appropriate laser safety goggles will be employed when aligning this laser. The protective glasses in the lab, with Laservision T5H03 glass filters installed, are rated for OD 4+ at 630-690 nm and are OD 5+ at the center frequency of this laser (675 nm). Inspect the glasses for any cracks in the frames, scratches or cracks in the filters, or other broken or damaged parts prior to using them. The glasses are supplied with retainer cords that may help ensure a tighter fit than the glasses alone. These glasses are designed to fit over standard prescription eyeglasses.
- 4.) Laser alignment procedures should be limited to approximately 50 mW optical. This corresponds to approximately 6.705 A of drive current.
- 5.) A laser alignment card may be used to better visualize the beam. Under no circumstances should the eye be placed near the beam path.

NORMAL EXPERIMENTAL OPERATION:

- 1.) Before activating the laser make sure that all access panels in the enclosure are shut and latched and that the curtain is closed.
- 2.) Once these checks have been completed, turn the key switch to the remote position.
- 3.) When ready to arm the laser system, rotate the emergency stop button to enable the laser output. Monitor the data collection and adjust laser power or other operating conditions as necessary.
- 4.) When done collecting visualization data, depress Emergency Stop button. This will place the laser power supply into an error condition. Turn the key switch to the off position and remove the key from the lock switch cylinder. Store the key in a safe location away from the power supply.

- 5.) Make sure to wait several minutes to ensure that a fire or other overheat condition has not started before leaving the laboratory.

Appendix D

Reprint of Carbo Theory Paper

This appendix provides a reprint of the paper from Carbo that presented the theoretical underpinnings for this experimental work.

Citation: Randy M. Carbo, Robert W. M. Smith, and Matthew E. Poese, “A computational model for the dynamic stabilization of Rayleigh-Bénard convection in a cubic cavity,” *J. Acoust. Soc. Am.* **135**(2), 654–668 (2014).

Permissions: Reproduced with the permission of the Acoustical Society of America.

A computational model for the dynamic stabilization of Rayleigh-Bénard convection in a cubic cavity

Randy M. Carbo^{a)}

Graduate Program in Acoustics, The Pennsylvania State University, P.O. Box 30, State College, Pennsylvania 16804

Robert W. M. Smith and Matthew E. Poese^{a)}

The Pennsylvania State University, Applied Research Laboratory, P.O. Box 30, State College, Pennsylvania 16804

(Received 21 November 2012; revised 12 December 2013; accepted 23 December 2013)

The dynamic stability of Rayleigh-Bénard convection with vertical vibration in a cubic container is computationally modeled. Two parametric drives are considered (sinusoidal and rectangular), as well as two thermal boundary conditions on the sidewalls (insulating and conducting). The linearized equations are solved using a spectral Galerkin method and Floquet analysis. Both the synchronous and the subharmonic regions of instability are recovered. The conditions necessary for dynamic stability are reported for a range of Rayleigh numbers from critical to 10^7 and for Prandtl numbers in the range of 0.1–7. The linear model is compared to the data set available in the literature where the performance of an inverted pulse tube cryocooler is measured.

© 2014 Acoustical Society of America. [<http://dx.doi.org/10.1121/1.4861360>]

PACS number(s): 43.35.Ud, 43.35.Ty, 43.28.Py, 43.25.Ts [RR]

Pages: 654–668

I. INTRODUCTION

The natural convection of a horizontal layer of fluid heated from below is a system whose dynamics were contemplated by Rayleigh and for which experimental work was first carried out by Henri Bénard in 1900. In many practical situations, however, it is desirable to stop the fluid mixing and enhanced heat transfer that result from the fluid motion of such a system, often referred to as Rayleigh-Bénard convection or instability. Similar to the fact that a rod on a pivot will stand up against gravity if the pivot point is oscillated up and down with particular combinations of oscillation amplitude and frequency, the convection cells expected in a fluid heated from below can be made still when the fluid (or container) is oscillated. This paper outlines a solution method to identify combinations of oscillation amplitude and frequency that will stabilize the convection cells present in a bounded container with side, top, and bottom walls. The solution results in a stability map, and a stability map is generated for and compared to a set of pulse tube stability measurements published recently in the *Journal of the Acoustical Society of America*.¹

The suppression of thermal convection through parameter modulation has several practical applications, although this study is motivated by the following: Thermoacoustic refrigerators can have large adverse (cold above hot) temperature gradients between heat exchangers and an intense acoustic field. If thermal convection is present, then a significant amount of heat is transferred between the heat exchangers from hot to cold by the convective instability and therefore the efficiency of the machine (intended to pump heat from cold to ambient temperature) decreases. Since the fluid is already oscillating in order to pump heat from the

cold to the hot (or ambient) exchanger, it seems possible that if that oscillation is designed to fall into the stable regime described in this paper the fluid motion of the convection cells could be suppressed.¹ In the following treatment of Rayleigh-Bénard convection, the parameter being modulated is the force of gravity on the fluid: Since the fluid is being accelerated by the acoustic field (often created by a linear motor oscillating a piston or diaphragm), the total force acting on the fluid is proportional to the linear superposition of the gravitational acceleration and the acoustic acceleration. Alternatively, the same effect can be reached experimentally by shaking the entire container that contains the fluid.

Outside of the primary motivation for this work, the fabrication process for certain crystals is difficult in a terrestrial environment because of thermosolutal convection.² The fabrication of these crystals in microgravity environments is also difficult because of small spacecraft vibration, also known as *g*-jitter. The control of convection with vibration and knowledge of jitter effects on directional solidification are paramount to producing high quality crystals. The parametric stability of convection in fluids and fluids in porous media has been studied extensively, however much of the computational work has focused on infinite layers and very little has been done experimentally. It is generally difficult to generalize one- or two-dimensional solutions to physical problems in three dimensions.

In fluid media, two-dimensional solutions of infinite layers heated from below with gravity modulation were exhaustively studied theoretically for horizontal planes³ and for inclined planes⁴ as well as three-dimensional solutions of horizontal planes.^{5,6} Two-dimensional rectangular enclosures with insulated sidewalls were studied⁷ for a wide range of aspect ratios and Rayleigh numbers close to critical. The only three-dimensional (3D) study found in the literature was that of infinitely long vertical cylinders.⁸

^{a)}Author to whom correspondence should be addressed. Electronic mail: poese@psu.edu

Three experimental investigations^{1,9,10} were found in the literature. All three examined cylindrical pulse tube cryocoolers for a number of inclination angles. The Swift and Backhaus¹ experiment is the most comprehensive of the three and uses a simple analogy to explain the data.

Within porous media, infinite two-dimensional fluid layers heated from below with gravity modulation were studied theoretically,¹¹ in two-dimensional rectangular enclosures,¹² and cylinders.¹³ In the latter two cases only free-slip sidewalls were considered.

This paper will contribute by computationally modeling the dynamic stability of Rayleigh-Bénard convection in a cubic container with gravity modulation. A summary of the necessary properties for dynamic stability will be provided for insulating and conducting rigid sidewalls over the range of Rayleigh numbers from 10^3 to 10^7 . Additionally, the stability map generated by the computational model will be compared to the data provided in Ref. 1.

II. LINEAR STABILITY

The system of interest is a fluid filled cubic cavity contained in $\Omega : [0, \ell_x] \times [0, \ell_y] \times [0, \ell_z]$ ($\ell_x = \ell_y = \ell_z$) with periodic gravity modulation. The xy plane is taken to be horizontal and the z axis is vertical. The $z=0$ face is maintained at a temperature T_0 and the $z = \ell_z$ face is maintained at a temperature $T_0 + \Delta T$. The contained fluid will be assumed to obey the Boussinesq approximation, i.e., density variations are small and dominated by thermal expansion.^{14,15} For the Boussinesq approximation to remain applicable for a vibrating fluid, the following condition must be satisfied:¹⁴

$$\ell_z/c \ll \tau \ll \min\{\ell_z^2/\nu, \ell_z^2/\chi\}, \quad (1)$$

where τ is the period of the vibration source, c is the speed of sound in the fluid, χ is the thermal diffusivity, and ν is the kinematic viscosity.

Stability at modest Rayleigh numbers and for Prandtl numbers between 0.7 and 7 will be the main concern of this paper, and linear analysis will be used to find solutions that are stationary in time. A numerical study that included the full set of nonlinear equations on a rigidly bounded infinite layer concluded, for the amplitudes they considered, that linear analysis adequately captures the stability thresholds.⁶ While the comparison by Biringen and Peltier was carried out at similar Prandtl numbers but much lower Rayleigh numbers than those considered here, the success of that comparison derives from the nature of the problem: In a stable condition, velocities are zero or very small, and remain so until a point of instability is reached. From a conceptual point of view the experiment can be conducted in a rather impractical, but otherwise acceptable sequence: One may begin with a fluid without a thermal gradient, but subject to an oscillatory gravity field, and then choose to increase the gradient until instability could be determined. Ryzhkov and Gaponenko provide the following condition on the amplitude for linear stability analysis to remain applicable:¹⁴

$$\frac{A}{\ell_z} \ll \frac{1}{\beta \Delta T}, \quad (2)$$

where A is the vibration displacement amplitude, and β is the thermal expansion coefficient. The linear governing dimensionless equations are

$$\frac{\partial \mathbf{u}}{\partial t} = -\nabla p + \text{RaPr}(1+\psi(t))\theta \hat{\mathbf{z}} + \text{Pr} \Delta \mathbf{u}, \quad (3)$$

$$\frac{\partial \theta}{\partial t} - w = \Delta \theta, \quad (4)$$

$$\nabla \cdot \mathbf{u} = 0, \quad (5)$$

where $\psi(t)$ is a periodic acceleration function (i.e., the dimensionless parametric excitation with period τ) and θ is the spatially dependent temperature deviation from the linear conduction profile³ that would exist absent an instability. Non-dimensionalization is done following Gershuni and Lyubimov¹⁶ where the length is scaled by the height, ℓ_z , of the container, time is scaled by the vertical transport of thermal diffusion, ℓ_z^2/χ , velocity is therefore scaled as χ/L , pressure is scaled as $\rho\nu\chi/L^2$. The Rayleigh number (Ra) and Prandtl number (Pr) are defined as follows:

$$\text{Ra} = \frac{g\beta\Delta T\ell_z^3}{\nu\chi}, \quad \text{Pr} = \frac{\nu}{\chi}, \quad (6)$$

where g is the gravitational acceleration. The mechanical boundaries for all walls are rigid (no-slip), expressed as $\mathbf{u} = 0$ on $\partial\Omega$. Both thermally insulating and conducting boundaries will be considered on the sidewalls; the upper and lower horizontal boundaries are assumed to be perfect conductors. The boundary conditions for thermally conducting walls are

$$\begin{aligned} \theta &= 0 \text{ at } z = 0, 1; & \theta &= 0 \text{ at } x = 0, \Gamma_x; \\ \theta &= 0 \text{ at } y = 0, \Gamma_y; \end{aligned} \quad (7)$$

and for insulating sidewalls

$$\begin{aligned} \theta &= 0 \text{ at } z = 0, 1; & \frac{\partial \theta}{\partial x} &= 0 \text{ at } x = 0, \Gamma_x; \\ \frac{\partial \theta}{\partial y} &= 0 \text{ at } y = 0, \Gamma_y, \end{aligned} \quad (8)$$

where $\Gamma_x = \ell_x/\ell_z$ and $\Gamma_y = \ell_y/\ell_z$. Separation of variables is impossible for a container with all rigid boundaries, thus a numerical approximation to the solution must be sought.

A. Galerkin method

A Chebyshev spectral Galerkin method developed by Gelfgat¹⁷ is used to approximate the spatial portion of Eqs. (3)–(5) by allowing time-varying coefficients. The method was chosen because of its computational efficiency, although other methods could be used. While space does not permit a detailed explanation of the Galerkin method, the general approach is outlined here and the references cited (in particular, the dissertation of Carbo¹⁸) provide further detail. In a Galerkin approach to solving the spatial dependence of partial differential equations, a set of linearly independent basis functions is chosen in such a way that each basis function will satisfy the boundary conditions. For the solution method

of this paper, each basis function is a Chebyshev polynomial (five terms appears to be enough) that satisfies the boundary conditions. A trial function composed of a sum of such linearly independent basis functions is created (using as many basis functions as computation time allows). The trial function is substituted into the governing differential equations to be solved. Since the weighting coefficients are unknown (and the trial function is already an approximation) this substitution cannot solve the equation. To obtain an optimum coefficient for the particular function, the inner product of the trial function and the governing ODE (Ordinary Differential Equation) is computed and the coefficient which minimizes the error is found. This process is repeated for each basis function comprising the trial function and thus the solution to the governing ODE is approximated.

The numerical problem is greatly simplified if the 3D velocity field is approximated by two basis vectors, referred to as *velocity projections*, provided the fluid is assumed incompressible. These velocity projections are defined from the continuity equation,

$$\mathbf{u} = \begin{bmatrix} u \\ v \\ w \end{bmatrix} = \begin{bmatrix} u \\ v \\ -\int \left(\frac{\partial u}{\partial x} + \frac{\partial v}{\partial y} \right) dz \end{bmatrix} \\ = \underbrace{\begin{bmatrix} u \\ 0 \\ -\int_0^z \frac{\partial u}{\partial x} dz \end{bmatrix}}_{\mathbf{w}^{(x)}} + \underbrace{\begin{bmatrix} 0 \\ v \\ -\int_0^z \frac{\partial v}{\partial y} dz \end{bmatrix}}_{\mathbf{w}^{(y)}}. \quad (9)$$

This method represents the velocity field in terms of the two *projections*, $\mathbf{w}^{(x)}$ and $\mathbf{w}^{(y)}$, given by Eq. (9). The motivation for use of these velocity projections, in addition to reducing the number of vectors, is also that the velocity projections are divergence free by definition. Thus, the pressure gradient is orthogonal to the velocity field and pressure is not required in the model.¹⁹ The velocity distribution is represented using a Chebyshev series with time dependent coefficients,

$$\mathbf{u} \approx \sum_{i=0}^{N_x} \sum_{j=0}^{N_y} \sum_{k=0}^{N_z} \left[c_{ijk}^{(x)}(t) \mathbf{w}_{ijk}^{(x)} + c_{ijk}^{(y)}(t) \mathbf{w}_{ijk}^{(y)} \right], \quad (10)$$

where

$$\mathbf{w}_{ijk}^{(y)} = \begin{bmatrix} 0 \\ \Gamma_y \mathcal{F}_i(x') \mathcal{H}_j(y') \mathcal{G}_k(z') \\ -\mathcal{F}_i(x') \mathcal{G}_j(y') \mathcal{H}_k(z') \end{bmatrix}; \\ \mathbf{w}_{ijk}^{(x)} = \begin{bmatrix} \Gamma_x \mathcal{H}_i(x') \mathcal{F}_j(y') \mathcal{G}_k(z') \\ 0 \\ -\mathcal{G}_i(x') \mathcal{F}_j(y') \mathcal{H}_k(z') \end{bmatrix}; \quad (11)$$

and $x' = (2x/\Gamma_x) - 1$; $y' = (2y/\Gamma_y) - 1$; $z' = 2z - 1$. The basis functions, \mathcal{F}_i , \mathcal{G}_i , and \mathcal{H}_i are defined as follows:

$$\mathcal{F}_m(\xi') = \sum_{\ell=0}^4 a_{m\ell} \mathcal{T}_{m+\ell}(\xi'), \quad (12)$$

$$\mathcal{G}_m(\xi') = \sum_{\ell=0}^4 b_{m\ell} \mathcal{U}_{m+\ell-1}(\xi'), \quad (13)$$

$$\mathcal{H}_m(\xi') = \sum_{\ell=0}^4 c_{m\ell} \mathcal{T}_{m+\ell}(\xi'), \quad (14)$$

where \mathcal{T} , \mathcal{U} are the Chebyshev polynomials of the first and second kind; ξ is the replacement variable for x , y , or z ; and m is the replacement variable for i , j , or k . Chebyshev polynomials were used because of their ability to accurately represent functions and the first and second kinds are related through differentiation.²⁰

The temperature distribution is expressed as

$$\theta(x, y, z; t) \approx \sum_{i=0}^{N_x} \sum_{j=0}^{N_y} \sum_{k=0}^{N_z} d_{ijk}(t) q_{ijk}(x, y, z), \quad (15)$$

where

$$q_{ijk}(x, y, z) = \mathcal{K}_i(x') \mathcal{K}_j(y') \mathcal{K}_k(z') \quad (16)$$

and

$$\mathcal{K}_i(\xi') = \sum_{\ell=0}^2 p_{i\ell} \mathcal{T}_{i+\ell}(\xi'). \quad (17)$$

The coefficients, a , b , c , and p can be determined by setting the lead coefficient to unity and substituting Eqs. (11) and (16) into Eq. (7) or (8).

Mechanical boundary conditions under the finite roll approximation are required in order to fully describe the system. The velocity projections are treated as incompressible two-dimensional flows, where the boundary conditions are described by $\mathbf{w}^{(x)} = \mathbf{w}^{(y)} = (0, 0, 0)$ on $\partial\Omega$. This set of boundary conditions introduces an approximation. Although Davies-Jones²¹ has shown that the approximation is not a valid solution for 3D linear convection, Mizushima and Matsuda²² have shown that the approximation agrees quite well with a three-basis-vector numerical evaluation. This so-called *two-dimensional finite roll approximation* was first used by Catton²³ along with the Galerkin method to investigate critical Rayleigh numbers for 3D rectangular enclosures absent vibration.

Mizushima and Nakamura²⁴ classified the solutions into eight classes based on the $\mathbb{Z}_2 \times \mathbb{Z}_2 \times \mathbb{Z}_2$ symmetry that Eqs. (3)–(5) exhibit; Table I outlines the classes. Classes seven and eight are degenerate for parallelepiped enclosures with square cross sections (i.e., have the same stability criteria), and therefore will be excluded from the analysis to follow. The velocity projections and temperature distribution can be constructed for each of the eight classes simply by restricting the orders of the Chebyshev polynomials used for the trial functions. Once the Galerkin method is applied, a system of Hill equations²⁵ remains,

TABLE I. Symmetry classes for 3D roll cells. The “o” represents an odd function about the midpoint and the “e” represents an even function. The ordered triplet, (·,·,·), expresses the symmetry in the x -, y -, and z -directions, respectively.

Class	$u(x, y, z)$	$v(x, y, z)$	$w(x, y, z)$	$\theta(x, y, z)$
1	(e,e,e)	(o,o,e)	(o,e,o)	(o,e,o)
2	(e,e,o)	(o,o,o)	(o,e,e)	(o,e,e)
3	(e,o,e)	(o,e,e)	(o,o,o)	(o,o,o)
4	(e,o,o)	(o,e,o)	(o,o,e)	(o,o,e)
5	(o,e,e)	(e,o,e)	(e,e,o)	(e,e,o)
6	(o,e,o)	(e,o,o)	(e,e,e)	(e,e,e)
7	(o,o,e)	(e,e,e)	(e,o,o)	(e,o,o)
8	(o,o,o)	(e,e,o)	(e,o,e)	(e,o,e)

$$\begin{aligned}
 & \underbrace{\begin{bmatrix} A_{xx} & A_{yx} & 0 \\ A_{xy} & A_{yy} & 0 \\ 0 & 0 & D \end{bmatrix}}_{\mathbf{M}} \underbrace{\begin{bmatrix} \frac{\partial}{\partial t} \mathbf{c}(x) \\ \frac{\partial}{\partial t} \mathbf{c}(y) \\ \frac{\partial}{\partial t} \mathbf{d} \end{bmatrix}}_{\partial \mathbf{X}(t)/\partial t} \\
 & = \underbrace{\begin{bmatrix} \text{PrB}_{xx} & \text{PrB}_{yx} & \text{PrRa}(1+\psi(t))C_x \\ \text{PrB}_{xy} & \text{PrB}_{yy} & \text{PrRa}(1+\psi(t))C_y \\ E_x & E_y & F \end{bmatrix}}_{\mathbf{L}(t)} \underbrace{\begin{bmatrix} \mathbf{c}(x) \\ \mathbf{c}(y) \\ \mathbf{d} \end{bmatrix}}_{\mathbf{X}(t)}. \tag{18}
 \end{aligned}$$

The inner product matrices generated from the Galerkin method are described in Table II, and have dimensions of $N \times N$, where $N = (N_x + 1)(N_y + 1)(N_z + 1)$. The system can be transformed into its canonical²⁶ form by isolating the differential term. This is accomplished by multiplying each side by \mathbf{M}^{-1} ,

TABLE II. Inner product matrices and their respective symmetry properties generated from the Galerkin method.

Matrix	Inner product	Property
A_{xx}	$\langle \mathbf{w}_{ijk}^{(x)}, \mathbf{w}_{pqr}^{(x)} \rangle$	$A_{xx} = A_{xx}^T$
A_{yy}	$\langle \mathbf{w}_{ijk}^{(y)}, \mathbf{w}_{pqr}^{(y)} \rangle$	$A_{yy} = A_{yy}^T$
A_{xy}	$\langle \mathbf{w}_{ijk}^{(x)}, \mathbf{w}_{pqr}^{(y)} \rangle$	$A_{xy} = A_{yx}^T$
A_{yx}	$\langle \mathbf{w}_{ijk}^{(y)}, \mathbf{w}_{pqr}^{(x)} \rangle$	$A_{yx} = A_{xy}^T$
B_{xx}	$\langle \Delta \mathbf{w}_{ijk}^{(x)}, \mathbf{w}_{pqr}^{(x)} \rangle$	$B_{xx} = B_{xx}^T$
B_{yy}	$\langle \Delta \mathbf{w}_{ijk}^{(y)}, \mathbf{w}_{pqr}^{(y)} \rangle$	$B_{yy} = B_{yy}^T$
B_{yx}	$\langle \Delta \mathbf{w}_{ijk}^{(y)}, \mathbf{w}_{pqr}^{(x)} \rangle$	$B_{yx} = B_{xy}^T$
B_{xy}	$\langle \Delta \mathbf{w}_{ijk}^{(x)}, \mathbf{w}_{pqr}^{(y)} \rangle$	$B_{xy} = B_{yx}^T$
C_x	$\langle q_{ijk} \hat{e}_z, \mathbf{w}_{pqr}^{(x)} \rangle$	$C_x = E_x^T$
C_y	$\langle q_{ijk} \hat{e}_z, \mathbf{w}_{pqr}^{(y)} \rangle$	$C_y = E_y^T$
E_x	$\langle \mathbf{w}_{ijk}^{(x)} \cdot \hat{e}_z q_{par} \rangle$	$E_x = C_x^T$
E_y	$\langle \mathbf{w}_{ijk}^{(y)} \cdot \hat{e}_z q_{par} \rangle$	$E_y = C_y^T$
D	$\langle q_{ijk}, q_{pqr} \rangle$	$D = D^T$
F	$\langle \Delta q_{ijk}, q_{pqr} \rangle$	$F = F^T$

$$\frac{\partial \mathbf{X}(t)}{\partial t} = \mathbb{N}(t) \mathbf{X}(t), \tag{19}$$

where $\mathbb{N}(t) = \mathbf{M}^{-1} \mathbf{L}(t)$. Marginal stability, absent vibration, can be evaluated by setting $\dot{\psi}(t) = 0$ and imposing the condition that velocity is stationary in time: Symbolically expressed as $\mathbb{L} \mathbf{X}(t) = 0$. The Galerkin method presented here is validated against published results; the critical Rayleigh number has been numerically determined using a spectral Galerkin method for a cubic cavity with insulating sidewalls²⁴ and conducting sidewalls²² (confirming the adequacy of the finite roll approximation). The inner products in this approach were computed analytically by building a catalog of one-dimensional Chebyshev integrals and constructing 3D integrals leveraging separation of variables—this prevented error from being introduced from numerical integration and made the method very efficient. The marginal state, i.e., the state that separates stable conditions from unstable conditions absent vibration, was computed in MATLAB using a QR (Orthogonal-triangular decomposition) method. The marginal state corresponds to the critical Rayleigh number of a fluid in a container. Table III summarizes the critical Rayleigh number as a function of the number of trial functions, N_x, N_y, N_z . It should be noted that this choice of basis converged faster than the basis used in Ref. 22, despite the two-dimensional finite roll approximation those authors used.

B. Floquet analysis

Dynamic stability was determined using Floquet analysis.²⁵ Floquet’s theorem states that the solution to Hill’s equation can be expressed $x(t) = e^{\mu_1 t} p_1(t) + e^{\mu_2 t} p_2(t)$, where $p_1(t)$ and $p_2(t)$ are periodic functions.²⁷ In other words, the idea of Floquet is that instead of having to find a solution at every point in time to determine if the solution is growing (unstable) or not (stable), stability can be determined by numerically evaluating the solution to the differential equation for a particular set of initial conditions at an interval of one period. For more details of the Floquet analysis, see Ref. 28.

In order to evaluate stability, the real parts of the exponents must be determined. To accomplish this, the system of Hill equations were solved up to one period of the parametric drive, $\psi(t)$, with each a complete set of orthogonal initial conditions,

TABLE III. Critical Rayleigh number validation as a function of the number of trial functions. The critical modes for insulating and conducting sidewalls belong to symmetry class 2.

(N_x, N_y, N_z)	Insulating	Conducting
	Ra_{crit}	Ra_{crit}
(1,1,1)	3393.86	6798.13
(2,2,2)	3388.73	6798.13
(3,3,3)	3388.55	6797.77
(4,4,4)	3388.53	6797.74
(5,5,5)	3388.53	6797.74
(6,6,6)	3388.53	6797.74
Ref. 23	3446	—
Ref. 24	3388.5	—
Ref. 22	—	6797.74

$$\mathbb{X}(t) = [\mathbf{X}_1(t) \mathbf{X}_2(t) \cdots \mathbf{X}_N(t)], \quad \mathbb{X}(0) = \mathbf{I}. \quad (20)$$

The system is stable (i.e., solutions do not grow in time), if all eigenvalues, λ , of $\mathbb{X}(t)$, the *fundamental matrix*, evaluated at one period have a modulus of less than one, where

$$\mathbb{X}(t + n\tau) = \mathbb{X}(t)\mathbb{X}^n(\tau) = \lambda^n\mathbb{X}(t), \quad (21)$$

remains bounded for all time.²⁵

1. Sinusoidal modulation

If the parametric drive is sinusoidal, i.e., $\psi(t) = \varepsilon \sin(\omega t)$, where ε is an acceleration scaled by the acceleration due to gravity, and ω is frequency scaled by $\ell_g^2 \chi^{-1}$, then there are no analytic solutions for arbitrary ε and ω . Therefore, a numerical technique is required to evaluate the solution at one period, as required for the Floquet analysis. For the specific case of a sinusoidal drive, Hill's equation is often referred to as the Mathieu equation.²⁹ The system of ODEs were solved numerically using the Adams-Bashforth-Moulton PECE routine in MATLAB and the complex eigenvalues were computed using a QZ algorithm.

2. Rectangular modulation

If the sinusoidal parametric drive is instead replaced by a rectangular drive, i.e., $\psi(t) = \varepsilon \cdot \text{sgn}(\sin(\omega t))$, then stability can be determined without having to numerically integrate the system of ODEs. The matrix $\mathbb{L}(t)$ becomes time independent over each half period, and consequently the system can be solved for the first half period with an eigenvalue technique, and then solved again over the second half period using the solutions from the first half period as an initial condition. If this process is repeated for each initial condition, then the solution at one period, $\mathbb{X}(\tau)$, can be determined and Floquet analysis can be performed.

The canonical system $\partial \mathbf{X}(t)/\partial t = \mathbb{N}(t)\mathbf{X}(t)$ has solutions

$$\mathbf{X}(t) = \sum_{i=1}^N c_i \mathbf{V}_i e^{\lambda_i t}, \quad (22)$$

where \mathbf{v}_i is an eigenvector of \mathbb{N} and λ_i is its corresponding eigenvalue. The vector of coefficients \mathbf{c} can be determined from the following expression:

$$\mathbf{c} = \mathbb{V}^{-1} \mathbf{X}(0), \quad (23)$$

where \mathbb{V} is a matrix whose columns are the eigenvectors of \mathbb{N} . For a rectangular drive, Hill's equation is often referred to as the Meissner³⁰ equation. The eigenvectors and eigenvalues were also computed in MATLAB.

III. MODEL RESULTS

In the (ε, ω) parameter space stability is broadly characterized by two unstable regions and one stable region, see Fig. 1 for a representative stability map for any value of Rayleigh number. The solutions in the region of large accelerations and small frequencies are unstable and are subharmonic with respect to the parametric drive frequency.

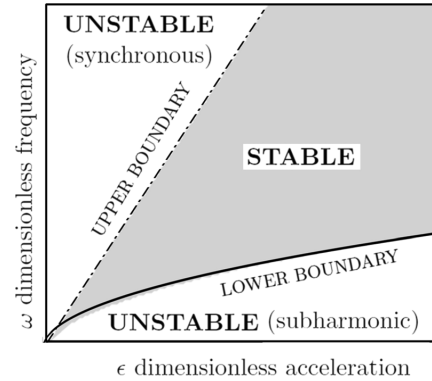


FIG. 1. Representative stability map in the (ω, ε) parameter space. The solid line is the square root approximation to the lower boundary and the dashed-dotted line is the straight line approximation to the upper boundary.

The solutions for very small drive amplitudes and finite frequencies are unstable and synchronous with respect to the drive frequency. The solutions in the intermediate region are stable and, in general, aperiodic. The stability for an inverted pendulum is quite similar;²⁸ however, unlike the continuum fluid case, the pendulum only has a single mode, whereas Fig. 1 characterizes the global stability. Toward appreciating a synoptic sense of trends, reducing this fairly simple diagram into one like that shown in Fig. 2(a) enables one to view stability as a function of Ra.

A. Upper boundary

The boundary that separates synchronous unstable solutions from stable solutions is well approximated by a straight line expressed^{31,32} as $\omega = S\varepsilon$. For Prandtl numbers in the range of 0.1 to 7, the present authors find the slope of this upper stability boundary to be proportional to the square root of the Prandtl number. A non-dimensional number, Ra_{vib} , can be formed as

$$\text{Ra}_{\text{vib}} = \text{Pr} \frac{\varepsilon^2 \text{Ra}^2}{2\omega^2}, \quad (24)$$

where Ra_{vib} is referred to as the vibrational Rayleigh number.¹⁶ When the ratio ω/ε equals the slope, S , the vibrational Rayleigh number is said to be *critical*. For slopes greater than S the system is unstable and for slopes less than S the system is stable. Each of the symmetry classes can be considered in isolation and a corresponding stability diagram can be determined for each. Figure 2(a) summarizes how the critical vibrational Rayleigh number behaves as a function of Rayleigh number for a cube with insulated sidewalls and a sinusoidal drive. The area above the collection of curves is stable and the area below the curve is unstable. The stability of the system must take into account all symmetry classes. If any one class is unstable, then the system is unstable. Each curve, noted as a class, refers to a symmetry class as detailed in Sec. II A and Table I. For example, the point $\text{Ra} = 5000$ and $\text{Ra}_{\text{vib}} = 1000$ is unstable because it is located below the critical curve (class two).

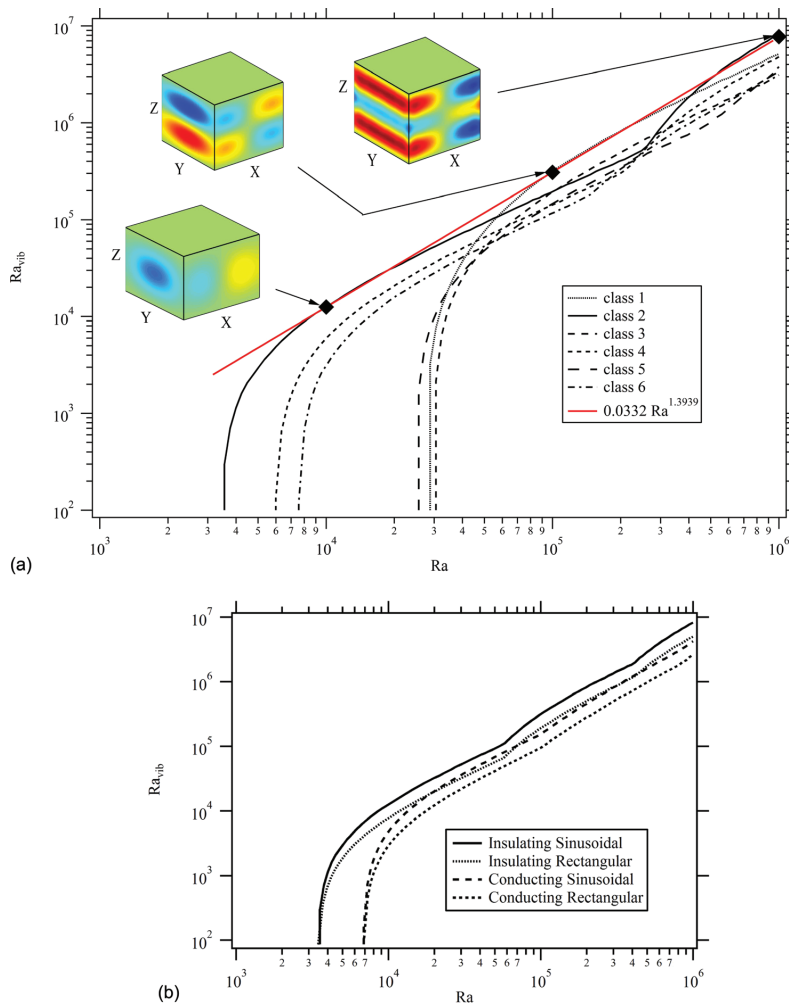


FIG. 2. Critical vibrational Rayleigh numbers are shown as a function of Rayleigh number in (a) for six symmetry classes and insulating sidewalls. The thermal profiles are also plotted for the critical state at $Ra = 10^4$, 10^5 , and 10^6 . The color represents θ , the temperature deviation from the linear gradient. In (b), critical vibrational Rayleigh numbers of a cubic cavity for two parametric excitations and two sets of thermal boundary conditions are shown: The composite curve in each case is the uppermost of any of the symmetry classes. Regions above the curve describing the critical vibrational Rayleigh number are stable against synchronous excitation. At sufficiently high vibration amplitudes these regions can still become unstable, as discussed in Sec. III B.

The six curves are monotonically increasing functions of Ra , however, a feature where the first derivative is discontinuous can be observed in each. These features will be referred to as corners for the remainder of the paper. Each corner represents a change in mode shape for the dominant mode near the critical state in a particular class. For example, the class 2 curve has a single corner occurring at approximately $Ra = 3 \times 10^5$; this marks a transition from a single roll cell solution aligned along the y axis to a solution with three stacked vertical roll cells aligned along the y axis; see thermal profiles in Fig. 2(a). The critical curve (of the system), consisting of classes one and two, has two corners, each indicating a mode shape change whereby an additional vertical roll cell aligned along the y axis is added as Ra increases. For an infinite layer with vertical vibration, the horizontal wavenumber decreases as a function of Rayleigh number and a single roll cell always governs stability.¹⁶ Cubic containers and infinite layers are similar because the roll cell aspect ratio increases with increasing Rayleigh number. However, for the bounded case the wavelength is

constrained by the container, so further increases in aspect ratio lead to a stack of multiple vertical roll cells, or in other words, an increase in vertical wavenumber.

Conducting sidewalls and rectangular modulation were also investigated; the critical vibrational Rayleigh number as a function of Rayleigh number is plotted for each of the four combinations in Fig. 2(b). Note that the critical vibrational Rayleigh number curve is a composite, constructed by joining the sections of curves associated with each of the symmetry classes. Over any range of Ra , the critical vibrational Rayleigh number has the largest value of Ra_{vib} and would thus require the largest vibration amplitude to stabilize. The same functional shape can be observed in all four curves, and although not shown, it was found that each corner represents the addition of a vertical roll cell as in Fig. 2(a). The corners are observed to occur at the same Rayleigh number regardless of modulation type, although critical Ra_{vib} varies somewhat.

In Fig. 2(a), six trial functions of the type described in Eq. (10) were used. The question arises as to the adequacy of

a particular number of trial functions. The numerical convergence of the critical vibrational Rayleigh numbers for both thermal boundary conditions as well as rectangular and sinusoidal parametric drives is summarized in Table IV. One may observe that the vibrational Rayleigh number converges smoothly from above, except for $Ra = 10^7$ where additional trial functions in the vertical direction are required to adequately capture a larger vertical wavenumber. On this basis, the number of trial functions appears adequate for purposes of evaluating stability since the addition of one more trial function produces an effect of less than 1%.

1. Sinusoidal vs rectangular modulation

In Fig. 2(b), the critical vibrational Rayleigh number for rectangular modulation appears to be uniformly vertically offset from the sinusoidal curve. This offset can be explained by examining the Fourier series for the rectangular drive,

$$\psi(t) = \epsilon \text{sgn}(\sin(\omega t)) \simeq \frac{4\epsilon}{\pi} \sum_{n=1,3,5,\dots}^{\infty} \frac{1}{n} \sin(n\omega t). \quad (25)$$

Neglecting the higher order terms the rectangular drive can be approximated as

$$\psi(t) \sim \frac{4\epsilon}{\pi} \sin(\omega t) = \underbrace{1.2732\epsilon}_{\epsilon'} \sin(\omega t), \quad (26)$$

where ϵ' is an *effective acceleration*. If the effective acceleration is substituted into Eq. (24) then a ratio can be created to approximate the offset between rectangular and sinusoidal modulation,

$$Ra_{\text{vib}} \propto \epsilon^2 \frac{(Ra_{\text{vib}})_{\text{sinus}}}{(Ra_{\text{vib}})_{\text{rect}}} \simeq 1.67. \quad (27)$$

This ratio was computed for four Rayleigh numbers, all four boundary and drive combinations, and the number of trial functions $(N_x, N_y, N_z) = (6, 6, 6)$, see Table IV. On average the ratio was computed to be 1.64; thus, the higher order terms have a negligible effect on stability. The implication is that stability can be determined using rectangular modulation and the critical acceleration can be multiplied by 1.27 to find the corresponding sinusoidal stability boundary. The determination of stability for rectangular modulation takes less than one-tenth the computational time of sinusoidal modulation, thus the reduction in time makes determining stability for large systems more computationally tractable. This result is not unique to the cube; several other aspect ratios were surveyed and the same multiplicative factor was found. The implication is that higher order harmonics are not important in determining stability for this study.

2. Scaling properties

In the region beyond the critical Rayleigh number (for static conditions), the critical vibrational Rayleigh number can be approximated by a tangent curve of the form Ra^z . As the Rayleigh number increases, so does the modal density: This is exhibited by a decreasing distance between corners. For the infinite layer, Gershuni and Lyubimov¹⁶ provide the following asymptotic scaling: $Ra_{\text{vib}} = (4.83 \times 10^{-4})Ra^2$. The scaling for the insulating and conducting cubes with sinusoidal modulation was determined by using the four points reported in Table IV. Their respective forms are: $Ra_{\text{vib}} = (3.32 \times 10^{-2})Ra^{1.3939}$ and $Ra_{\text{vib}} = (9.0 \times 10^{-3})Ra^{1.4364}$. Therefore, the inclusion of side-walls has a significant effect on the critical vibrational Rayleigh number scaling.

B. Lower boundary

The lower boundary in a stability plot of the type shown in Fig. 1 can be approximated by a simple square root

TABLE IV. Convergence analysis as a function of the number of trial functions for the critical vibrational Rayleigh for two types of parametric excitation and two thermal boundary conditions.

	(N_x, N_y, N_z)	Insulating Ra				Conducting Ra			
		10^4	10^5	10^6	10^7	10^4	10^5	10^6	10^7
Rectangular		$\times 10^3$	$\times 10^5$	$\times 10^6$	$\times 10^8$	$\times 10^3$	$\times 10^4$	$\times 10^6$	$\times 10^8$
	(1,1,1)	8.26	2.14	5.63	1.20	3.00	10.5	7.40	1.54
	(2,2,2)	7.85	1.96	5.11	1.01	2.94	9.60	3.06	1.75
	(3,3,3)	7.74	1.90	4.93	1.15	2.90	9.36	2.55	0.778
	(4,4,4)	7.69	1.89	4.80	1.17	2.89	9.26	2.34	0.737
	(5,5,5)	7.67	1.88	4.74	1.16	2.88	9.21	2.28	0.670
(6,6,6)	7.65	1.87	4.71	1.15	2.88	9.19	2.27	0.606	
Sinusoidal		$\times 10^4$	$\times 10^5$	$\times 10^6$	$\times 10^8$	$\times 10^3$	$\times 10^5$	$\times 10^6$	$\times 10^8$
	(1,1,1)	1.35	3.51	9.26	1.98	4.92	1.74	12.1	2.52
	(2,2,2)	1.29	3.23	8.41	1.67	4.82	1.59	5.03	2.87
	(3,3,3)	1.25	3.14	8.11	1.89	4.78	1.54	4.20	1.28
	(4,4,4)	1.25	3.09	7.90	1.93	4.74	1.52	3.85	1.21
	(5,5,5)	1.25	3.09	7.79	1.91	4.73	1.51	3.77	1.10
(6,6,6)	1.25	3.08	7.74	1.89	4.73	1.51	3.73	0.997	
Ratio		1.63	1.65	1.64	1.64	1.64	1.64	1.64	1.64

function, $\omega = P\sqrt{\epsilon}$, where P is defined here as the *parametric number*, and the enclosed region is often referred to as the *parametric resonance* region.³¹ In numerical trials, this square root relationship was found to be an acceptable fit for Prandtl numbers in the range of 0.1 to 7. At higher Pr the relationship is more complicated. A non-dimensional number P_{vib} can be created in much the same way as Ra_{vib} for the upper boundary,

$$P_{\text{vib}} = \text{Pr} \frac{\epsilon \text{Ra}^2}{2\omega^2}, \quad (28)$$

where P_{vib} is referred to as the vibrational parametric number. Figure 3(a) summarizes how the critical vibrational parametric number behaves as a function of Rayleigh number for a cube with insulated sidewalls and a sinusoidal drive. The vibrational parametric number increases monotonically without corners, in contrast with the critical vibrational Rayleigh number. Symmetry classes 1, 3, and 5 all lay on one curve and the remaining three classes lie on a second curve. Regions above the critical vibrational parametric number curves shown for each symmetry class are unstable.

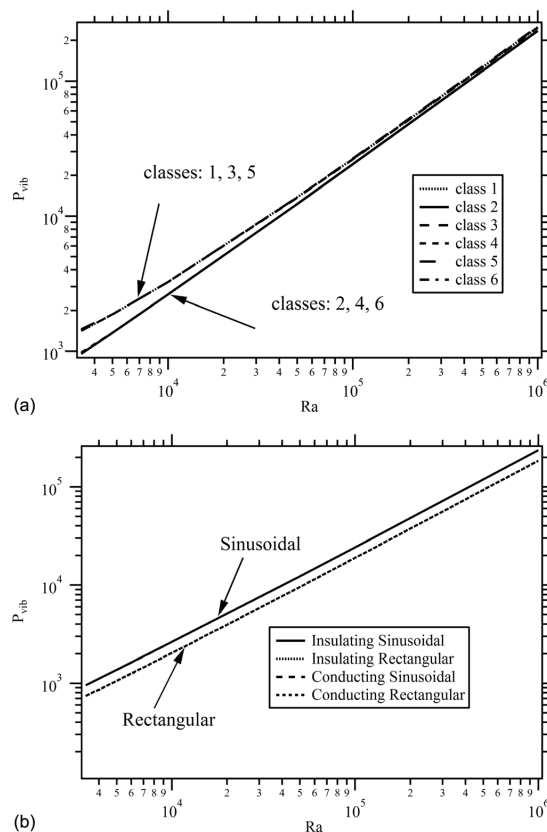


FIG. 3. Critical vibrational parametric numbers are shown as a function of Rayleigh number in (a) for six symmetry classes for insulating sidewalls and in (b) for two parametric excitations and two sets of thermal boundary conditions. In both figures, regions above the critical vibrational parametric number are unstable.

The parametric resonance region exists for Rayleigh numbers below critical and even containers heated from above.

Conducting sidewalls and rectangular modulation were also investigated; the critical vibrational parametric number as a function of Rayleigh number is plotted for the four combinations in Fig. 3(b). A surprising result can be observed: The critical vibrational parametric number is independent of thermal boundary conditions. This phenomenon can be understood through a simpler fluid analogy such as Faraday waves. Rogers *et al.* remark that for Faraday waves the wavelength excited is strongly determined by the parametric drive frequency and weakly by the geometrical boundary conditions.³³ This stands in contrast to the other unstable (synchronous) region where the wavelengths are strongly impacted by geometrical aspects.

1. Drive comparison

The vibrational parametric number for the rectangular drive is also uniformly offset from the sinusoidal drive. If the effective acceleration is substituted into Eq. (28), then the offset can be determined from the ratio of vibrational parametric numbers,

$$P_{\text{vib}} \propto \epsilon \frac{(P_{\text{vib}})_{\text{sinus}}}{(P_{\text{vib}})_{\text{rect}}} \simeq 1.27. \quad (29)$$

This ratio was computed for four Rayleigh numbers, all four boundary and drive combinations, and the number of trial functions $(N_x, N_y, N_z) = (6, 6, 6)$, see Table V. In all cases the ratio was computed to be 1.28. This agrees with the Fourier approximation to within 1% and further corroborates the idea that higher order terms are negligible for determining stability in this study.

2. Scaling properties

The vibrational parametric scaling is more straightforward than the critical vibrational Rayleigh number. The critical vibrational parametric number varies linearly with the Rayleigh number over the entire parameter region considered and does not depend on thermal boundary conditions for the cubic case. The determined functional form for a cube is $P_{\text{vib}} = 7.3\text{Ra} + P_{\text{int}}$, where P_{int} is the P_{vib} intercept. The vibrational parametric number was not calculated for small Rayleigh numbers (i.e., $\text{Ra} < 10^3$) because of poor numerical stability of the solver. It is suspected that the curve is not linear in that range.

IV. COMPARISON TO PUBLISHED EXPERIMENTAL RESULTS

Swift and Backhaus considered the dynamic stability as a function of different inclination angles with respect to the direction of gravity of five tubes like those used in thermoacoustic cryocoolers. Each of the five tubes is a stainless steel cylindrical pipe with a different aspect ratio. The tubes used have two copper heat exchangers attached to flow straighteners; these components are separated by a distance L and bound the “pulse tube” section of the tube. A large

TABLE V. $P_{\text{vib}} \times 10^5$. Convergence analysis of the vibrational parametric number as a function of the number of trial functions at $\text{Ra} = 10^6$ for all six symmetry classes and for two types of parametric excitation and two thermal boundary conditions.

(N_x, N_y, N_z)	Insulating class						Conducting class					
	1	2	3	4	5	6	1	2	3	4	5	6
<i>Rectangular</i>												
(1,1,1)	2.84	2.19	2.63	2.11	3.20	2.30	2.35	1.94	2.21	1.91	2.65	2.02
(2,2,2)	2.14	1.90	2.08	1.87	2.20	1.93	1.99	1.85	1.96	1.85	2.03	1.86
(3,3,3)	1.96	1.84	1.94	1.84	1.98	1.85	1.93	1.84	1.92	1.84	1.94	1.85
(4,4,4)	1.90	1.84	1.90	1.84	1.91	1.84	1.91	1.84	1.90	1.84	1.91	1.84
(5,5,5)	1.90	1.83	1.90	1.83	1.90	1.84	1.90	1.83	1.90	1.83	1.90	1.83
<i>Sinusoidal</i>												
(1,1,1)	3.63	2.80	3.36	2.70	4.09	2.94	3.00	2.48	2.82	2.43	3.39	2.58
(2,2,2)	2.37	2.42	2.66	2.40	2.75	2.46	2.55	2.37	2.52	2.37	2.60	2.38
(3,3,3)	2.50	2.36	2.48	2.35	2.53	2.36	2.48	2.36	2.47	2.35	2.49	2.36
(4,4,4)	2.45	2.35	2.44	2.35	2.45	2.35	2.45	2.35	2.44	2.35	2.45	2.35
(5,5,5)	2.43	2.35	2.43	2.35	2.44	2.35	2.43	2.35	2.43	2.35	2.44	2.35
<i>Ratio</i>	1.28	1.28	1.28	1.28	1.28	1.28	1.28	1.28	1.28	1.28	1.28	1.28

“bounce space” is located on the side of the hot heat exchanger opposite the pulse tube section and has length L_{bounce} . Figure 4 shows a schematic of this apparatus. The

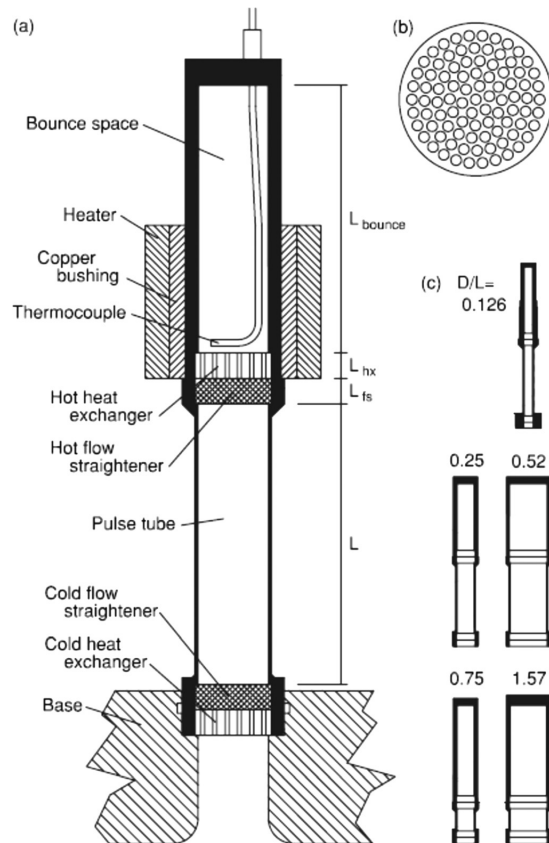


FIG. 4. Swift and Backhaus experimental apparatus. (a) Dimensioned cross section of pulse tube cryocooler, (b) copper heat exchanger, and (c) scaled cross sections of the pulse tube cryocoolers. [Images (a)–(c) are taken from Ref. 1.]

vibration source is a piston mounted on a linear motor located beneath the cold heat exchanger (although neither the motor nor the piston is shown in Fig. 4). Instead of the gravity being modulated externally by vibrating the container, the gravity modulation is accomplished by an acoustic standing wave in the fluid driven by the piston. The pulse tube cryocooler is filled with high pressure (3.1 MPa) helium gas. The hot and cold heat exchangers are held at 523 and 293 K, respectively. The thermophysical properties of the helium are summarized in Table VI.

In Swift and Backhaus’s experiment, the stability of the fluid was evaluated by examining the heat transfer characteristics as a function of the normalized acoustic pressure amplitude evaluated at the midpoint between the two heat exchangers (see Fig. 4). Heat transfer can be used to determine stability because a stable fluid can only transfer heat through conduction while an unstable fluid can advect heat and consequently more heat can be transferred over the same

TABLE VI. Thermophysical properties of high pressure helium at 100 Hz and 408 K. Values were calculated in DeltaEC.

Variable	Symbol	Value	Units
Mean pressure	p	3.1	[MPa]
Hot side temperature	T_H	523	[K]
Cold side temperature	T_C	293	[K]
Temperature difference	ΔT	230	[K]
Average density	$\langle \rho \rangle_z$	3.6575	[kg/m ³]
Specific heat capacity	c_p	5193.4	[J/kgK]
Ratio of specific heats	γ	1.667	[-]
Vol. coeff. of expansion	β	2.4510×10^{-3}	[1/K]
Thermal diffusivity	χ	1.0001×10^{-5}	[m ² /s]
Dynamic viscosity	μ	2.4576×10^{-5}	[kg/ms]
Kinematic viscosity	ν	6.7193×10^{-6}	[m ² /s]
Speed of sound	c	1188.5	[m/s]
Molar mass (He)	M	4.00	[g/mol]
Viscous b.l. thickness	δ_ν	1.462×10^{-4}	[m]
Thermal b.l. thickness	δ_κ	1.7842×10^{-4}	[m]
Prandtl number	Pr	0.67	[-]

temperature difference. While the theoretical development and numerical results presented focus in detail on the cubic cavity, it is readily extended to containers with square cross-section but arbitrary height. Numerical trials of such rectangular parallelepiped containers show similar convergence trends.

A. Differences between 3D model and experiment

Due to the paucity of experiments designed to investigate this instability, comparing the results of the model presented here with the experiment performed by Swift and Backhaus is expedient despite some significant departures between the experiment and the assumptions inherent in the model. There are four aspects in which the experiment departs from the model presented earlier in this paper:

- (1) Model is formulated for rectangular coordinates while the tubes used in the experiment are cylindrical.
- (2) Boussinesq approximation is not well satisfied in the experiment.
- (3) In the model, the top and bottom surfaces of the container are solid and have well described boundary conditions. The heat exchangers that form the upper and lower boundaries of the container in the experiment allow gas to pass through them. This boundary condition is not captured in the model.
- (4) The oscillating fluid velocity amplitude in the model is assumed to be uniform within the container. In the experiment, the oscillating velocity of the fluid is not uniform.

1. Comparing rectangular to cylindrical container

There are several alternative ways to compare rectangular and cylindrical geometries: Matching perimeters ($\Gamma = 0.7854\Gamma_\phi$), cross sectional areas ($\Gamma = 0.8862\Gamma_\phi$), or the fundamental wavenumber ($\Gamma = 0.9256\Gamma_\phi$, assuming free slip boundaries). Since the conversion factors for these three possibilities are between $\sqrt{2}/2$ and 1, these perimeters, shown in Fig. 5, are sufficient because they adequately bound the problem of interest. The pulse tube cryocoolers are made of stainless steel and can be approximated as an ideal thermal conductor relative to the helium gas contained by the tube.

2. Experimental conditions compared to Boussinesq conditions

Using the Boussinesq approximation to model the Swift and Backhaus data set is questionable, because the temperature

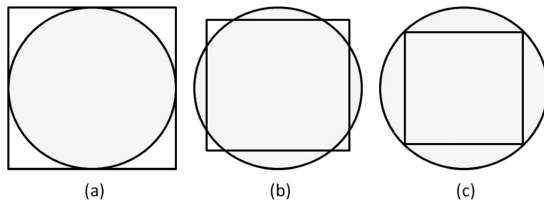


FIG. 5. Aspect ratio conversion between rectangular and cylindrical enclosures (a) inscribed $\Gamma_\phi = \Gamma$, (b) $\Gamma_\phi = \frac{1}{2}(1 + \sqrt{2}/2)$, and (c) circumscribed $\sqrt{2}\Gamma = \Gamma_\phi$.

condition is not well satisfied. In the experiment, the product $\beta\Delta T = 0.56$ which is not small compared with unity as required by the approximation. The Boussinesq approximation is a key simplification that makes solving the governing equations tractable, but caution should be exercised when interpreting the comparison to this particular experiment.

3. Top and bottom surfaces of the container

Because the boundaries are heat exchangers and not rigid surfaces, fluid flows through them. The model presented in this paper assumes these to be rigid boundaries. It is not clear how to model penetrable boundaries like the ones in the experiment with the formalism used in this paper.

4. Oscillating fluid motion amplitude

Swift and Backhaus provide the following approximate expression to calculate the acoustic particle displacement amplitude as a function of distance L between the heat exchangers,

$$A(z) = \frac{p_a}{\gamma p_m} \times \left(z + \gamma \phi_{fs} L_{fs} + \left[1 + (\gamma - 1) \frac{\delta_x}{R_{hx}} \right] \phi_{hx} L_{hx} + L_{bounce} \right), \quad (30)$$

where p_a and p_m are the acoustic and mean pressures, respectively, and the other variables are defined in Fig. 4 and their values can be found in Table VII. The acoustic amplitude at the center of the pulse tube cryocooler, A_M , is approximately $A_M = A(1/2L) = 0.068m(p_a/p_m)$ for all aspect ratios. Because the closed end of the bounce space is a velocity node, and a standing wave is present, the fluid oscillation amplitude varies as a sinusoid but is approximated to be linear from the end of the bounce space. The amplitude (or equivalently acceleration) gradient and the ratio of amplitude at the midpoint, A_M , to separation distance, L , were calculated to provide some measure of this effect, and they can be found in Table VIII.

B. Interpreting stability in the experiment

The determination of stability from the heat transfer measurements made by Swift and Backhaus is not straightforward and subjectivity is involved in the interpretation. If

TABLE VII. Geometrical properties of the apparatus used in the Swift and Backhaus experiment. The variables below the break are not described here but their values are required for (6.1), see Ref. 1 for their descriptions.

Γ_ϕ	0.126	0.249	0.521	0.750	Units
d	0.88	1.74	3.64	1.74	[cm]
ℓ	6.98	6.99	6.99	2.32	[cm]
ℓ_{bounce}	6.66	6.74	6.74	9.02	[cm]
X_A	0.61	2.38	10.4	2.38	[cm ²]
ℓ_{fs}	0.64	0.64	0.64	0.64	[cm]
ϕ_{fs}	0.82	0.82	0.82	0.82	[-]
ℓ_{hx}	0.56	0.56	0.56	0.56	[cm]
No. of hx holes	19	91	331	91	[-]
ϕ_{hx}	0.427	0.521	0.436	0.521	[-]
Holes' R_{hx}	0.66	0.66	0.66	0.66	[mm]

TABLE VIII. Stability predictions for the Swift and Backhaus data based on the current model. A_C and A_H are the accelerations at the cold and hot boundaries, respectively. The quantity ϵ_{pred} is the predicted critical acceleration based on the midpoint acceleration, $\Gamma = 1/2\Gamma_\phi(1 + \sqrt{2}/2)$.

Γ_ϕ	Ra	ϵ^*	ϵ_{pred}	A_M/L	A_C/A_H
0.750	9.87×10^5	60–100	90	0.06–0.11	1.2
0.521	2.7×10^7	70–?	230	0.02–?	1.9
0.249	2.7×10^7	65–100	132	0.02–0.04	1.9
0.126	2.7×10^7	60–70	58	0.02	1.9

stability were to be determined theoretically, then the system would be considered stable if the heat transfer is purely conductive. The conductive heat transfer can be measured by reversing the temperature gradient, i.e., heating from above. In the experiment, however, the heat transfer measurements of the non-inverted configuration are not always stationary with respect to driving amplitude and sometimes appear to increase quadratically. Swift and Backhaus suspected streaming as a potential cause of the quadratic relationship between heat transfer drive amplitude, but ruled it out with a calculation. The cause remains unknown. Also, there is added complexity because the inverted measurements appear to approach the conductive values asymptotically rather than at a discrete acceleration value. Thus a region of acceleration, ϵ^* , interpreted by the present authors, is provided over which the transition from unstable to stable is assumed to occur; see Fig. 6 for the defined ϵ^* regions for each aspect ratio.

For purposes of the following comparison of these data to the model, each experimental data point has been assigned, by the present authors, uncertainty bars in aspect ratio and acceleration. The aspect ratio uncertainty is not due to experimental error, but rather the estimated uncertainty expected by approximating a cylinder by a rectangular

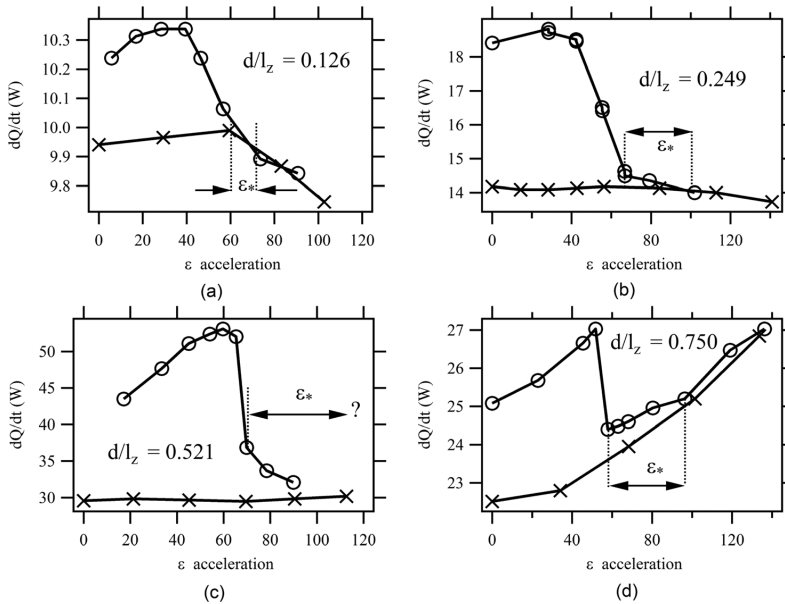


FIG. 6. Heat transfer measurements evaluating the stability of pulse tube cryocoolers (Ref. 1). Open circles represent inversion, i.e., heated from below, and crosses represent heating from above. The range indicated by ϵ^* indicates the region over which stability is tabulated. (a) $\Gamma_\phi = 0.126$, (b) $\Gamma_\phi = 0.249$, (c) $\Gamma_\phi = 0.521$, and (d) $\Gamma_\phi = 0.750$ (original data was plotted against p_c/p_m).

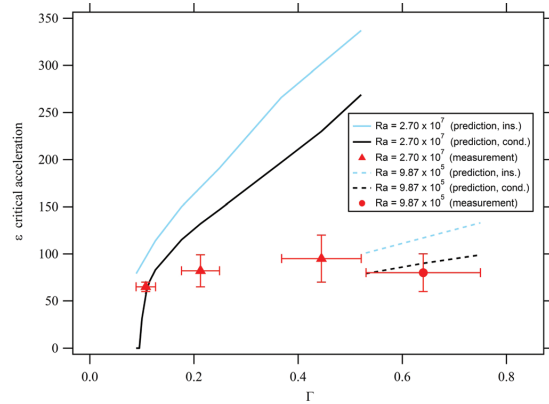


FIG. 7. Comparison of current model with experimental data taken by Swift and Backhaus. The four curves correspond to the predictions made by the model in rectangular geometries. The experimental data points are represented as individual points with error bars. $Pr = 0.67$, $f = 100$ Hz.

enclosure over the range illustrated in Fig. 5. The uncertainty in acceleration corresponds to the region over which stabilization is interpreted to have occurred. The stabilizing accelerations, ϵ , reported in Table VIII and Fig. 7 for the experimental data set, were evaluated at the midpoint between the heat exchangers using the following equation:

$$\epsilon_M = \frac{A\omega^2}{g} = 2739.3 \left(\frac{p_a}{p_m} \right). \quad (31)$$

C. Comparison of experimental data to model

The stability for each of the aspect ratios was evaluated at the vibration parameters and Rayleigh numbers considered by

Swift and Backhaus; the results are summarized in Fig. 7 and Table VIII. The relevant instability in the case of Swift and Backhaus is the synchronous type (lying above the upper boundary illustrated in Fig. 1) and is characterized by the critical vibrational Rayleigh number. Accelerations in Swift and Backhaus's experiment were not large enough to reach the lower stability boundary for which the critical vibrational parametric number is the relevant parameter. Four curves are plotted: Two pairs of curves for the two experimental Rayleigh numbers, where each pair represent stability for insulating and conducting sidewalls, and the data points obtained by Swift and Backhaus. Each aspect ratio will be examined individually, beginning with the smallest. To test the sensitivity of thermal wall impedance, both insulating and conducting sidewalls will be considered. In total, six models for each aspect ratio are considered. The critical Rayleigh numbers for all 24 cases are plotted in Fig. 8.

The predicted stability boundary for $\Gamma_\phi = 0.126$ is very sensitive to aspect ratio and wall conductivity because the Rayleigh number is close to critical and the smaller of the two aspect ratios considered ($0.707\Gamma_\phi$) with conducting sidewalls is subcritical (see Fig. 8), thus, the fluid would be stable absent vibration. At $\Gamma_\phi = 0.126$ there is excellent agreement between the experimental data point and the conducting prediction as may be seen in Fig. 7. There is a peculiar feature in the heat transfer measurements made at that aspect ratio, seen in Fig. 6(a) for $\epsilon > 60$. For the non-inverted configuration, the heat transfer begins to decrease beyond some acceleration even below pure conduction and the inverted case follows the same trend. This decrease in heat transfer might result from the experimental challenge in determining small changes in heat transfer imposed on a large bias (i.e., $\Delta\dot{Q} = 0.4\text{ w}$ and $\dot{Q} = 9.9\text{ w}$).

For the next experimental aspect ratio, $\Gamma_\phi = 0.249$, the present model is conservative and over estimates the amount of acceleration required, relative to observation.

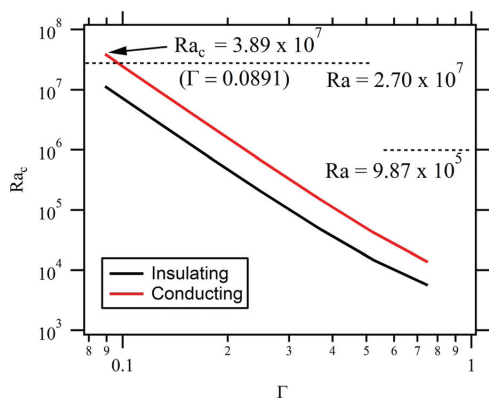


FIG. 8. Critical Rayleigh number curves (absent vibration) for the 16 cases considered in the Swift and Backhaus comparison. For Swift's three smallest aspect ratios [cases (a), (b), and (c) of Fig. 6], the experiments were conducted at a Rayleigh number of 2.7×10^7 ; for the largest, the experiment was conducted at 9.87×10^5 . Notice that the critical Rayleigh number for $\Gamma_\phi = 0.0891$ with conducting sidewalls is greater than the Rayleigh numbers from the experiment. In other words, for conducting sidewalls this configuration would already be stable absent vibration. This indicates some sensitivity to boundary conditions.

A significant departure from the present model is observed for ($\Gamma_\phi = 0.521$). There is again an unexplained feature in the heat transfer data: The amount of heat transferred, relative to conduction, nearly doubles before the gas is stabilized (see $20 < \epsilon < 60$), while the heat transfer is stationary for the case of heating from below as seen in Fig. 6(c). Linear stability analysis predicts that the growth rate decreases monotonically from zero vibration up to the stable point. The reason for the increase in heat transfer may be due to a change in the fluid flow pattern.

In the $\Gamma_\phi = 0.75$ case, a different Rayleigh number from the first three aspect ratios was considered by Swift and Backhaus. The model with conducting boundary conditions closely agrees with the experimental data. In this case, the heat transfer measurements reveal that the non-oscillating bias is not stationary with time and changes significantly over the accelerations considered, but with opposite sign relative to $\Gamma_\phi = 0.126$. The inverted measurement also has the same changing bias so it is suspected not to be related to buoyancy.

In general, the model most closely agrees with the data for conducting sidewalls. In all four cases the experimental region of stability is bounded by the four cases modeled. In two cases agreement is close, and in the other two, present theory suggests larger amplitudes would be required compared to what was observed experimentally. Considering just the experimental results to within the confidence bands established above, these data do not show any dependence with aspect ratio. This suggests that an unmodeled mechanism plays a significant role in the behavior of the experimental system.

As mentioned in Sec. IV A, the fact that heat transfer was measured instead of fluid flow creates added ambiguity in determining stability. There may exist a case where there is fluid motion and yet very little heat is transferred, in which case the fluid is mathematically unstable but from a heat transfer measurement appears stable. This may happen when there are several vertical roll cells.³⁴ To determine if such a case exists, the full nonlinear equations would have to be solved, so that heat transfer could be determined. It is enticing to try to visualize the flow experimentally to verify the conjecture of such a partial stabilization.

D. Impact of the differences between model and experiment

Now that a comparison has been presented, three of the differences between the model and the experimental conditions can be examined in more detail: Penetrable boundaries of the heat exchangers; acceleration gradients due to the standing wave field; and the significance of the gas compressibility not included in the model by making the Boussinesq approximation.

The flow of the fluid through the boundary is not treated, but the effect can be speculated upon within the current framework. Since the gas is not confined between the heat exchangers, the temperature gradient can be advected with the flow (see Fig. 9). When the particle displacement is non-zero, the linear portion of temperature gradient spans a

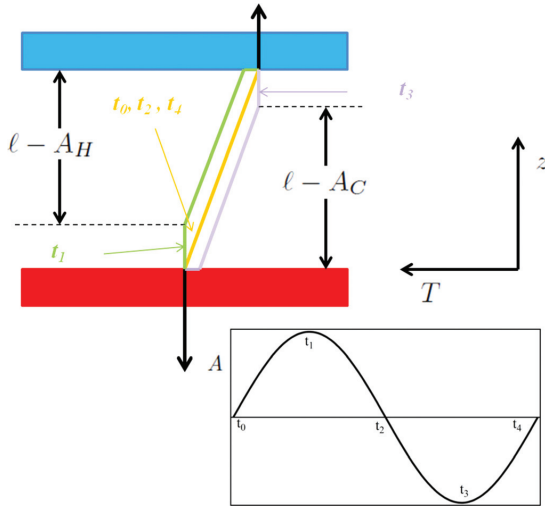


FIG. 9. Temperature gradient advection through one period of the drive is shown at three different phases of an acoustic cycle: The green and blue lines represent the gradient at the extremes of gas displacement while the orange curve is the gradient when the acoustic displacement is zero (and the acoustic velocity is maximum). In these representative diagrams, the fluid is in a state of quasi-equilibrium (the gas is experiencing no convection flow, only acoustic oscillation).

shorter distance, $L - A$, and the effective temperature difference is reduced. One may be tempted to shorten the characteristic length of the cavity by scaled displacement amplitude, A , and/or the temperature difference, ΔT . In either case the “effective” Rayleigh number would decrease, recall $Ra \propto \Delta T \ell^3$. If the Rayleigh number were decreased, then in all of the cases examined by Swift and Backhaus, the acceleration required to stabilize the flow at 100 Hz would be predicted by the present model to increase (see Fig. 10 for a representative curve).

This can be understood by examining a simple analog: The inverted pendulum. For the inverted pendulum, without

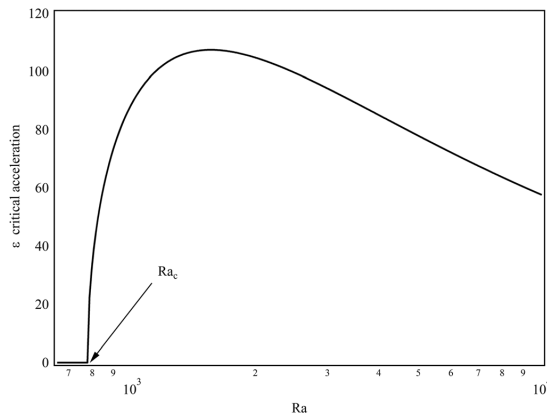


FIG. 10. Representative function for critical acceleration versus Rayleigh number. The global maximum is located just above the critical Rayleigh number in all cases studied.

damping, the synchronous stability boundary is $\omega/\omega_0 = \epsilon/\sqrt{2}$, where ω_0 is the natural frequency of the hanging pendulum.²⁸ As the natural frequency decreases, the acceleration required to stabilize the inverted pendulum increases. For thermally stratified fluids, the internal wave frequency is related to $PrRa$, thus as the Rayleigh number decreases so does the natural frequency, and the required acceleration must increase to suppress convection. However, very close to critical, the required acceleration must decrease. The analogy used by Swift and Backhaus relies on the inverted pendulum and therefore does not include a second restoring force, analogous to a spring, so that the decrease in acceleration close to critical is not predicted in their approach.

With regard to acceleration gradients, because the fluid is vibrated with an acoustic standing wave of finite frequency there is an acceleration gradient between the heat exchangers, and in principle this requires $g(z)$ in our approach. The effect of the gradient can be determined by specifying the gradient in the momentum equation,

$$\frac{\partial \mathbf{u}}{\partial t} = -\nabla p + Pr\Delta \mathbf{u} + PrRa(1 + \epsilon(z) \sin(\omega t))\theta \hat{e}_z. \quad (32)$$

Since the wavelength is substantially greater than the length of the pipe, $\epsilon(z)$ is approximated by a linear function between the heat exchangers, defined by

$$\epsilon(z) = \frac{2\epsilon_M}{1 + \delta} [(1 - \delta)z + \delta] \quad \delta = \frac{A_C}{A_H}, \quad (33)$$

where A_H and A_C are the particle displacement amplitudes at the hot and cold heat exchangers, respectively. For the sake of expedience, a two-dimensional rectangular enclosure will be considered. Upon application of the Galerkin method, the following system is obtained:

$$\begin{bmatrix} \mathbb{A}_{xx} & 0 \\ 0 & \mathbb{D} \end{bmatrix} \begin{bmatrix} \frac{\partial}{\partial t} \mathbf{c}^{(x)} \\ \frac{\partial}{\partial t} \mathbf{d} \end{bmatrix} = \begin{bmatrix} Pr\mathbb{B}_{xx} & PrRa\mathbb{C}_x + PrRa\epsilon_M \sin(\omega t)\mathbb{C}_x^{(z)} \\ \mathbb{E}_x & \mathbb{F} \end{bmatrix} \begin{bmatrix} \mathbf{c}^{(x)} \\ \mathbf{d} \end{bmatrix}, \quad (34)$$

where $\mathbb{C}_x^{(z)} = \langle q_{ik} \epsilon(z) \hat{e}_z, \mathbf{w}_{pr} \rangle$. Stability diagrams for $\Gamma = 1$, $Ra = 10^4$, and Pr are plotted for two different values of δ in Fig. 11. There is no noticeable difference between the two diagrams, and the aspect ratios in the Swift and Backhaus experiment lie between the values used in the approximation. It is thus suspected that the acceleration gradient has a negligible effect on dynamic stability in the experiment.

The effects of the heat exchangers beyond a time varying gradient are unknown and a possible source of the disagreement is suspected to result from assuming ideal rigid impenetrable boundary conditions. The departure from the Boussinesq restrictions indicates that the large temperature variations may have a significant impact. Further numerical analysis that removes these assumptions is required to fully

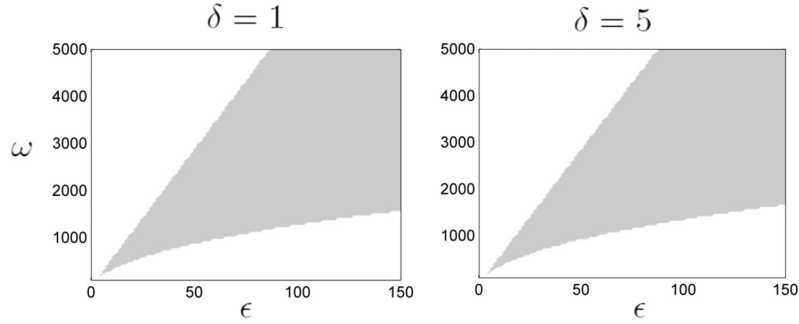


FIG. 11. Stability diagrams for two acceleration gradients. (Right) no gradient, (left) acceleration decreases by a factor of 5. The two plots appear to be nearly identical, showing that the presence of a significant vertical gradient in acceleration level through the fluid does not appear to produce substantial changes in the stability diagram. This suggests that this difference between the experiment and the present analysis is not likely due to the presence of an acceleration gradient in the experiment.

characterize the effects. Alternatively, an experiment could be conducted with the same fluid and geometrical properties except with rigid horizontal boundaries.

E. Synthesis of model and experimental results

In an effort to compactly summarize the experimental data, Swift and Backhaus created a non-dimensional group referred to as the *pulse tube convection number*,

$$N_{\text{ptc}} = \frac{A^2 \omega^2}{g\ell} (\beta \Delta T) = \frac{\text{Ra}_{\text{vib}}}{\text{Ra}}, \quad (35)$$

to characterize dynamic stability. This is analogous to the pendulum where a dimensionless group, N_{pendulum} , defined by

$$N_{\text{pendulum}} = \frac{A^2 \omega^2}{g\ell}, \quad (36)$$

characterizes stability, specifically if $N_{\text{pendulum}} > 2$, the pendulum is stable. Swift and Backhaus observed that N_{ptc} was not a linear function of ΔT , and appeared better approximated by a square root dependency. They then defined a modified N_{ptc} that reflected their experimental findings while maintaining the pendulum-like dependence,

$$N'_{\text{ptc}} = \frac{A^2 \omega^2}{g\ell} (\beta \Delta T)^{1/2}. \quad (37)$$

It should be noted that Eqs. (35) and (37) do not include χ , Γ , and ν ; thus it is not clear how to interpret their pulse tube convection number. Unlike the pendulum, stability cannot be characterized when the non-dimensional group exceeds a single number, because N_{ptc} does not include several variables known to be important. Therefore, the pulse tube convection number, N_{ptc} , has a functional dependence on those variables. The present numerical model determines the functional form of Ra_{vib} , allowing determination of the critical pulse tube convection number. For the aspect ratios examined, the scaling from the cubic enclosure was preserved, i.e., $\text{Ra}_{\text{vib}} \simeq f(\Gamma) \text{Ra}^{1.4}$, which allows a link between the present work and Swift's N_{ptc} :

$$(N_{\text{ptc}})_{\text{crit}}(\Gamma, \text{Ra}) = f(\Gamma) \text{Ra}^{0.4} \propto (\beta \Delta T)^{0.4}, \quad (38)$$

where $f(\Gamma)$ is some monotonic function of aspect ratio. Since there is no discussion by Swift and Backhaus on how an

exponent of 0.5 was chosen (although it is empirically suggested), it is assumed to be a rough estimate. The theoretical prediction of 0.4 is quite close to 0.5 and provides a scaling not directly predicted by the analogies presented in Swift and Backhaus's analysis.

V. CONCLUSION

The stability boundaries recovered from including side-walls differ significantly from the infinite layer. In particular the asymptotic scaling for the upper (synchronous) boundary changes from $\text{Ra}_{\text{vib}} \propto \text{Ra}^2$ for infinite layers to $\text{Ra}_{\text{vib}} \propto \text{Ra}^{1.4}$ for 3D bounded rectangular cavities over the range of aspect ratios and Rayleigh numbers considered here.

This change in scaling was also experimentally verified and previously not understood. For a cube, the critical state is not restricted to a single roll cell perpendicular to gravity for all Rayleigh numbers as is the case with an infinite layer; the number of vertical roll cells tends to increase as the Rayleigh number increases. The parametric resonance stability boundary was found to be insensitive to thermal boundary conditions, and a non-dimensional group (vibrational parametric number) was created that captures the boundary's location. The group can be fit with a linear function in Rayleigh number.

Rectangular and sinusoidal modulation were investigated as parametric drives. The rectangular drive has the obvious computational advantage over sinusoidal drive because it only requires an eigenvalue/vector solver whereas the sinusoidal drive requires numerical solution of a large number of ODEs with periodic coefficients. The harmonics introduced by the rectangular drive were discovered to be negligible and therefore only the fundamental is important. Fourier analysis allows the two drives to be compared by a multiplicative factor.

The spectral Galerkin method used here converges faster than other bases used in the literature, and analytical determination of the inner products guaranteed small errors and computational efficiency. The finite-roll approximation was again shown to coincide with the three velocity basis analysis.

The linear model was compared to one available data set: Pulse tube cryocooler heat transfer measurements as a function of inclination angle. The model was found to bound all data and agrees reasonably well for two of the four aspect ratios. The experiment has several features not captured in

the model: Velocity gradients, large density variations, penetrable horizontal boundaries, and a cylindrical geometry. Additional experiments need to be conducted within the framework of the linear model to further verify the model and determine the effect of each feature not captured.

ACKNOWLEDGMENTS

This work is supported by the Department of the Navy, Office of Naval Research, the Joseph and Irene Tobis Fellowship, and Applied Research Laboratory Exploratory and Foundational Research Program. Special thanks to Alexander Yu. Gelfgat.

- ¹G. W. Swift and S. Backhaus, "The pulse tube and the pendulum," *J. Acoust. Soc. Am.* **126**, 2273–2284 (2009).
- ²A. A. Wheeler, G. B. McFadden, B. T. Murray, and S. R. Coriell, "Convective stability in the Rayleigh-Bénard and directional solidification problems: High frequency gravity modulation," *Phys. Fluids A* **3**, 2847 (1991).
- ³P. M. Gresho and R. L. Sani, "The effects of gravity modulation on the stability of a heated layer," *J. Fluid Mech.* **40**, 783–805 (1970).
- ⁴G. Z. Gershuni and E. M. Zhukhovitskii, *Convective Stability of Incompressible Fluids* (Keterpress, Jerusalem, 1976), 330 pp.
- ⁵R. M. Clever, G. Schubert, and F. H. Busse, "Three-dimensional oscillatory convection in a gravitationally modulated fluid layer," *Phys. Fluids A* **5**, 2430–2437 (1993).
- ⁶S. Biringen and L. J. Peltier, "Numerical simulation of 3-D Bénard convection with gravitational modulation," *Phys. Fluids A* **2**, 754–764 (1990).
- ⁷I. Cisse, G. Bardan, and A. Mojtabi, "Rayleigh Bénard convective instability of a fluid under high-frequency vibration," *Int. J. Heat Mass Trans.* **47**, 4101–4112 (2004).
- ⁸M. Wadhi and B. Roux, "Natural convection in a long vertical cylinder under gravity modulation," *J. Fluid Mech.* **193**, 391–415 (1988).
- ⁹R. G. Ross and D. L. Johnson, "Effect of gravity orientation on the thermal performance of Stirling-type pulse tube cryocoolers," *Cryogenics* **44**, 403–408 (2004); 2003 Space Cryogenics Workshop.
- ¹⁰G. Thummes, M. Schreiber, R. Landgraf, and C. Heiden, "Convective heat losses in pulse tube coolers: Effect of pulse tube inclination," in *Cryocoolers 9*, edited by R. G. Ross (Plenum Press, New York, 2004), pp. 393–402.
- ¹¹S. Govender, "Linear stability and convection in a gravity modulated porous layer heated from below: Transition from synchronous to subharmonic solutions," *Transp. Porous Media* **59**, 227–238 (2005).
- ¹²S. Govender, "Stability of convection in a gravity modulated porous layer heated from below," *Transp. Porous Media* **57**, 113–123 (2004).
- ¹³S. Govender, "Stability of a gravity driven convection in a cylindrical porous layer subjected to vibration," *Transp. Porous Media* **63**, 489–502 (2006).
- ¹⁴I. Ryzhkov and Y. A. Gaponenko, "On the Boussinesq approximation in the problems of convection induced by high-frequency vibration," *J. Siberian Fed. Univ., Math. Phys.* **4**, 433–449 (1991).
- ¹⁵E. A. Spiegel and G. Veronis, "On the Boussinesq approximation for a compressible fluid," *Astrophys. J.* **131**, 442–447 (1960).
- ¹⁶G. Z. Gershuni and D. V. Lyubimov, *Thermal Vibration Convection* (Wiley, New York, 1998), 358 pp.
- ¹⁷A. Y. Gelfgat, "Different modes of Rayleigh-Bénard instability in two- and three-dimensional rectangular enclosures," *J. Comp. Phys.* **156**, 300–324 (1999).
- ¹⁸R. M. Carbo, "Dynamic stabilization of the Rayleigh-Benard instability in rectangular enclosures: A computational approach" (Order No. 3534708, The Pennsylvania State University). ProQuest Dissertations and Theses, 226. Retrieved from [http://search.proquest.com/docview/1272368305?accountid=13158\(1272368305\)](http://search.proquest.com/docview/1272368305?accountid=13158(1272368305)).
- ¹⁹A. Y. Gelfgat, "Two- and three-dimensional instabilities of confined flows: Numerical study by a global Galerkin method," *Comp. Fluid Dyn. J.* **9**, 437–448 (2001).
- ²⁰J. P. Boyd, *Chebyshev and Fourier Spectral Methods* (Dover, New York, 2000), 668 pp.
- ²¹R. P. Davies-Jones, "Thermal convection in an infinite channel with no-slip sidewalls," *J. Fluid Mech.* **44**, 695–704 (1970).
- ²²J. Mizushima and O. Matsuda, "Onset of 3d thermal convection in a cubic cavity," *J. Phys. Soc. Jpn.* **66**, 2337–2341 (1997).
- ²³I. Catton, "The effect of insulating vertical walls on the onset of motion in a fluid heated from below," *Int. J. Heat Mass Trans.* **15**, 665–672 (1972).
- ²⁴J. Mizushima and T. Nakamura, "Onset of three-dimensional thermal convection in a rectangular parallelepiped cavity," *J. Phys. Soc. Jpn.* **72**, 197–200 (2003).
- ²⁵D. Richards, *Advanced Mathematical Methods with Maple* (Cambridge University Press, Cambridge, 2002), 878 pp.
- ²⁶P. Blanchard, R. L. Devaney, and G. R. Hall, *Differential Equations* (Brooks/Cole, Pacific Grove, CA, 1998), 732 pp.
- ²⁷W. Magnus and S. Winkler, *Hill's Equation* (Dover, New York, 1979), 138 pp.
- ²⁸R. M. Carbo, R. W. M. Smith, and M. E. Poese, "Stability of the parametrically excited damped inverted pendulum: Theory and experiment," *J. Acoust. Soc. Am.* **128**, 1623–1631 (2010).
- ²⁹N. W. McLachlan, *Theory and Application of Mathieu Functions* (Oxford University Press, London, 1947), 401 pp.
- ³⁰S. Simakhina, "Stability analysis of Hill's equation," Master's thesis, University of Illinois at Chicago, 2003, pp 18–21.
- ³¹G. H. Wolf, "Dynamic stabilization of the interchange instability of a liquid-gas interface," *Phys. Rev. Lett.* **24**, 444–446 (1970).
- ³²V. V. Bolotin, V. I. Vorob'ev, V. A. Semenov, and V. K. Chernov, "Parametric stabilization of unstable forms of equilibrium of mechanical systems," *Izv. AN SSSR, Meckhanika Tverdogo Tela* **14**, 33–38 (1979).
- ³³J. L. Rogers, M. F. Schatz, J. L. Bougie, and J. B. Swift, "Rayleigh-Bénard convection in a vertically oscillating fluid layer," *Phys. Rev. Lett.* **84**, 87–90 (2000).
- ³⁴J. C. K. Tong, E. M. Sparrow, and J. P. Abraham, "Unified treatment of natural convection in tall narrow and at wide rectangular enclosures," *Numer. Heat Trans. A* **54**, 763–776 (2008).

Bibliography

- [1] E. L. Koschmieder, *Bénard Cells and Taylor Vortices*, Cambridge Monographs on Mechanics and Applied Mathematics (Cambridge University Press) (1993).
- [2] H. Bénard, “Les tourbillons cellulaires dans une nappe liquide,” *Rev. Gén. Sciences Pure Appl.* **11**, 1261–1271 (1900).
- [3] L. Rayleigh, “On convection currents in a horizontal layer of fluid when the higher temperature is on the under side,” *Philos. Mag.* **32**, 529–546 (1916).
- [4] A. R. Low, “Instability of viscous fluid motion,” *Nature* **115**, 299–300 (1925).
- [5] G. Venezian, “Effect of modulation on the onset of thermal convection,” *J. Fluid Mech.* **35**, 243–254 (1969).
- [6] R. G. Finucane and R. E. Kelly, “Onset of instability in a fluid layer heated sinusoidally from below,” *Int. J. Heat Mass Transfer* **19**, 71–85 (1976).
- [7] J. J. Niemela and R. J. Donnelly, “External modulation of Rayleigh-Bénard convection,” *Phys. Rev. Lett.* **59**, 2431–2434 (1987).
- [8] P. M. Gresho, “Time-dependent thermoconvective instability,” Ph.D. thesis, University of Illinois (1969).
- [9] P. Gresho and R. Sani, “The effects of gravity modulation on the stability of a heated fluid layer,” *J. Fluid Mech.* **40**, 783–806 (1970).
- [10] S. L. Garrett and M. E. Poese, “There’s (still) plenty of room at the bottom,” *Appl. Therm. Eng.* **61**, 884–888 (2013).
- [11] S. L. Garrett, “Thermoacoustic engines and refrigerators,” in *The 4th International Meeting of Advances in Thermofluids (IMAT 2011)*, volume 1440(1), 9–22 (AIP Publishing) (2012).
- [12] R. A. Johnson, S. L. Garrett, and R. M. Keolian, “Thermoacoustic cooling for surface combatants,” *Nav. Eng. J.* **112**, 335–345 (2000).

- [13] M. E. Poese, R. W. M. Smith, S. L. Garrett, R. van Gerwen, and P. Goselin, “Thermoacoustic refrigeration for ice cream sales,” in *Proc. 6th Gustav Lorentzen Conf. on Natural Working Fluids, IIR, Glasgow, Scotland* (2004).
- [14] M. E. Poese, R. M. Keolian, R. W. M. Smith, S. L. Garrett, and E. C. Mitchell, “Performance estimates of a helium-based thermoacoustic-Stirling chiller,” *Int. J. Low-Carbon Tech.* **8**, i79–i84 (2013).
- [15] P. Lengsholm and P. H. Pedersen, “Development of energy saving ice cream cabinet,” Final Report, Danish Technical Institute (Energy), Taastrup, Denmark (2000).
- [16] R. M. Carbo, “Dynamic stabilization of the Rayleigh-Bénard instability in rectangular enclosures: A computational approach,” Ph.D. thesis, The Pennsylvania State University (2012).
- [17] R. M. Keolian, “Modulations of driven nonlinear surface waves,” Technical Report 44, Department of Physics, University of California, Los Angeles (1985), Office of Naval Research Contract 4-484024-25895.
- [18] E. I. Butikov, “On the dynamic stabilization of an inverted pendulum,” *Am. J. Phys.* **69**, 755–768 (2001).
- [19] G. Wolf, “The dynamic stabilization of the Rayleigh-Taylor instability and the corresponding dynamic equilibrium,” *Z. Physik* **227**, 291–300 (1969).
- [20] H. Holitzner and G. Wolf, “The use of resonance for the dynamics stabilization of the Rayleigh-Taylor instability and for the excitation of the related parametric instabilities,” *Rev. Sci. Inst.* **44**, 988–990 (1973).
- [21] F. Troyon and R. Gruber, “Theory of the dynamic stabilization of the Rayleigh-Taylor instability,” *Phys. Fluids* **14**, 2069–2073 (1971).
- [22] O. Sutton, “On the stability of a fluid heated from below,” *Proc. R. Soc. London, Ser. A* **204**, 297–309 (1950).
- [23] L. A. Segel, “Distant side-walls cause slow amplitude modulation of cellular convection,” *J. of Fluid Mech.* **38**, 203–224 (1969).
- [24] I. Catton, “The effect of insulating vertical walls on the onset of motion in a fluid heated from below,” *Int. J. Heat Mass Transfer* **15**, 665–672 (1972).
- [25] D. Mukutmoni and K. T. Yang, “Thermal convection in small enclosures: an atypical bifurcation sequence,” *Int. J. Heat Mass Transfer* **38**, 113–126 (1995).

- [26] J. Mizushima and O. Matsuda, “Onset of 3D thermal convection in a cubic cavity,” *J. Phys. Soc. Jpn.* **66**, 2337–2341 (1997).
- [27] J. Mizushima and T. Nakamura, “Onset of three-dimensional thermal convection in a rectangular parallelepiped cavity,” *J. Phys. Soc. Jpn.* **72**, 197–200 (2003).
- [28] C. Normand, Y. Pomeau, and M. G. Velarde, “Convective instability: A physicist’s approach,” *Rev. Mod. Phys.* **49**, 581–624 (1977).
- [29] R. M. Carbo, R. W. M. Smith, and M. E. Poese, “A computational model for the dynamic stabilization of Rayleigh-Bénard convection in a cubic cavity,” *J. Acoust. Soc. Am.* **135**, 654–668 (2014).
- [30] G. Ahlers, “Trends: Turbulent convection,” *Physics* **2**, 10.1103 (2009).
- [31] G. Ahlers, “Heat transfer and large scale dynamics in turbulent Rayleigh-Bénard convection,” *Rev. Mod. Phys.* **81**, 503–537 (2009).
- [32] G. Z. Gershuni and D. Lyubimov, *Thermal Vibrational Convection* (John Wiley & Sons) (1998).
- [33] S. Biringen and L. J. Peltier, “Numerical simulation of 3-D Bénard convection with gravitational modulation,” *Phys. Fluids A* **2**, 754–764 (1990).
- [34] G. V. Smith, “The effect of vibration on natural convection in rectangular enclosures,” Master’s thesis, Mississippi State University (1968).
- [35] R. E. Forbes, “The effect of vibration on natural convective heat transfer in a rectangular enclosure,” Ph.D. thesis, Mississippi State University (1968).
- [36] R. E. Forbes, C. T. Carley, and C. J. Bell, “Vibration effects on convective heat transfer in enclosures,” *J. Heat Transfer* **92**, 429–437 (1970).
- [37] J. L. Rogers, “Modulated pattern formation: Stabilization, complex-order, and symmetry,” Ph.D. thesis, Georgia Institute of Technology (2001).
- [38] J. L. Rogers, M. F. Schatz, J. L. Bougie, and J. B. Swift, “Rayleigh-Bénard convection in a vertically oscillated fluid layer,” *Phys. Rev. Lett.* **84**, 87–90 (2000).
- [39] J. L. Rogers, M. F. Schatz, O. Brausch, and W. Pesch, “Superlattice patterns in vertically oscillated Rayleigh-Bénard convection,” *Phys. Rev. Lett.* **85**, 4281–4284 (2000).
- [40] J. L. Rogers, W. Pesch, and M. F. Schatz, “Pattern formation in vertically oscillated convection,” *Nonlinearity* **16**, C1–C10 (2003).

- [41] J. L. Rogers, W. Pesch, O. Brausch, and M. F. Schatz, “Complex-ordered patterns in shaken convection,” *Phys. Rev. E* **71**, 066214 (2005).
- [42] G. W. Swift and S. Backhaus, “The pulse tube and the pendulum,” *J. Acoust. Soc. Am.* **126**, 2273–2284 (2009).
- [43] G. Thummes, M. Schreiber, R. Landgraf, and C. Heiden, “Convective heat losses in pulse tube coolers: Effect of pulse tube inclination,” in *Cryocoolers 9*, edited by R. G. Ross, 393–402 (Springer) (1997).
- [44] R. G. Ross and D. L. Johnson, “Effect of gravity orientation on the thermal performance of Stirling-type pulse tube coolers,” *Cryogenics* **44**, 403–408 (2004).
- [45] M. Ishikawa and S. Kamei, “Instabilities of natural convection induced by gravity modulation,” *Microgravity Sci. Technol.* **6**, 252–259 (1993).
- [46] A. Mialdun, I. I. Ryzhkov, D. E. Melnikov, and V. Shevtsova, “Experimental evidence of thermal vibrational convection in a nonuniformly heated fluid in a reduced gravity environment,” *Phys. Rev. Lett.* **101**, 084501 (2008).
- [47] V. Shevtsova, I. I. Ryzhkov, D. E. Melnikov, Y. A. Gaponenko, and A. Mialdun, “Experimental and theoretical study of vibration-induced thermal convection in low gravity,” *J. Fluid Mech.* **648**, 53–82 (2010).
- [48] V. Shevtsova, “IVIDIL experiment onboard the ISS,” *Adv. Space Res.* **46**, 672–679 (2010).
- [49] S. Mazzoni, V. Shevtsova, A. Mialdun, D. Melnikov, Y. Gaponenko, T. Lyubimova, and M. Z. Saghir, “Vibrating liquids in space,” *Europhys. News* **41**, 14–16 (2010).
- [50] A. A. Ivanova and V. G. Kozlov, “Thermal vibrational convection in a cavity under nontranslational oscillations,” *Fluid Dyn.* **38**, 372–386 (2003).
- [51] W. Merzkirch, *Flow Visualization*, 2nd edition (Academic Press, Orlando, FL) (1987).
- [52] G. S. Settles, *Schlieren and Shadowgraph Techniques: Visualizing Phenomena in Transparent Media* (Springer, Berlin) (2001).
- [53] L. E. Kinsler, A. R. Frey, A. B. Coppens, and J. V. Sanders, *Fundamentals of Acoustics*, 4th edition (John Wiley & Sons, Inc., Hoboken, NJ) (2000).
- [54] I. I. Ryzhkov and Y. A. Gaponenko, “On the Boussinesq approximation in the problems of the convection induced by high-frequency vibrations,” *J. Siberian Federal University* **3**, 433–449 (2010).

- [55] E. W. Lemmon, M. O. McLinden, and D. G. Friend, “Thermophysical properties of fluid systems,” in *NIST Chemistry WebBook, NIST Standard Reference Database Number 69*, edited by P. Linstrom and W. Mallard (National Institute of Standards and Technology, Gaithersburg, MD) (2013), <http://webbook.nist.gov>.
- [56] M. Conde Engineering, “Thermophysical properties of humid air: Models and background,” Technical Report, M. Conde Engineering, Zurich, Switzerland (2007).
- [57] G. Lang and D. Snyder, “Understanding the physics of electrodynamic shaker performance,” *Sound and Vibration* **35**, 24–33 (2001).
- [58] R. M. Carbo, R. W. M. Smith, and M. E. Poese, “Stability of the parametrically excited damped inverted pendulum: Theory and experiment,” *J. Acoust. Soc. Am.* **128**, 1623–1631 (2010).
- [59] H. M. Jaeger, S. R. Nagel, and R. P. Behringer, “Granular solids, liquids, and gases,” *Rev. Mod. Phys.* **68**, 1259–1273 (1996).
- [60] N. J. Mansfield and M. J. Griffin, “Difference thresholds for automobile seat vibration,” *Appl. Ergon.* **31**, 255–261 (2000).
- [61] R. Behringer, E. van Doorn, R. R. Hartley, and H. K. Pak, “Making a rough place ‘plane’: why heaping of vertically shaken sand must stop at low pressure,” *Granular Matter* **4**, 9–15 (2002).
- [62] R. J. Meijer, “The Philips Stirling thermal engine: Analysis of the rhombic drive mechanism and efficiency measurements,” Ph.D. thesis, Technical University Delft (1960).
- [63] J. Rienitz, “Schlieren experiment 300 years ago,” *Nature* **254**, 293–295 (1975).
- [64] S. Rasenat, G. Hartung, B. Winkler, and I. Rehberg, “The shadowgraph method in convection experiments,” *Experiments in Fluids* **7**, 412–420 (1989).
- [65] S. M. A. Aftab, O. Younis, and M. Al-Atabi, “Four decades of utilizing shadowgraph techniques to study natural convection in cavities: Literature review,” in *1st International Conference on Mechanical Engineering Research 2011*, volume 36 of *IOP Conf. Series: Materials Science and Engineering*, 012021 (2012).
- [66] I. Rehberg, E. Bodenschatz, B. Winkler, and F. H. Busse, “Forced phase diffusion in a convection experiment,” *Phys. Rev. Lett.* **59**, 282–284 (1987).

- [67] P. Kolodner, R. W. Walden, A. Passner, and C. M. Surko, “Rayleigh-Bénard convection in an intermediate-aspect-ratio rectangular container,” *J. Fluid Mech.* **163**, 195–226 (1986).
- [68] J. Whitehead and M. M. Chen, “Thermal instability and convection of a thin fluid layer bounded by a stably stratified region,” *J. Fluid Mech.* **40**, 549–576 (1970).
- [69] W. Schöpf, J. C. Patterson, and A. M. H. Brooker, “Evaluation of the shadowgraph method for the convective flow in a side-heated cavity,” *Experiments in Fluids* **21**, 331–340 (1996).
- [70] J.-Q. Zhong and J. Zhang, “Thermal convection with a freely moving top boundary,” *Phys. Fluids* **17**, 115105 (2005).
- [71] J. Zhang, S. Childress, and A. Libchaber, “Non-Boussinesq effect: Thermal convection with broken symmetry,” *Phys. Fluids* **9**, 1034–1042 (1997).
- [72] A. Belmonte, A. Tilgner, and A. Libchaber, “Turbulence and internal waves in side-heated convection,” *Phys. Rev. E* **51**, 5681–5687 (1995).
- [73] J.-Q. Zhong and J. Zhang, “Dynamical states of a mobile heat blanket on a thermally convecting fluid,” *Phys. Rev. E* **75**, 055301 (2007).
- [74] J. Zhang and A. Libchaber, “Periodic boundary motion in thermal turbulence,” *Phys. Rev. Lett.* **84**, 4361–4364 (2000).
- [75] H.-D. Xi, S. Lam, and K.-Q. Xia, “From laminar plumes to organized flows: the onset of large-scale circulation in turbulent thermal convection,” *J. Fluid Mech.* **503**, 47–56 (2004).
- [76] R. J. Schmidt and O. A. Saunders, “On the motion of a fluid heated from below,” *Proc. R. Soc. London, Ser. A* **165**, 216–228 (1938).
- [77] J. G. A. de Graaf and E. F. M. van der Held, “The relationship between the heat transfer and the convection phenomena in enclosed plane air layers,” *Appl. Sci. Res. A* **3**, 393–409 (1953).
- [78] A. Graham, “Shear patterns in an unstable layer of air,” *Phil. Trans. R. Soc. Lond. A* **232**, 285–296 (1934).
- [79] K. Chandra, “Instability of fluids heated from below,” *Proc. R. Soc. London, Ser. A* **164**, 231–242 (1938).
- [80] D. W. Ruth, K. G. T. Hollands, and G. D. Raithby, “On free convection experiments in inclined air layers heated from below,” *J. Fluid Mech.* **96**, 461–479 (1980).

- [81] H. Inaba, “Experimental study of natural convection in an inclined air layer,” *Int. J. Heat Mass Transfer* **27**, 1127–1139 (1984).
- [82] M. W. Thompson, “Measurement of acoustic streaming in a standing wave using laser doppler anemometry,” Ph.D. thesis, The Pennsylvania State University (2004).
- [83] K. E. Torrance, L. Orloff, and J. A. Rockett, “Experiments on natural convection in enclosures with localized heating from below,” *J. Fluid Mech.* **36**, 21–31 (1969).
- [84] S. Kimura and A. Bejan, “Mechanism for transition to turbulence in buoyant plume flow,” *Int. J. Heat Mass Transfer* **26**, 1515–1532 (1983).
- [85] M. K. Peck and L. H. Scott, “A flow visualization apparatus for natural convection,” *J. Phys. E: Sci. Inst.* **16**, 251–252 (1983).
- [86] F. Corvaro and M. Paroncini, “Experimental analysis of natural convection in square cavities heated from below with 2D-PIV and holographic interferometry techniques,” *Exp. Therm Fluid Sci.* **31**, 721–739 (2007).
- [87] H. M. Vivas, P. Merati, and J. Montefort, “Natural convection from a cylinder in a rectangular cavity using PIV,” Technical Report MAE-03-07, Western Michigan University (2003).
- [88] N. Rouger and F. Penot, “Experimental investigation of natural convection of air in a differentially heated cavity partitioned with a lintel,” in *5th European Thermal-Sciences Conference, The Netherlands* (2008).
- [89] F. Ampofo and T. G. Karayiannis, “Experimental benchmark data for turbulent natural convection in an air filled square cavity,” *Int. J. Heat Mass Transfer* **46**, 3551–3572 (2003).
- [90] J. T. Lir and T. F. Lin, “Visualization of roll patterns in Rayleigh-Bénard convection of air in a rectangular shallow cavity,” *Int. J. Heat Mass Transfer* **44**, 2889–2902 (2001).
- [91] C.-R. Yang, T.-C. Lin, and F.-H. Chang, “Particle size distribution and PAH concentrations of incense smoke in a combustion chamber,” *Environ. Pollut.* **145**, 606–615 (2007).
- [92] Y. S. Cheng, W. E. Bechtold, C. C. Yu, and I. F. Hung, “Incense smoke: Characterization and dynamics in indoor environments,” *Aerosol Sci. Technol.* **23**, 271–281 (1995).
- [93] A. Melling, “Tracer particles and seeding for particle image velocimetry,” *Meas. Sci. Technol.* **8**, 1406–1416 (1997).

- [94] S. G. K. Tennakoon and R. P. Behringer, “Vertical and horizontal vibration of granular materials: Coulomb friction and a novel switching state,” *Phys. Rev. Lett.* **81**, 794–797 (1998).
- [95] D. Rubin, N. Goldensohn, and G. A. Voth, “Failure and strengthening of granular slopes under horizontal vibration,” *Phys. Rev. E* **74**, 051307 (2006).
- [96] R. Son, J. A. Perez, and G. A. Voth, “Experimental measurements of the collapse of a two-dimensional granular gas under gravity,” *Phys. Rev. E* **78**, 041302 (2008).
- [97] J. R. de Bruyn, E. Bodenschatz, S. W. Morris, S. P. Trainoff, Y. Hu, D. S. Cannell, and G. Ahlers, “Apparatus for the study of Rayleigh-Bénard convection in gases under pressure,” *Rev. Sci. Instr.* **67**, 2043–2067 (1996).
- [98] R. J. Schmidt and S. W. Milverton, “On the instability of a fluid when heated from below,” *Proc. R. Soc. London, Ser. A* **152**, 586–594 (1935).
- [99] H. A. Thompson and H. H. Sogin, “Experiments on the onset of thermal convection in horizontal layers of gases,” *J. Fluid Mech.* **24**, 451–479 (1966).
- [100] S. M. ElSherbiny, G. D. Raithby, and K. G. T. Hollands, “Heat transfer by natural convection across vertical and inclined air layers,” *Trans. ASME* **104**, 96–102 (1982).
- [101] M. A. H. Mamun, D. A. Johnson, K. G. T. Hollands, and W. H. Leong, “Piv measurements of the flow field inside an enclosed cubical cavity in natural convection,” in *12th International Symposium on Applications of Laser Techniques to Fluid Mechanics, Lisbon, July 12-15, 2004* (2004).
- [102] F. van der Graaf, “Heat flux sensors,” in *Sensors: A Comprehensive Survey*, edited by W. Göpel, J. Hesse, J. N. Zemel, T. Ricolfi, and J. Scholz, volume 4, chapter 8, 295–322 (VCH, Weinheim, Germany) (1990).
- [103] O. F. Turan, S. E. Semercigil, and G. Chukkapalli, “Effect of structural vibrations on hot-wire probe response,” *Meas. Sci. Technol.* **4**, 1416–1425 (1993).
- [104] D. B. Thomas and A. A. Townsend, “Turbulent convection over a heated horizontal surface,” *J. Fluid Mech.* **2**, 473–492 (1957).
- [105] G. E. Willis and J. W. Deardorff, “Measurements on the development of thermal turbulence in air between horizontal plates,” *Phys. Fluids* **8**, 2225–2229 (1965).

- [106] Y. S. Tian and T. G. Karayiannis, “Low turbulence natural convection in an air filled square cavity: Part I: the thermal and fluid flow levels,” *Int. J. Heat Mass Transfer* **43**, 849–866 (2000).
- [107] E. L. Koschmieder and M. I. Biggerstaff, “Onset of surface-tension-driven Bénard convection,” *J. Fluid Mech.* **167**, 49–64 (1986).
- [108] R. Krishnamurti, “On the transition to turbulent convection. part 1. the transition from two- to three-dimensional flow,” *J. Fluid Mech.* **42**, 295–307 (1970).
- [109] H. J. Palmer and J. C. Berg, “Convective instability in liquid pools heated from below,” *J. Fluid Mech.* **47**, 779–787 (1971).
- [110] A. Visioli, *Practical PID Control*, Advances in Industrial Control (Springer, London) (2006).
- [111] F. J. Krieger, “Calculation of the viscosity of gas mixtures,” Technical Report, The RAND Corporation, U.S. Air Force, Santa Monica, CA (1951).
- [112] H. Cheung, L. A. Bromley, and C. R. Wilke, “Thermal conductivity of gas mixtures,” *AIChE J.* **8**, 221–228 (1962).
- [113] S.-C. Lee and B. Wang, “Characteristics of emissions of air pollutants from burning of incense in a large environmental chamber,” *Atmos. Environ.* **38**, 941–951 (2004).
- [114] D. J. Wollkind and L. M. Zhang, “The effect of suspended particles on Rayleigh-Bénard convection I. A nonlinear stability analysis of a thermal equilibrium model,” *Math. Comput. Modell.* **19**, 11–42 (1994).
- [115] D. J. Wollkind and L. M. Zhang, “The effect of suspended particles on Rayleigh-Bénard convection II. A nonlinear stability analysis of a thermal disequilibrium model,” *Math. Comput. Modell.* **19**, 43–74 (1994).
- [116] G. A. Milliken and D. E. Johnson, *Analysis of Messy Data*, 2nd edition (CRC Press, Taylor & Francis Group, Boca Raton, FL) (2009).
- [117] R. C. Littell, G. A. Milliken, W. W. Stroup, R. D. Wolfinger, and O. Schabenberger, *SAS for Mixed Models*, 2nd edition (SAS Press, Cary, NC) (2006).
- [118] J. Taylor, “Statistics 203: Introduction to regression and analysis of variance: Model selection: General techniques,” Stanford University, Department of Statistics: Lecture Notes (2005), URL: <http://statweb.stanford.edu/~jtaylo/courses/stats203/notes/selection.pdf>.

- [119] S. Hu, “Akaike information criterion,” Slides from Invited Lecture for the Statistical and Applied Mathematical Sciences Institute, Durham, NC (2012), URL: http://www4.ncsu.edu/~shu3/Presentation/AIC_2012.pdf.
- [120] A. Swaminathan, S. L. Garrett, and R. W. M. Smith, “Inhibition of Rayleigh-Bénard convection via oscillatory acceleration,” *J. Acoust. Soc. Am.* **137**, 2224 (2015), conference presentation: 169th Meeting of the Acoustical Society of America, 18 May 2015, Pittsburgh, PA USA.
- [121] G. W. Swift, *Thermoacoustics: A unifying perspective for some engines and refrigerators* (Acoustical Society of America, Melville, NY) (2002).
- [122] A. B. Berryhill and P. Spoor, “High-frequency pulse tubes can’t always be tipped,” *AIP Conference Proceedings* **1434**, 1593–1599 (2012), *Advances in Cryogenic Engineering*.
- [123] M. Shiraishi, K. Takamatsu, M. Murakami, and A. Nakano, “Dependence of convective secondary flow on inclination angle in an inclined pulse tube refrigerator revealed by visualization,” *Cryogenics* **44**, 101–107 (2004).
- [124] M. Shiraishi, M. Murakami, A. Nakano, and T. Iida, “Visualization of secondary flow in an inclined double-inlet pulse tube refrigerator,” in *Cryocoolers 14*, edited by S. D. Miller and R. G. Ross, 277–284 (International Cryocooler Conference, Inc) (2007).

Vita

Anand Swaminathan

Anand Swaminathan was born in 1987 in Philadelphia, PA. Raised in Lakewood Township, NJ, he attended grades 5-8 in the non-sectarian professional choir, the American Boychoir School, where he traveled to over 35 U.S. states, singing nightly concerts while completing schoolwork on the tour bus. He attended high school at Phillips Academy (Andover, MA), graduating in 2005, where he kindled a love for physics, history, theatre technology and production, and sound engineering. He graduated with honors from Wesleyan University (Middletown, CT) in 2009 with a BA in Physics. While at Wesleyan, he conducted research in the Quantum Fluids Laboratory, under the direction of Dr. Fred M. Ellis, where he studied vortex mediated dissipation of third sound flows in superfluid helium, leading to an undergraduate thesis. He also won several awards and scholarships in Physics and was inducted into the Phi Beta Kappa honor society. He joined the Graduate Program in Acoustics at Penn State in 2010, where he was a graduate research assistant in the Physical Acoustics group, working on convection in thermoacoustic devices, and also assisting with a variety of thermoacoustic development projects, leading to a Ph.D. During his graduate studies, he was advised by Drs. Matthew E. Poese, Robert W. M. Smith, and Steven L. Garrett. He has also been involved with the Acoustical Society of America, in the Penn State student chapter, as a representative on the ASA Student Council, and through service on several committees and initiatives. He is the first author on a peer-reviewed paper and has given five conference presentations.

Anand took his first job in theatre at the age of 13. From that beginning, he has worked as a sound designer and engineer for musicals, straight plays, dance productions, and musical concerts. He has also been employed as a stage electrician, lighting programmer, video technician, set carpenter, stagehand, flyman/rigger, and deck supervisor. He spent three summers at a Six Flags theme park, rising to the position of Assistant Technical Director. He also spent one year as a graduate fellow at Wesleyan, supporting theatrical productions and the teaching efforts of the Theatre and Dance Departments.

Anand lives in State College, PA, with his wife, the poet and university lecturer Lisa Mangini, where he also volunteers as an EMT and CPR instructor.